Pawel Jerzy Wojcik

Licenciado em Electrónica

Printable organic and inorganic materials for flexible electrochemical devices

Dissertação para obtenção do Grau de Doutor
em Nanotecnologias e Nanociências

Orientador: Doutora Elvira Maria Correia Fortunato, Professora Catedrática, Faculdade de Ciências e Tecnologia da Universidade Nova de Lisboa

Co-orientador: Doutor Rodrigo Ferrão de Paiva Martins, Professor Catedrático, Faculdade de Ciências e Tecnologia da Universidade Nova de Lisboa

Júri:

Presidente: Professor Doutor José Júlio Alves Alferes

Arguentes: Prof. Doutora Verónica Cortés de Zea Bermudez
Professor Doutor Albano Augusto Cavaleiro Rodrigues de Carvalho
Prof. Doutora Maria Manuela Silva Pires Silva

Vogais: Professor Doutor Rodrigo Ferrão de Paiva Martins
Professora Doutora Elvira Maria Correia Fortunato
Prof. Doutor Rogério Manuel dos Santos Simões
Prof. Doutor Luís Miguel Nunes Pereira
Doutor Diogo Miguel Franco dos Santos

FACULDADE DE CIÊNCIAS E TECNOLOGIA
UNIVERSIDADE NOVA DE LISBOA

Outubro de 2013

Pawel Jerzy Wojcik

Licenciado em Electrónica

Printable organic and inorganic materials for flexible electrochemical devices

Dissertação para obtenção do Grau de Doutor
em Nanotecnologias e Nanociências

Orientador: Doutora Elvira Maria Correia Fortunato, Professora Catedrática, Faculdade de Ciências e Tecnologia da Universidade Nova de Lisboa

Co-orientador: Doutor Rodrigo Ferrão de Paiva Martins, Professor Catedrático, Faculdade de Ciências e Tecnologia da Universidade Nova de Lisboa

Júri:

Presidente: Professor Doutor José Júlio Alves Alferes

Arguentes: Prof. Doutora Verónica Cortés de Zea Bermudez
Professor Doutor Albano Augusto Cavaleiro Rodrigues de Carvalho
Prof. Doutora Maria Manuela Silva Pires Silva

Vogais: Professor Doutor Rodrigo Ferrão de Paiva Martins
Professora Doutora Elvira Maria Correia Fortunato
Prof. Doutor Rogério Manuel dos Santos Simões
Prof. Doutor Luís Miguel Nunes Pereira
Doutor Diogo Miguel Franco dos Santos

Outubro de 2013

Printable organic and inorganic materials for flexible electrochemical devices

Acknowledgements

I would like to express my gratitude to all of those that directly or indirectly contributed and supported my work.

First of all, I would like to thank my supervisors Professor Elvira Fortunato and Professor Rodrigo Martins for the opportunity and privilege to perform scientific work at CENIMAT/CEMOP laboratories. They have been constantly forcing me to remain focused on achieving my goals. Their observations and comments helped me to establish the overall direction of the research and to move forward with investigation in depth. They always encourage me when needed and provide opportunities to present the results at international level.

I also owe a large thanks to my fellow CENIMAT/CEMOP/UNINOVA members. I would like to thank the whole group including all the members that came and went over the past 6 years, for making it an enjoyable time.

I want to thank in particular to Dr. Vitor Figueiredo with whom I shared an office, MSc. Ricardo Correia and future Dr. Jonas Deuermeier. The hilarious discussions and jokes (only the funny ones) always made the day much better. There were also several people that deserve special thanks for the professional relation. To Dr. Luís Pereira my close co-worker, with whom I enjoyed common journeys to project meetings and conversations about new ideas and innovative approaches in our common research work. To future Dr. Lidia Santos and MSc. Ana Sofia Cruz, my laboratory companions that significantly contributed to the work I am presenting in this dissertation. To Dr. Rita Branquinho, Dr. Joana Vaz Pinto, MSc. Alexandra Gonçalves and Eng. Sónia Pereira, which always provide advice and help concerning the laboratory facilities. To Manuel Quintela, Joel Figueiredo, Ricardo Ferreira, Salomão Lopes and Carlos Alcobia for all the help and technical support concerning laboratory infrastructure problems.

I would like to thank Portuguese Science Foundation (FCT-MCTES) for financing my work through project Electra PTDC/CTM/099124/2008 and the PhD grant SFRH/BD/45224. Moreover, I would like to thank for other financial support: Professor E. Fortunato's ERC 2008 Advanced Grant (INVISIBLE contract number 228144), "APPLE" FP7-NMP-2010-SME/262782-2 and "SMART-EC" FP7-ICT-2009.3.9/258203.

My mother and father, Ewa Wojcik and Piotr Wojcik, deserve special thanks. Over the years of my education you have provided me with time, emotional support, and the financial support I needed to reach this point of my life. I hope I will be able to provide the same for my children. I could not forget about my siblings: Anna Borysiuk, Tomasz Wojcik, Aleksandra Krypska and their families; my

grandparents: Helena Wojcik and Stanisław Wojcik, my whole family and family-in-law. Thank you for believing in me, and all the support you provided.

Large thanks to all my outside-of-work friends. To my lifelong friends: Magdalena Dąbek, Maciej Aleksiejczuk, Michał Aleksiejczuk, Maciej Rejniak, Janusz Kawka and Łukasz Kołodziej. Without you folks, my life would be much less enjoyable.

I am also thankful to Katarzyna Karpowicz-Osowska, Maciej Osowski, adorable Marysia Osowska, Izabela Stapor and to the family of Filonovich, to Sergej, Marina and Nastia for the time we spent together, for all the help to set up a home away from home and for always being someone to talk to.

Finally, I want to give special thanks to my beautiful wife Iwona Bernacka-Wojcik and daughter Aniela Anna Wojcik. Iwona, you have provided me with immeasurable emotional and practical support over the past six years of our marriage, and a long time before that. Aniela, you always help brighten a bad day and I thoroughly enjoyed the time I spent with you over this first year of your life. I look forward to a wonderful family friendship with you.

Resumo

A crescente procura do consumidor em eletrónica impressa tal como cartões inteligentes, embalagens inteligentes, *displays* de automóveis, papel eletrónico entre outros, levou ao crescente interesse em dispositivos electroquímicos obtidos exclusivamente por impressão. Estes componentes deverão ser desenvolvidos com base em filmes finos impressos que derivem de compostos pouco dispendiosos e largamente acessíveis. Nesta dissertação é apresentada a extensa investigação que foi desenvolvida para alcançar conceitos com eficiência energética obtidos por impressão tais como *displays* electrocrómicos e janelas inteligentes. Dentro deste vasto tema, o presente estudo teve um número específico de objetivos, contudo, o objetivo fulcral foi desenvolver sistemas com materiais de baixo custo (i.e misturas para impressão) a uma escala de laboratório, que seja compatível com uma escala industrial num processo *roll-to-roll*. Os resultados apresentados estão relacionados com três tópicos principais: (i) materiais electrocrómicos inorgânicos com dupla fase processados a baixa temperatura, (ii) melhoria da performance electrocrómica via engenharia de nanopartículas metal-óxido e (iii) electrólito no estado sólido altamente condutor e mecanicamente estável. Os primeiros dois tópicos estão relacionados com a estrutura cristalográfica dos filmes metal-óxido derivados do percursor sol-gel, que demonstrou ser crítica para a performance electroquímica. O método proposto para o controlo da microestrutura permite o desenvolvimento de filmes electrocrómicos que superam as estruturas amorfas ou nanocristalinas análogas apresentadas no estado da arte, devido à superioridade das suas propriedades químicas e físicas. Os materiais e processos desenvolvidos resultaram em dispositivos electroquímicos que exibem densidades ópticas na ordem de 0.82 e tempos de resposta menores que 3 segundos, atingindo performances que permitem aplicações práticas. O terceiro tópico diz respeito a um novo conceito de electrólito no estado sólido baseado num polímero cristalino dopado com sal de lítio, disperso na rede de uma resina polimérica termoendurecível. Este electrólito quasi-sólido imprimível vai de encontro aos requerimentos pretendidos para aplicações electrocrómicas, exibindo condutividades iónicas de 10^{-6} - 10^{-4} S cm^{-1} à temperatura ambiente, Módulo de Young numa gama de 0.1 -1.4 MPa e temperaturas de utilização até 115°C. De forma a extrair informação da massiva quantidade de dados computacionais, dos modelos dos sistemas de materiais desenvolvidos e da otimização da composição, foi aplicada uma eficiente metodologia matemática baseada em técnicas estatísticas. Esta abordagem reduz significativamente o número de experiências a realizar, mantendo no entanto uma elevada exatidão da análise. Através desta abordagem o número de experiências foi reduzido de 162 para 30 no caso dos filmes electrocrómicos de dupla fase, e de 729 para 28 no estudo do electrólito de estado sólido (quando comparados com a abordagem clássica de fatorial completo de nível três). A união entre métodos estatísticos e a formulação de materiais electroquimicamente ativos revela o potencial para maximizar as aptidões destes sistemas.

Keywords: *dispositivos electrocrómicos, electrónica por impressão, engenharia de nanopartículas, electrólito sólido compósito, nanoelectroquímica, óxido de tungsténio, desenho de experiências.*

Abstract

The growing demand of consumer printed electronics such as smart cards, smart packaging, automotive displays, electronic paper and others led to the increased interest in fully printed electrochemical devices. These components are expected to be developed based on printed thin films derived from cheap and widely accessible compounds. This dissertation presents the long stretch of technical research that was performed to realize printed energy efficient concepts such as electrochromic displays and smart-windows. Within this broad theme, the presented study had a number of specific objectives, however, the overall aim was to develop low-cost material systems (*i.e.* printable mixtures) at a lab-scale, which would be compatible with large-scale roll-to-roll processing. Presented results concern three main topics: (i) dual-phase inorganic electrochromic material processed at low temperature, (ii) enhancement in electrochromic performance *via* metal-oxide nanoparticles engineering, and (iii) highly conductive and mechanically stable solid-state electrolyte. First two topics are related to crystallographic structure of metal-oxide films derived from sol-gel precursor, which is shown to be critical for electrochemical performance. The proposed method of microstructure control enables development of electrochromic films which outperform their amorphous or nanocrystalline analogues presented in the state-of-the-art due to their superior chemical and physical properties. Developed materials and processes resulted in electrochemical devices exhibiting optical density on the level of 0.82 and switching time shorter than 3 seconds, reaching performance at practical level. Third topic concerns a new concept of solid state electrolyte based on plastic crystal doped with lithium salt, dispersed in a thermosetting polymer resin network. This soft matter printable electrolyte meets requirements for electrochromic applications, exhibiting ionic conductivities of 10^{-6} - 10^{-4} S cm^{-1} at ambient temperature, Young's Modulus in the range of 0.1 - 1.4 MPa and operational temperature up to 115 °C. In order to extract information from massive computational data, model developed material systems and optimize composition, an efficient mathematical methodology based on statistical techniques was applied. This approach significantly reduces the number of experiments to be realized, while maintaining a high accuracy of the analysis. Using this approach the number of experiments has been reduced from 162 down to 30 in case of dual-phase electrochromic films, and from 729 down to 28 in study on solid-state electrolyte (when comparing to classical three-level full factorial approach). Coupling of statistical methods with formulation of electrochemically active materials shows the potential to maximize the capabilities of these systems.

Keywords: *electrochromic devices, printed electronics, nanoparticle engineering, solid composite electrolyte, nanoelectrochemistry, tungsten oxide, design of experiments*

Table of contents

List of Figures

List of Tables

List of symbols, acronyms and abbreviations

α	-	angle between b and c in unit cell [°]
β	-	angle between a and c in unit cell [°]
β_i	-	main factor coefficient
β_{ii}	-	2nd order factor coefficient of quadratic element
β_{ij}	-	2nd order factor coefficient
β_{ijk}	-	3rd order factor coefficient
β_o	-	coefficient of the intercept
γ	-	angle between a and b in unit cell [°]
δ_{ij}	-	coefficient of binary elements $X_i X_j (X_i - X_j)$ and $X_i X_j X_k$ in canonical form of Scheffé models
ΔOD	-	optical density
ε	-	random error
λ	-	wave length [nm]
σ	-	ionic conductivity [S cm^{-1}]
σ_{NPs}	-	standard deviation of particle distribution [nm]
σ_{RT}	-	ionic conductivity at 20 °C
σ_0	-	ionic conductivity at 0 °C [S cm^{-1}]
σ_{-10}	-	ionic conductivity at -10 °C [S cm^{-1}]
σ_{40}	-	ionic conductivity at 40 °C [S cm^{-1}]
τ	-	certain period of time [s]
τ_{bl}	-	bleaching time [s]
τ_{col}	-	coloration time [s]
a	-	unit cell axes dimension
A	-	pre-exponential coefficient in Arrhenius equation
A3ple	-	Autonomous Printed Paper products for functional Labels and Electronics, European project realized within 7th Framework Programme for Research and Technological Development co-financed by European Commission (FP7-NMP-2010-SME/262782-2)
Ag/AgCl	-	silver chloride electrode
ANOVA	-	analysis of variance
AR	-	aspect ratio
A_r	-	number of surface active centers in MO_X cluster
A_r [%]	-	percentage of surface active center in MO_X cluster
ATO	-	antimony tin oxide
ATR TF-IR	-	attenuated total reflectance Fourier transform infrared spectroscopy
a-WO_3	-	amorphous tungsten trioxide
b	-	unit cell axes dimension
b_j	-	number of counts in j-th bin of a histogram plot
B_r	-	total number of active centers in MO_X cluster
c	-	unit cell axes dimension
CA	-	chronoamperometry

CAbs	-	chronoabsorptometry
CAD	-	computer aided drafting
CE	-	coloration efficiency
CHP	-	cumene hydroperoxide
CM	-	conductive matrix for ions
CQ	-	chronocoulometry
C_r	-	number of active centers in the bulk in MO_X cluster
C_r [%]	-	percentage of bulk active center in MO_X cluster
CV	-	cyclic voltammetry
d	-	arithmetic mean particle size
D	-	specified degree of mid-points identification
d_a	-	thickness of spin-coated film
d_b	-	thickness of dip-coated film
d_c	-	thickness of electrodeposited film
d_h	-	thickness of the hollow sphere, which determines the surface of interaction with ions in MO_X cluster; this value corresponds also to the bin size in a histogram plot
d_k	-	desirability value
d_m	-	thickness of solid-state electrolyte membrane
D_n	-	overall desirability
DOD	-	Drop-On-Demand
DOE	-	Design Of Experiments
DSC	-	differential scanning calorimetry
DSSC	-	dye-sensitized solar cells
E	-	Young's Modulus
e^-	-	electronic charge, electron
E_a	-	activation energy
$E_a^{\text{Zone A}}$	-	activation energy at temperature > 20 °C
$E_a^{\text{Zone B}}$	-	activation energy at temperature < 20 °C
EC	-	electrochromic *e.g.* EC display, EC window, EC film precursor or EC properties
EG-TFT(s)	-	electrolyte-gated thin film transistor or transistors
ETPTA	-	ethoxylated trimethylolpropane triacrylate
F Ratio	-	value of F-statistics computed from the ANOVA results
$f_k(Y_k)$	-	desirability function
FP7	-	7th Framework Programme for Research and Technological Development co-financed by European Commission
GF	-	geometrical factor of the electrochemical cell in Impedance Spectroscopy method
i	-	number of factors
$I(hkl)_i$	-	observed XRD intensity of $(hkl)_i$ plane
$I(t, A)$	-	electric current flowing within the defined period of time through limited cross-section area
i.e.p.	-	isoelectric point
$I_0(hkl)_i$	-	XRD intensity of $(hkl)_i$ reflection of polycrystalline sample
$i_{bleaching}$	-	anodic current peak value (bleaching of WO_3 based film)
$i_{coloring}$	-	anodic current peak value (bleaching of WO_3 based film)
ICSD	-	Inorganic Crystal Structure Database (FIZ Karlsruhe, Germany)

IGZO	-	indium gallium zinc oxide used as semiconductor
i_h	-	number of bins in a histogram plot
I_k	-	significance of the response
IPT	-	Inkjet Printing Technology
IS	-	Impedance Spectroscopy
ITO	-	tin doped indium oxide used as electronically conductive coating
IZO	-	indium zinc oxide used as electronically conductive coating
IZTO	-	indium zinc thin oxide used as electronically conductive coating
j	-	bin number in a histogram plot
k	-	number of a surface response
k_B	-	Boltzmann's constant
l	-	variable length of cylindrical electrochemical cell
L	-	number of levels for selected factor
L_1	-	length of an inner electrode in a cylindrical electrochemical cell
L_2	-	cell depth of a cylindrical electrochemical cell
LDPE	-	low-density polyethylene foil
Li^+	-	lithium ion
Li_yWO_3	-	tungsten bronze, where y is the fractional number of sites filled in the WO_3 lattice
$\log\sigma_0$	-	logarithm of ionic conductivity at 0 °C
$\log\sigma_{-10}$	-	logarithm of ionic conductivity at -10 °C
$\log\sigma_{40}$	-	logarithm of ionic conductivity at 40 °C
$\log\sigma_{RT}$	-	logarithm of ionic conductivity at 20 °C
m	-	order of mathematical function
m_{CM}	-	weight of conductive matrix consisting of plastic crystal and lithium salt
MEKP	-	methyl ethyl ketone peroxide
MO_X	-	metal oxide
m_{RPP}	-	weight of resin pre-polymer consisting of resin monomer (together with comonomers), activator and promoters
m_t	-	total mass of the mixture
m_{TiO2}	-	weight of TiO_2 nanopowder
m-WO_3	-	monoclinic tungsten oxide
$M_x^1M_y^2O_z$	-	ternary metal oxide where M^1 and M^2 are metals such as In, Ga, Sn or Zn
n	-	total number of surface responses
N	-	total number of reflections
n_a	-	number of nanoparticles in a population
NIR	-	near infra-red electromagnetic radiation (765 – 3200 nm)
NP(s)	-	nanoparticle or nanoparticles
NRMSE	-	Normalized Root Mean Square Error
Nylon 6	-	polycaprolactam
OAD	-	oxalic acid
OLED	-	organic light emitting device
ortho-$WO_3 \cdot 0.33H_2O$	-	orthorhombic tungsten oxide hydrate
OTP	-	One Time Password
p	-	number of coefficients in a canonical form of Scheffé model

$p(T)$	-	saturation water vapor pressure
p_0	-	saturation water pressure at 0 °C
PAN	-	polyacrylonitrile
PC	-	personal computer
PEDOT:PSS	-	poly(3,4-ethylenedioxythiophene) doped with poly(styrene-sulfonate)
PEG	-	polyethylene glycol
PEGDMA	-	polyethylene glycol dimethacrylate
PEN	-	polyethylene naphthalate foil (used as plastic substrates in printed electronics)
PEO	-	polyethylene oxide
PET	-	polyethylene terephthalate foil (used as plastic substrates in printed electronics)
pH	-	measure of the acidity or basicity of an aqueous solution
PI	-	polyimide foil (used as plastic substrates in printed electronics)
pre-TCSE	-	liquid mixture for thermosetting composite solid electrolyte development
Prob > F	-	significance probability in analysis of variance
PSS	-	poly(sodium 4-styrenesulfonate)
Pt	-	platinum
PTFE	-	polytetrafluoroethylene, known also as Teflon
PVA	-	polyvinyl alcohol
p-value	-	value of F-statistics computed from the ANOVA results
PVD	-	Physical Vapor Deposition
PVdF-HFP	-	polyvinylidenefluoride-co-hexafluoropropyle
q	-	specified number of mixture components
$Q(\tau, A)$	-	charge transferred within the defined period of time through limited cross-section area
Q_{INS}	-	charge density inserted
r	-	variable diameter of cylindrical electrochemical cell
R_1	-	diameter of an inner electrode in a cylindrical electrochemical cell
R_2	-	diameter of an outer electrode in a cylindrical electrochemical cell
R^2	-	coefficient of determination
R^2-adj()	-	adjusted coefficient of determination for given response
R2R	-	roll-to-roll printing processing
R_a	-	resistance of the sample in Impedance Spectroscopy measurement
r_h	-	outer diameter of the MO_X cluster
RMSE	-	root mean square error
RPP	-	resin pre-polymer
SA:V	-	surface-to-volume ratio
$SA:V^{(a)}$	-	surface-to-volume atomic ratio
SCN	-	Succinonitrile, plastic crystal
$SCN:Li^+$	-	mixture of Succinonitrile and lithium salt
Smart-EC	-	Heterogeneous integration of autonomous smart films based on electrochromic transistors, European project realized within 7th Framework Programme for Research and Technological Development co-financed by European Commission (FP7-ICT-2009.3.9/258203)

$SS_{residuals}$	-	sum-of-squares of the residuals
SS_{total}	-	sum of squares of the distances from a horizontal line through the mean of all Y values
t	-	time
T	-	temperature
$T(t, \lambda)$	-	transmittance at certain time and wave length
$TC(hkl)_i$	-	texture coefficient
TCO(s)	-	transparent conductive oxide(s)
T_{cp}	-	crystalline/plastic crystal phase transition temperature
TCSE	-	thermosetting composite solid state electrolyte
TCSE*	-	thermosetting composite solid state electrolyte after water wash-out
TFT(s)	-	thin film transistor(s)
TG	-	thermogravimetry
T_m	-	plastic crystal/liquid phase transition temperature
t-ratio	-	value of t-statistics
UPR	-	unsaturated polyester resin
UV	-	ultra violet electromagnetic radiation (300 – 400 nm)
UVS	-	spectrometer working in a range of ultra violet and visible electromagnetic radiation (frequently abbreviated as UV-Vis spectrometer)
VIS	-	visible electromagnetic radiation (400 – 765 nm)
V_{opt}	-	optimum coloring voltage
w_{CM}	-	stands for weight fraction of conductive matrix consisting of plastic crystals and lithium salt
W_k	-	weight of response
w_{OAD}	-	oxalic acid weight fraction
WO_X	-	tungsten oxide, in general
$WO_X \cdot aH_2O$	-	general formula of tungsten oxide hydrate, in which $a \in \{1, 1/3, 2\}$
w_{PTA}	-	peroxotungstic acid weight fraction
w_{RPP}	-	weight fraction of resin pre-polymer consisting of resin monomer (together with comonomers), activator and promoters
$w_{solvent}$	-	solvent weight fraction
wt%	-	concentration expressed in weight percent
w_{TiO2}	-	titanium dioxide weight fraction
w_{WOX}	-	tungsten trioxide weight fraction
X	-	stoichiometry of tungsten oxide expressed by WO_X; two forms are in use in this thesis: stoichiometric ($X = 3$, *yellow*) and sub-stoichiometric ($X = 2.9$, *blue*)
x_a	-	weight percent of lithium salt in a conductive matrix
x_b	-	weight percent of benzoyl peroxide
x_c	-	weight percent of N,N – dimethylaniline
x_d	-	weight percent of 6% cobalt naphthenate
x_h	-	orthogonal coordinate of an active site in MO_X cluster
X_i	-	an independent factor
XRD	-	X-ray Diffraction
y_h	-	orthogonal coordinate of an active site in MO_X cluster
Y_k	-	characteristic surface response

Y_k^{max}	-	maximum obtained value of response
Y_k^{min}	-	minimum obtained value of response
z_h	-	orthogonal coordinate of an active site in MO_X cluster
ZTO	-	zinc tin oxide used as semiconductor
1D	-	one-dimensional structure *e.g.* rod or wire
2D	-	two-dimensional structure *e.g.* lamella, plate or disk
3D	-	three-dimensional structure *e.g.* cube or sphere

Chapter 1

General introduction

Chapter 1. General introduction

Chapter 1. General introduction

Summary

This chapter includes an annotated literature review, placing the scope and results of following chapters in a wider context of current state-of-the-art. It supplements the publications appended in this thesis with motivation of the chosen scope, research objectives and methods.

1.1. Fundamental

1.1.1. Printed electronics

In recent years, the thin film technology has grown world-wide into a major research area. The importance of new material syntheses and cost-efficient processing for the industry has also resulted in a tremendous increase of innovative technologies. Printing techniques apart from being widely used in graphics, are promising and attractive fabrication methods for a cost-efficient electronics. An innovative and dynamic research in this area results in new materials and devices continue to emerge, demonstrating their potential to cope with ever-changing requirements and challenges of the electronic market. Some of the ultimate examples of high-performance partially or fully printed electronic devices include, among others, organic light emitting device (OLED) [1], bulk hetero-junction photovoltaic cells [2–4], biosensor (enzyme immobilization) [5], multilayer ceramic capacitor [6] and microwave antenna [7]. The growing demand for energy efficient applications, associated to the restricted power management of printed electronic systems, has also driven the research on electrochemical devices such as flexible electrochromic (EC) displays [8–10], electrochemical transistors [10–13], dye-sensitized solar cells and thin film batteries [9]. Main activity in this area is now directed to find low cost materials with semi-conductive and ion conductive properties that ensure desired functionality and are compatible with printed techniques.

The potential of electrochemical applications as practical devices is supported by the commercial interest in early-market prototypes of printed EC displays. In 2006 NTERA Inc. (USA) presented EC display (see Figure 1.1a) based on nanomaterials (NanoChromics^{TM} technology), namely titanium dioxide (titania, TiO_2) nanoparticles (NPs) coated with bis(2-phosphonoethyl)-4,4'-bipyridinium dichloride [9, 14]. A high contrast ratio was achieved by application of a white reflector comprising inorganic white pigment (*e.g.* rutile TiO_2 or zinc oxide - ZnO). The use of organic optically active material (viologen) guarantees fast switching speed of ~30 ms.

A flexible EC passive and active matrix addressed displays (see Figure 1.1b) have been demonstrating by ACREO Swedish ITC (Sweden) since 2007 [10, 11, 15–17]. Displays developed using solution processing based on standard printing and coating manufacturing techniques are based on conductive

polymer (poly(3,4-ethylenedioxythiophene) doped with poly(styrene- sulfonate, PEDOT:PSS) as EC material, exhibiting switching time below 1s.

In 2008 Aveso Inc. (USA, acquired in 2011 by Gemalto S.A., France) presented EC display embedded in a prototype of One Time Password (OTP) smart card (see Figure 1.1c) resulting in a good-quality, long-lasting (lifespan up to 5 years) and convenient product. The technology is based on application of organic pH single- or multi-color indicators (*e.g.* bromocrescol purple) which change color when a change in pH occurs [18].

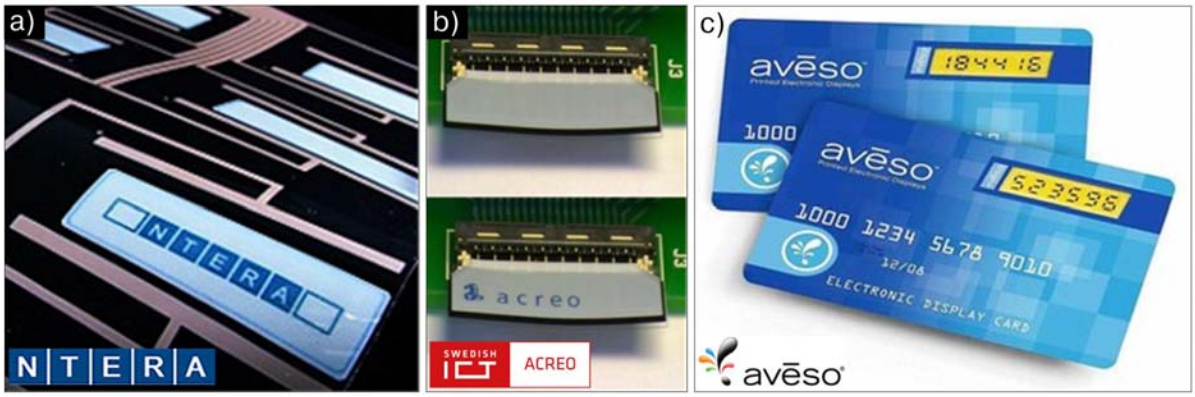

Figure 1.1. Early-market prototypes of printed EC displays based on organic EC materials presented by a) NTERA Inc. (http://www.ntera.com), b) ACREO SWEDISH ICT (http://www.acreo.se) and c) AVESO Inc. (http://www.avesodisplays.com)

EC window is an example of another electrochemical application in which printing technology is a potential key to successful commercialization. Existing commercial solutions of EC windows are manufactured using relatively slow and energy-intensive Physical Vapor Deposition (PVD) techniques, such as sputtering. Such solutions are available on the market since 2006 developed among others by VIEW http://www.viewglass.com (see Figure 1.2a) or SAGE Electrochromics http://www.sageglass.com (see Figure 1.2b), offering switching time in a range of 3 to 5 minutes, with relatively high power consumption of ~400 μW cm^{-2}.

Recently, the attention of researchers has been directed to printing techniques in order to drive down high manufacturing costs and increase throughput. National Renewable Energy Laboratory NREL (USA) have been developing printing methods for making EC windows based on inorganic rather than organic materials [19]. In 2009 they announced an innovative approach in which two electrodes make up the color changing part of the device. In the new EC window, counter electrode (nickel oxide, NiO) is impregnated with lithium ions while the working electrode (tungsten trioxide, WO_3) is drained of ions. Both electrodes are made by sprayed down cheap metal oxide precursors followed by thermal treatment (at 300° C). Applied voltage promotes ion movement between electrodes and causes the two electrodes to color in less than 30 s.

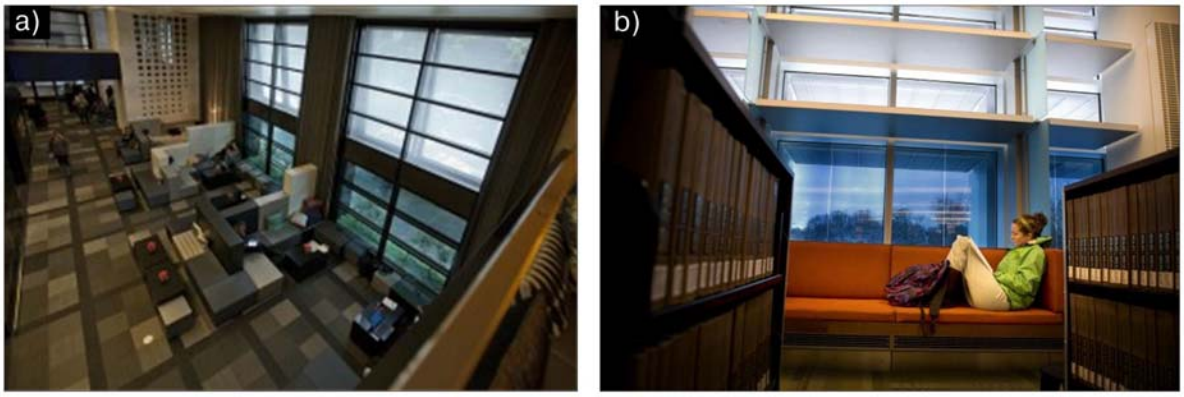

Figure 1.2. EC windows developed *via* PVD techniques installed by a) VIEW in W San Francisco Hotel, USA [20] and b) SAGE Electrochromics in Library of , While Bear Lake, MN, USA [21]

Presented examples show that niche applications of EC displays in *e.g.* smart cards, smart packaging labels and automotive displays have already been identified. Likewise, EC windows are slowly becoming a reality in energy efficient buildings. However, new applications such as aircraft glazing from Gentex (http://www.gentex.com) are being announced regularly as this is still an emerging technology area.

1.1.2. Printing techniques

There are various methods of printing used in printed electronics *e.g.* inkjet printed technology (IPT), electrophoretic, gravure-, flexography screen- or offset printing. More information and technological details about these techniques can be found in several books [22, 23]. The characteristics of these printing techniques offer many possibilities to a wide range of applications. Printing techniques in a field of electronics are used to apply coatings, to accurately deposit precise patterning or even to develop micro-structures. The list of advantages of printing technologies in research and industrial production seems endless. Concerning the lab-scale device development, the following aspects seem to be the most beneficial:

- fast prototyping;
- control on the film microstructure (possibility to fabricate coatings of mixed and doped composition by simple addition of NPs or MO_X precursor to the printable mixture);
- small amount of material needed to perform single functionality tests;
- low costs of printing facilities (*e.g.* standard desktop inkjet printer ~70 €, or basic manual screen-printing stage > 500 €);
- when it comes to industrial production following advantages determine the attractiveness of printing methods:
- reduction of manufacturing costs;

- ability to process large scale devices;
- reduction of waste;
- deposition on a flexible substrate in a roll-to-roll (R2R) processing;
- cost-efficiency of manufacturing (assembling of components is not required);

The selection of the printing method for intended research was dictated either by the requirements concerning printed films or level of printing system complexity. Due to the fact that direct development of printable mixtures for R2R systems is difficult at lab-scale, sheet-based techniques with a low-volume throughput such as IPT, stencil and screen-printing were used at this stage of research. The only experiments with R2R system were performed in collaboration with Centre Technique du Papier (Grenoble, France) using lab-scale flexographic printing system. A brief description of printing systems below, addresses only these techniques that have been actually used in this work.

IPT is a method suited for low-viscosity inks (1 – 20 cP), which patterns material by expelling picoliter droplets of liquid ink from the nozzle one at a time as the printhead is moved above the substrate in two directions. The application of IPT for EC device development is especially beneficial for optically active film deposition, as it offers precise patterning with volume accuracy and thickness in a range between hundreds of nanometers up to of several micrometers. Section 1.4.3.1 contains detailed description of the IPT system used in this research.

Preliminary experiments with pastes deposition were performed using stencil printing method (known also as doctor-blade). Stencil process uses a squeegee to press the fluid through defined opening onto the substrate. The pattern is determined by the stencil (*e.g.* scotch tape or laser cut PET foil), and the wet thickness of the printed film is equal to the thickness of the stencil. This technique was employed in preliminary tests on pastes development for EC film deposition and thermosetting composite solid state electrolyte (TCSE) pre-polymer.

Screen printed is probably the most versatile of all printing techniques used, due to its simplicity and reproducibility. In order to deposit material, a squeegee is used to move paste through a patterned screen to deposit onto rigid or flexible substrate. The squeegee provides shear stress to the paste to reduce viscosity and allows it to flow through the screen. This technique is especially interesting for TCSE pre-polymer deposition as it can provide sufficient wet thickness (15 - 40 μm) in a single printing pass, in contrast to most other printing techniques. Screen printing has also been used to develop prototypes of fully printed EC displays using both, commercial pastes (*e.g.* carbon and silver) and custom formulations (*e.g.* EC paste, TCSE, optical passivation or etching mask). Both stencil and screen printable pastes generally are of intermediate viscosity in a range of 1000 – 50000 cP. Section 1.4.3.1 contains detailed description of the screen printing system used in this research.

Flexographic printing process utilizes a flexible relief plate to transfer the ink from laser-etched roll called Anilox (supply the ink in a certain volume) to the flexible substrate. This technique uses low-viscosity inks of 50 - 500 cP formulated with volatile solvents. Wet thickness achievable in a single printing pass is 0.75 - 2 μm. In these studies flexographic printing was used to deposit conductive electrodes (*i.e.* carbon and silver) on paper substrate and EC film precursor on tin doped indium oxide (ITO, In_2O_3:Sn) coated PET foil to develop prototype of EC display on paper.

In theory, material processing *via* printing techniques is simple and does not cause major problems in understanding. In practice, implementation of the technology is usually complex and requires multidisciplinary skills. Reliable operation depends on careful design, implementation and operation of a complete system where no element is trivial.

1.1.3. Basics of electrochromism

Electrochromism is the unique property of the material whose color changes in response to the insertion/extraction of ions and electrons driven by an external potential. Due to the specific property of tungsten oxide (WO_X), developed devices have the ability to change their optical state from dark blue to near or fully transparent in a controllable and reversible way. Such optical switching is performed by insertion/extraction of electrons together with alkali ions such as Li^+.

Let's use the classical electrochemical cell presented in Figure 1.3 to explain the basics of EC device operation. Such electrochemical (or more precisely electrolytic) cell is made of two electrodes immersed in an electrolyte containing ions (*i.e.* cations). When the external voltage is supplied between electrodes the oxidation and reduction reactions occur respectively on anode and cathode. Two different kinds of EC materials exist, depending if they are colored upon charge insertion (cathodic) or extraction (anodic). As the presented work is focused on devices developed based on cathodic material (WO_X), the optically active material (working electrode) is placed on a cathode which attracts cations (Li^+). External voltage shuttles ions into and out (reversed polarization) of the material causing coloring (Figure 1.3a) and bleaching action (Figure 1.3b), respectively.

Generalized mechanism of electrochemical reaction for cathodic EC material causing coloring and bleaching action can be expressed by Equations 1.1 and 1.2, respectively.

$$WO_X + y(Li^+ + e^-) \Rightarrow Li_yWO_X \quad (1.1)$$

$$Li_yWO_X - y(Li^+ + e^-) \Rightarrow WO_X \quad (1.2)$$

According to above reaction, EC material in transparent state (WO_X) can be switched reversibly to a colored state by both insertion of ions and electrons to form tungsten bronze (Li_yWO_X, where y is the fractional number of sites filled in the WO_3 lattice). The response rate of the EC material depends of the electrons and cations dynamics. Consequently, low resistance of EC material together with

highly conductive electrolyte is the key to realize EC device with switching time at practical level. From the other hand, high number of electrochemically active centers available for reaction guarantees high contrast between colored and bleach state (high optical modulation).

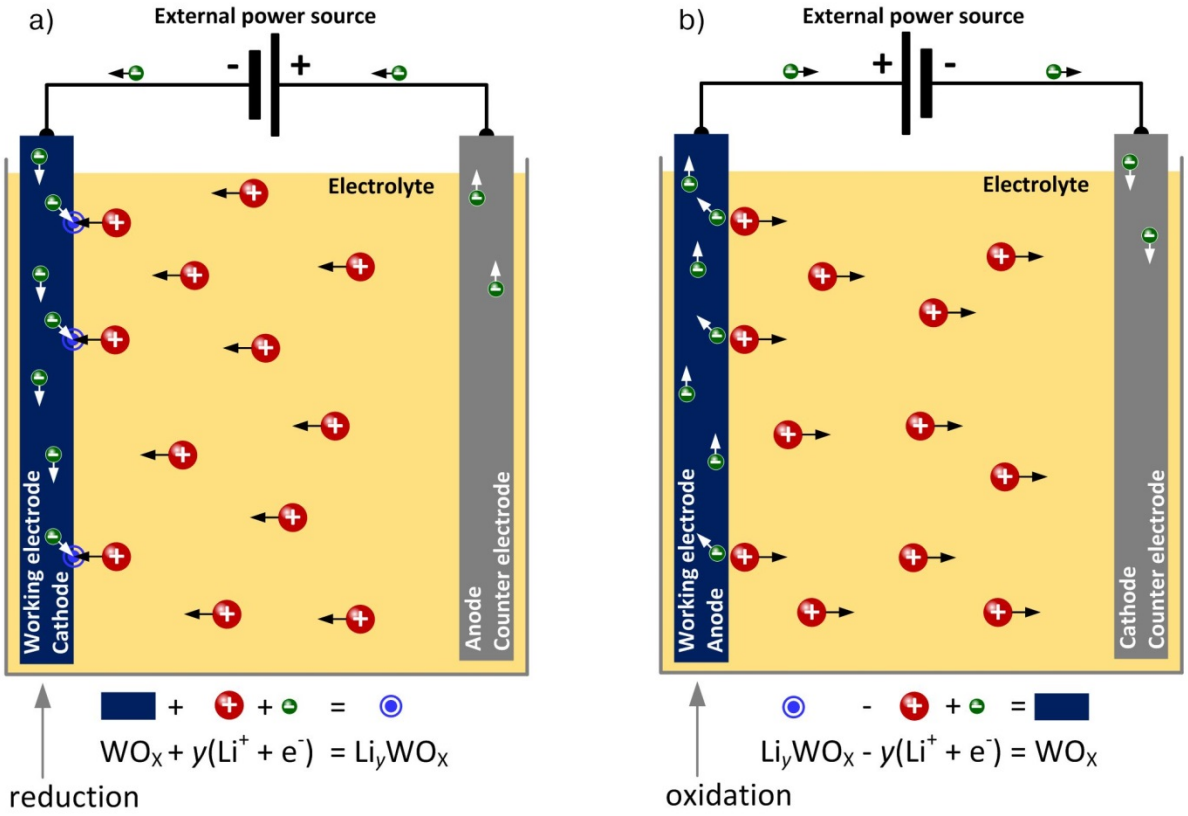

Figure 1.3. Schematic representation of EC device operation in a configuration of electrolytic cell during a) coloration and b) bleaching action

1.1.4. Energy efficient concepts

The growing demand of consumer printed electronics such as smart cards, smart packaging, automotive displays, electronic paper and others is expected to contribute to the high sales growth of fully printed displays. Integration of display seems to be essential in above applications as it delivers microcontroller output to the operator through visual media. The displays integrated in such devices are powered from batteries which are limited in size and capacity. Moreover, displays are expected to consume more energy as their size and resolution will continue to increase with the larger amount of data to be displayed. As the energy consumption aspects related to displays operation are crucial, the goal of energy efficiency is to reduce the amount of energy required to provide functionality of these products. Due to the memory effect (zero-power consumption) EC display do not require continuous refreshing. Rewriting is only performed for picture information changes. Moreover, an electrolyte loaded with highly reflective NPs (*e.g.* TiO_2) increases the contrast between background and colored

electrode, so that the backlight is not required (see Figure 1.4a). The fact that bistable EC display working in reflection mode requires extremely low energy to operate makes it one of the best candidates for these applications.

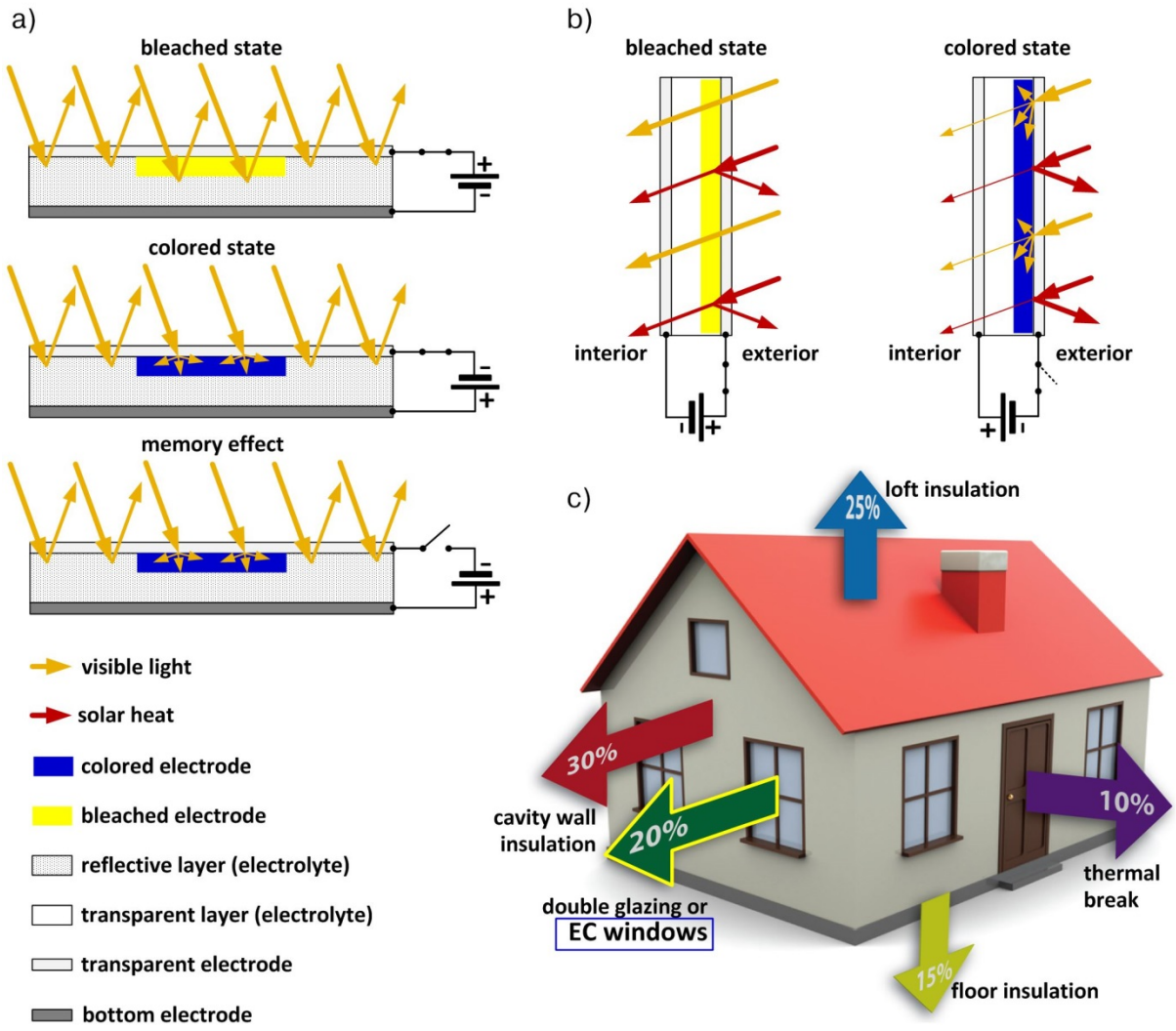

Figure 1.4. Diagrams showing the principles of energy efficiency concept in a) EC display and b) EC window; c) estimated values of the heat loss through building elements with possible solutions to reduce the adverse effect of insufficient insulation

Let's consider smart window as another example of energy efficient solution in which the use of electrochromism has been identified and supported by the commercial interest. This type of device dynamically controls daylight (electromagnetic radiation range: ultra violet, UV, 300 – 400 nm; visible, VIS, 400 – 765 nm; near infra-red, NIR, 765 – 3200 nm) and solar heat gain by dimming to a dark state as it is presented in Figure 1.4b. Even in a clear state, EC windows reflect substantial amount of solar heat while maintaining a transparent view to the outdoors. Such devices increase solar heat gain in winter and decrease solar heat gain in summer, while reducing lighting costs under all atmospheric conditions. Therefore, EC widows allow a building to use less heating or cooling energy

to achieve and maintain comfortable conditions. When considering the heat loss through building elements, it turns out that windows are one of the weakest points (see Figure 1.4c). It is relatively easy to insulate other elements of the building by providing proper insulation, however in case of windows the most reasonable is to mount double glazing or install EC windows.

Resuming, all-solid-state printed EC devices working either as displays or smart windows are of considerable technological and commercial interest mainly due to their power efficiency. The work presented in this thesis aims at providing scientific methods that could increase the ability to solve existing technological problems and contribute the popularization of those solutions.

1.1.5. Structure of printed EC device

Application of EC materials in smart windows and bistable displays are the most widely given examples of electrochromism in practical use. A printed EC device can be developed in two variants, namely sandwich-like structure (Figure 1.5a) and thin film layer stack (Figure 1.5b). Both illustrate standard construction based on inorganic EC material that allows basic features of the device under simple operating conditions.

Presented structures comprise of five functional layers namely, two electron conductors, electrolyte, EC film and counter electrode. Constituent materials are formed between two or on top of a single substrate, ensuring sufficient mechanical support. A single thin EC film has to be deposited on an electronically conductive and transparent substrate, typically a glass or plastic foil (*e.g.* polyethylene terephthalate - PET, polyethylene naphthalate - PEN or polyimide - PI) coated with transparent conductive oxide or oxides (TCO, *e.g.* ITO). The electrolyte which binds the structure and ensures electrical integrity between working and counter electrode plays dual role in the device. Firstly, contains lithium ions (Li^+) and hence, serves as ion storage. Secondly, enables ion transport while being insulating for electrons. Such ion storage and conductor can be either liquid, gel, semi-solid or solid-state material, depending on the device functionality and expected performance.

Liquid and gel electrolyte are typically used in lab-testing devices or electrochemical cells, enabling convenient measurements of the EC film properties. Semi-solid and solid-state electrolytes are a reasonable choice as long as the commercial application of the EC device is concerned. A transparent substrate coated with TCO, the EC film (WO_X) as working electrode and an electrolyte, are the three elements common in both structures. The opposite electrode consists of counter electrode (*e.g.* WO_X or C) and electronically conductive coating either deposited on a second substrate (typically ITO on glass, polymer foil or paper) or printed on top of the device structure (*e.g.* silver). Sometimes the counter electrode is omitted during the device development as the electronically conductive coating made of metal oxide exhibits charge capacity high enough to balance the electrochemical reaction. However, this may lead to significant deterioration in long term stability

(due to TCO degradation). The requirement of the transparency for the opposite electrode depends of the device functionality. EC displays usually contain opaque electrolyte in order to increase contrast and enhance readability, and thus the opposite electrode does not need to be transparent. However, in case of EC windows which are seen through in a bleached state, all the elements must be transparent.

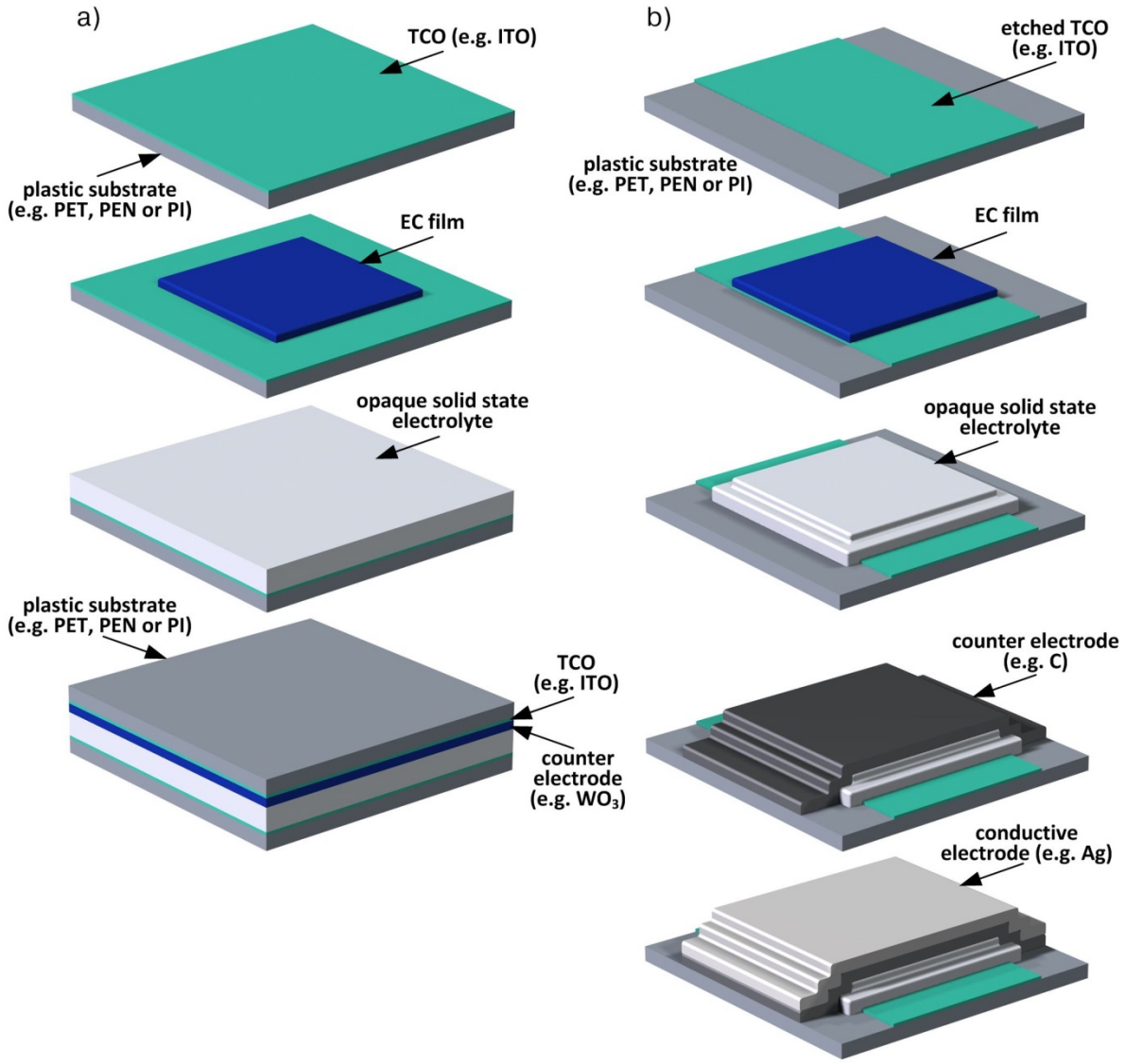

Figure 1.5. Schematic drawing of printed EC device in a) a sandwich-like and b) thin film layer stack configuration

Another aspects related to device structure are the encapsulation, sealing and protective barriers. EC devices comprising liquid, gel or solid-state polymer electrolyte (majority of the state-of-the-art prototypes) are sensitive to the environment as the transport properties of the ions depends upon the humidity. To prolong device lifetime, many different types of protection were used to render it insensitive to the surrounding environment *e.g.* hot-press of Surlyn (DuPont) [24], sealing with transparent polymer film [8, 25] or thermocure epoxy sealant [14]. The solution to overcome labor intensive and time consuming encapsulation is to develop a solid-state electrolyte with superior

stability and enhances mechanical properties. Such material would encapsulate the EC device by itself by strong adhesion to the substrates, in between which is placed (*i.e.* in sandwich-like structure shown in Figure 1.5a). Overprinting by such electrolyte would also provide encapsulation of all films below that layer and provide anti-scratching surface in device with thin film layer stack configuration (see Figure 1.5b). Solid-state electrolyte that meets these expectations was developed within the work described in this thesis. Chapter 6 is devoted to this topic, containing details on formulation, application and performance of this material.

1.2. Motivation

A literature on electrolytes suitable for EC devices is vast. However, none of the reported materials fully complies with requirements imposed by printing techniques. In order to develop printable electrolytes, several studies have been conducted including inkjet printing of ionic liquid-polymer gel [12, 26] and semi-dry polymer electrolyte [27, 28], screen-printing of ionic polymers [10] or drop-casting of liquid electrolyte followed by specific encapsulation [9]. Although the results of these studies are very promising and greatly enrich current state of knowledge, provided solutions are not satisfactory, as far as their application in mass production is concerned. As reported from Löffelmann *et al.* [26] an inkjet printed ionic liquid-polymer gel with acrylate and methacrylate monomers exposed to UV irradiation under ambient atmosphere does not polymerize due to the inhibiting influence of oxygen on radical polymerization. In order to overcome this problem, an inert atmosphere is required for curing and deposition process, which significantly reduces capabilities of such material system. Other studies performed by Dasgupta *et al*. [27, 28] report on using IPT for a deposition of semi-dry polymer electrolyte resulted in well performing fully printed electrolyte-gated thin film transistor (EG-TFT) processed at ambient atmosphere. However, as the operation of such device depends of the water content in the ion conductive film, and thus the environment conditions, it is most probable that a specific encapsulation is required when it comes to practical applications. The use of ionic polymers (*e.g.* poly(sodium 4-styrenesulfonate), PSS) as electrolyte processed *via* IPT [11] or screen printing [10] performed at Linköping University together with Acreo Swedish ICT, despite the fact of being very effective, is restricted to the application in devices based on a specific organic EC film (PEDOT:PSS), limiting its use in printed electronics at large. Ultimately, the application of drop-casted liquid electrolyte in printed electrochemical devices requires a sophisticated encapsulation, *e.g.* glass beads separated electrodes sealed with UV curable glue under vacuum conditions [9], which is time-prohibitive in mass production process, as it requires additional assembling of components.

Development of printed films derived from inorganic nanostructured semiconductors is also not a trivial task. It represents a continuing, main path of activity in nanotechnology. An interest of

researchers is driven by many attractive attributes of those nanoscale materials (*e.g.* enhances charge transport or high specific surface area) especially favorable for electrochemical applications. Many attempts have been made to deposit various metal oxide (MO_X) NPs in order to form an electrochemically active nanocrystalline film. Study performed by Liu and Coleman [8] reports on screen-printed TiO_2, silicon dioxide (SiO_2, also known and silica) and aluminum oxide (Al_2O_3, also known as alumina) nanocrystals coated with antimony tin oxide (ATO), applied as optically active film in EC display. The use of printed films containing TiO_2 nanocrystals was also reported by Corr [14] and Pettersson *et al*. [24], however instead of inorganic coating the mesoporous electrode was modified with organic viologens. These reports demonstrated that the application of printing techniques for deposition of MO_X dispersion provides an excellent method for the production of EC electrodes. However, a high temperature is necessary to form a conductive functional film, which excludes the application of these methods in flexible electronics.

Unsuitable or inconvenient nature of those materials in intended applications initiated studies aimed at all-printable devices, whereby all components including ion conductive solid-state electrolyte and inorganic semiconductive layer are built up step by step onto the same substrate, preferably in R2R processing under ambient atmosphere. This approach eliminates additional assembling and allows for integration of functional films within components significantly reducing circuit complexity. The principal motivation was thus, to overcome technological issues and develop materials and processes compatible with printing processing.

The work described in following chapters of this dissertation was performed mainly within two European FP7 projects (7^{th} Framework Programme for Research and Technological Development) Smart-EC (FP7-ICT-2009.3.9/258203) and A3Ple (FP7-NMP-2010-SME/262782-2) co-financed by European Commission. Smart-EC aims at the development of self-powered (energy harvesting and storage) EC device integrating printed components on a flexible substrate for energy saving, comfort and security in automotive (reconfigurable icons and controlled reflection surfaces), e-cards and smart packaging sectors. Within A3Ple, a new generation of sustainable paper electronics products with specific autonomous functionalities aiming at interacting with their users and/or reporting changes in their environment is developed. Development of printed flexible electronics at which both project are aiming requires integration of EC display being the main scope of presented dissertation, with circuitry and power source on a flexible or semi-flexible substrates. Participation in these projects provides additional motivation and guarantees a high level of interdisciplinary collaboration between many academic and industrial partners from other European countries. On the other hand it also ensures exploitation of results *via* proper technology transfer to industry at all product chain levels (materials, devices and end users).

1.3. Objectives and research hypotheses

In general, presented thesis aims at two targets. Firstly, mastering a specific subject concerning development of materials and processes for printed electrochemical devices, in particular EC devices. Secondly, extending the body of existing knowledge related to this research topic, by providing new solutions and expertise.

Printing manufacturing of electronics creates a room for electronic innovations that are lightweight, flexible, and could be produced on cheap and flexible materials such as plastic foil or paper. Printed electronics processes use standard equipment *e.g.* IPT, screen-printing or flexography. Therefore, innovation lies mainly in the formulation of electronically functional printable mixture, used to print working purposeful devices such as EC displays. The overall aim of this study was thus, to develop material systems (*i.e.* printable mixtures) at a lab-scale, which would be compatible with large-scale printing, R2R processing.

With the use of printing system, films with different functions are deposited by building up layers using additive deposition processes (*i.e.* coating and patterning) combined with post-treatment processes (*e.g.* in-line furnace or UV-irradiation unit) until an electronic device is generated. Thus, a suitable material system can be selectively deposited and treated in order to obtain a functional or passive film. For practical reasons, such printable material should be formulated as a mixture curable/drying at room or elevated temperature, or by UV exposure. Temperature and moisture content of printing environment can affect the rate of cure/drying and the physical properties of the film (most likely only the surface). However, properly formulated printable mixture processed in a controlled area results in a properly cured/dried film.

A typical functional material used in printed electronics is basically less complicated mixture of chemical compounds when comparing to the typical dye based formulations used in printed graphics. Of particular concern is the solvent in which material is dispersed since it is often identified as hazardous and possess objectionable odors. Solvent is vitally important when any printable mixture formulation is concerned, as it keeps the material in a liquid form when it is transferred to the substrate. As the printed mixture must not dry out on the printing element, an exposure to air for several hours with no solvent evaporation is required for industrial screen-printing process. Solvents with a low vapor pressure at room temperature are preferable. In the most of screen-printable pastes, solvent (*e.g.* long chain esters, half alcohol esters or terpenes) is completely decomposed or burned-off during film post-treatment leaving no trace of it in the final film [29]. In contrary, other printing processes *e.g.* the gravure and flexographic printing require a solvent that evaporates rapidly such as water, volatile alcohols or short chain esters. When the drying process is required, the removal of the solvent is considerable. Furthermore, the adaptation of printing facility leading to lesser exposure of wet film to air may be necessary in order to comply with safety issues. Emission of volatile cleaning

solvent used in a cleanup process after TCSE printing is of a great concern to the health and safety in a workplace. The emissions of solvents can be controlled through a good working practice, and substitution with water-based solvents substitutes.

Rheology is one of the most important properties controlled during the printable mixture formulation step in order to ensure desirable performance in a specific printing system. The rheology strongly affects the processing condition depending on the organic components composition as well as inorganic solid content in which concentration size and distribution of *e.g.* NPs is crucial.

The formulation of a printable materials must take into account the characteristics of the material of which the substrate is made or the surface properties of coating already existing on the substrate. Proper adhesive properties between adjacent layers are important in achieving the full performance of printed device. Moreover, film shrinkage either chemical or thermal is notorious for its potentially serious consequences, depending on the application of the material. In case of printed films for which an energetic post-processing is required, residual stress may be formed leading the creation of channel cracks and device delamination.

The stability of printable mixtures is an important consideration when it comes to in their commercialization. In most cases the material stability is limited by a shelf life of the organic content (if any), or spontaneous reaction between mixture components.

Resuming, many factors had to be considered, and each issue had to be addressed in order to reach the main objective and develop materials and processes compatible with printing processing. Within this broad theme, the study had a number of specific objectives concerning the printable mixtures formulation in general, as well as EC film precursor and electrolyte pre-polymer at individual bases. Concerning the printable materials in general following objectives were formulated:

- optimum composition of materials in terms of device performance (optimization process based on measured responses and predictive mathematical model),
- processability *via* selected printing method (*i.e.* adjusted rheology and appropriate physical composition),
- possibly the simplest technological protocol (reducing the number of system components till it contain only essential ones),
- compatibility with low temperature processing (preferably < 150 °C),
- low energy processing,
- material stability at operational temperature,
- good adhesion and chemical stability with the adjacent layers,
- high quality of printed films (*i.e.* high definition, uniformity and homogeneity),
- low shrinkage in post-processing,
- mechanical integrity of final devices,

- long term stability against UV-light and ambient atmosphere,
- low cost of raw materials and inexpensive methods of synthesis,
- compliance with safety issues,

Objectives related specifically to EC film precursor and electrolyte pre-polymer concern desired electrical and optical functionality of final device. In order to comply with these requirements for the EC film precursor development, the following objectives are formulated:

- short switching time, preferably at a level of several seconds,
- optical contrast ensuring comfortable read-out,
- decreased power consumption, when comparing with analogues material counterparts developed *via* other solution processed techniques,

The formulation of electrolyte pre-polymer involves careful selection of thermosetting resin in order to optimize this material for its application. In terms of electrolyte pre-polymer formulation, the objectives are the following:

- high ionic conductivity, between 10^{-4} - 10^{-6} S cm^{-1},
- low electronic conductivity,
- optical properties according to the application (white opaque film or EC displays and transparent colorless film for EC windows),

Table 1.1 contains specific testable predictions called hypotheses, constructed about the variables in presented research work. They will be tested based on values of variable results obtained from measurements (responses).

Table 1.1. The hypotheses corresponding to individual topics, constructed to be tested within a research work

Topic	Hypotheses
Solution processed EC films, based on sol-gel deposition *via* IPT (Chapters 2 and 3)	If the EC inorganic film has dual-phase composition (amorphous and crystalline), its electrochemical response will be altered, when comparing with single phase counterpart. If the EC inorganic film has dual-phase composition (amorphous and crystalline), its switching dynamics between optical states will be faster, when comparing with pure amorphous phase. If the required number of experiments is significantly decreased by application of statistical methods, the reliable analysis of results will be still possible.
Engineering rules governing the selection or synthesis of MO_X NPs for electrochemical applications (Chapters 4 and 5)	If a careful attention is given to the size-shape characteristics of NPs on the ink formulation stage, the EC performance of resulting film will be enhanced. If 1D nanostructures are incorporated to the film instead of 2D with similar specific surface area, the agglomeration process will have less adverse effect on electrochemical performance
Thermosetting composite solid-state electrolyte (Chapter 6)	If the plastic crystal phase of succinonitrile (SCN) is mechanically reinforced with thermosetting resin, the ionic conductivity of resulting composite will be maintained at sufficiently high level. If the TiO_2 NPs are added to the blend of TCSE pre-polymer in order to turn it opaque, the mechanical and electrical properties of resulting material will not be deteriorated. If there is a clear relation between ionic conductivity and Young's Modulus, then it will be possible to select the point at which material will satisfy both requirements.

1.4. Methods used

1.4.1. Research approach

The pronounced interdisciplinary nature of nanotechnology and nanosciences is perhaps one of their striking features, when comparing to classical disciplines. The methods discussed in this dissertation range as widely as the nanosciences themselves. Therefore, to understand and fully exploit the potential related to application of printed techniques in the development of electrochemical devices, an interdisciplinary approach is required. This involves the combination of information, data, techniques, tools, perspectives, concepts and theories from many academic disciplines or bodies of specialized engineering knowledge into this research activity. Figure 1.6 aims at resuming disciplines of science applied in this research work.

The disparate aspects of material synthesis and formulation of printable precursors of EC films and TCSE pre-polymers incorporate knowledge from nanoscience and nanotechnology, material science, chemistry and environmental science. Due to the approach used in this research, applied statistics is

also an important element as it enables to design experiments. Printing process includes but is not limited to elements of very specialized engineering knowledge, involving various areas of physics, electronics and computer aided drafting (CAD) design. Characterization uses methods of analytical and physical chemistry, however full understanding of results is not possible without laws of physics. Science behind the data analysis process encompasses mainly methods of statistics with tools provided by informatics.

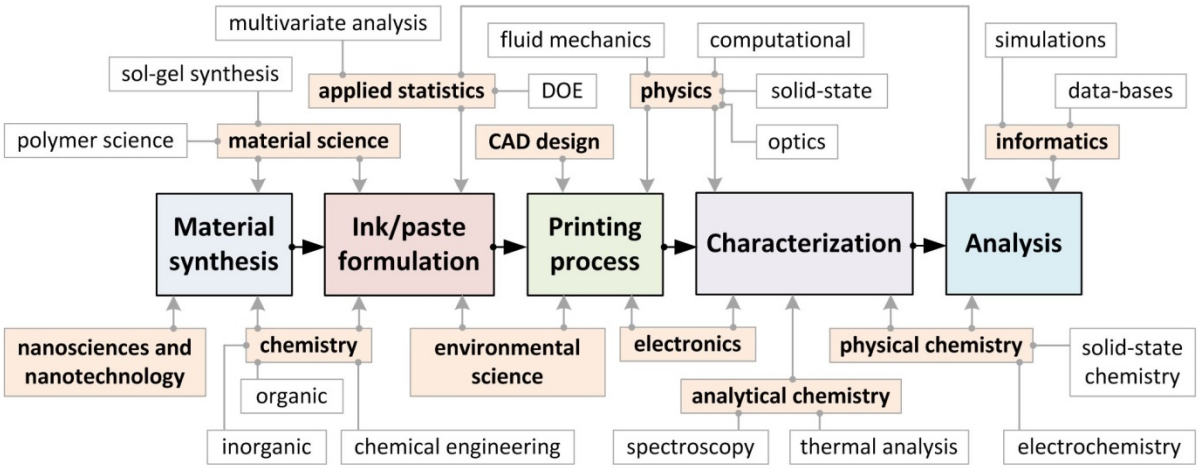

Figure 1.6. The concept of an interdisciplinary approach applied in the thesis

A quantitative approach was selected for this research work. This strategy involves collecting and converting data into numerical form so that statistical analysis can by performed. This method implies postulating hypotheses and performing quantitative experiments. Statistical analysis of the measured data enables to sustain or reject the hypotheses concerning formulated mixtures, *i.e.* printable precursors for EC film and pre-polymer of TCSE. Hypotheses include predictions about possible influence of mixture components (main effects) as well as relationships between those components (interactions). In order to address these questions, an instrumentation described in Section 1.4.2, as well as defined plan of actions were used. Statistical analysis of results allowed to determine to what extend main effects and interactions exist.

The results of statistical analyses are presented in Chapters 2, 3, 5 and 6 in a standard way widely used in a field of material science. It was the intention of the author, to describe the results obtained during the PhD research work in a format easily comprehensible to a wide audience of scientists from different fields, and society of engineers at large. In order to provide an interdisciplinary background, systematic literature reviews were prepared for each chapter of this dissertation, discussing current knowledge in various fields, using a common and understandable terminology. These summaries include journal papers, periodic written reviews, conferences and accessible software with databases that contain the collected knowledge on material synthesis, characterization and properties.

Chapters 2 – 6 contain an experimental section intended to provide a succinct but complete description of the applied methods and procedures. In order to ensure repeatability of the scientific work by other researchers, additional descriptions of experiments and data analysis were included in the Supplementary Information sections.

1.4.2. Characterization methods

In order to reveal the structure of materials being under scope of this thesis and understand how this structure determines material properties, various characterization techniques were applied. Based on obtained results, materials could be evaluated against their technological application in printed devices. According to the diagram of interdisciplinary approach presented in Figure 1.6, basic principles of physics, physical chemistry, analytical chemistry and electronics were essential in performing measurements and data treatment.

This section provides brief information on selected characterization techniques. Table 1.2 summarizes analytical tools applied in measurements of liquid precursors, while Table 1.3 and Table 1.4 refer to solid films and membranes.

Table 1.2. Analytical techniques used to characterized printable inks and pastes (macroscopic properties)

Property of the printable mixture	Characterization method
Intrinsic viscosity	Capillary viscometer: CANNON-UBBELOHDE, 9721-K53 CUC Series
Surface tension	Glass stalagmometer: Rohr A, NEUBERT-GLAS
Density of liquids	Standard pycnometer and analytical balance
Heat flux vs. temperature	Differential scanning calorimetry (DSC): Differential Scanning Calorimeter (STA 449 F3 Jupiter, Netzsch)
Weight loss vs. temperature	Thermogravimetry (TG): Thermogravimetric Analyzer (STA 449 F3 Jupiter, Netzsch)

Since all listed techniques are considered as standard tools in material science and applied electrochemistry, their detailed description is omitted. However, all customized solutions developed to extend capabilities of these techniques and ensure measurement reproducibility were emphasized in Section 1.4.3.3.

Data were collected following strict procedure and prepared for statistical analysis. Proper sample installation and corresponding protocols of measurement methods and calculation-based methods were developed. Selected elements of these protocols are included in Supplementary Information sections at the end of selected chapters of this thesis. The statistical analysis was performed using JMP 8.0 (SAS Institute Inc., Cary, NC, USA) computer software.

Table 1.3. Analytical techniques used to characterized printed thin films (macroscopic properties)

Film property	Characterization method
Macroscopic	
Spectral response	Spectrophotometry: HR4000 High-Resolution Spectrometer (Ocean Optics) coupled with Halogen Light Source HL-2000-FHSA (Mikropack) and QP600-2-SR/BX optical fibers (type – SR, core diameter - 600 µm, connector – QSMA, jacketing – BX)
Transmission, reflection and absorbance	Chronoabsorptometry (CAbs): HR4000 High-Resolution Spectrometer (Ocean Optics) coupled with Halogen Light Source HL-2000-FHSA (Mikropack) and QP600-2-SR/BX optical fibers (type – SR, core diameter - 600 µm, connector – QSMA, jacketing – BX) and High Current Source Measure Unit (KEITHLEY 238)
Ionic conductivity	Impedance Spectroscopy (IS): Gamry Reference 600 Potentiostat, Gamry Instruments
Ionic conductivity vs. temperature	Impedance Spectroscopy (IS) coupled with custom-made thermoelectric module: Gamry Reference 600 Potentiostat, Gamry Instruments
Current vs. applied voltage response	Cyclic voltammetry (CV): Gamry Reference 600 Potentiostat, Gamry Instruments
Charge vs. time response	Chronocoulometry (CQ): Gamry Reference 600 Potentiostat, Gamry Instruments
Current vs. time response	Chronoamperometry (CA): Gamry Reference 600 Potentiostat, Gamry Instruments
Thickness	Profilometry: Ambios XP-200
Heat flux vs. temperature	Differential scanning calorimetry (DSC): Thermogravimetric Analyzer (STA 449 F3 Jupiter, Netzsch)
Weight loss vs. temperature	Thermogravimetry (TG): Thermogravimetric Analyzer (STA 449 F3 Jupiter, Netzsch)
Stress vs. strain	Tensile Measurements: Low-load Horizontal Tensile Test Machine (Minimat 2000)

Table 1.4. Analytical techniques used to characterized printed thin films (microscopic properties)

Property of the printable mixture	Characterization method
Topography	Scaning Electron Microscopy (SEM): Auriga SEM-FIB, Zeiss
Chemical composition	Energy-dispersive X-ray spectroscopy (EDS): integrated with Auriga SEM-FIB, Zeiss
Crystallographic structure	X-ray Diffraction (XRD): XPert PRO, PANalytical and Brucker D8 Focus Advance diffractometer, Bruker-AXS Inc.
Infrared spectrum of absorption	Attenuated Total Reflectance Fourier Transform Infrared Spectroscopy (ATR FT-IR): Nicolet 4700 FT-IR Spectrometer coupled with Smart iTR^{TM} ATR accessory
Roughness	Profilometry: Ambios XP-200

1.4.3. Custom-made solutions

A number of custom-made instruments for manufacturing and academic research have been designed and developed during these studies due to the very specialized needs that have arisen. Whereby, a highly technological workspace have been created combining research facilities from the area of printed electronics and applied electrochemistry. Each of instruments presented in following subsections has been designed, assembled and brought to use by the author of this thesis in collaboration with in-house technicians and external companies. Some of those systems are simple setups of commercial components or their modifications, while others are completely custom-made solutions.

Provided custom-made solutions for film deposition and characterization result in increased ability of research institution to perform further tests on printed films using other material systems or developing different types of devices. Beside results published in scientific journals, these facilities constitute a value-added in themselves.

1.4.3.1.Printing facilities

Three different methods of printing were used in order to provide a process that best suits realization of work objectives. The fabrication of the active EC layer for characterization and device prototyping was performed either by IPT, stencil or screen-printing technique. A digital printing *via* IPT was performed using standard commercial office printers *e.g.* Canon PIXMA IP4500/IP4850 (Canon Virginia, Inc., Newport News, USA) shown in Figure 1.7 or advanced R&D inkjet printer PixDRO LP50 (ROTH & RAU B.V, OTB Solar, Eindhoven, The Netherlands). While the first one was found more suitable for coating processes and rapid prototyping, the second is more suitable for evaluation of inkjet materials and precise patterning.

Another aspect related to usage of those systems was related to the price of the printheads. While Canon offers printheads for ~ 50 € each, the cost of Spectra S-class printhead for PixDOR LP50 system vary between 700 € and 800 € per unit. As each printhead should be used exclusively for one type of material and regular replacements with new elements are required to ensure reliable printing, the use of Canon printing system seems to be more reasonable at early stage of the research.

Standard desktop printers were modified to suit the individual requirements dictated by the need of custom-made inks use. Figure 1.7 describes the modification concept giving guidelines on how to carry out changes of the commercial office printer to be used at lab-scale film deposition. This thermal-type standard resolution (9600×2400 dpi) printing unit (Canon PIXMA IP4500/IP4850) allows deposition of the material by a digital printing process, where the ink is ejected directly onto a substrate from 1536 nozzles (Magenta or Cyan channel) driven by an electronic signal (see Section

2.5.1 for information how to select proper printer for lab work). The fabrication of the EC films by IPT was performed at room temperature and atmospheric pressure.

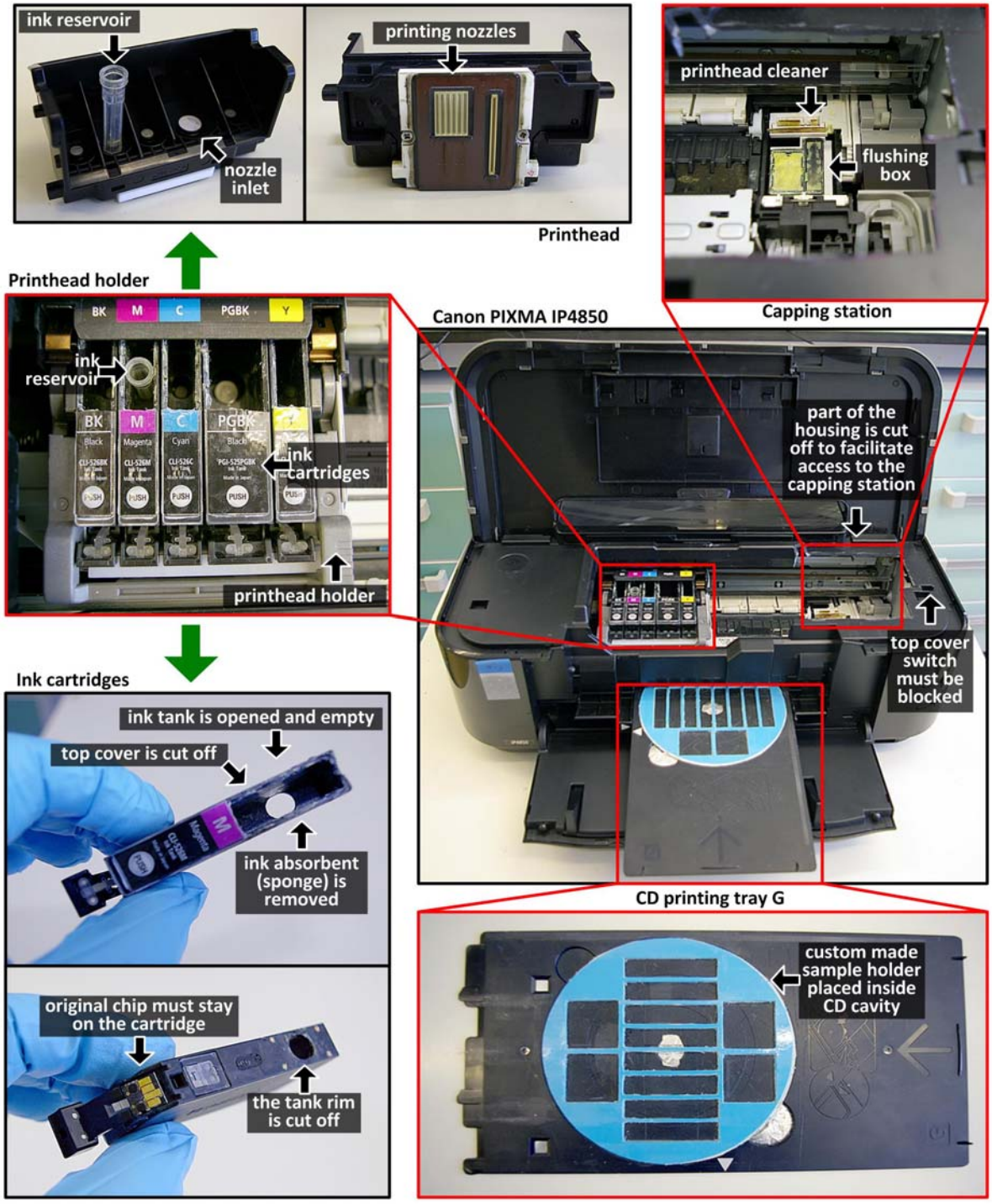

Figure 1.7. Modifications applied to standard desktop inkjet printer (*i.e.* Canon PIXMA IP4850); presented instruction may vary depending on the printer model, however the main idea has a universal character

A custom-made screen printing station shown in Figure 1.8 was used in development of entire EC displays with thin film layer stack configuration (see Figure 1.5b). This system has been used to

develop prototypes of EC displays using both, commercial pastes (*e.g.* carbon and silver) and custom formulations (*e.g.* EC paste, electrolyte, optical passivation or ITO etching mask). The total cost of such device does not exceed 150 €, while commercial solutions are available at price starting from 500 €. However, the main concern and motivation to build custom-made screen-printing system was related to compatibility of materials from which the construction of device is made with solvents used to formulate pastes. A typical printable paste used in graphics differs in composition from those used in printed electronics, which preclude acquiring standard commercial product for intended application. Therefore materials for printing stage were selected in order to ensure resistance to solvents used in formulation of printable pastes (*i.e.* polytetrafluoroethylene laminate PTFE, known also as Teflon). Patterned polyester screens with various parameters (*i.e.* aperture and thread diameter) were designed and ordered in a local polygraphic company (I.C.M. Graf, Portugal) in accordance to the required wet film thickness.

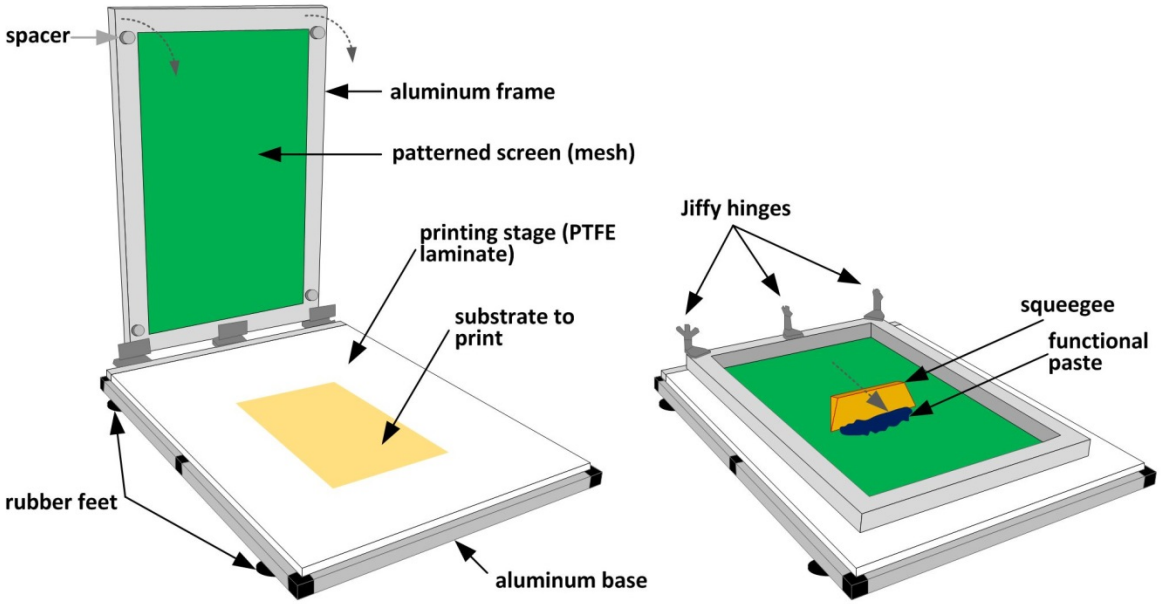

Figure 1.8. Schematic drawing of custom-made screen-printing system

1.4.3.2.Mold casting

The most suitable physical form of ion conductive solid-state material for characterization purposes is a free-standing thin, film-like structure (membrane) with uniform thickness and homogenous composition. However, in practice it is usually difficult to obtain such samples without the use of specialized equipment. In this work, the development of TCSE membranes suitable for electrochemical, optical and mechanical measurements was performed *via* casting technique. In this method a mold is filled with liquid pre-polymer, which then hardens upon polymerization reaction induced by proper curing agent (room, or elevated temperature curing when coupled with hotplate).

Due to the fact that commercial solutions are rare, and existing ones are made of not durable materials, the effort to develop custom solution was undertaken. A custom-made mold shown in Figure 1.9 was designed and developed at relatively low cost using stainless steel sheets as starting material. Surfaces being in contact with casted mixture were coated with PET foil in order to provide anti-adhesive layer. Such mold, if properly operated can be used for an unlimited number of castings.

In this solution, degassed electrolyte pre-polymer is poured into one of four inlets and pulled down by gravity into the cavity defined by gasket. At the same time, the air is pushed out from the mold by moving liquid front (laminar flow) of pre-polymer through remaining three inlets. As the result, a uniform-shaped free-standing membrane with homogenous thickness and composition is obtained (dimension of 100 x 100 mm with thickness of 0.5, 1 or 1.5 mm depending of applied gasket and decreased by the shrinkage effect; total weight of mixture for single membrane casting is approximately 11 g).

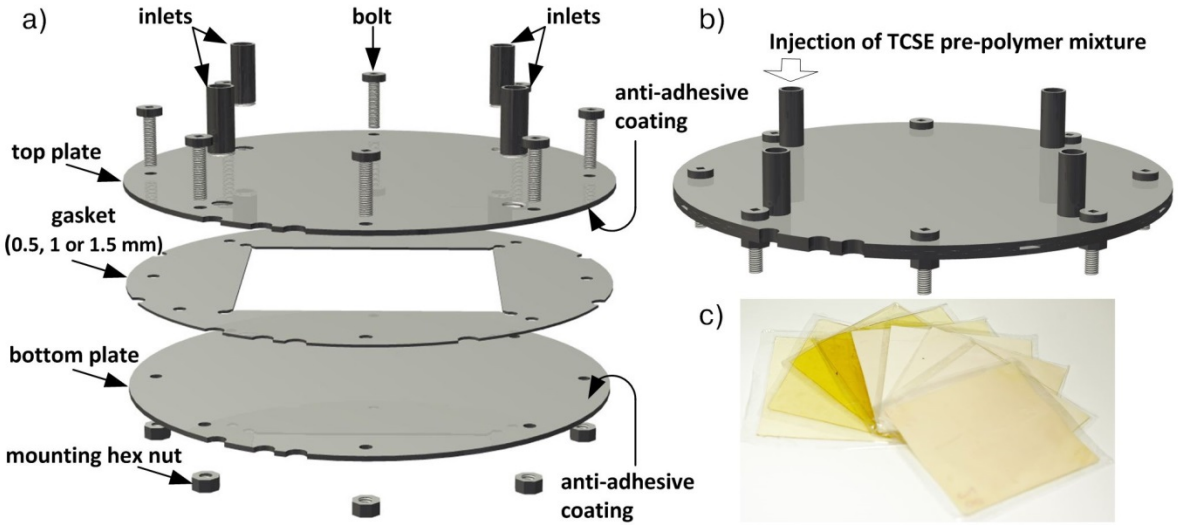

Figure 1.9. Construction of custom-built stainless steel mold for TCSE membrane casting in a) disassembled and b) assembled form; photograph c) shows 100 x 100 x 1 mm samples of cured TCSE protected with two plastic foils; the mold is compatible with standard laboratory hot plate if the curing at elevated temperature is required; see Appendix 1for detailed drafting (CAD)

1.4.3.3.Measurement accessories

A sufficient degree of agreement between successive optical or electrochemical measurements (measurement reproducibility) is one of the main principles of the scientific methods used in this work. In order to ensure reproducibility at degree to which repeated measurements under unchanged conditions show results with possibly lowest deviation, a set of custom-made accessories was designed and developed.

A convenient and reproducible way to perform optical measurements of EC devices (CAbs) was possible using custom-made device holder shown in Figure 1.10. This simple accessory compatible with spectrophotometer offers fast device mounting and easy connection of electrical wiring, while assuring reproducible optical path.

Electrochemical measurements were conducted either in device (*in-situ*) or in electrochemical cell setup. In the first case, experiment investigates the overlapped reactivity of both working and counter electrode (two-electrode experiment). Such *in-situ* measurement is conducted when the performance of the whole device is investigated rather than properties of EC film itself. This approach does not require specific instrumentation, and the measurement is performed by simply connecting wiring to the device like it is in CAbs technique. The shortcomings of this method are related to difficulties with maintaining a constant potential on working electrode due to the redox events on counter electrode.

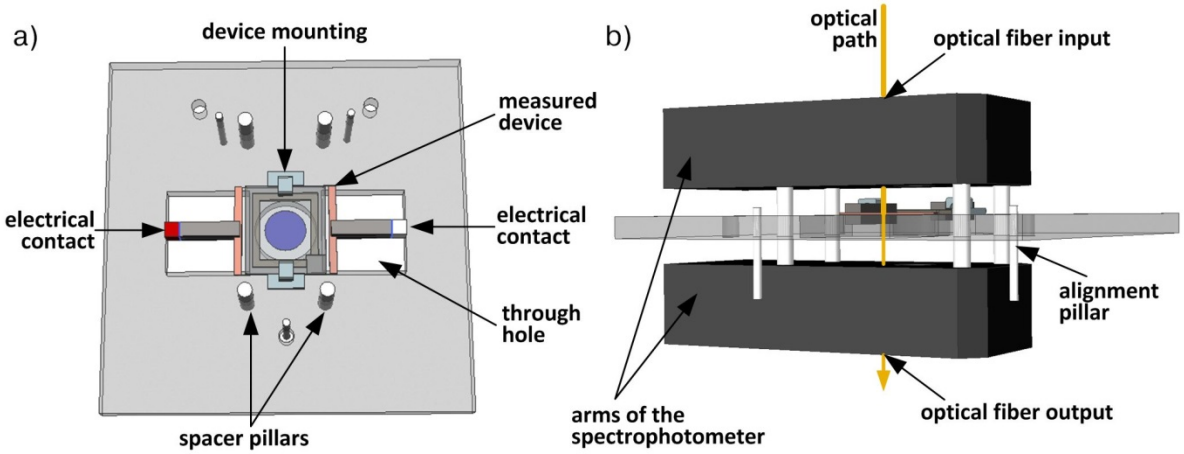

Figure 1.10. Schematic drawings of custom-made device holder with a) testing device (25 x 30 mm), b) mounted between the arms of the spectrophotometer.

In the second case, experiment is performed using electrochemical cell, which depending on the design and purpose consists of two or three electrodes. Simultaneous measurements of optical and electrochemical responses can be performed through specially designed transparent opto-electrochemical cells. As the electrochemical reaction causes optical change, recording both signals simultaneously ensures that measured responses are really those that are claimed to be. This approach provides a true snapshot of the EC behavior, and significantly increases capabilities of the characterization method. Opto-electrochemical cells were developed in two variants. First one shown in Figure 1.11 enables opto-electrochemical measurements in two-electrode setup.

In this configuration experiment investigates the half-cell reactivity (working electrode), while the second electrode (auxiliary electrode, *i.e.* platinum, Pt) acts as the other half of the cell and is used to gauge the potential and balance the charge added or removed by the working electrode. Although,

simultaneous fulfillment of these requirements is difficult and corresponding analysis may be complex, two-electrode setup is typically used in a couple general cases, including EC systems.

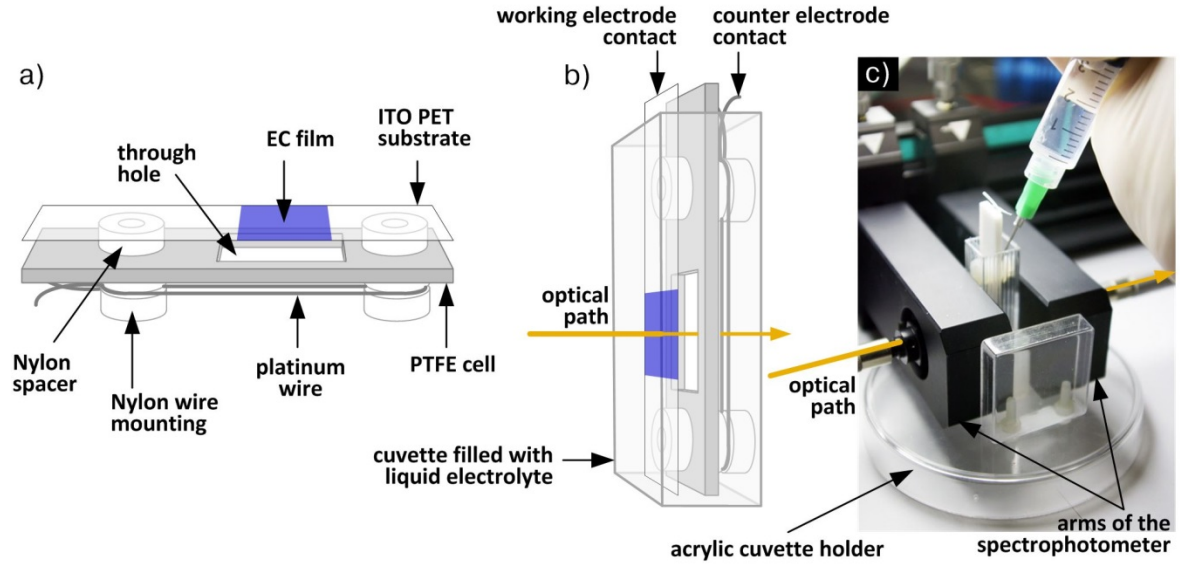

Figure 1.11. Schematic drawing and photograph of custom-made opto-electrochemical cell with two-electrode configuration; a) cell with sample of EC film printed on 10 x 45 mm PET substrate; b) cell installed in the cuvette filled with electrolyte; c) picture of the assembled cell installed in custom-made acrylic cuvette holder for spectrophotometer

In the second variant of opto-electrochemical cell shown in Figure 1.12, a third electrode is added (reference electrode, *i.e.* silver/silver chloride electrode - Ag/AgCl) extending the setup to three-electrode configuration.

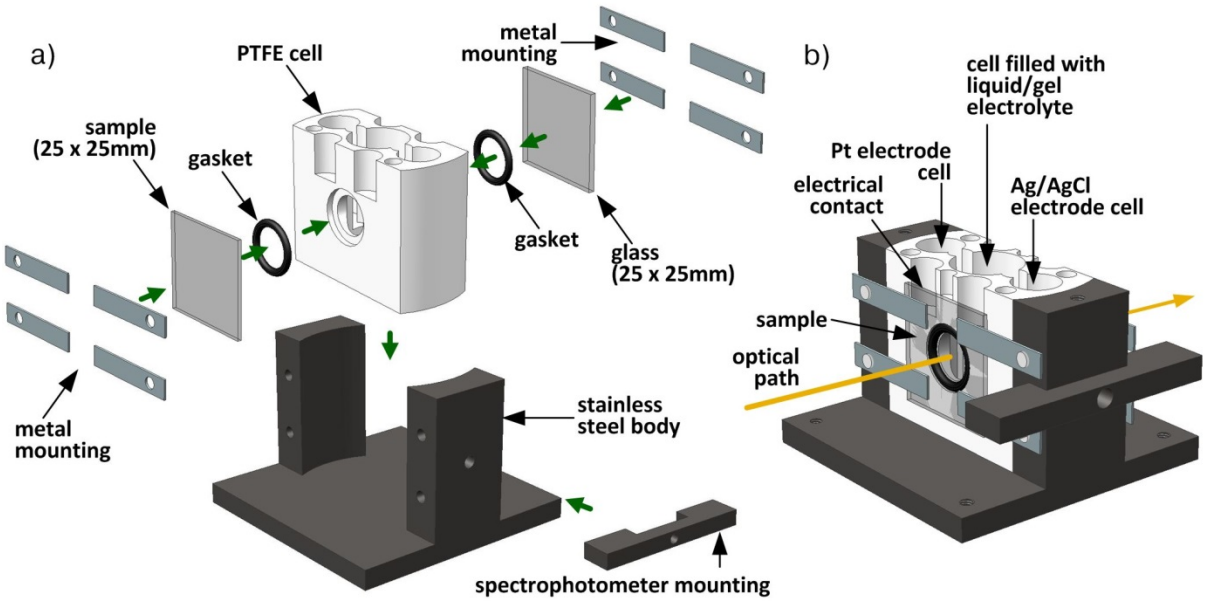

Figure 1.12. Schematic drawing of custom-made opto-electrochemical cell with three-electrode configuration in a) disassembled and b) assembled form; see Appendix 2 for detailed drafting (CAD)

Third electrode is a half electrode with known potential which acts as reference in measuring and controlling the working electrode potential while passing no current. All the current needed to balance reactions on working electrode is supplied by auxiliary electrode (*i.e.* Pt).

The possibilities for combined optical and electrochemical measurements using opto-electrochemical three-electrode cell go far beyond work described in this thesis. Unique construction of the cell allows researchers to capture various complementary data without the need to change their setup or move samples to another instrument. The use of other accessories (*e.g.* thermoelectric element) further expands the possibilities by providing setup versatility, maximizing the data available for the sample and eliminating equipment change hassles.

Materials used in custom-made electrochemical cells were selected with accordance to their suitability and chemical resistance to components of liquid/gel electrolyte used in measurements (see the last paragraph of Section 2.2.3 for detailed formulation). Another aspect of material selection is related to their easiness in mechanical machining and availability at reasonable price. Raw plastic material such as bars and sheets of PTFE were found to be the most suitable material for this purpose. Fasteners made of polycaprolactam (Nylon 6) were used to assemble the cells. Sealing was performed with Nylon 6 and PTFE gaskets.

Among available characterization techniques there are some in which a relatively long time of single measurement and workload prevent their use in screening studies involving high number of samples. Due to the time constraints and limited budged these techniques are usually omitted, unless a solution to increase throughput in provided. A typical example of such technique is Impedance Spectroscopy coupled with thermostat, used in a field of electrochemistry as a standard technique for ionic conductivity vs. temperature measurements. This labor intensive and time consuming method merely allows characterization of one sample within ~3.5 h (can vary depending on system used), in temperature range between -10 and 100 °C with 5 °C step. Designed and developed custom-made matrix of electrochemical cells coupled with thermoelectric module is a convenient alternative to single sample setups that have been used in our laboratory, previously.

Two variants of cell matrixes were implemented because of the different physical state of the samples. First one shown is Figure 1.13 is suitable for liquid, gel or semi-solid mixtures (molten prior to injection into the cells). It consists of 9 cylindrical cells with geometrical factor (*GF*) of 0.279 cm^{-1} and required sample volume of 0.36 ml each (see Section 6.2.4 for more detailed information). Second variant shown in Figure 1.14 was designed to be loaded with circular disk shaped samples of solid-state electrolyte with area of 1 cm^2 each. It consists of 9 circular cavities in which samples sandwiched in between two stainless steel electrodes are placed.

Each matrix of cells can be interchangeably installed in the custom-made thermoelectric system presented in Figure 1.15 consisting of Thermoelectric Power Generation Peltier Module (200C, 6.4V,

3.1W, Thermovoltaik), Temperature Controller (TC-XX-PR-59, Supercool AB) operated *via* personal computer (PC) and Liquid Cooling System (Bigwater 760is, Thermaltake). All elements of the system are placed inside nitrogen filled glove-box (Captair Pyramid Glove Bag) providing inert gas atmosphere during the measurement or sample conditioning. The output of the system is connected to the potentiostat (Gamry Reference 600 Potentiostat, Gamry Instruments).

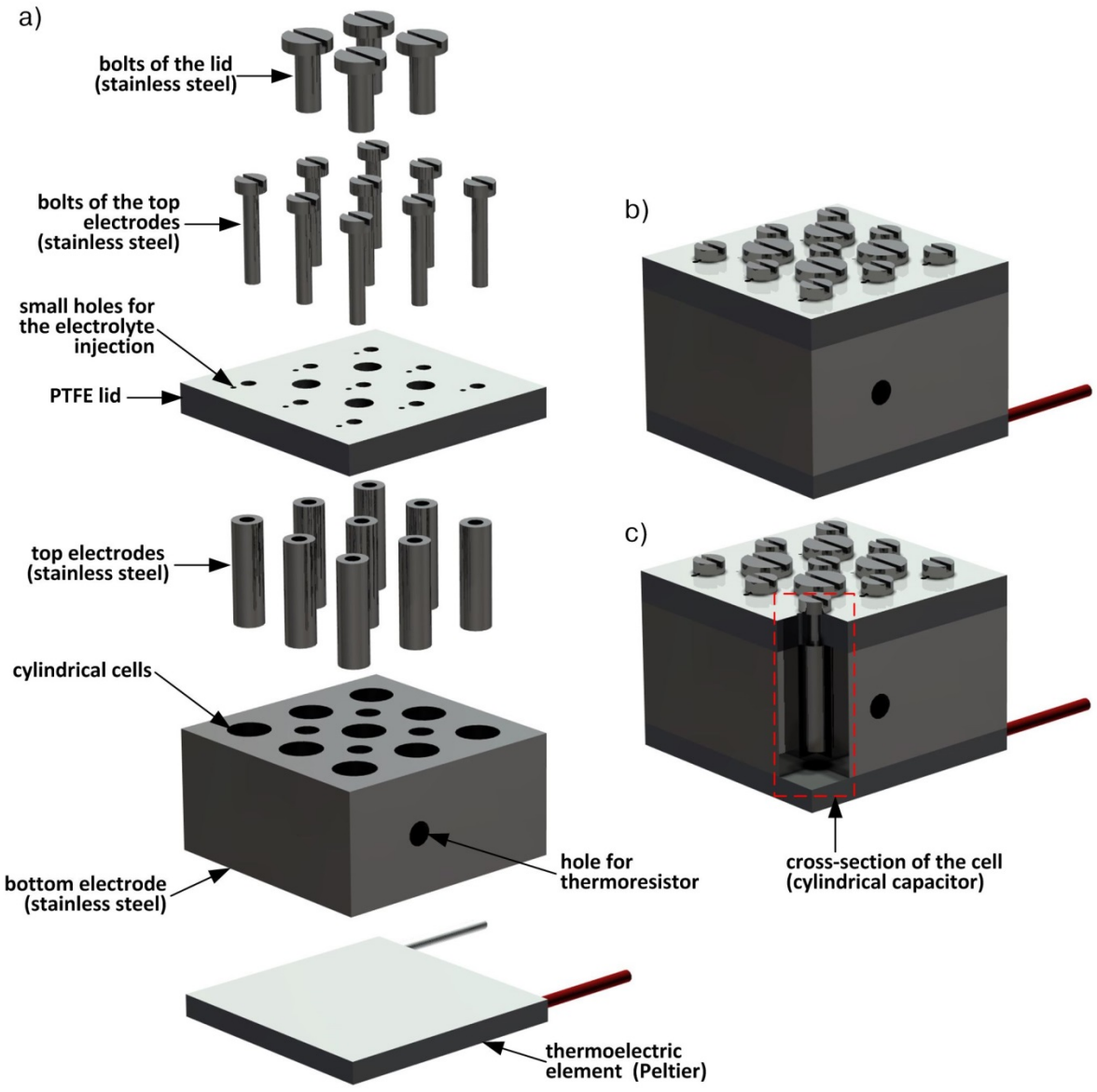

Figure 1.13. Construction of custom-made matrix of 9 cylindrical cells for Impedance Spectroscopy measurements of liquid, gel or semi-solid samples in a) disassembled and b) assembled form; c) cross-section of a single cylindrical cell; see Appendix 3 for detailed drafting (CAD)

The signal is collected from multiple independent samples (manual selection) at selected temperature level. A multiplex measurements using developed solution offer rapid (~20 min/sample) and reproducible reading of conductivity vs. temperature (between -10 and 100 °C; the range may vary depending of the Peltier module used), while offering easy and convenient installation of samples. It

is a perfect tool for high throughput ionic conductivity and activation energy screening of liquid, gel, semi-solid and solid ion conductive samples. It can also be used to follow polymerization reaction at selected temperature in order to monitor changes in ionic conductivity.

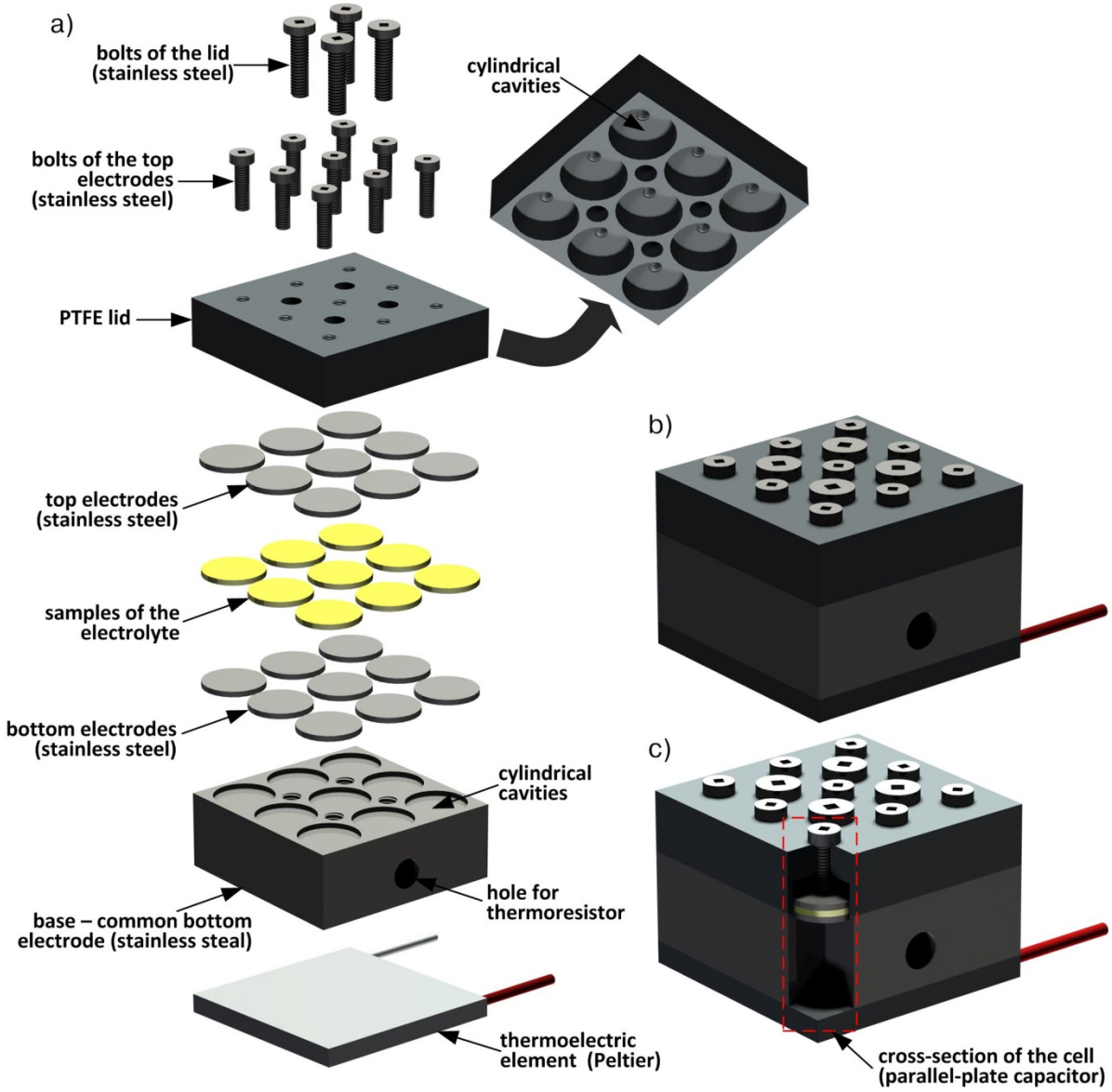

Figure 1.14. Construction of custom-made matrix of 9 plane cells for Impedance Spectroscopy measurements of solid-state membranes in a) disassembled and b) assembled form; c) cross-section of a single parallel-plate cell; see Appendix 4 for detailed drafting (CAD)

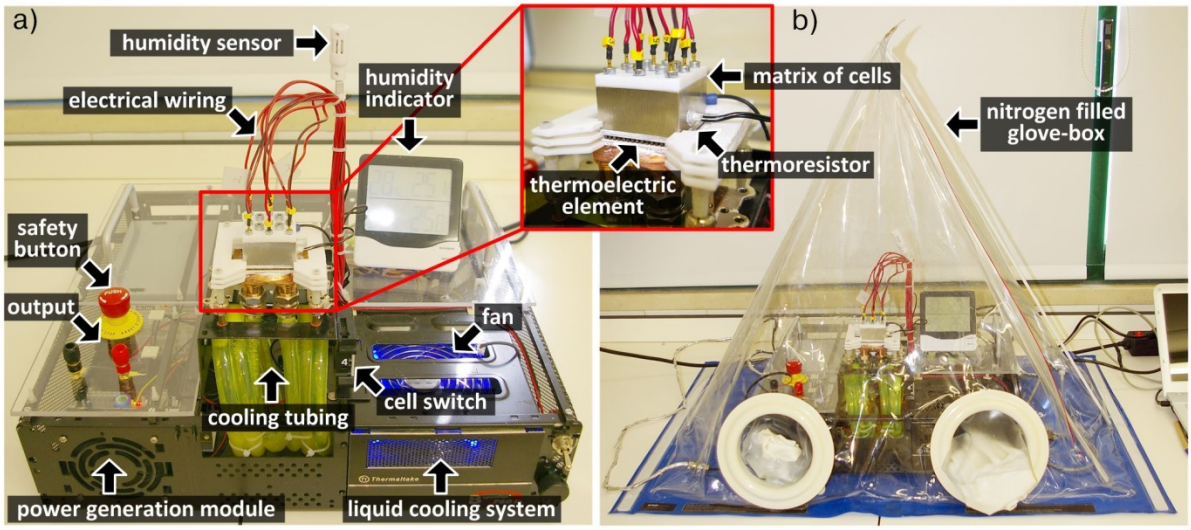

Figure 1.15. Picture of a) custom-built thermoelectric system with matrixes of electrochemical cells for Impedance Spectroscopy measurements b) installed inside of the nitrogen filled glove-box (inset: matrix of cells installed on top of the thermoelectric element)

1.5. Content

The dissertation is organized in the following way. The general introduction chapter is followed by chapters written based on publications already published or being under revision by scientific journals and book publishing house. Please note, that chapters are not exact versions of corresponding publications, and were modified in order to ensure consistency of the thesis in a broader sense. Moreover, this work contains some recent results and findings which were unpublished and have not been submitted for publication yet. The thesis is completed with summary chapter which constitutes a summary of the publications appended in this thesis. Each chapter includes its own introductory section providing a literature review to the issue, definitions of terms as well as its own conclusions.

Thematically, the above thesis is composed of three topics related to electrochemical devices, in particular, to printed EC applications.

Chapters 2 and 3 present an innovative method for the development of solution processed EC films, based on sol-gel deposition *via* IPT. Chapter 2 describes analytical side of this approach, while Chapter 3 presents microstructural aspects related to this method by comparing the characteristics of films deposited based on standard wet deposition techniques such as dip-coating, spin-coating and electrodeposition *versus* IPT.

Chapters 4 and 5 are devoted to engineering rules governing the selection or synthesis of MO_X NPs and their application in electrochemically active films. Chapter 4 presents a survey of NPs engineering rules in applied electrochemistry, based on performed simulations and literature. This

rather theoretical approach scientifically explains the impact of the size and shape of NPs on electrochemical performance of printed dual-phase films. These engineering rules were applied in a complete worked-out case study described in Chapter 5.

Chapter 6 describes a new concept of solid-state electrolyte (*i.e.* TCSE) developed within this PhD research work. Its electrical, mechanical and optical properties as well as application in printed electrochemical devices are discussed in this chapter.

Finally, a brief history of prototypes development followed by summary and future perspectives is given in Chapter 7.

Chapter 2

Statistical mixture design and multivariate analysis of inkjet printed *a*-WO_3/TiO_2/WO_X films

This chapter is written based on:

Wojcik, P.J., Pereira, L., Martins, R., Fortunato, E.: Statistical mixture design and multivariate analysis of inkjet printed *a*-WO_3/TiO_2/WO_X electrochromic films. ACS Comb. Sci. 16 (1) 5-16 (2014)

Chapter 2. Statistical mixture design and multivariate analysis of inkjet printed *a*-WO_3/TiO_2/WO_X films

Chapter 2. Statistical mixture design and multivariate analysis of inkjet printed *a*-$WO_3/TiO_2/WO_X$ films

Summary

An efficient mathematical strategy in a field of solution processed EC films is outlined in this chapter as a combination of an experimental work, modeling and information extraction from massive computational data *via* statistical software. Design of Experiment (DOE) was used for statistical multivariate analysis and prediction of mixtures through a multiple regression model, as well as the optimization of a five-component sol-gel precursor subjected to complex constraints. This approach significantly reduces the number of experiments to be realized, from 162 in the full factorial (L = 3) and 72 in the extreme vertices (D = 2) approach down to only 30 runs, while still maintaining a high accuracy of the analysis. By carrying out a finite number of experiments, the empirical modeling in this study shows reasonably good prediction ability in terms of the overall EC performance. Development of an optimized ink formulation based on this model allowed for reaching the maximum performance. Coupling of DOE with chromogenic materials formulation shows the potential to maximize the capabilities of these systems and give increased productivity for many potential solution-processed electrochemical applications.

2.1. Introduction

Statistical design of mixture experiments is an established and proven methodology in organic chemistry [30], biochemistry [31], environmental science [32], chromatography [33] and drug delivery [34, 35], however so far very few studies have been carried out regarding optimization of solution-processed inorganic EC materials [36]. This chapter presents the work on EC thin films processed by IPT. This method, offers flexibility in deposited film composition, high throughput and simplicity in material selection, when compared to the conventional methods. However, optimization of the printing process by evaluating all possible combinations of factors using single factor experiments is time prohibitive. As there are several factors to evaluate and potential interactions exist between the factors, multi-factorial design of experiment (DOE) should be explored as an alternative to traditional single variable experiments. This technique is a time and cost-effective approach for testing the effects of many variables simultaneously. There were three experimental design objectives. To start with, the few important main effects (components) should be selected from the many less important ones. For another thing, to estimate interactions between mixture components, and therefore have an idea of the local shape of the response surface we are investigating (development of empirical model). And thirdly, to find the optimum ink composition in order to obtain the most preferable performance of printed EC devices.

The chemical deposition in which a fluid precursor undergoes a chemical change at a solid surface, leaving a solid thin-film involves formulation (mixture) problem. The discussion presented in this chapter and following Chapter 3, concerns the mixture situation in which the proportions of some or all of the components are restricted by constrains, so the entire simplex known from standard DOE approach cannot be used, and the feasible region is a polytope. In a mixture experiment in general, the independent factors (X_i) are proportions of different components of a blend which must be nonnegative and additionally satisfy the condition described by Equation 2.1.

$$\sum_{i=1}^{q} X_i = 1 \qquad (2.1)$$

The response is assumed to depend only on the relative proportions of components present in the mixture and not on the amount of the mixture. Moreover, it is assumed that the errors are independent and identically distributed with the zero mean and common variance.

A common experimental methodology is called full factorial design with all possible combinations of all the input factors. In case of the constrained mixture design with a specified number of components (q), a full factorial experiment can be performed in the proportions or amounts of only $q - 1$ of the components while the q^{th} stays unused [37]. After all, the q^{th} component can be calculated as a missing part of the complete mixture. In a complete experiment, all combinations of the levels (L) of all $q - 1$ factors are tested. The number of experimental runs in the full factorial design grows exponentially with the number of mixture components according to the $L^{(q-1)}$ formula as it is shown in Figure 2.1a. Despite the high number of experimental runs the interpretation of significant terms can be unclear, because variances and covariances of the coefficients can be large. Therefore, the independent variable experiments such as full factorial design are rarely used for blends giving way to more adequate mixture designs.

As the mixture experiment with constrained region is not feasible in the standard mixture design, other designs that cover only a sub-portion or smaller space within the simplex are required. One approach is called the extreme vertex design [38] in which all of the vertices of the polytope are used, as well as the centroids of the region, edges, faces etc. As it is shown in Figure 2.1b, the extreme vertex design requires much smaller number of experimental runs. Also, the region of interest in such design is defined for mixture more naturally than it was in case of full factorial approach.

Other approach is to use D-optimal design provided by a computer algorithm [39–41]. Unlike standard full factorial design, the computer-aided D-optimal mixture design is always non-orthogonal because effect estimates are correlated. D-optimal algorithm is looking for a design in which the factor effects are maximally independent of each other. This optimality criterion results in minimizing the generalized variance of the parameter estimates for a pre-specified model.

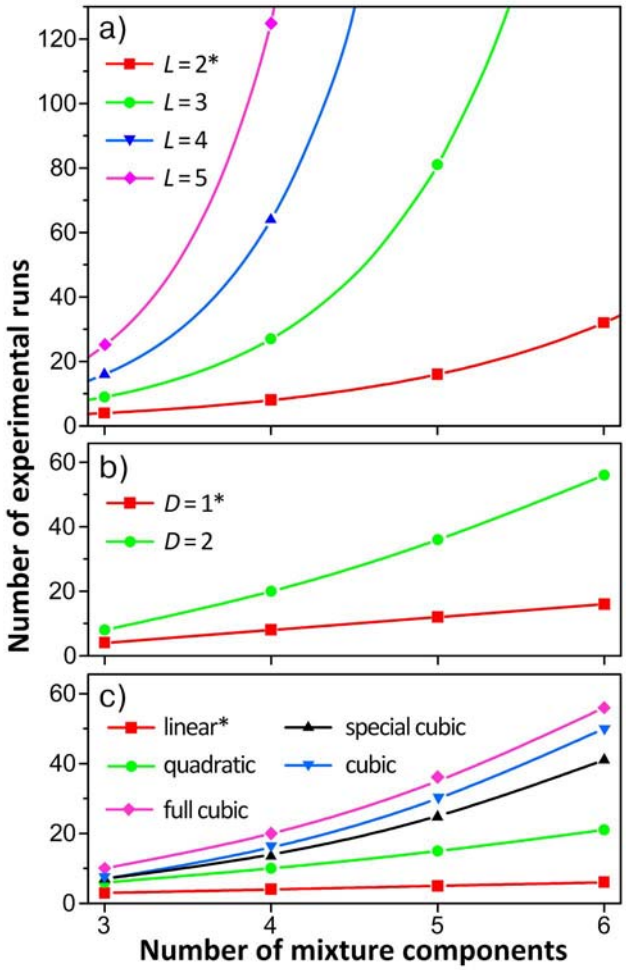

Figure 2.1. Relationship between minimum number of experimental runs and number of components in the constrained mixture for a) full factorial (*L* stands for number of levels) b) extreme vertices (*D* stands for a specified degree of mid-points identification) and c) D-optimal designs; * number of experimental runs taking under account only main effects

Among all known mathematical models considered for mixture experiments in which response surface is continuous over the region being studied, the most usual are Scheffé models [42] expressed by their canonical forms in Equations 2.2 (linear), 2.3 (quadratic), 2.4 (special cubic), 2.5 (cubic with no main effects) and 2.6 (full cubic).

$$Y_{\mathrm{k}} = \sum_{\mathrm{i}=1}^{q} \beta_{\mathrm{i}} X_{\mathrm{i}} \tag{2.2}$$

$$Y_{\mathrm{k}} = \sum_{\mathrm{i}=1}^{q} \beta_{\mathrm{i}} X_{\mathrm{i}} + \sum_{\mathrm{i}=1}^{q-1} \sum_{\mathrm{j}=\mathrm{i}+1}^{q} \beta_{\mathrm{ij}} X_{\mathrm{i}} X_{\mathrm{j}} \tag{2.3}$$

$$Y_{\mathrm{k}} = \sum_{\mathrm{i}=1}^{q} \beta_{\mathrm{i}} X_{\mathrm{i}} + \sum_{\mathrm{i}=1}^{q-1} \sum_{\mathrm{j}=\mathrm{i}+1}^{q} \beta_{\mathrm{ij}} X_{\mathrm{i}} X_{\mathrm{j}} + \sum_{\mathrm{i}=1}^{q-2} \sum_{\mathrm{j}=\mathrm{i}+1}^{q-1} \sum_{\mathrm{k}=\mathrm{j}+1}^{q} \beta_{\mathrm{ijk}} X_{\mathrm{i}} X_{\mathrm{j}} X_{\mathrm{k}} \tag{2.4}$$

$$Y_{\mathrm{k}} = \sum_{\mathrm{i}=1}^{q-1} \sum_{\mathrm{j}=\mathrm{i}+1}^{q} \beta_{\mathrm{ij}} X_{\mathrm{i}} X_{\mathrm{j}} + \sum_{\mathrm{i}=1}^{q-2} \sum_{\mathrm{j}=\mathrm{i}+1}^{q-1} \sum_{\mathrm{k}=\mathrm{j}+1}^{q} \delta_{\mathrm{ij}} X_{\mathrm{i}} X_{\mathrm{j}} \left(X_{\mathrm{i}} - X_{\mathrm{j}}\right) +$$

$$+ \sum_{\mathrm{i}=1}^{q-2} \sum_{\mathrm{j}=\mathrm{i}+1}^{q-1} \sum_{\mathrm{k}=\mathrm{j}+1}^{q} \beta_{\mathrm{ijk}} X_{\mathrm{i}} X_{\mathrm{j}} X_{\mathrm{k}} \tag{2.5}$$

$$Y_k = \sum_{i=1}^{q} \beta_i X_i + \sum_{i=1}^{q-1} \sum_{j=i+1}^{q} \beta_{ij} X_i X_j + \sum_{i=1}^{q-2} \sum_{j=i+1}^{q-1} \sum_{k=j+1}^{q} \delta_{ij} X_i X_j (X_i - X_j) +$$

$$+ \sum_{i=1}^{q-2} \sum_{j=i+1}^{q-1} \sum_{k=j+1}^{q} \beta_{ijk} X_i X_j X_k \quad (2.6)$$

The function expressed by Equation 2.2 connects each characteristic response (Y_k) with defined q factors (X_i) taking under account only main effects (β_i) while the quadratic and cubic functions (Equations 2.3 to 2.6) considers also 2nd (β_{ij}) and 3rd (β_{ijk}) order interactions, respectively. The $X_i X_j (X_i - X_j)$ and $X_i X_j X_k$ terms in Equations 2.4 to 2.6 model cubic blending of binaries and ternaries, respectively. The coefficients of binaries are symbolized by δ_{ij}. All these models differ from full polynomial models, because do not contain intercept value (β_o for $i = 0$). Such simplification occurs according to the Equation 1.1. Note that model expressed by Equation 2.2 do not imply an underlying physical relationship connecting responses with independent factors. Rather, this empirical model is used to estimate statistical significance. Just as the quadratic model is an augmented linear model, the cubic ones are augmented quadratic models. The first order quadratic model ($m = 1$) expressed by Equations 3 has ability to supply high regression coefficient while simultaneously minimizing overall number of coefficients (p) relative to cubic (Equations 2.4 to 2.6) or second order ($m = 2$) models, which can be summarized (excluding special cubic model) by the Equation 2.7.

$$p = \frac{(q+m-1)!}{m!(q-1)!} \quad (2.7)$$

The D-optimal design not only reduces the number of experimental runs as it is shown in Figure 2.1c, but also keeps the more reasonable analysis for the experimental data than the fractional factorial experimental design or extreme vertex design. Additionally, the D-optimal design enables including of a certain number of experiments already performed and consider them during the analysis, which is not possible in case of any classical design. D-optimal design seems to be the most powerful tool to cope with a situation when the region of interest is subjected to complex constraints, as the main objective is to conduct reliable analysis of the mixture with the least number of runs. According to this method, a mathematical model is obtained which helps to transport the complexity of studied problem into an easy to handle and practical form.

In the present study, a screening design method has been selected to characterize the inkjet printing process of dual phase *a*-WO_3/TiO_2/WO_X films, because studied problem involves a large number of input factors. Such experimental plan is intended to find the few significant factors from a list of many potential ones and identify significant effects. The second goal is to build a predictive model for the ink formulation optimization, which requires precise mathematical modeling. Thus, the DOE approach for mixtures with constrains consists of following phases: (i) factors identification (mixture components) that affects the outcome of the experiment and responses that give a measure of the outcome; (ii) selection of appropriate experimental design for screening/surface modeling; (iii) generation of design matrix, determining which experiments will be conducted; (iv) conducting the

experiments and data collection; (v) data fitting and generating mathematical models for each response; (vi) analysis of significance; (vii) mixture optimization and (viii) drawing of conclusions.

2.2. Materials and methods

2.2.1. Model selection

The studied material system shown schematically in Figure 2.2 can be described as a-WO_3/TiO_2/WO_X, where a-WO_3 stands for amorphous matrix formed by sol-gel reaction from peroxopolytungstic acid (PTA) precursor, while TiO_2 and WO_X are titanium dioxide and tungsten oxide nanocrystals, respectively. An additional component of the mixture is oxalic acid (OAD).

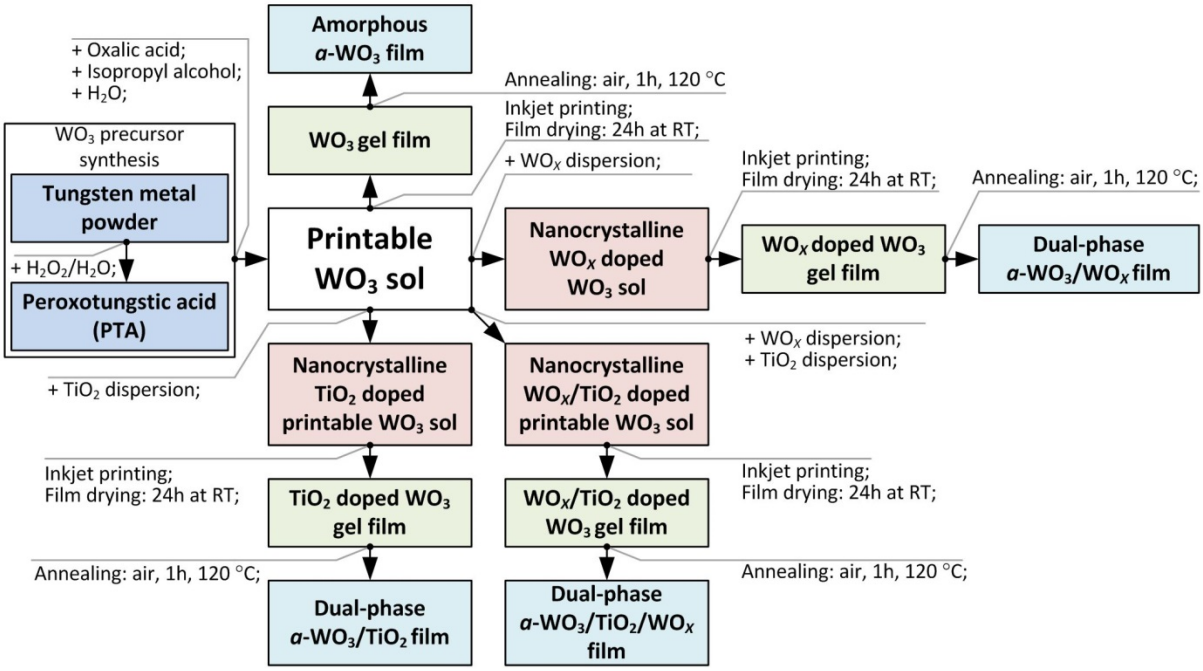

Figure 2.2. Schematic diagram representing the elements of the studied material system and corresponding technological steps

Films developed based on such material system can be either amorphous or dual-phase containing one or both kinds of metal oxide. Therefore, the designed mixtures can be described as quinary systems solvent-PTA-OAD-TiO_2-WO_X with one additional non-mixture factor X, which stands for WO_X nominal particle oxygen content (dual-level categorical factor with values of 2.9 for *blue* and 3 for *yellow* nanopowder).

Mixtures (inks) must meet strict physicochemical properties (viscosity, surface tension and maximum particle size) which impose several constrains. The ink composition based on solvent with isopropyl alcohol to water ratio of 0.3:0.7 by weight containing less than 20 wt % of PTA and less than 5 wt % of OAD result in the viscosity and the surface tension values of 1.5 – 2 cP and 30 - 40 dyne cm^{-1}

respectively, acceptable for conventional office printer (see Section 2.5.2 for more details concerning ink rheology measurements). The maximum nanoparticle size should be at least one hundred times smaller than nozzle diameter (9 μm) which gives 90 nm (according to Canon FINE technology specification).

Additionally all samples must contain PTA component (≥ 1 wt %) in order to ensure the existence of amorphous phase which guarantees EC effect by allowing electronic conduction to take place at low temperature process. Based on imposed restrictions, the values of individual weight fraction ranges and categorical levels of factors were defined as follow: $0 \leq w_{\mathrm{solvent}} \leq 0.99$, $0.01 \leq w_{\mathrm{PTA}} \leq 0.2$, $0 \leq w_{\mathrm{OAD}} \leq 0.05$, $0 \leq w_{\mathrm{TiO_2}} \leq 0.99$, $0 \leq w_{\mathrm{WO_X}} \leq 0.99$ and X = {2.9: *blue*, 3: *yellow*} (X is defined as categorical variable because two types of commercially available WO_X nanoparticles were used; see Section 2.2.3 for more details). Due to the complexity of such constricted experimental area, the application of D-optimal algorithm for experimental design seems to be essential. A detailed technical description of how D-optimal design is constructed is beyond the scope of this chapter, and the thesis at all. In simple terms, D-optimal design is straight optimization based on both, the optimality criterion and the model that will be fitted. The optimality criterion results in minimizing the variance of the parameter estimates for a pre-specified model. Based on pre-existing information gained in preliminary experiments, we can hypothesize a model more complex than linear for a studied mixture.

Figure 2.3 shows Average Variance of Prediction calculated by D-optimal algorithm, as a function of the number of experimental runs. A design that has lower Average Variance of Prediction for a considered number of runs is preferred. Therefore, properly designed experiment results in a low Average Variance of Prediction, while keeping the number of runs within determined budget for the time and materials.

Supporting of a quadratic model requires fewer experimental runs than supporting any of cubic models and results in more accurate prediction. Furthermore, the quadratic model is sufficient for both, screening procedure which enables identification of components of the model that have no effect on the response, and creating response surface model necessary for the optimization purposes. Resuming, the quadratic, first order polynomial function (Scheffé model) expressed by Equation 2.3 was proposed as an appropriate model for modeling the response data as functions of so defined mixture components with one categorical factor (see Section 2.5.6 for more details). The minimum number of runs in the computer aided D-optimal design for six factors studied that could fit main effects and two-factor interactions is 20, while the default number suggested by the design generator is 30. As the number of runs of 30 does not exceed the determined budget of time and materials, the final design was composed of 30 experiments.

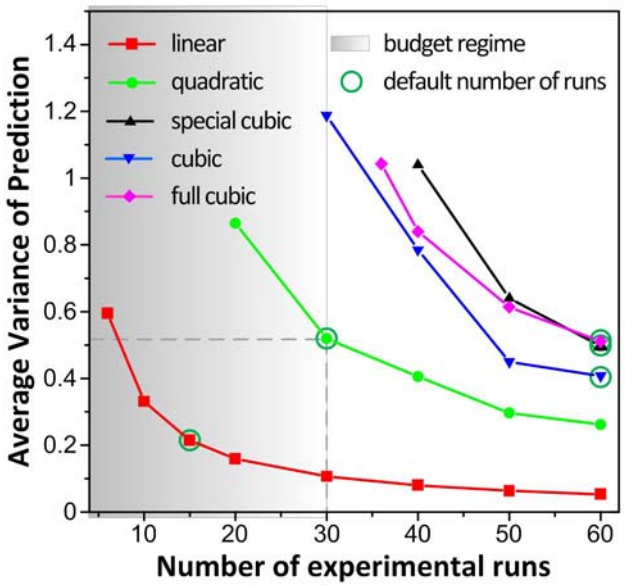

Figure 2.3. Design diagnostic by evaluation of Average Variance of Prediction as a function of the number of experimental runs for quinary system with one additional non-mixture factor *X*; default number of runs suggested by the D-optimal algorithm for each Scheffé model is marked as well as the determined budged of time and materials

2.2.2. Design of experiments

Once a decision had been made about mathematical form to fit the responses, the next step was to develop a suitable DOE to adequately support such model. A screening design has been performed according to the Design of Experiment methodology using JMP 8.0 statistical software (S.A.S. Institute Inc., Cary, NC, USA). Flexible JMP's Custom Designer has been applied to determine the main factors, interactions effects and to investigate the changes of the responses by varying each factor in order to predict the device performance for all possible ink recipe combinations. The D-optimal design using 30 runs is shown in Table 2.1and Figure 2.4. Please note that the final design for the same input parameters may be different depending on the software used, as different procedures for generating D-optimal designs can be implemented. A graphical representation of the generated design is presented in Figure 2.4 as a ternary plot (w_{solvent}, $w_{\mathrm{TiO_2}}$, w_{WO_X}) with 2D sub-plots (w_{PTA}, w_{OAD}) and colored points (X), enabling visualization how all design points are allocated in the design space. It can be observed that the D-Optimal design tends to assign design points at the borders and corners of design space, which is typical for this algorithm. The major edges of analysis were indicated and numbered in the plot according to: (1) the increase in nanocrystalline solid concentration with fixed ratio of 1:1 between TiO_2 and WO_X, (2) the increase in TiO_2 nanocrystals concentration (no WO_X content), (3) increase in WO_X nanocrystals concentration (no TiO_2 content), and (4) proportions of TiO_2 and WO_X dispersions in the ink without pure solvent. The order of runs

was fully randomized to minimize the effect of uncontrolled factors that could affect the final result. This is a particular case of the mixture design coupled with one categorical factor which requires the use of a number of runs at least equal to the doubled number of unknown coefficients in Equation 2.3. Since w_{WO_X} and X factors are dependent, each pair of runs (5, 18), (8, 26), (10, 17) and (14, 22) describe the same experiments.

Table 2.1. The list of experimental trials (design matrix) according to *mixture design with one non-mixture component* methodology

Run Number	Factors					
	Mixture components					Categorical
	$w_{solvent}$ (wt)	w_{PTA} (wt)	w_{OAD} (wt)	w_{TiO_2} (wt)	w_{WO_X} (wt)	X
1	0.539	0.010	0	0	0.451	*yellow*
2	0	0.200	0	0	0.800	*blue*
3	0	0.113	0.050	0.837	0	*blue*
4	0	0.200	0	0.800	0	*yellow*
5	0.800	0.200	0	0	0	*yellow*
6	0.575	0.010	0	0.415	0	*yellow*
7	0	0.010	0.050	0	0.940	*blue*
8	0	0.010	0.050	0.940	0	*yellow*
9	0	0.010	0	0.498	0.492	*blue*
10	0.940	0.010	0.050	0	0	*yellow*
11	0	0.010	0	0	0.990	*yellow*
12	0	0.200	0.050	0	0.750	*blue*
13	0	0.010	0	0	0.990	*blue*
14	0	0.010	0	0.990	0	*yellow*
15	0	0.200	0	0	0.800	*yellow*
16	0.465	0.010	0.026	0	0.499	*blue*
17[a]	0.940	0.010	0.050	0	0	*blue*
18[a]	0.800	0.200	0	0	0	*blue*
19	0.866	0.109	0.025	0	0	*yellow*
20	0.441	0.010	0.026	0.523	0	*blue*
21	0	0.081	0.024	0.445	0.451	*yellow*
22[a]	0	0.010	0	0.990	0	*blue*
23	0	0.200	0.023	0.777	0	*blue*
24	0	0.200	0.050	0.750	0	*yellow*
25	0.990	0.010	0	0	0	*blue*
26[a]	0	0.010	0.050	0.940	0	*blue*
27	0.351	0.200	0.050	0	0.399	*yellow*
28	0	0.010	0.050	0	0.940	*yellow*
29	0.401	0.108	0	0.491	0	*blue*
30	0.750	0.200	0.050	0	0	*blue*

[a] duplicates.

Those experiments cannot be merged, because deleting the duplicates would cause necessity of a new D-optimal model generation. Ultimately, there were 26 independent runs in D-optimal design and

additional 4 runs serving as checkpoints for mathematical model. The selected experimental design is sufficient not only to fit the proposed quadratic first order polynomial model, but allows testing the model adequacy as well.

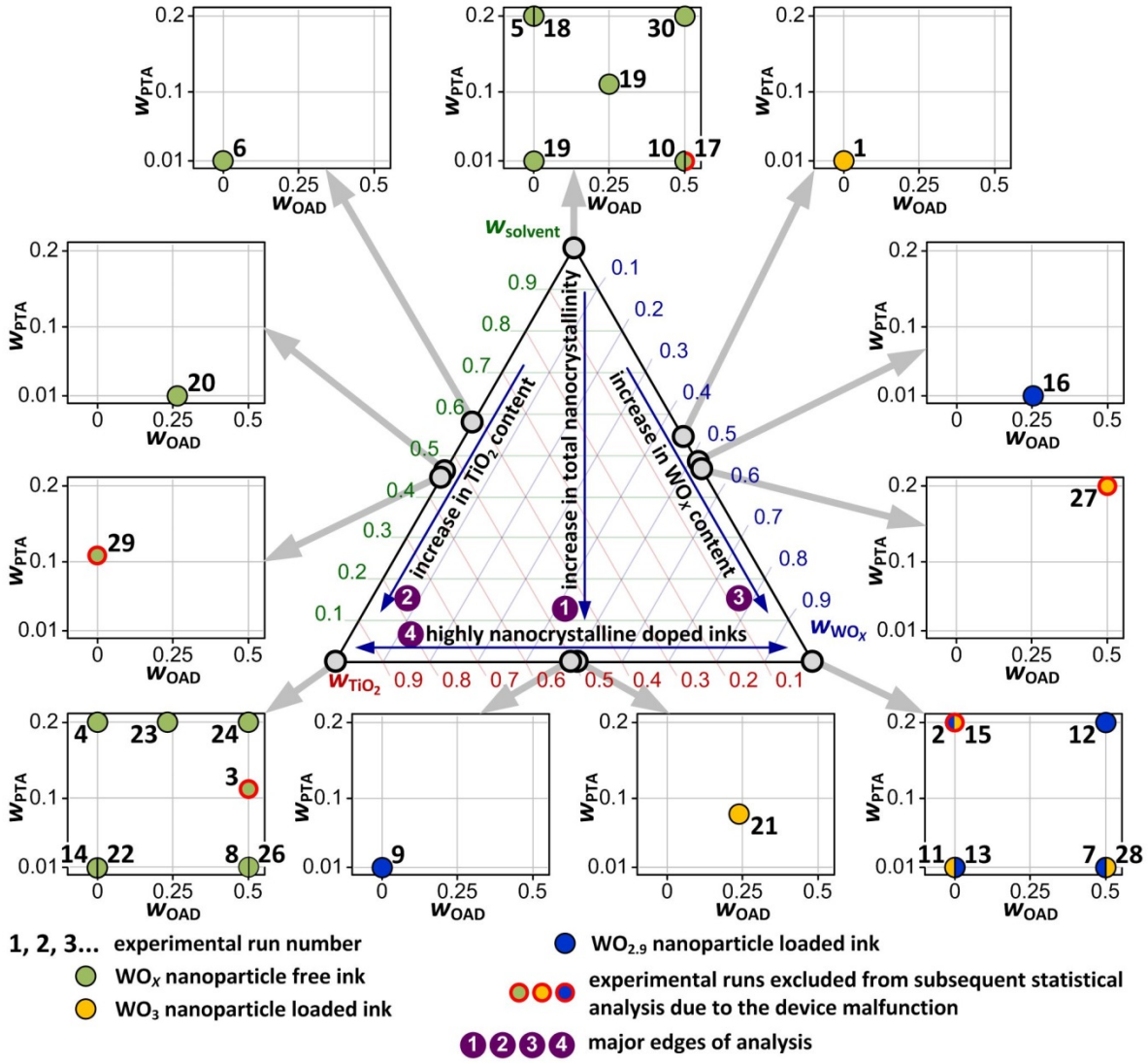

Figure 2.4. Graphical visualization of the experimental design generated according to *mixture design with one non-mixture component* methodology for a quadratic Scheffé model; variables: w_{solvent}, w_{PTA}, w_{OAD}, $w_{\mathrm{TiO_2}}$, $w_{\mathrm{WO_X}}$, and X stand for weight fractions of solvent, PTA (precursor), oxalic acid, TiO_2 dispersion, WO_X dispersion and oxygen stoichiometry of WO_X nanocrystals, respectively.

The use of the computer aided D-optimal design successfully reduced the number of overall experimental trials from 162 defined for three-level full factorial design or 72 defined for second-degree extreme vertices design down to 30 runs in the present studies. For each of experimental runs, a printable solution and targets were freshly prepared just before the use in laboratory experiment.

2.2.3. Materials

Peroxopolytungstic acid used as *a*-WO_3 precursor, was synthesized based on the procedure reported by Tetsuichi Kudo [43, 44]. The tungsten metal monocrystalline powder (Aldrich, 0.6-1μm, 99.9 %) was carefully added to 50 ml mixture (50:50) of distilled water (Millipore) and hydrogen peroxide (Sigma-Aldrich, 30 % by weight). The cooling was employed and the solution was kept slowly stirring for 24 hours in a refrigerator to prevent thermal changes due to the strong exothermic nature of the dissolution. The excess of tungsten powder was then removed by filtration (Roth, 0.45 μm syringe filter) leading to a transparent solution. In order to remove the excess of hydrogen peroxide, the solution was dried at 65º C and washed several times with the distilled water. After drying, a water soluble orange crystal powder (PTA) [45] was obtained. It should be noted that the PTA synthesized in present study and used as a sol-gel precursor of the amorphous phase may differ from the ones presented by other authors in terms of composition. The PTA expressed by empirical formula $WO_3 \cdot xH_2O_2 \cdot yH_2O$ was found to be crystalline or amorphous depending on x [44]. The H_2O_2 content depends of the applied evaporation procedure (hot plate, N_2 bubbling or rotary evaporation) in precursor synthesis [45, 46] and storage conditions, therefore obtaining reproducible products in different laboratories is difficult. Although an analytical determination of x and y was not performed in present study, it was observed that the solid obtained from PTA has an amorphous structure and is easily soluble in water at RT. As it is known from elsewhere [44], such properties indicate that synthesized substance has structure expressed by formula $WO_3 \cdot (1>x\geq 0.53)H_2O_2 \cdot (1.5>y\geq 3)H_2O$. It was therefore expected, that the variable amount of chelating peroxo groups $[O_2]^{2-}$ may affect morphological evolution during the film formation and post-treatment, and thus results in different EC performance. As it was crucial to obtain reproducible products for full set of designed experiments, the synthesis was optimized to ensure its repeatability by implementation of a very detailed protocol. Additionally in order to unify the input material for an ink formulation, products of many syntheses were mixed and grinded together. As the PTA crystals are known for their instability, the final product was stored at low temperature (-18 °C).

Two types of commercially available WO_X nanoparticles were used as a source of crystalline phase, WO_3 referred as *yellow* (Aldrich, < 100 nm) and $WO_{2.9}$ referred as *blue* (Super Conductor Materials, 99.99 %, ceramic oxide target, ~30 nm). Titania paste (Solaronix, Ti-Nanoxide T/SC, 15 - 20 nm, 3 % by weight) was used as a source of nanocrystalline TiO_2. These nanoparticles were used in a form of aqueous (Millipore) alcohol (Merck, 2-propanol, 99.8 %) dispersions in a fixed proportion of 30:70, and solid content of 0.01 % by weight. The Oxalic Acid Dihydrate (Merck) was used as received (see Section 3.5.1 for XRD spectra of raw materials).

In order to obtain 3 g of gel electrolyte, 0.36 g of PMMA (Fluka), 0.21 g of PEO-PPO (Zeon Chemicals), 0.33 g of $LiClO_4$ (Fluka) and 1.75 g of propylene carbonate (Fluka, 99 %) were mixed

with 4 ml of tetrahydrofuran (Aldrich, 99.9 %) and followed by stirring for about 4 hours until a transparent uniform lightly viscous gel was obtained. A detailed procedure is described elsewhere [47].

2.2.4. Ink formulation

Due to the limitations implemented in a standard desktop printer, such as CANON PIXMA IP4500 or IP4850 used in present studies, there is no direct access to the print-head driver. Therefore, the jetting parameters can be controlled only by proper adjustment of ink fluid parameters. To assure proper printability, the custom ink should have similar rheology to the genuine CANON inks (grey horizontal bars in Figure 2.5).

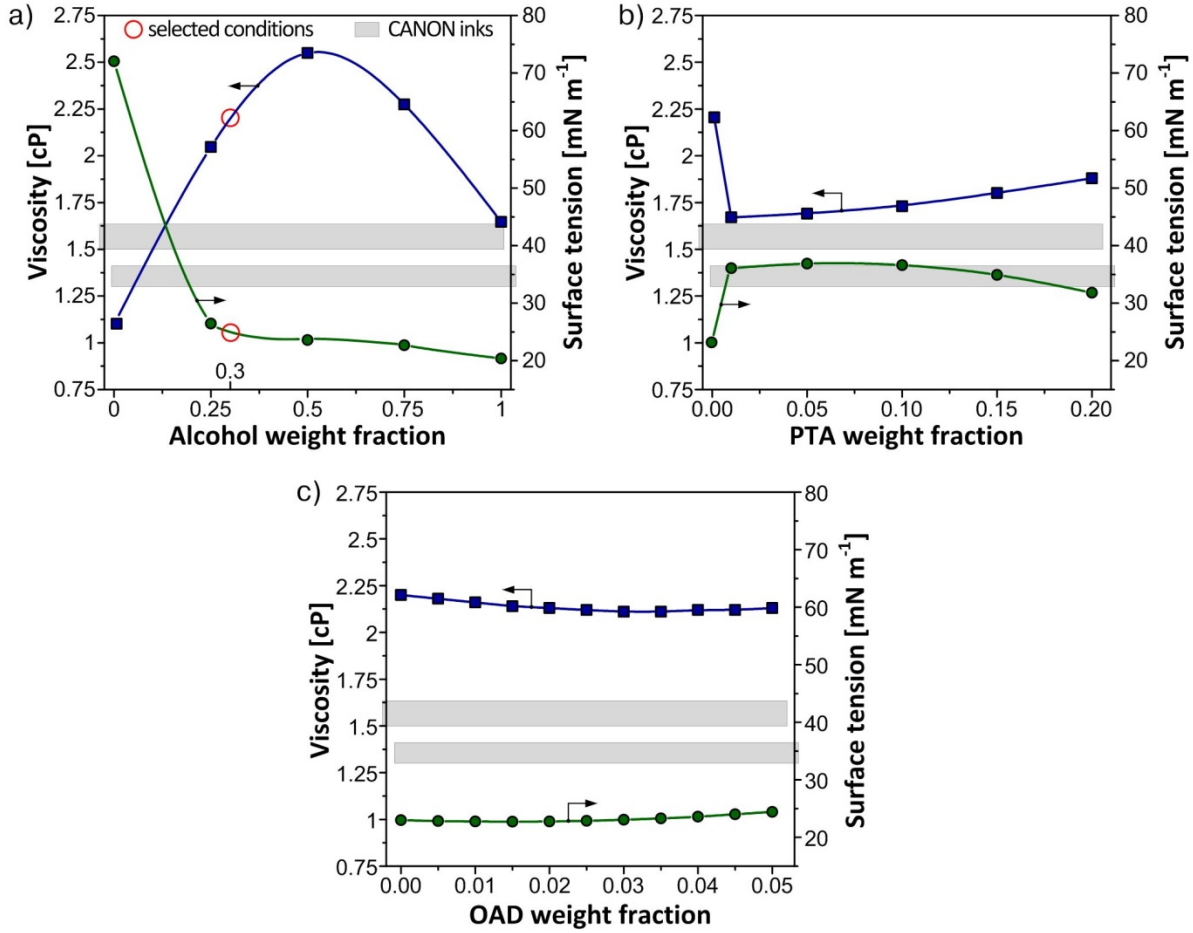

Figure 2.5. The viscosity and the surface tension of an alcohol aqueous a) ink vehicle as a function of ethanol weight fraction, b) WO_3 precursor as a function of PTA weight fraction for and c) (0.3:0.7) OAD solution as a function of OAD weight fraction; the regime of genuine CANON inks (CLI-526 cyan, magenta and yellow) is shown in grey

In order to adjust the viscosity and the surface tension of the ink vehicle (alcohol aqueous solution) to the range acceptable by the printer, the isopropyl alcohol weight fraction of 0.3 was selected. Such

concentration results in values of 2.2 cP and 25 mN m^{-1}, respectively (see Figure 2.5a). The viscosity of obtained vehicle is too high when comparing with genuine CANON inks, but addition of PTA and OAD in weight fractions used in this study, transfer the viscosity value into CANON inks regime, as shown in Figure 2.5b and Figure 2.5c. Thus, the viscosity and the surface tension of all mixtures formulated within set constraints lay inside or near the preferable regime, assuring expected printability (assuming that the influence of TiO_2/WO_X nanocrystalline solid content on ink fluid parameters is negligible). Further measurements of the viscosity and the surface tension performed on formulated inks confirmed the validity of this methodology (see Table 2.6 and Figure 2.10).

2.2.5. Printing process

An ink was formulated according to DOE recipe for each lab-testing device. Particular layers (1 cm^2) were printed using modified Canon PIXMA IP4500 desktop printer (see Figure 1.7 in Section 1.4.3.1, and Section 2.5.1 for detailed information) in regular intervals of around 1 min while being exposed to a relative humidity of 50 %, at 28 ºC on ITO PET substrates (Sigma-Aldrich, 1000 Å of ITO, 60 Ω/sq, T > 75 % at 550 nm). All films were dried at room temperature for 24 h and annealed in air at 120 °C (EHRET, TK4067, Germany) for 1 h.

2.2.6. Device assembly

The stability and durability of EC devices strongly depend on device assembly, especially when liquid electrolyte is involved in the device structure. In order to ensure reliable measurements, a simple and effective encapsulation procedure was developed (see Figure 2.6).

The lab-testing devices were assembled in a sandwich-like structure according to diagram shown in Figure 1.5a, and successive steps of the encapsulation process are shown in Figure 2.6. Applied structure includes inkjet printed EC film (working electrode), a gel electrolyte for ion storage and two transparent conductors (ITO PET foils) separated by double-sided tape spacer (Ceys, 1 mm thick). The main purpose of using a double site tape as a spacer is to limit the volume of electrolyte and to provide a constant thickness of the device. The device has been filled with liquid electrolyte using a syringe with a needle, and sealed with thermoplastic glue (iTools Thermoplastic Gun) in order to prevent the electrolyte leakage.

Optionally, the conductive tape may be used in order to improve the electrical contact. It is important to ensure that the volume of electrolyte inside the device does not contain air bubbles, because their presence may interfere with measurements. The optically active area of the device changes from dark blue color to transparent when stimulated by an electric current applied to electrodes. As both targets

are made of transparent plastic foil, the EC device can be seen clearly through it when active layer is bleached.

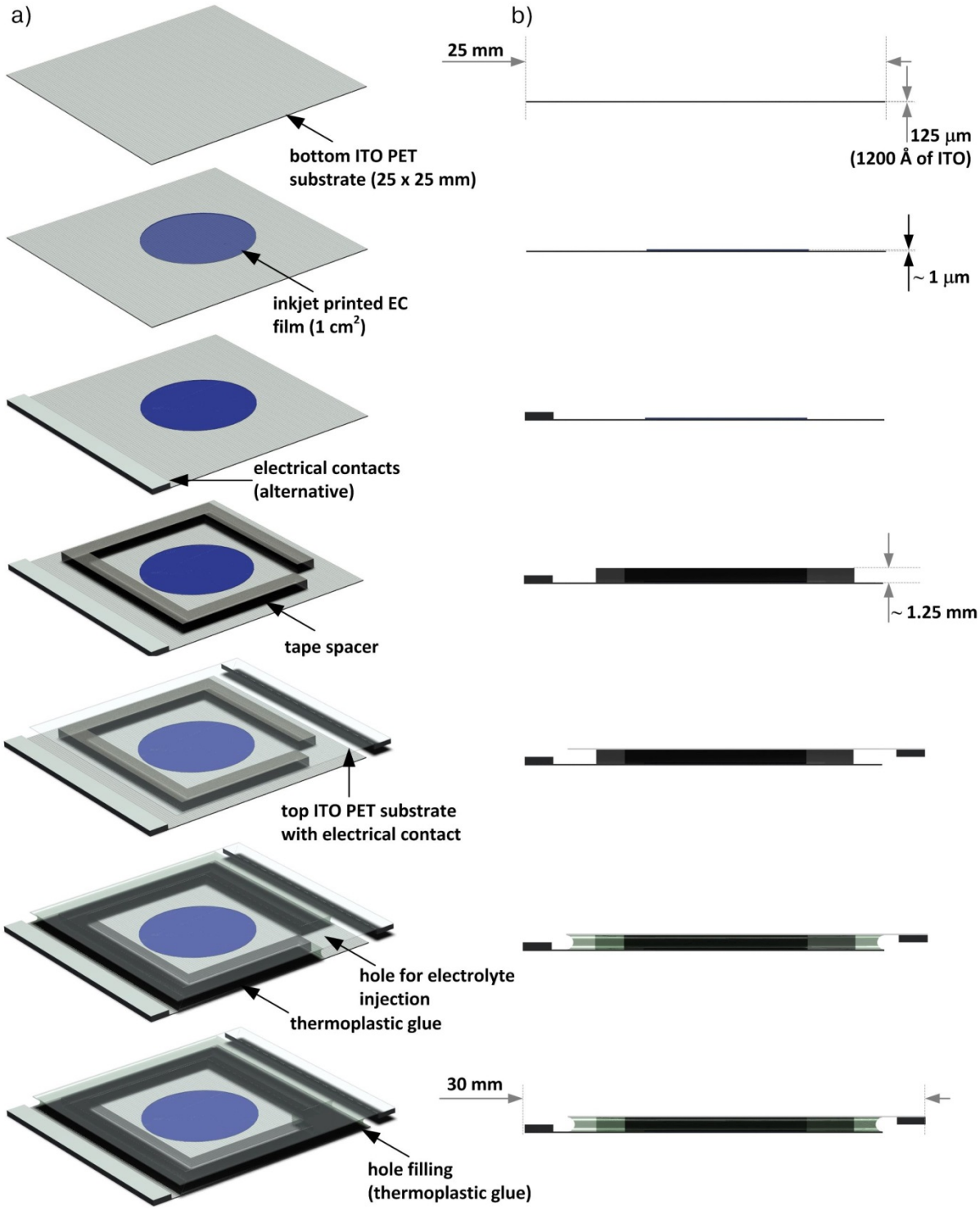

Figure 2.6. Schematic diagram of EC device encapsulation process in a) an isomeric and b) cross-section view

2.2.7. Characterization

The structural analysis of EC printed films was supported by SEM measurements (Auriga SEM-FIB, Zeiss).

Optical measurements were performed using a spectrometer setup consisting of HR4000 High-Resolution Spectrometer (Ocean Optics), Halogen Light Source HL-2000-FHSA (Mikropack), High Current Source Measure Unit (KEITHLEY 238) and QP600-2-SR/BX optical fibers (type – SR, core diameter - 600 μm, connector – QSMA, jacketing – BX). The spectral response was measured in a wide range of wavelength (400 to 900 nm) for the films colored and bleached after a constant time period (1 min) at operating voltage values of 4 and -4 V respectively (see Section 2.5.4 for detailed system description).

The electrochemical measurements (Gamry Reference 600 Potentiostat, Gamry Instruments) were performed on assembled devices in two-electrode configuration in which *working* and *working sense* are connected to a working electrode and *reference* and *counter* are connected to a second (ITO) electrode (see Section 2.5.3 for detailed system description).

2.3. Results and discussion

2.3.1. Fitting of experimental data

The Design of Experiment and statistical data analysis were performed using JMP 8.0 (S.A.S. Institute Inc., Cary, NC, USA). Ternary contour graphical presentations of the models were generated in JMP 8.0 and processed graphically in Visio 2010 (Microsoft Corp., Redmond, USA) diagramming tool.

The mathematical fitting based on multiple regression have been performed for each categorical factor level using the first order polynomial function (quadratic) expressed by the Equation 2.8.

$$Y_{1\leq k\leq 16} = \sum_{i=1}^{5} \beta_i X_i + \sum_{i=1}^{4} \sum_{j=i+1}^{5} \beta_{ij} X_i X_j + \varepsilon \qquad (2.8)$$

Surface responses $Y_k (1 \leq k \leq 16)$ were determined by five controlled mixture components $X_i (1 \leq i \leq 5)$, coefficients of the main factors and the coefficients of the first order interactions β_i, β_{ij}, respectively, and ε which represents a random error of the method. This model can be used to predict the response for any condition within the experimental space.

From the measurements of developed devices 16 responses were obtained: mechanical, optical, electrical, fluidic (ink) and overall performance parameters. Due to the complexity of analysis and the high number of studied responses, the considerations are limited to the main parameters that describe switching kinetics and overall performance of EC films, namely coloration time (τ_{col}), bleaching time (τ_{bl}), optical density (ΔOD) and coloration efficiency (CE) (see Section 2.5.5 for definitions and

calculation procedure). The measured values of selected parameters corresponding to each experimental run are presented in Table 2.2.

Table 2.2. Measured values of selected parameters corresponding to each experimental run

Run	τ_{col} (s)	τ_{bl} (s)	ΔOD (x10^{-2})	CE (cm^2C^{-1})
1	14	9	36.18	188.42
(2)	-	-	-	-
(3)	-	-	-	-
4	2[a]	3	4.25	29.13
5	3	4	11.5	83.95
6	4	5	46.05	225.72
7	9	4	8.25	70.51
8	4	4	3.84	34.87
9	10	7	37.73	474.01[b]
10	4	3	10.23	73.6
11	4	2[a]	23.31	187.99
12	11	9	38.72	175.2
13	10	7	26.85	80.88
14	3	3	50.98	383.31
(15)	-	-	-	-
16	8	6	4.5	15.29
(17)	-	-	-	-
18	6	2[a]	1.36[a]	2.84[a]
19	4	8	75.3	404.82
20	2[a]	4	6.95	43.72
21	14[b]	12[b]	82.64[b]	454.09
22	4	5	46.44	305.56
23	4	2[a]	20.72	199.22
24	5	5	18.21	130.05
25	3	2[a]	17.56	91.96
26	8	5	9.39	46.48
(27)	-	-	-	-
28	9	2[a]	13.12	48.04
(29)	-	-	-	-
30	5	6	55.93	321.43

[a] minimum response obtained (Y_k^{min});
[b] maximum response obtained (Y_k^{max});
( ) experimental runs excluded from subsequent statistical analysis due to the device malfunction caused by uncontrollable factors (incorrect encapsulation, film failure, etc…).

The modeled responses presented in Figure 2.7 were generated at the major edges of analysis defined in Figure 2.4. By analyzing those plots, it is clear that a substantial reduction in τ_{col} and τ_{bl} value is obtained when increasing the TiO_2 content, while increasing the WO_X content results in opposite effect. This observation can be explained by increased volume of grain boundaries in highly WO_X doped films, which enhances trapping of free charge carriers. On the other hand, when increasing the TiO_2 content in the film, the amount of residual charges in *a*-WO_3/WO_X film decreases due to the enhancement of the reversibility of the redox process. Modeled ΔOD response in Figure 2.7d indicates that films containing a large amount of TiO_2 nanoparticles (0.76 wt%) with a small

share of WO_X content (0.22 wt%) in amorphous matrix exhibit the highest transmission modulation ($\Delta OD = 0.38$), which is attributed to two mechanisms. Firstly, the TiO_2 nanocrystals conduct Li^+ ions into the film much easier than *a*-WO_3 or WO_X. Secondly, the TiO_2 nanocrystals increase the surface area of optically active *a*-WO_3 matrix providing higher number of electrochemically reactive sites. The overall device performance expressed by CE is closely related to the optical modulation and reveals similar behavior as a function of TiO_2/WO_X solid content.

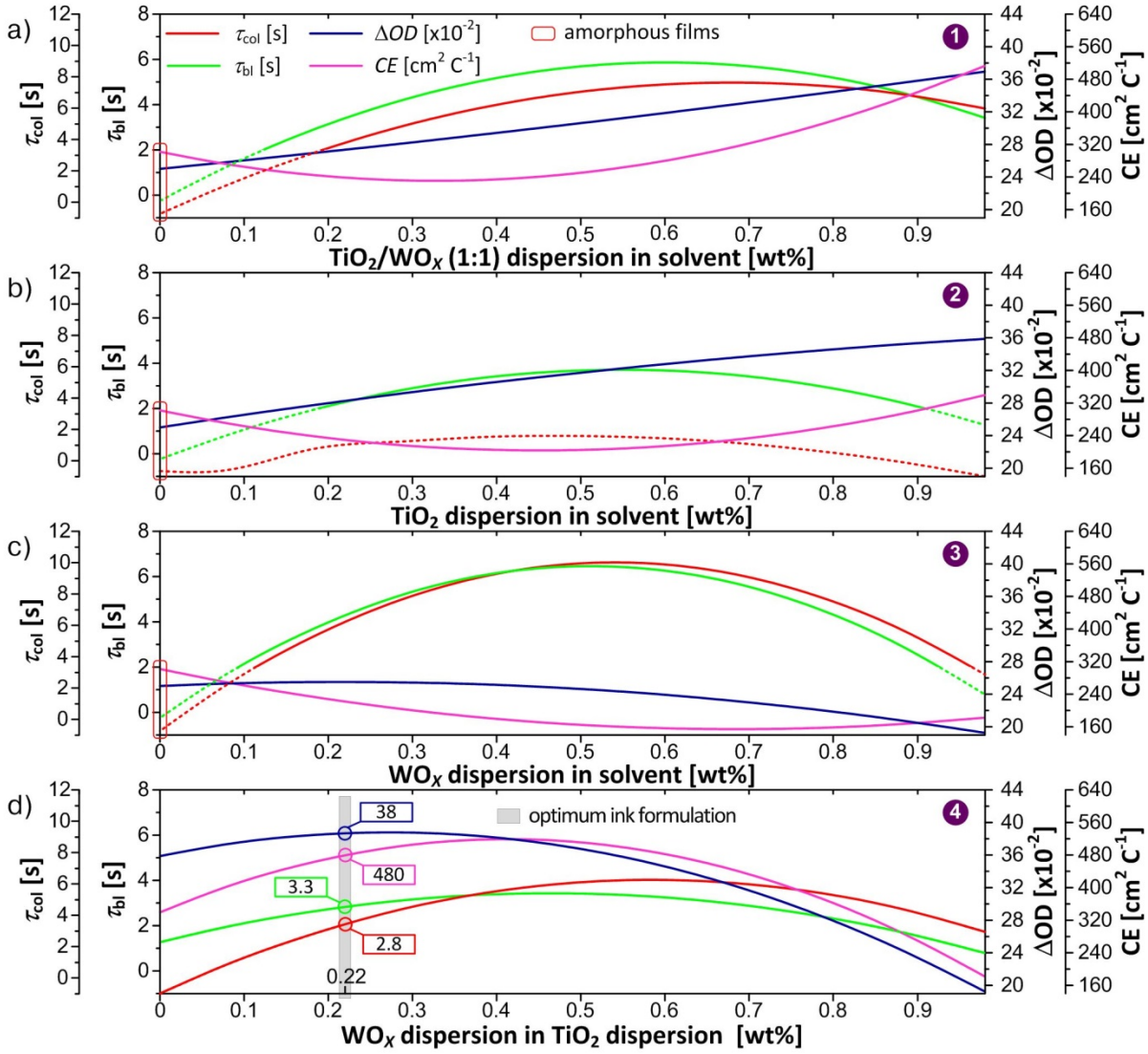

Figure 2.7. Modeled response plots presenting variation in τ_{col}, τ_{bl}, ΔOD and CE at the major edges of analysis defined in Figure 2.4; $w_{PTA} = 0.01$, $w_{OAD} = 0.01$, $X = 3\{yellow\}$; dash line represents physically unreliable data (values of τ_{col} and τ_{bl} below 2s were not recorded); the optimum ink formulation and related values of responses were indicated

The contour plot on a trilinear coordinate scale was used to present predictions of experimental results obtained *via* the multiple regression fitting. This graphical methodology provides an easy way to demonstrate the efficacy of the enhanced performance of printed EC films. Ternary plots were

generated as a function of TiO_2/WO_X nanocrystalline content while the concentrations of other components (*i.e.* PTA, OAD) were kept constant (Figure 2.8). The third axis stood for pure alcoholic aqueous solvent in order to quantify the amount of nanocrystals dispersed in the ink and afterwards transferred to the printed films. The effect of the type and content of metal oxide nanoparticles in the precursor sol formulated in various Peroxopolytungstic Acid (PTA) and Oxalic Acid (OAD) proportions on EC film properties have been comprehensively described in Chapter 3.

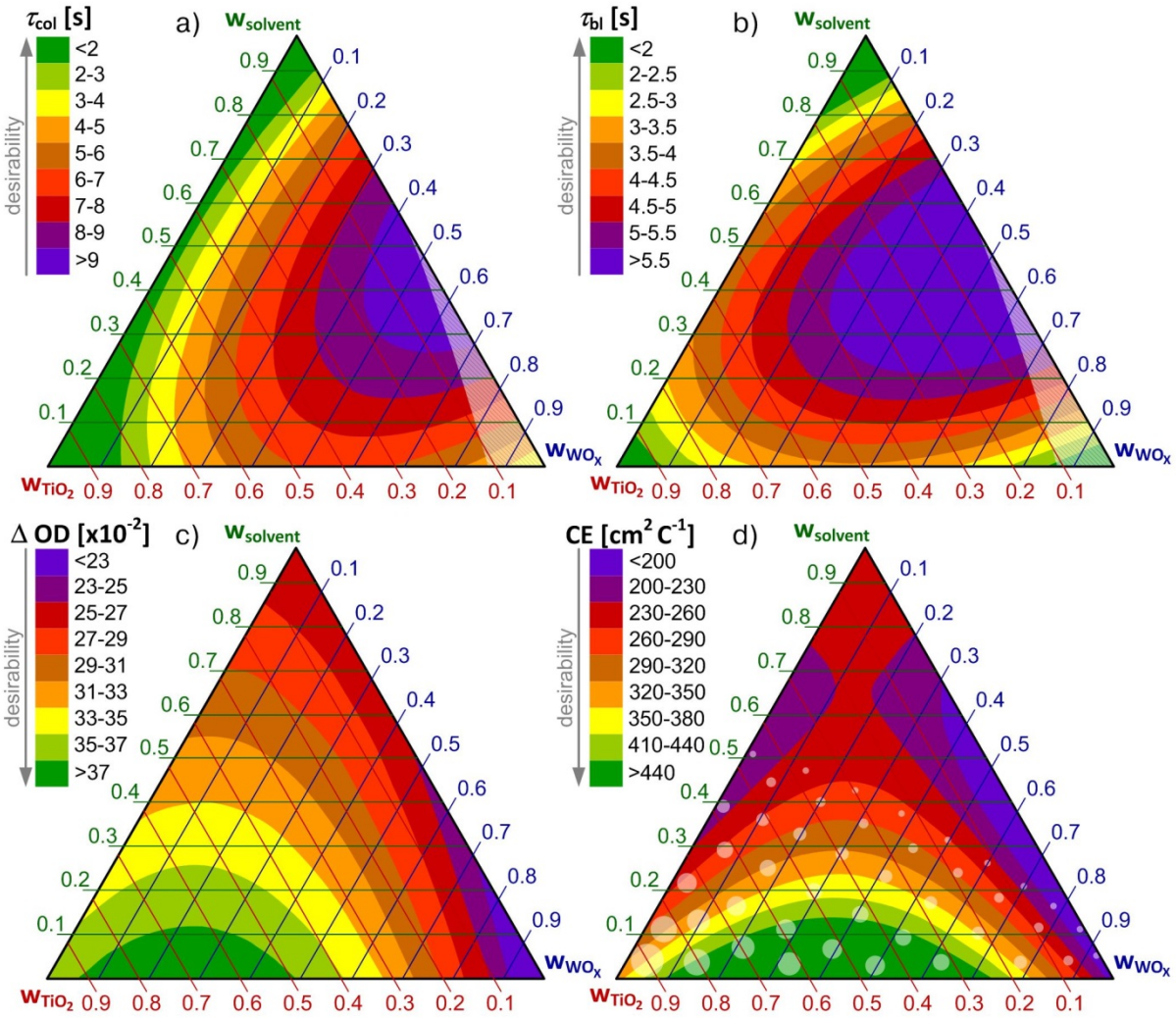

Figure 2.8. Empirical response contour plots presenting variation in a) coloration time (τ_{col}), b) bleaching time (τ_{bl}), c) optical density (ΔOD) and d) coloration efficiency (CE) as the weight fractions of TiO_2 and WO_X dispersions are varied (w_{PTA} = 0.01, w_{OAD} = 0.01, X = 3{*yellow*}, values selected *via* ink optimization); the triangle faded region indicates unreliable measurements due to the low optical modulation (see Section 2.5.5 for more details), while the region of rounded faded marks indicates concentrations for which discontinuous patterns were obtained (detailed discussion on the influence of film discontinuity on data reliability is presented in Chapter 3)

A detailed discussion on the microstructural and morphological aspects related to inkjet printed dual-phase *a*-WO_3/TiO_2/WO_X films is presented in Chapter 3.

2.3.2. Empirical model validation

The model optimality was evaluated based on a summary of fit (*i.e.* the least square regression) and analysis of variance (ANOVA) parameters summarized in Table 2.3 and Table 2.4, respectively. Following parameters were considered: coefficient of determination (R^2, Equation 2.9), adjusted coefficient of determination (R^2-adj, Equation 2.10), Root Mean Square Error (RMSE, Equation 2.11), Normalized Root Mean Square Error (NRMS, Equation 2.12), mean value, F-ratio statistics (F-ratio) and the ANOVA probability (Prob > F).

$$R^2 = 1 - \frac{SS_{\text{residuals}}}{SS_{\text{total}}} \tag{2.9}$$

$$R^2\text{-adj} = 1 - \frac{\frac{SS_{\text{residuals}}}{n-K}}{\frac{SS_{\text{total}}}{n-1}} \tag{2.10}$$

$$\text{RMSE} = \sqrt{\frac{\sum_{i=1}^{n}\left(Y_i^{\text{actual}} - Y_i^{\text{predicted}}\right)^2}{n}} \tag{2.11}$$

$$\text{NRMSE} = \frac{100 \cdot \text{RMSE}}{(Y_k^{\max} - Y_k^{\min})}\,(\%) \tag{2.12}$$

where: $SS_{\text{residuals}}$ is the sum-of-squares of the residuals, SS_{total} is the sum of squares of the distances from a horizontal line through the mean of all *Y* values, *n* is the number of data points, and *K* is the number of parameters fit by regression.

The R^2 parameter of 1 means, that the prediction model represents actual data with no error, while the 0 value indicates that the prediction model serves no better than overall response mean. The R^2-adj adapts the R^2 and makes it more comparable within models with different number of parameters.

Mean value represents overall mean (i.e. arithmetic average) of the response. The F-ratio is a measure of how different the means are relative to the variability within each sample. The larger this value, the greater the likelihood that the differences between the means are due to something other than chance alone (F-ratio > 1). The Prob > F value is a probability of obtaining F-ratio greater than 1 calculated if there is no difference in the population group means. Values smaller than 0.05, are considered evidence that the predicted model is statistically better than the overall response mean.

The polynomial responses modeling (quadratic) offered by the screening design appeared to be sufficient for the optical density (ΔOD) and coloration efficiency (CE) due to its ability to supply high coefficient of determination *i.e.* R^2-adj(ΔOD) = 0.87 and R^2-adj(CE) = 0.98, indicating a good correspondence between the model prediction (fitting) and the experiments, while simultaneously

minimizing the overall number of coefficients. The ANOVA significance probabilities (Prob > F) of 0.0235 and 0.0006, respectively, support the accuracy of the model. In case of coloration time (τ_{col}) and bleaching time (τ_{bl}), the regression coefficients were R^2-adj(τ_{col}) = 0.51 and R^2-adj(τ_{bl}) = 0.72 while significance probabilities were 0.2228 and 0.0893, respectively, indicating that the models for those responses are only slightly better than the overall response mean giving a small number of significant regression factors. The size of a random noise (residual variance), as measured by Normalized Root Mean Square (NRMSE), is reflecting the same prediction abilities for τ_{col}, $\tau_{bl,}$ ΔOD and CE giving values of 21%, 14%, 10.3% and 4.5%, respectively. As no non-linear response was detected for τ_{col} and τ_{bl} (Residual by Predicted Plot with a random pattern – not shown here), a more-complex design-type is not required, and the lack of fit comes from difficulties associated with accurate measurements of those responses (see Section 2.5.5 for more details).

Table 2.3. Model validation parameters based on least square regression

Response	R^2	R^2-adj	RMSE	NRMSE
τ_{col} (s)	0.91	0.51	2.52 (s)	21.0 (%)
τ_{bl} (s)	0.95	0.72	1.40 (s)	14.0 (%)
ΔOD (x10^{-2})	0.98	0.87	8.38 (x10^{-2})	10.3 (%)
CE (cm^2C^{-1})	1	0.98	21.27 (cm^2C^{-1})	4.5 (%)

Table 2.4. Model validation parameters based on analysis of variance

Response	mean	F-ratio	Prob > F
τ_{col} (s)	6.25 (s)	2.27	0.2228
τ_{bl} (s)	4.96 (s)	4.13	0.0893
ΔOD (x10^{-2})	27.08 (x10^{-2})	8.87	0.0235
CE (cm^2C^{-1})	169.63 (cm^2C^{-1})	57.70	0.0006

Resuming, the proposed experimental design methodology turned out to offer a sufficiently accurate mathematical modeling with a complete coverage of experimental trials (R^2 values of 0.91, 0.95, 0.98 and 1 for τ_{col}, $\tau_{bl,}$ ΔOD and CE respectively) while the total number of designed experiments has been reduced from 162 in the full factorial (L = 3) and 72 in the extreme vertices (D = 2) approach down to only 30 runs.

2.3.3. Analysis of significance

The initial tests of significance of all effects (*i.e.* factors and interactions) have been performed graphically using leverage plots [48]. However, due to the complexity of this representation, the

leverage graphs are not presented here, but their qualitative results were included in the Table 2.5 (see Section 2.5.7 for more details).

Quantitatively, estimated effects of all factors or their interactions are represented *via* the absolute value of the *t*-ratio and *p*-value, graphically described in Figure 2.9. The *t*-ratio shows how strong is the evidence that selected variable contributes something of additional relevance, while all the other variables in the current model are already taken into account. The *p*-value tests the null hypothesis that each coefficient is statistically zero. A typical value of confidence for rejecting this hypothesis occurs usually for (1 – *p*-value) > 0.95. Thus, a large absolute value of *t*-ratio indicates that the element should be included in the model, while a *p*-value less than 0.05 is regarded as significant.

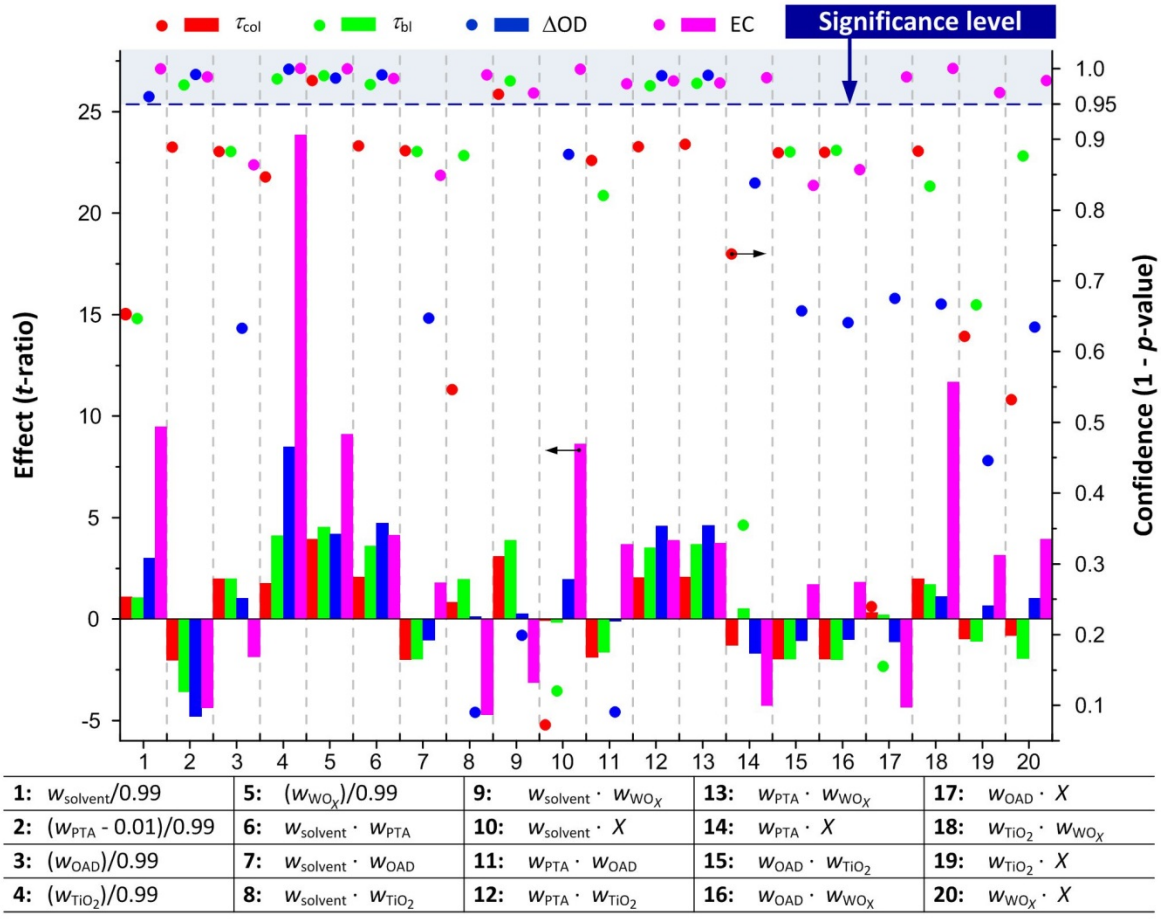

Figure 2.9. Effect plot for all factors and interactions under consideration in screening design analysis for τ_{col}, τ_{bl}, ΔOD and CE

Analysis results of all effects based on the leverage plots method and Student's *t*-test statistics for τ_{col}, τ_{bl}, ΔOD and CE responses lead to the conclusions shown in Table 2.5. Elements marked by (+) indicate these coefficients that were determined to be significant meaning that the factor (or factor interactions) had a major effect on a particular response value quantifying their importance. As the emphasis of DOE was screening, the *importance* (*i.e.* imp.) column indicate the most significant effects (starting from value 1) sorted by the absolute value of the *t*-ratio which lists the test statistics

for the hypothesis that each parameter is zero. Each *t*-ratio value expresses a ratio of particular parameter estimate to its standard error, and has a Student's *t*-distribution if the hypothesis is true.

Table 2.5. Results of the factorial analysis obtained *via* the leverage plots method and Student's *t*-test statistics

Effect	Response model							
	τ_{col}		τ_{bl}		ΔOD		CE	
	result	imp.	result	imp.	result	imp.	result	imp.
w_{solvent}	-		-		+	6	+	3
w_{PTA}	-[a]		+[a]	6	+[a]	2	+[a]	7
w_{OAD}	-[a]		-[a]		-[a]		-[a]	
$w_{\mathrm{TiO_2}}$	-		+	2	+	1	+	1
$w_{\mathrm{WO_X}}$	+	1	+	1	+	5	+	4
$w_{\mathrm{solvent}} \cdot w_{\mathrm{PTA}}$	-		+	5	+	3	+	10
$w_{\mathrm{solvent}} \cdot w_{\mathrm{OAD}}$	-		-		-		-	
$w_{\mathrm{solvent}} \cdot w_{\mathrm{TiO_2}}$	-		-		-		+	6
$w_{\mathrm{solvent}} \cdot w_{\mathrm{WO_X}}$	+	2	+	3	-		+	16
$w_{\mathrm{solvent}} \cdot X$	-		-		-		+	5
$w_{\mathrm{PTA}} \cdot w_{\mathrm{OAD}}$	-		-		-		+	14
$w_{\mathrm{PTA}} \cdot w_{\mathrm{TiO_2}}$	-		+	7	+	5	+	12
$w_{\mathrm{PTA}} \cdot w_{\mathrm{WO_X}}$	-		+	4	+	4	+	13
$w_{\mathrm{PTA}} \cdot X$	-		-		-		+	9
$w_{\mathrm{OAD}} \cdot w_{\mathrm{TiO_2}}$	-		-		-		-	
$w_{\mathrm{OAD}} \cdot w_{\mathrm{WO_X}}$	-		-		-		-	
$w_{\mathrm{OAD}} \cdot X$	-		-		-		+	8
$w_{\mathrm{TiO_2}} \cdot w_{\mathrm{WO_X}}$	-		-		-		+	2
$w_{\mathrm{TiO_2}} \cdot X$	-		-		-		+	15
$w_{\mathrm{WO_X}} \cdot X$	-		-		-		+	11

imp.- importance;
(-) not significant;
(+) significant;
[a] colinearity;

In general, the model predicts that EC performance of printed films is enhanced by dual-phase composition, which means that metal oxide nanocrystals concentration is critical. In detail, the significance analysis leads to the conclusion that the τ_{col} depends mainly on the quantity of WO_X nanocrystals in the EC layer. The τ_{bl} is influenced by the quantity of WO_X and TiO_2 nanocrystals and also depends of the WO_3 amorphous content formed from the PTA precursor. The ΔOD, which describes the optical contrast between colored and bleached states, depends mainly on quantity of TiO_2 nanocrystals and WO_3 amorphous content. The significant factors with regards to their impact on CE, which describes overall device performance, depends to a greater or lesser extent on almost all mixture components and their interactions, but the most significant are TiO_2 and WO_X crystalline

nanoparticles. The colinearity indicated by (*) obtained for main effects derived from PTA and OAD components indicates that those two coefficients have no independent variation to support fitting of any presented response variation, because they are linear function of other factors. While the role of PTA is evident from coefficients of the first order interactions, the OAD impact on the EC performance is almost negligible. The OAD component may therefore be eliminated from consideration without detriment to the EC effect, simplifying the method by reducing the number of ingredients. However, it will be shown in following sections, that small amount of OAD (w_{OAD} = 0.01) was identified as a component of optimal ink formulation.

2.3.4. Ink optimization

One of the reasons to fit a mathematical model to experimental data is to find combinations of the component proportions in a mixture setting to reach the maximum possible performance. Response surface maps of experimental regions presented in Figure 2.8 facilitate the decision-making process when determining the most appropriate ink formulation for desired individual EC responses. However, a numerical multi-response optimization offered by software enables to find the specific point that maximizes the global desirability, and thus, optimal overall EC performance [49]. In such simultaneous optimization, the desirability values (d_k) of n responses (Y_k) are combined to create an overall desirability (D_n) as it is described by Equation 2.13. Such definition insures that if any single desirability is equal to zero (*i.e.* undesirable), the overall desirability is 0 as well.

$$D_n = \left(\prod_{k=1}^{n} d_k^{I_k}\right)^{1/\sum_{k=1}^{n} I_k} = \left(\prod_{k=1}^{n} f_k(Y_k)^{W_k \cdot I_k}\right)^{1/\sum_{k=1}^{n} I_k} \quad (2.13)$$

Thus, W_k is the weight, I_k is the significance and the one-sided function $f_k(Y_k)$ depends on the response's optimization goal (minimize or maximize) according to Equation 2.14 showing maximization of Y_k response (minimization is equivalent to maximization of -Y_k).

$$f_k(Y_k) = \begin{cases} 0, & Y_k \le Y_k^{min} \\ \left(\frac{Y_k - Y_k^{min}}{Y_k^{max} - Y_k^{min}}\right), & Y_k^{min} < Y_k < Y_k^{max} \\ 1, & Y_k \ge Y_k^{max} \end{cases} \quad (2.14)$$

The applied desirability function $f_k(Y_k)$ is a transformation of each estimated response variable to the desirability value in a 0 to 1 scale, where 0 represents a completely undesirable response and 1 represents the most desirable response.

In order to determine the best performing EC ink formulation, the optimization goal was to minimize values of coloration and bleaching times and maximize values of the optical density and coloration efficiency. Weights and Importance values were set as equal (W_k = I_k = 1), while desired response limits (Y_k^{min}, Y_k^{max}) were defined according to the experimental results (indicated in Table 2.2), which

simplifies the overall desirability to the geometric mean of individual desirability values expressed by Equation 2.15.

$$D_{\mathrm{n}} = (\prod_{\mathrm{k}=1}^{\mathrm{n}} d_{\mathrm{k}})^{1/n} = (\prod_{\mathrm{k}=1}^{\mathrm{n}} f_{\mathrm{k}}(Y_{\mathrm{k}}))^{1/n} \quad (2.15)$$

The resulting optimum ink formulation is described by following factors values (wt%): w_{solvent} = 0, w_{PTA} = 0.01, w_{OAD} = 0.01, w_{TiO_2}= 0.76, w_{WO_X} = 0.22 and X = 3{yellow}, giving the maximum overall desirability value of 0.89. The examination of results from desirability profiler gives the performance prediction for optimized EC device in which τ_{col} = 3.3 s, τ_{bl} = 2.8 s, ΔOD = 0.38 and CE = 480 $\mathrm{cm^2C^{-1}}$ (see Figure 2.7d), thereby fulfilling all of the optimization requirements.

2.4. Conclusions

This work demonstrates that combination of IPT as a novel deposition technique and DOE methodology provides an effective means to explore and predict the behavior of high performance EC devices. Using the D-optimal mixture design with one no-mixture component could reduce the total number of experimental trials from 162 in full factorial (L = 3) and 72 in extreme vertices (D = 2) approach down to only 30 runs, while still maintaining high accuracy of analysis. Very high determination coefficients of the empirical models have proven the method abilities to predict the optimal ink formulation. The inkjet printed EC films shows outstanding performance when comparing with the state-of-the-art counterparts derived from analogous precursor *via* other deposition techniques. Coloration and bleaching time of optimized films reached 3.3 and 2.8 s, respectively (state-of-the-art: coloration time of 20 - 35 s for dip-coated [50, 51], 30 - 53 s for spin-coated [51, 52] and 94 s for electrodeposited [53, 54] films; bleaching time typically of 5 – 20 s [51–54]). Optical modulation of 0.38 is comparable to other films derived from PTA [52, 55, 56]. Superior overall performance of optimized films is reflected in coloration efficiency reaching 480 $\mathrm{cm^2\ C^{-1}}$ (state-of-the-art: 40 - 60 $\mathrm{cm^2\ C^{-1}}$ for dip-coated [51], 40 – 55 $\mathrm{cm^2\ C^{-1}}$ for spin-coated [51, 55] and 60 $\mathrm{cm^2\ C^{-1}}$ for electrodeposited [53, 54] films). The identification of the critical process factors *via* screening experiment was essential for method optimization itself and resulted in reduced number of system components, greatly simplifying the technological process.

2.5. Supporting information

In this section, several diagrams, pictures and plots are provided for more detailed description of the methodology, arguments and conclusions presented in above chapter. It provides information about inkjet printing system, ink rheology, electrochemical measurements setup, optical measurements

setup, definitions of parameters (responses), design diagnostic, and initial tests of significance (leverage plots).

2.5.1. Inkjet printing system selection

The selection of inkjet printing system for experiments was dictated by the printer functionality, which should satisfy two requirements. Firstly, the printer enables printing on CDs using dedicated CD tray. Secondly, cartridges are not integrated with the printhead. Canon PIXMA desktop printers compatible with CD printing were found to be the most suitable for this task. Full tests were performed with models Canon PIXMA MP600 (tray F), IP4500 (tray F) and IP4850 (tray G). However, there are many potentially useful models available which differ mainly in CD printing tray used, for example:

- tray B - IP3000, IP4000, IP5000, IP6000, IP6000D, IP8500, MP750, MP760, MP780;
- tray C - IP4200, IP5200, IP6700D, MP950;
- tray D - MP500, MP530, MP800, MP830;
- tray E - Pro9000, Pro9500;
- tray F - IP4300, IP5300, MP610, MP810, MX850, MP960, MP970;
- tray G - MG5240, MG6140, MG6150, MG8140, MG8150, IP4600, IP4680, IP4700, IP4780, IP4820, IP4840, MG8120, MG6120, MG6220, MG5320, MG5220, MG5250;
- tray J - IP7200, MG6300, MG5400.

2.5.2. Ink rheology

Table 2.6 contains values of intrinsic viscosity and surface tension of all inks formulated according to DOE table. The viscosity was measured using glass capillary viscometer (CANNON-UBBELOHDE, 9721-K53 CUC Series), while the surface tension was measured with glass stalagmometer (Rohr A, NEUBERT-GLAS).

The viscosity of mixtures within DOE set vary between 1.52 and 2.05 cP, while values of surface tension are in range between 31.45 and 41.02 mN m^{-1}. Therefore viscosity and surface tension of all mixtures lay in the acceptable range for selected printing system. The data from the Table 2.6 were fitted using first order polynomial function (quadratic) expressed by Equation 2.8. The resulting contour plots shown in Figure 2.10 present change in viscosity and surface tension as the ink composition is varied.

Increasing TiO_2 NPs concentration in the ink increases its viscosity. In turn, increasing WO_X NPs content decreases the ink viscosity. It can be explained by the fact that WO_X NPs have much lower isoelectric point (pH of i.e.p. ~1) than TiO_2 NPs (pH of i.e.p. ~6.7). In the neutral environment of

PTA (pH of i.e.p. ~5.5), both WO_X and TiO_2 NPs tend to agglomerate, resulting in increased viscosity. Variation in values of surface tension was observed to be small, which means that all formulated mixtures are comparable, and the impact of surface tension variation on printability is negligible.

Table 2.6. Measured values of the viscosity and the surface tension for each experimental run

Run	Viscosity [cP]	Surface tension [mN m^{-1}]
1	1.63	40.87
(2)	1.99	31.79
(3)	1.95	32.8
4	2.01	34.8
5	1.88	31.45
6	1.66	38.32
7	1.64	37.44
8	1.67	36.92
9	1.55	37.25
10	1.61	37.22
11	1.54	39.61
12	1.9	33.45
13	1.52	40.81
14	1.72	40.66
(15)	1.89	33.99
16	1.56	41.02
(17)	1.54	40.46
18	1.88	32.38
19	1.69	37.28
20	1.58	38.39
21	1.62	34.12
22	1.57	39.03
23	1.98	34.1
24	2.05	33.53
25	1.6	36.31
26	1.7	40.02
(27)	1.96	34.18
28	1.56	37.88
(29)	1.69	37.98
30	1.99	35.66

( ) Experimental runs excluded from subsequent statistical analysis due to the device malfunction caused by uncontrollable factors (incorrect encapsulation, film failure, etc…).

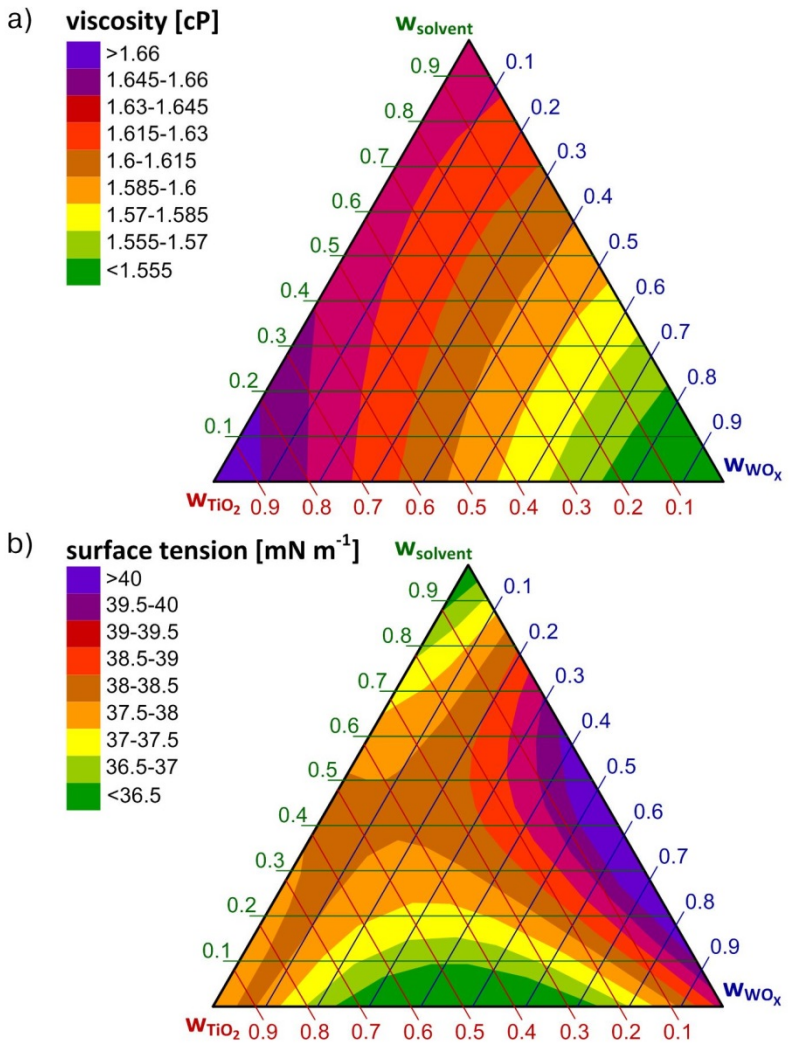

Figure 2.10. Empirical response contour plots presenting variation in a) viscosity and b) surface tension, as the weight fractions of TiO_2 and WO_X dispersions are varied (w_{PTA} = 0.01, w_{OAD} = 0.01, X = 3{*yellow*}, values selected *via* ink optimization)

2.5.3. Electrochemical measurement setup

The electrochemical measurements were performed on assembled devices in two-electrode configuration shown in Figure 2.11a. *Working* and *working sense* are connected to the ITO PET substrates coated with optically active *a*-WO_3/TiO_2/WO_X electrode, while *reference* and *counter* are connected to a second electrode (ITO). All electrochemical measurements were performed using Gamry Reference 600 Potentiostat from Gamry Instruments (see Figure 2.11b and Figure 2.11c).

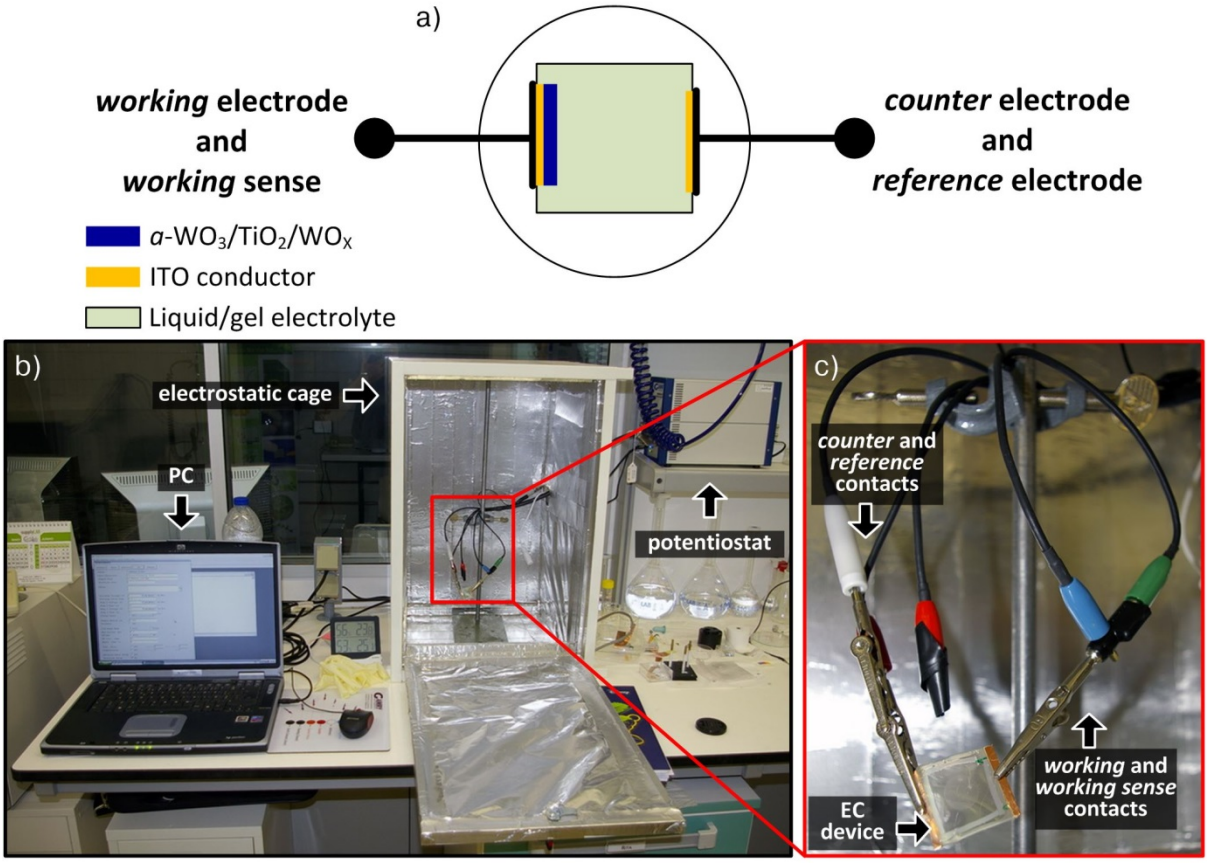

Figure 2.11. Electrochemical measurement system in a) schematic representation of two-electrode electrochemical cell setup, b) picture showing its configuration and c) EC device installation

2.5.4. Optical measurement setup

Optical measurements were performed using spectrometer setup shown in Figure 2.12. The protocol showing proper installation of a lab-testing device inside the spectrometer setup is shown in Figure 2.13.

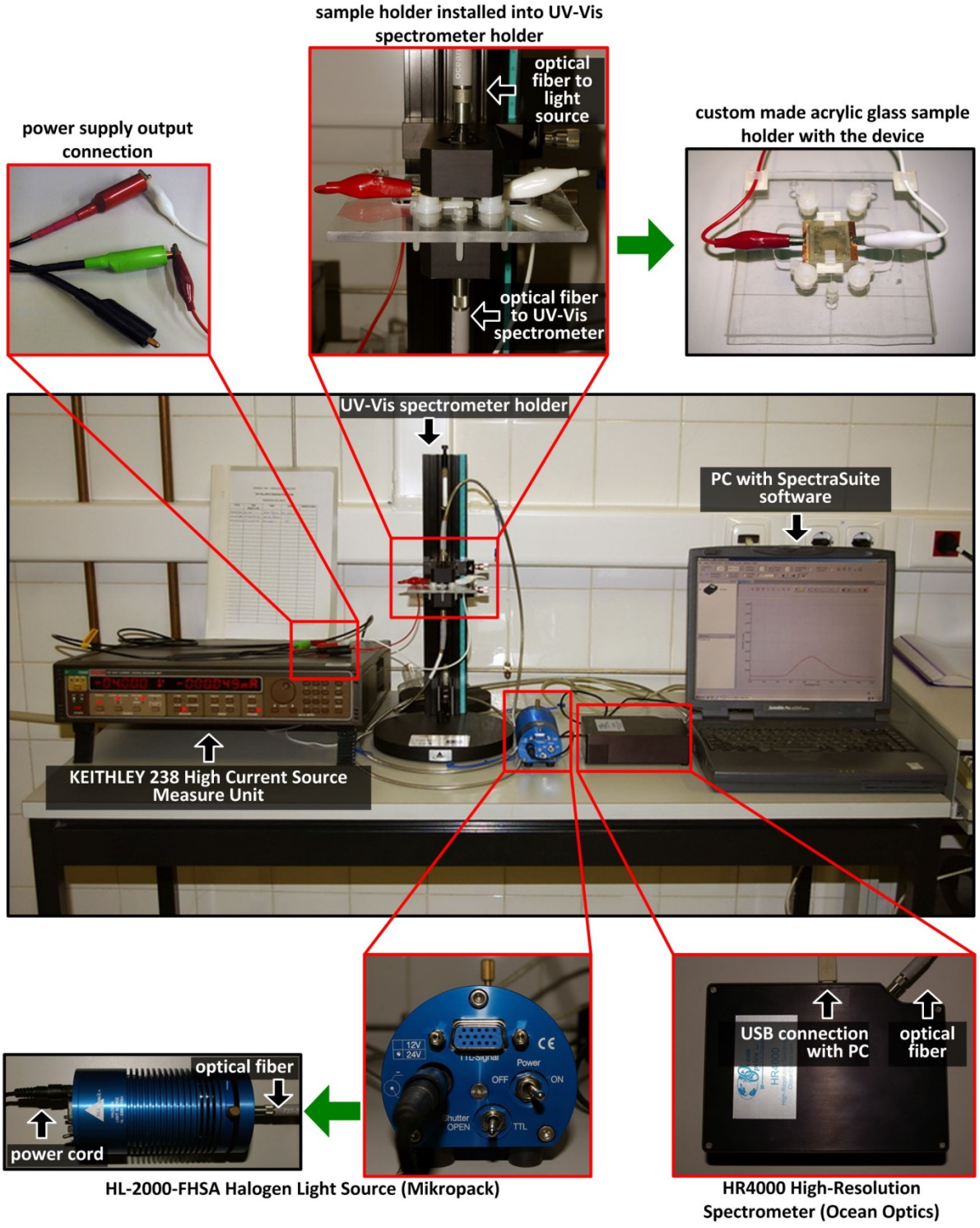

Figure 2.12. Optical measurement system setup; UVS stands for UV-Vis spectrometer

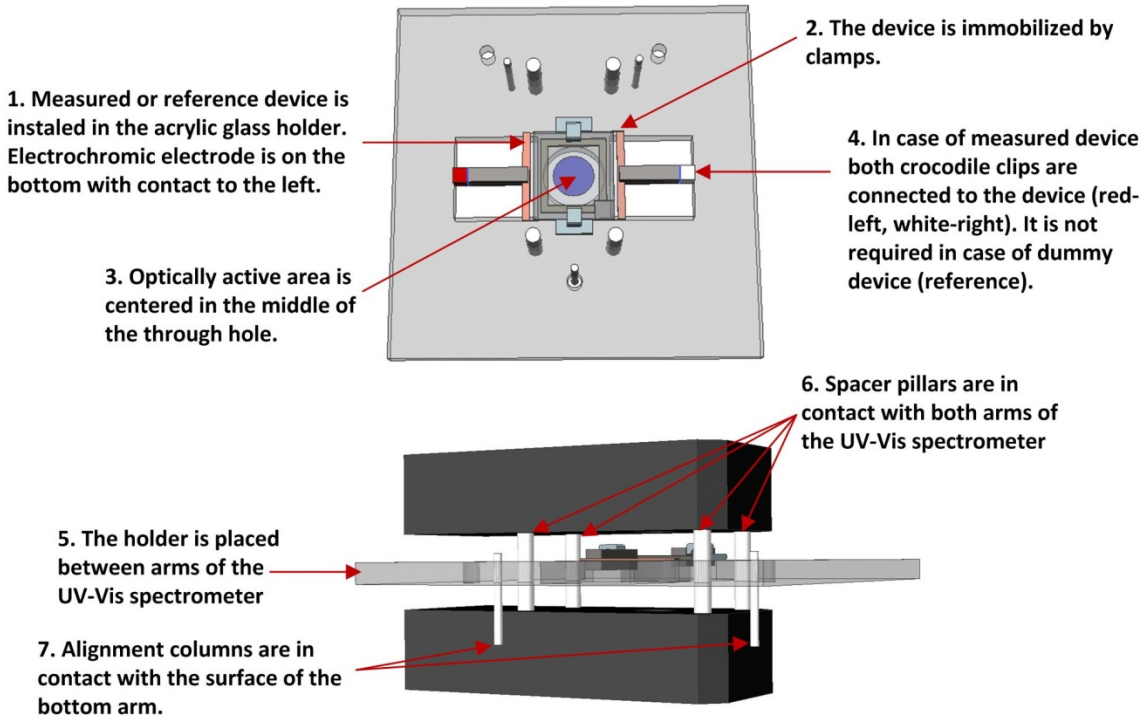

Figure 2.13. Protocol for EC device installation inside custom made acrylic glass sample holder; detailed technical drafting of the holder is available on request

2.5.5. Definitions of parameters (responses)

Optical measurements are based on CAbs technique which is a square-wave potential step method coupled with optical spectroscopy used for analysis of switching kinetics and contrast of the film. The electrochromic testing was processed within an appropriate voltage range (-4 V to 4 V), so as to avoid electrolyte oxidation and (eventual) ITO reduction. The main output from CAbs measurements is the change in optical density (ΔOD), which indicates how much the transmittance of the electrochromic layer is reduced during the coloring process (or increased during bleaching). The change in optical density is calculated using Equation 2.16.

$$\Delta\mathrm{OD} = ln\left(\frac{T(t_1,\lambda)}{T(t_2,\lambda)}\right) \approx ln\left(\frac{T(t'_2,\lambda)}{T(t'_1,\lambda)}\right) \qquad (2.16)$$

where: $T(t_1,\lambda)$ and $T(t_2,\lambda)$ are transmittances of the films at λ = 900 nm before (t_1,) and after (t_2) coloration process, respectively (Figure 2.14a and Figure 2.14c). Alternatively, ΔOD can be determined for inverse supply polarization, where: $T(t'_2,\lambda)$ and $T(t'_1,\lambda)$ are transmittances of the films at λ = 900 nm before (t'_1) and after (t'_2) bleaching process, respectively (Figure 2.14b and Figure 2.14d).

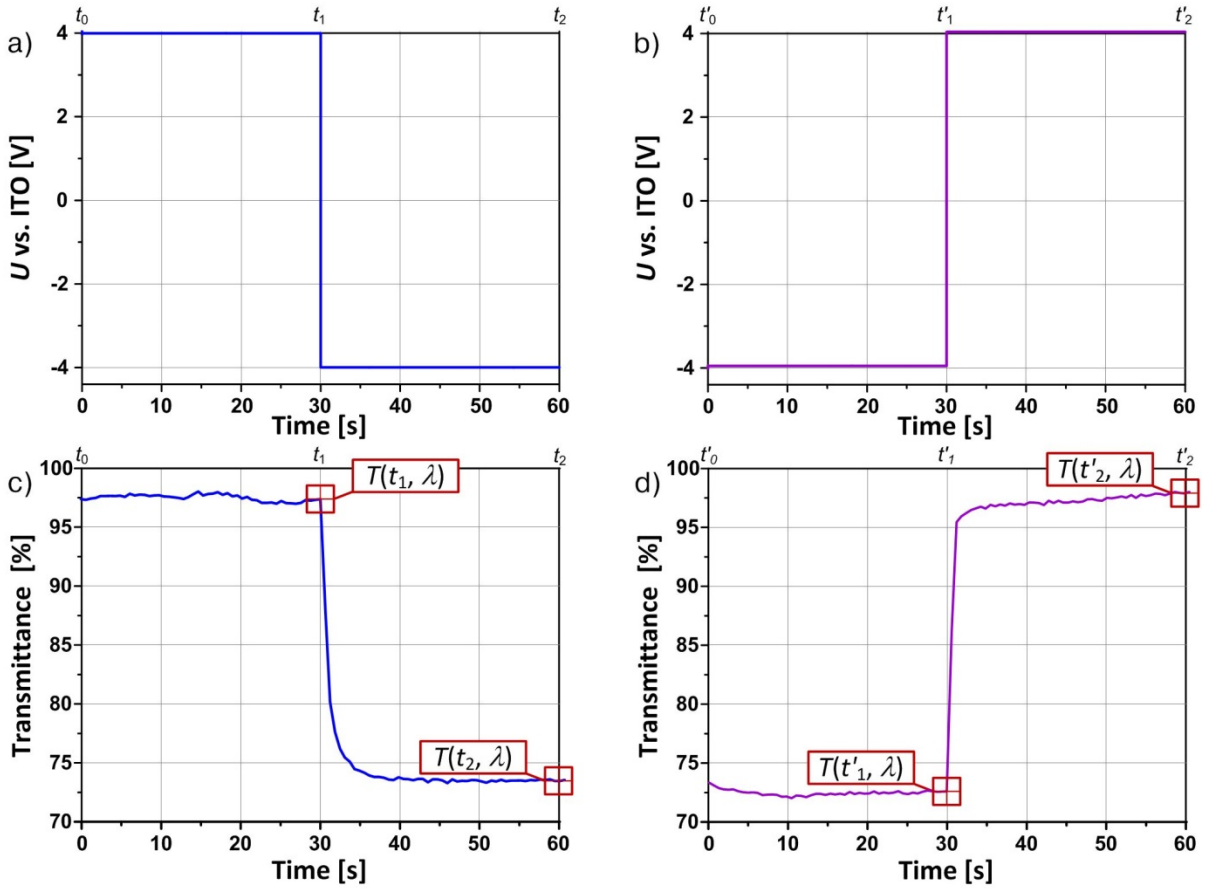

Figure 2.14. Determination of ΔOD based on CAbs technique in which a) positive-to-negative or b) negative-to-positive square wave potential with period of 60 seconds is supplied to the device and its optical response is measured as the change in transmittance during c) coloring or d) bleaching process

Data obtained from CAbs enable estimation the switching time for coloring and bleaching process. The coloration time (τ_{col}) is defined as the time required for an electrochromic device to change from its bleached to colored state. In present studies the coloration time is defined as the requisite time for reduction of the device's transmittance to 80% of the final reduction according to Equation 2.17 (see also Figure 2.15a).

$$\tau_{\mathrm{col}} = f^{-1}\left(T(t_2,\lambda) + 0.2\big(T(t_1,\lambda) - T(t_2,\lambda)\big)\right) - t_1 \qquad (2.17)$$

The bleaching time (τ_{bl}) is defined as the time required for an electrochromic device to change from its colored to bleached state. In these studies the bleaching time is defined as the requisite time for change of the device's transmittance to 80% of the final bleach level, according to Equation 2.18 (see also Figure 2.15b).

$$\tau_{\mathrm{bl}} = \mathrm{f}^{-1}\left(\mathrm{T}(\mathrm{t'}_2,\lambda) - 0.2\big(\mathrm{T}(\mathrm{t'}_2,\lambda) - \mathrm{T}(\mathrm{t'}_1,\lambda)\big)\right) - \mathrm{t'}_1 \qquad (2.18)$$

The fitting of model expressed by Equation 2.8 to responses τ_{col} and τ_{bl} resulted in relatively low regression coefficients, 0.51 and 0.72, respectively. The lack of fit comes from difficulties associated with accurate measurements of those responses. In case of films with low optical modulation ($\Delta OD < 0.25$), it is difficult to calculate switching time using method expressed by Equations 2.17 and 2.18. The spectroscopic signal is distorted (see Figure 2.15c) due to the limited smoothing of the signal (*i.e.* average of 10 scans) and influence of the environment. Unreliable measurements regime is indicated in Figure 2.8a and Figure 2.8b by faded triangles.

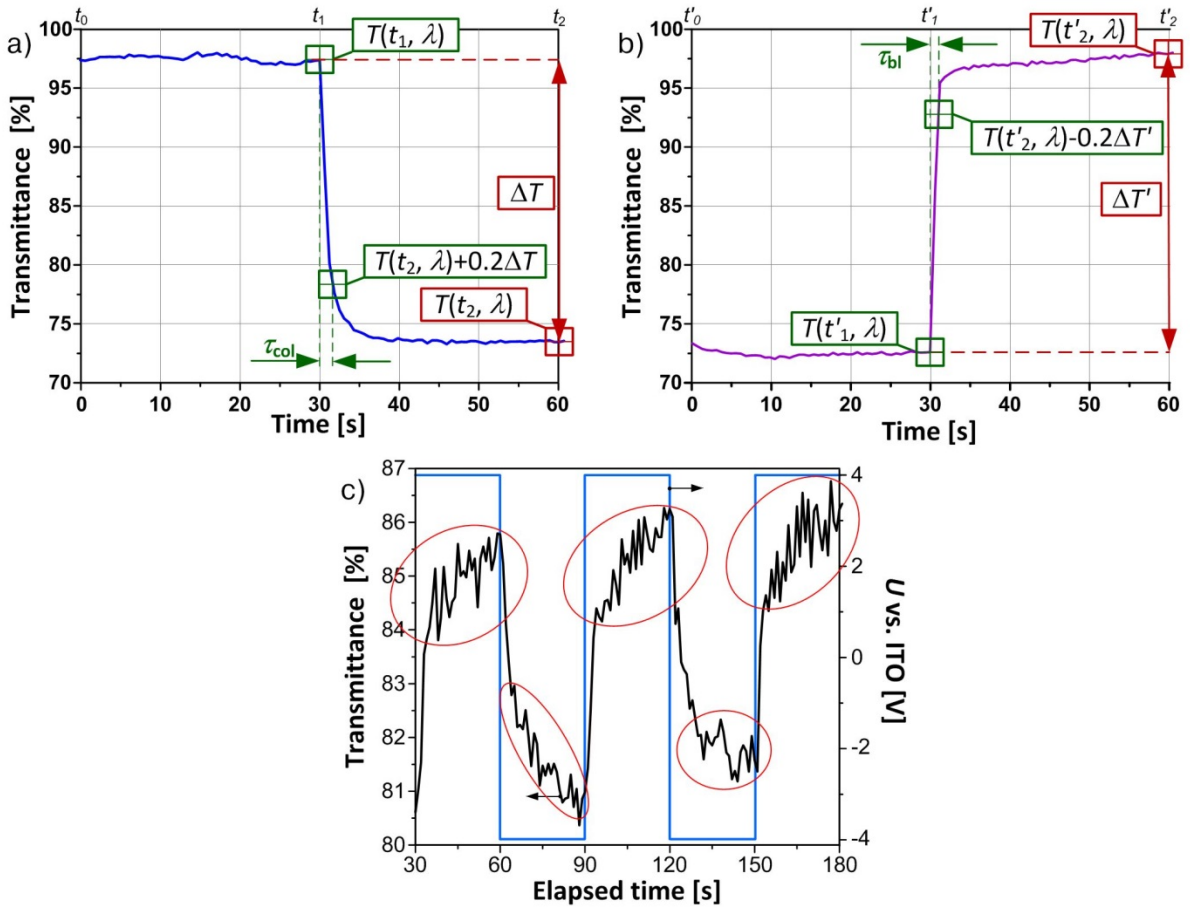

Figure 2.15. Determination of a) coloring and b) bleaching time and c) related problems due to the signal distortions (inside red ovals) in case of films with low optical modulation (*e.g.* highly loaded with WO_X) powered by square wave potential; signal instability prevents accurate determination of switching time using establish methodology for films with $\Delta OD < 0.25$.

The electrochemical measurements are based on CQ technique performed using galvanostatic method. The CQ which involves the measurement of charge moving inside the device as a function of time is a controlled-potential technique with a potential step wave form according to Figure 2.14a. During the measurements, a positive voltage (4 V) is applied between t_0 and t_1 and, due to the oxidation reaction, the device remains in a bleach state. Then, stepping the potential to a negative value at t_1 (-4 V), the reduction reaction occurs and the device switches to its colored state. The coloration efficiency (CE)

(calculated based on CQ) is a parameter usually used as an overall device performance indicator. It expresses the optical modulation color caused by the charge consumed during such action. Similarly to ΔOD, CE value depends on the selected wavelength and is represented by the Equation 2.19.

$$\mathrm{CE} = \frac{\Delta \mathrm{OD}}{Q_{\mathrm{INS}}} \tag{2.19}$$

where: ΔOD is the change in optical density for λ = 900 nm and Q_{INS} is the charge density inserted to the device. The value of charge density is calculated based on charge-current continuity relation expressed by Equation 2.20.

$$I(t, A) = \frac{dQ(t,A)}{dt} \tag{2.20}$$

The charge transferred within defined period of time τ is calculated by integrating both sides according to Equation 2.21 (see also Figure 2.16a and Figure 2.16b).

$$Q(\tau, A) = \int_0^{\tau} I(t, A)\, dt \tag{2.21}$$

where: I is the current flowing through a limited surface A, and Q is the electric charge contained within the volume defined by the surface. The value of Q_{INS} is defined according to the plot shown in Figure 2.16b, as the difference in charge density at t_1 and t_2.

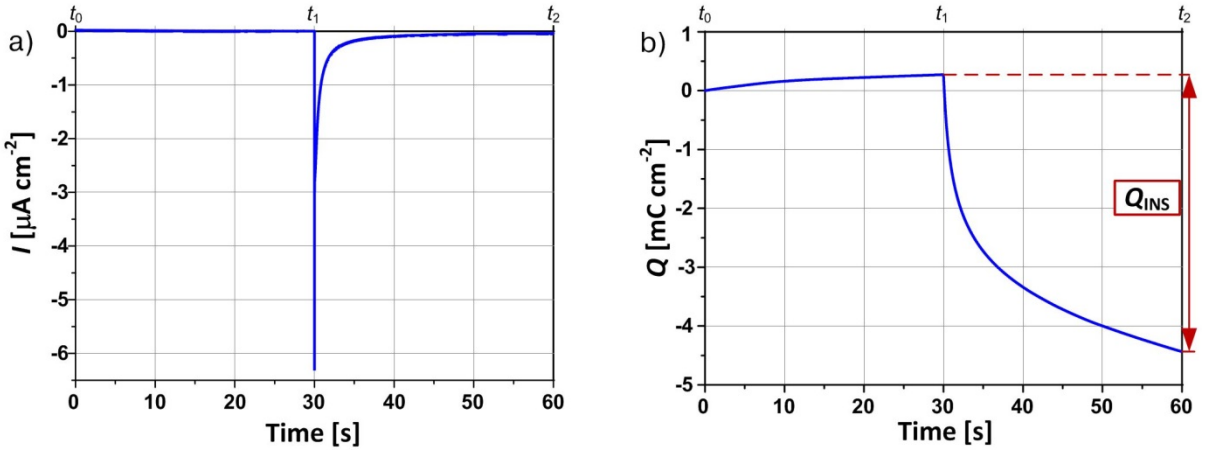

Figure 2.16. Determination of Q_{INS} by supplying the device with positive-to-negative square wave potential with period of 60 seconds, measuring of a) an electrical response (*i.e.* current density), and b) integration of the current density over time

2.5.6. Design Diagnostic

For mixture experiments of quinary (q = 5) system solvent-PTA-OAD-TiO_2-WO_X, following efficiency measures were considered [40]:

$$D - \text{efficiency} = 100\left(\frac{1}{N}|X'X|^{\frac{1}{p}}\right) \tag{2.22}$$

$$G - \text{efficiency} = 100\left(\frac{\sqrt{\frac{p}{N}}}{\sigma_M}\right) \quad (2.23)$$

$$A - \text{efficiency} = 100\left(\frac{p}{trace(N(X'X)^{-1})}\right) \quad (2.24)$$

where: N stands for the number of points in the design, p is the number of effects in the model (see Equation 2.7), and σ_M is the maximum standard error for prediction over the design points.

The efficiency measures expressed by Equations 2.22, 2.23 and 2.24 are single numbers attempting to quantify each mathematical design characteristic. These D, G and A -efficiencies are used to compare competitive designs with the same model rather than as some absolute measure of design quality. Table 2.7 and Table 2.8 show supplementary data to Figure 2.3 containing D, G and A -efficiencies calculated for minimum and default number of runs.

Table 2.7. Design diagnostic parameters for studied mixture fitted by linear, quadratic and special cubic form; green frame indicates selected mathematical model in present studies.

	Mathematical model					
Diagnostic parameter	**Linear**		**Quadratic**		**Special cubic**	
Number of experimental	min.	def.	min.	def.	min.	def.
trials*	6	15	20	30	40	60
D-efficiency	6.194875	6.958609	0.169413	0.177458	0.01412	0.016092
G-efficiency	85.27035	93.08281	66.84127	75.29487	53.94737	83.2663
A-efficiency	0.320261	0.35281	1.34E-05	1.76E-05	1.82E-06	3.37E-06
Average Variance of Prediction	0.597289	0.214867	0.864747	0.519463	1.039342	0.497109

min. – minimum number of experimental runs; def. – default number of experimental runs

Table 2.8. Design diagnostic parameters for studied mixture fitted by cubic (no main effects) and full cubic form

	Mathematical model			
Diagnostic parameter	**Cubic (no main effects)**		**Full Cubic**	
Number of experimental	min.	def.	min.	def.
trials*	30	60	36	60
D-efficiency	0.001555	0.001788	0.001942	0.00218
G-efficiency	52.49173	82.88022	67.0134	81.5094
A-efficiency	6.86E-07	1.16E-06	7.27E-10	9.08E-10
Average Variance of Prediction	1.187198	0.407081	1.042443	0.51079

*min. – minimum number of experimental runs; def. – default number of experimental runs

It is clear that design quality of each model enhances with increased number of experimental runs, which results in lower Average Variance of Prediction.

Actual-by-predicted plots of τ_{col}, τ_{bl}, ΔOD and CE are shown in Figure 2.17. If the points fall along the diagonal line, the predicted values are similar to the actual values. It is a graphical measure of goodness-of-fit, and for a perfect fit, all the points would be on this diagonal.

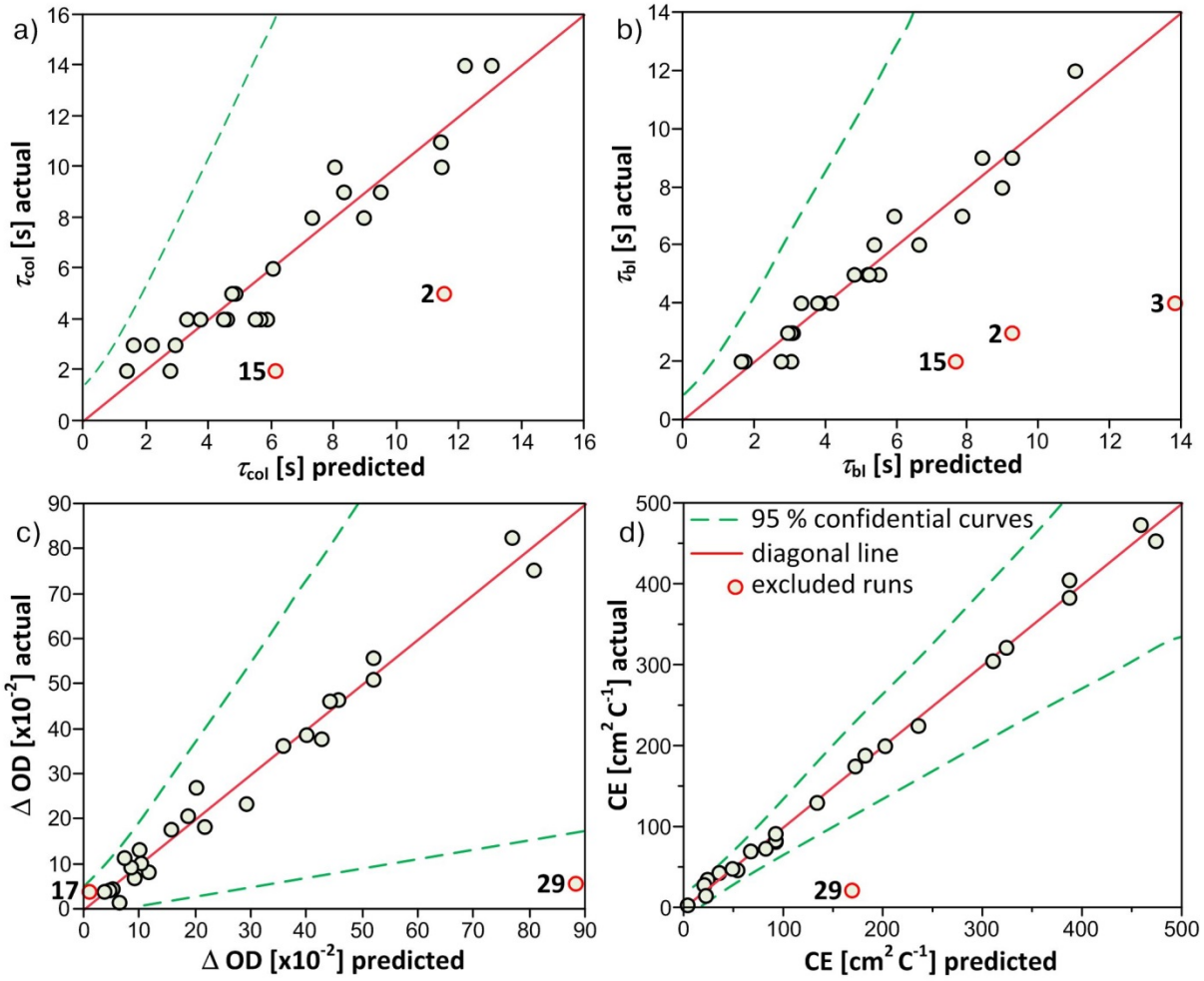

Figure 2.17. Actual by Predicted plot for a) τ_{col}, b) τ_{bl}, c) ΔOD and d) CE

2.5.7. Initial tests of significance (leverage plots)

To graphically view the significance of the model or to evaluate whether an effect is significant, the data should be displayed by focusing the hypothesis for that effect. The effect in a model is tested for significance by comparing the *sum of squared residuals* to the *sum of squared residuals* to the model with the effect removed. The graphical display of an effect significance test is called a leverage plot (Figure 2.18). Therefore, the leverage plots for each factor illustrates the residuals as they are and as they would be if that component were removed from the model.

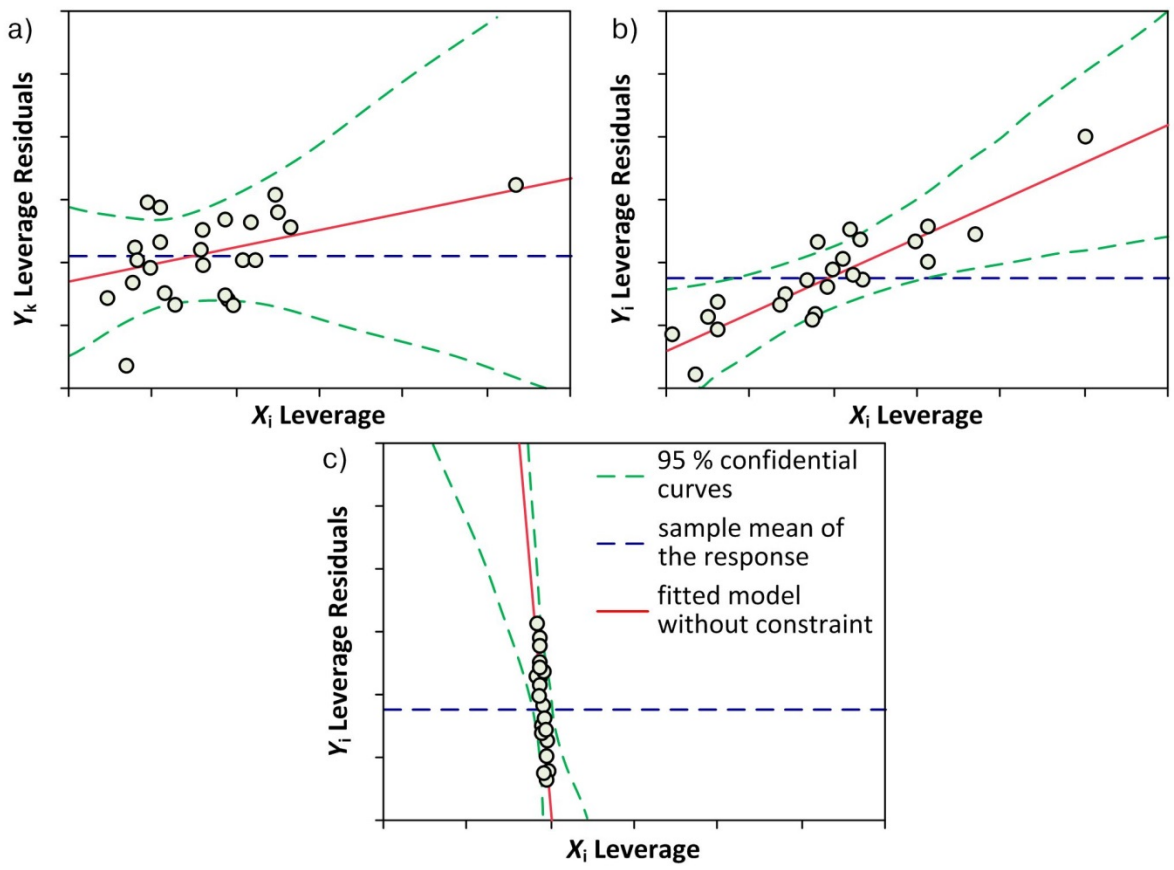

Figure 2.18. Examples of leverage plots showing three different results of significance test for response y_i: a) factor x_i is not significant, b) factor x_i is significant and c) factor x_i is collinear with other factors

The points on a leverage plot for simple regression are actual data coordinates, while the slanted red solid line is the fitted model without constraint, and the horizontal blue dotted line is the sample mean of the response. The main idea of leverage plots is to see whether the line of fit on the effect's leverage plot carries the points significantly better than does the horizontal line. Each observation is positioned as a point in the plot such that the vertical distance from that point to the slanted line is the unconstrained residual and the distance from the point to the horizontal line is the residual constrained by the hypothesis [48]. It is important to clarify that residuals are fitting errors. For each response, the residual is the difference between the real response and the estimated function value. The confidence curves are also showed in the leverage plots as dotted red lines. They indicate whether the test is significant at the 5% level by showing a confidence region for the line of fit. If the confidence region between the curves contains the horizontal dotted blue line, then the effect is not significant (Figure 2.18a). On the other hand, the significance of each effect is indicated on leverage plot by the confidence interval line crossing the mean line (Figure 2.18b). The factor shrinkage on leverage plot measures how collinear the particular factor is with the other factors. The factor shrinkage is obtained in Figure 2.18c meaning that tested factor x_i is not linearly orthogonal to the other factors. This factor

shrinks almost completely and has no independent variation to support fitting y_i response variation. It means that x_i is an exact linear function of other factors. The shrinkage along the abscissa axis in a leverage plots makes an especially compelling picture, since it also portrays the instability of the line of fit due to the colinearity. This phenomenon may translate into high standard errors for the parameter estimates, because a small random error in the narrow direction can have a huge effect on the slope of the correspondent fitting plane [57].

2.5.8. Movie details

A short movie is attached to this thesis, so as to facilitate the understanding of presented method. The raw footage and selected shots were combined into the sequence using Adobe Premier CS3 software. Compression was performed using FreeStudio v. 2013 platform containing Free AVI Video Converter v. 5.0.24 build 430 (DVDVideoSoft, http://www.dvdvideosoft.com). Resulting file: size – 45 MB; video - AVI, 640x480, MPEG-4 (XVID, DIVX compatible), 2Mbit/s; audio - MP3 112Kbit/s, 44.1kHz. The movie is available on-line at http://youtu.be/GE5rOymU5i4

Chapter 3

Microstructure control of dual-phase inkjet printed *a*-WO_3/TiO_2/WO_X films

This chapter is written based on:

Wojcik, P.J., Cruz, A.S., Santos, L., Pereira, L., Martins, R., Fortunato, E.: Microstructure control of dual-phase inkjet-printed *a*-$WO_3/TiO_2/WO_X$ films for high-performance electrochromic applications. Journal of Materials Chemistry. 22, 13268 (2012).

Contributions of Co-Authors:

A.S. Cruz assisted in carrying out the experiments, characterization and data treatment. Selected results of this study were included in her M.Sc. Thesis entitled: Dual-phase Inkjet Printed Electrochromic Layers based on PTA and WO_X/TiO_2 Nanoparticles for Electrochromic Applications, Faculty of Science and Technology, New University of Lisbon, 2010

L. Santos assisted in carrying out the experiments and characterization.

L. Pereira performed SEM characterization.

Chapter 3. Microstructure control of dual-phase inkjet printed *a*-WO_3/TiO_2/WO_X films

Chapter 3. Microstructure control of dual-phase inkjet printed *a*-WO_3/TiO_2/WO_X films

Summary

The microstructural aspects related to crystalline or amorphous structure of as-deposited and annealed films of sol-gel derived WO_3 are shown in the literature to be critical for electrochromic (EC) performance [50, 52–54]. In consideration of ion insertion materials, there is a need for developing light and at the same time nanocrystalline structure to improve both coloration efficiency and switching kinetics. By controlling microstructure and morphology, one could design a material with optimal EC performance.

This chapter compares the microstructural and morphological characteristics of standard WO_3 wet deposition techniques versus IPT, correlating these features with their optical and electrochemical performances, emphasizing the importance of the dual phase *a*-WO_3/TiO_2/WO_X film composition proposed in this work for high performance EC applications. The effect of the type and content of metal oxide nanoparticles in the precursor sols formulated in various Peroxopolytungstic Acid (PTA) and Oxalic Acid (OAD) proportions on film properties is comprehensively studied using multi-factorial Design of Experiment (DOE). The proposed method enables development of EC films which irrespective to their composition (*a*-WO_3, *a*-WO_3/TiO_2 or *a*-WO_3/TiO_2/WO_X) outperform their amorphous or nanocrystalline analogues presented in the state-of-the-art due to their superior chemical and physical properties.

3.1. Introduction

A considerable effort has been devoted to the study of WO_3 films prepared from wet chemistry routes as sol-gel processing [50, 52] and electrodeposition [53, 54] which offer several advantages over conventional vacuum processed techniques such as electron beam evaporation [58] or radio frequency magnetron sputtering [59]. Besides higher film uniformity, wet deposition allows also for microstructure control by modifying precursor composition and post-treatment conditions. Although the application of IPT for WO_3 nanoparticles deposition from aqueous dispersion has been recently reported [60], no attempt has been made to print WO_3 coatings from sol-gel precursor. The transition from well-known wet coating techniques to IPT is dictated by the need to deposit patterns on large surfaces without necessity of lithography, as those technological aspects are critical in mass production. Moreover, IPT allows precise patterning with reduced raw material waste, therefore significantly lowering the costs of producing. Figure 3.1, Figure 3.2 and Figure 3.3 attempt to expound the evolution of microstructure in WO_3 films deposited *via* peroxo route (wherein tungsten metal is dissolved in hydrogen peroxide) by various wet deposition techniques as a function of

temperature. The aim is to compare changes in thickness, crystallinity and estimated grain size of films subjected to different post-deposition annealing temperatures. By examining those structures, we have an idea of how this processing-property relationship works. This brief overview will also serve as background for the evaluation of the results obtained *via* IPT.

Studies on morphological and microstructural evolution of spin- and dip-coated films as a function of temperature have been rarely reported in electrochromic literature [50, 52]. It has been observed (XRD, SEM) that annealing temperature induces amorphous to hexagonal to triclinic structure transition of those films [53]. The beginning of crystallization was observed at 250 ºC when a small volume of grains (1.2 - 25 nm for spin- and 55 - 80 nm for dip-coated films) appeared (see Figure 3.1 and Figure 3.2).

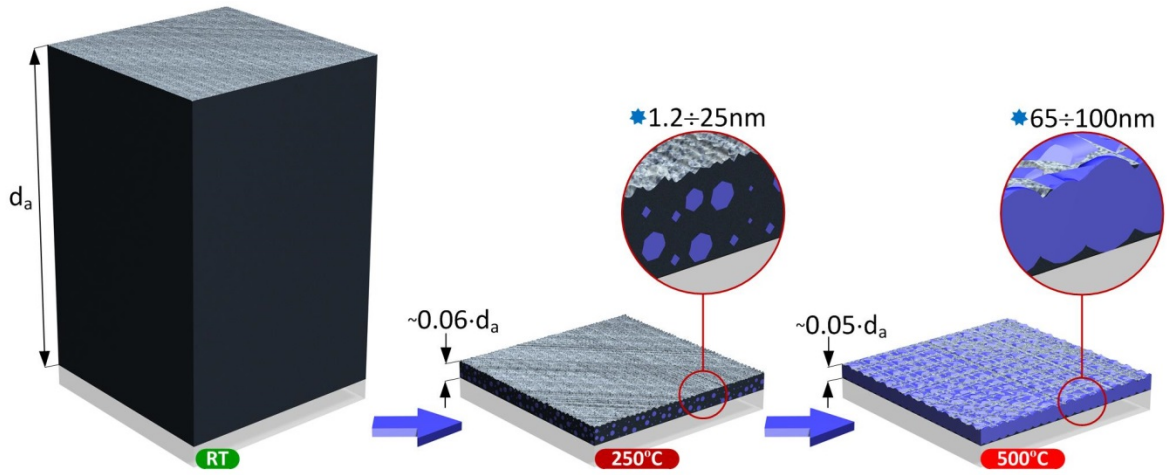

Figure 3.1. The evolution of microstructure and surface morphology in WO_3 films deposited *via* peroxo route by spin-coating as a function of annealing temperature; symbols d_a stands for film thickness

Further increase in annealing temperature up to 500 ºC led to a considerable improvement in the crystallinity of both spin- and dip-coated films (65 - 100 nm and 75 - 100 nm, respectively). Moreover, data shows that thickness values of as-deposited and annealed spin- and dip-coated films reduce upon raising the annealing temperature. The thickness (d_a) of spin-coated film annealed at 250 °C for 1 hour decreases by 94 %, while further annealing for an additional hour in 500 °C decreases this value by additional 1 % compared to the initial thickness of as-deposited film.

For dip-coated films, the thickness (d_b) during the same treatment drops by 92 % and additional 2 %, respectively. The analysis of nanostructured thin films deposited by those two techniques revealed a superior EC performance of dip-coated films in terms of optical and electrochemical activity [50]. At the same time, dip-coated films could sustain higher number of cycles, which is a direct repercussion of grain size. It has been ascertained that among sol-gel derived WO_3 spin- and dip-

coated films, the EC performance of films annealed at 250 ºC is far superior in comparison with their amorphous or polycrystalline counterparts obtained upon annealing at different temperatures.

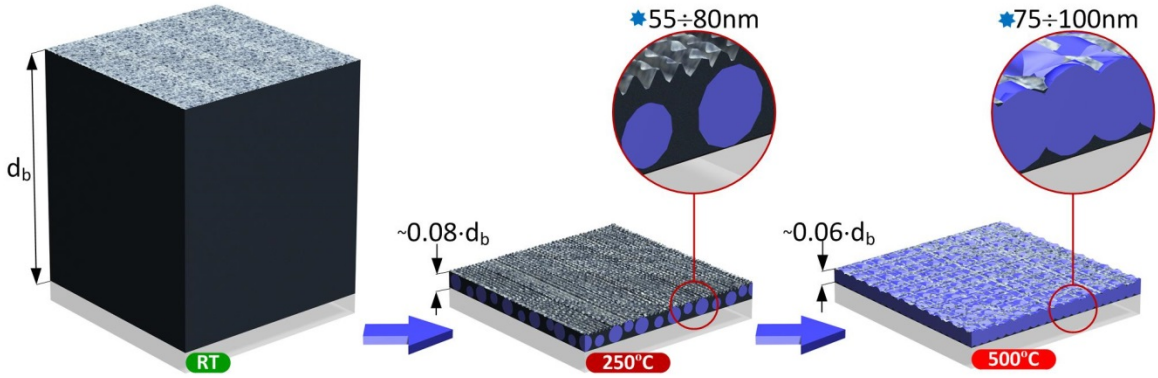

Figure 3.2. The evolution of microstructure and surface morphology in WO_3 films deposited *via* peroxo route by dip-coating as a function of annealing temperature; symbols d_b stands for film thickness

Potentiostatic electrodeposition is the unique among wet processing methods, that allows the low temperature deposition of nanocrystalline WO_3 films, which additionally are chemically more stable than their amorphous counterparts while having similar performance [53]. Detailed study of annealing temperature effects on the structure and EC performance of electrodeposited WO_3 films have been reported by M. Deepa *et al.* [53, 54]. Authors observed (XRD, TEM) that as-deposited WO_3 film is composed of grains with estimated size of 10 - 20 nm embedded in nanoporous amorphous matrix. Increasing the temperature (> 100 °C) causes the crystals size growing systematically.

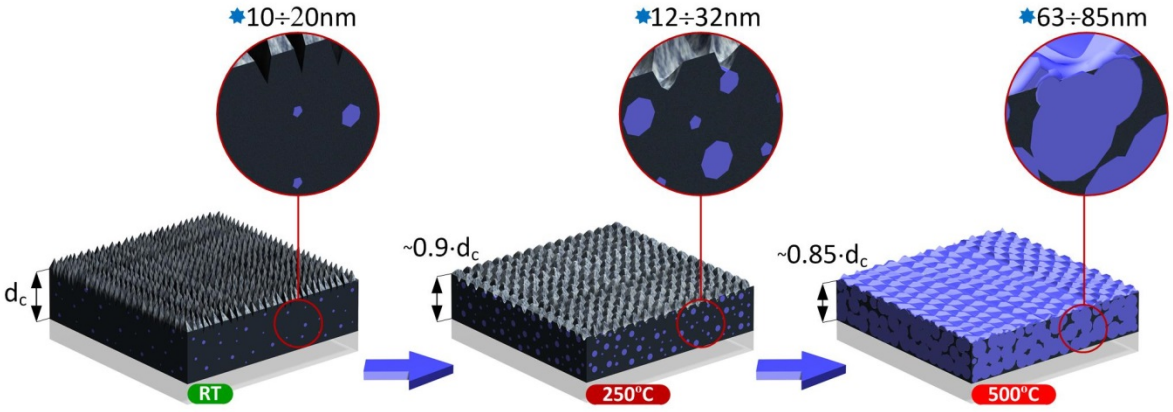

Figure 3.3. The evolution of microstructure and surface morphology in WO_3 films deposited *via* peroxo route by electrodeposition as a function of annealing temperature; symbols d_c stands for film thickness

A significant improvement in chemical stability due to a uniform distribution of grains (12 - 32 nm) was observed for films annealed at 250 °C (see Figure 3.3). Successive annealing up to 500 °C manifest further particle sizes increase (63 - 85 nm). Simultaneously, the thermal treatment resulted in

a slight decrease in the film volume. The film thickness (d_c) after heat treatment at 250 °C for 1 hour was about 90 % of the thickness value of as-deposited layer, while further annealing for an additional hour in 500 °C decreases this value down to 85 %. The fastest switching kinetics of as-deposited film, the authors attributed to the presence of nanocrystallites, which increases active surface area while the highest optical modulation was observed in amorphous films dried at 60 °C.

With crystallization at high temperature the structure not only becomes ordered, but increases in density, which is known to inhibit electrochromism. Sensitive to the microstructure lithium ion diffusion is significantly limited in heat-treated dens, or crystalline films which contain limited number of insertion sites to accommodate the Li^+ ions [53]. This situation is presented in corresponding micrographs models of films annealed at 500 ºC which reveal a dense, compactly packed microstructure of polycrystalline metal oxide irrespectively of the deposition technique. When small nanocrystals are dispersed in an amorphous matrix, EC properties depend on degree of crystallinity and density of both phases. Therefore, optimal EC properties of the films are a balance among network formation, organic burnout, porosity, and crystallization. This dependence has been observed in all above examples [50, 52–54]. Taylor *et al.* [50] reported that films annealed in temperature which promote nanocrystals creations, exhibits lower optical modulation due to the fact that there is less amorphous material with fewer sites available for coloration. Authors concluded that crystallinity does not prohibit electrochromism and that the lower EC performance of annealed films is attributed to the microstructure.

Optimal EC performance of wet processed WO_3 films is a balance among chemical stability, response time, transmission modulation, ion storage capacity and coloration efficiency. If fast coloring/bleaching operating is required for application, then nanocrystalline film is most suited but at the penalty of lower optical modulation. On the other hand, an amorphous film is the most sensible choice when high coloration efficiency is desired and kinetics is of secondary importance. Concluding, spin- and dip- techniques do not offer much room for EC performance optimization, due to the film densification caused by high temperature involved in nanocrystals creation. Electrodeposition partially overcomes limitations of those techniques by reducing process temperature for dual-phase films creation. However, deposition process is restricted by the substrate shapes, the expensive equipment and poor crystallinity of final product. Disadvantages of all described deposition methods are even more apparent when the large-area assembly of EC films is considered.

In this work the sol-gel films are processed by IPT, which as the core of presented method offers flexibility of deposited film composition, high throughput and simplicity in material selection, when compared to the conventional techniques. However, fully optimizing printing process by evaluating all possible combinations of factors using single factor experiments is time prohibitive. The

conclusions presented in this chapter were constructed based on DOE methodology coupled with multivariate analysis described in Chapter 2.

3.2. Materials and methods

An experimental section of this chapter is equal to Section 2.2, as both chapters describe the same set of experiments and analyze the same results, showing two different aspects of this work. While in Chapter 2 an analytical side of the study is described, here the microstructure of printed films and its impact on EC performance are the main topics. Therefore, as both chapter overlap at this point, an experimental section is omitted in this chapter in order to avoid repetition.

The only difference is information concerning X-ray diffraction measurements (XRD), which haven't been mentioned before. The XRD of WO_X powders were carried out using Brucker D8 Focus Advance diffractometer (Bruker-AXS Inc.). The PTA, OAD and TiO_2 powders as well as selected inkjet printed films were measured using XPert PRO diffractometer (PANalytical).

3.3. Results and discussion

3.3.1. Microstructure and morphology

The micrograph of inkjet printed amorphous *a*-WO_3 film shown in Figure 3.4a represents continuous film. Sporadically, the cracks caused by stress are revealed, which is shown here in order to expose film cross-section. The imminent difference obvious at a glance between the morphological characteristics of WO_3 films deposited *via* standard wet techniques and IPT at low magnifications is that while continuous layers are observed in first case for annealed nanocrystalline films [51], their inkjet printed dual-phase *a*-WO_3/TiO_2/WO_X counterparts are characterized by discontinuous pattern as may be seen in Figure 3.4b and Figure 3.5. Film discontinuity is caused by existence of solid nanoparticles in liquid sol-gel precursor, which significantly changes its rheological behavior.

A clear distinction between the nanocrystalline grains distributed randomly throughout an amorphous phase can be observed in resultant 'chocolate with nuts'-like structure. At high magnifications, however, the surfaces of printed films exhibit a rather homogenous topography. The stress caused by the decomposition of the precursor and the solvent removal at elevated temperature leads to the creation of cracks. According to studies conducted by Yamanaka *et al.* [43], those cracks have no significant effect on electrochemical properties of sol-gel processed films.

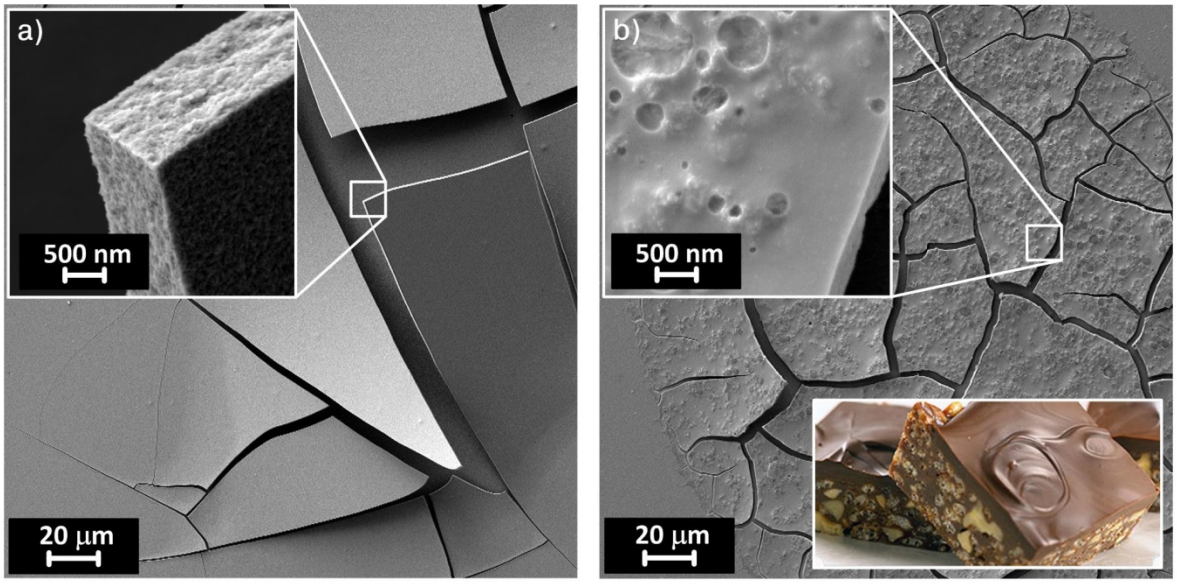

Figure 3.4. SEM images of inkjet printed a) amorphous (a-WO_3) and b) dual-phase (a-$WO_3/TiO_2/WO_X$) films deposited on ITO PET substrates; insets: ULC-magnified cross-sectional images; BRC-comparison of printed dual-phase films to chocolate with nuts

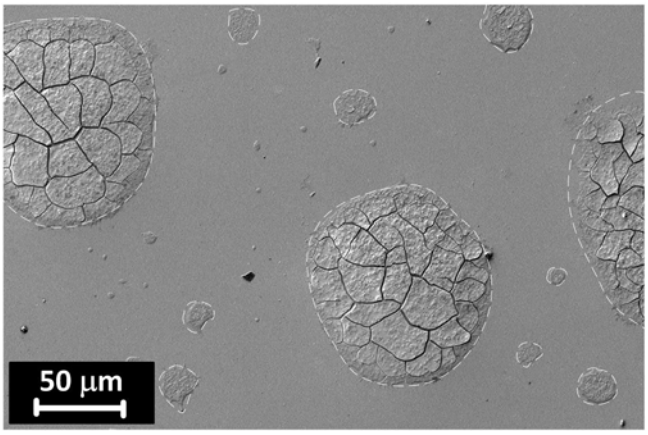

Figure 3.5. SEM images of inkjet printed dual-phase (a-$WO_3/TiO_2/WO_X$) film deposited on ITO PET substrates; the pattern boundaries are indicated by dashed line

According to the electrochromism theory, the optical modulation in crystalline WO_3 phase arises due to the increasing Drude type (metallic) reflection, observed especially in IR region, with increasing free electron/lithium injection [61]. In amorphous phase, the most widely accepted model assumes that the optical modulation upon the double injection occurs through increasing absorption arising from the transfer of localized electrons between W^{5+} and W^{6+} sites, so called small polaron absorption [62, 63]. However, the improvement in EC performance of printed films shown in next text paragraph is related to the film microstructure, which is not subjected to densification during deposition and post-treatment, than to local electronic states.

Because of low temperature involved, no shrinkage is applied, which differ inkjet printed amorphous (see Figure 3.6a) and dual-phase (see Figure 3.6b) films from those developed in other wet deposition techniques. Regardless of the composition of printed layers, annealing process at 120 ºC does not significantly affect the thickness of the layer. Systematic solvent evaporation between passes and low temperature applied cause low shrinkage. Such a light structure with nanocrystalline phase dispersed in amorphous matrix, tends to reduce the diffusion path length in the film and improve kinetics, as switching speed is predominantly governed by the solid-state diffusion of lithium ions in WO_3. Both, crystallinity induced by high temperature from sol-gel derived tungsten oxide [50] and incorporated to the film *via* IPT exist as small crystallites dispersed in an amorphous matrix of tungsten oxide and not as continuous crystalline phase. The grain size, crystallinity and stoichiometry of nanoparticles dispersed in an inkjet printed films can be modified by merely changing the source of particles loaded into the ink. Aside from the electrolyte accessible surface area and crystallinity, the oxygen deficiency in crystalline phase also affects the EC properties of printed dual-phase films. It has been observed that the stoichiometry of WO_X nanoparticles (x = 3 or x = 2.9) leads to a slightly different electrochemical (*i.e.* EC) behavior, indicating that the right choice of WO_3 nanoparticles results in higher overall performance of printed EC devices. However, several important aspects concerning the WO_X particle stoichiometry remained unclear and further studies are going to be performed in this matter.

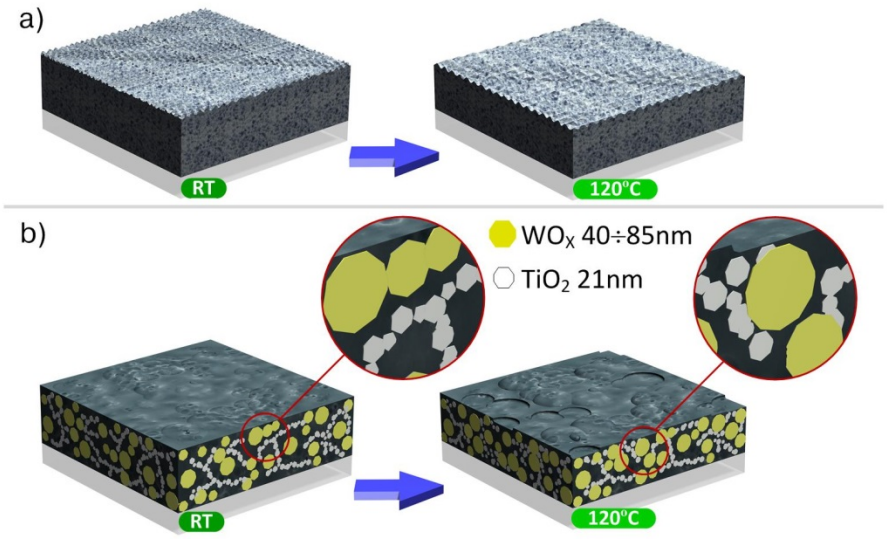

Figure 3.6. Microstructure and morphology of inkjet printed a) amorphous (a-WO_3) and b) dual-phase (a-WO_3/TiO_2/WO_X) films after drying at room temperature and annealed for 1h at 120 ºC

Since different WO_X nanomorphologies can be obtained in a range of crystal phases *via* various material synthesis techniques [64], almost unlimited selection of nanocrystalline content for ink formulation is possible. Furthermore, doping of WO_X nanoparticles during its synthesis is another important area worth of further exploration, because it opens new opportunities for ion intercalation with significantly enhanced chromic response. The combination of doped WO_X nanocrystals synthesis

with a new presented method would allow for a dual-phase film development with different nanoscale composition of each phase.

3.3.2. Electrochromic performance

Lab-testing reversible devices have been developed as a four-layer stack between two flexible PET substrates. The optically active film is printed onto a transparent conducting ITO electrode and coupled to a gel electrolyte (ionic conductor with dispersed lithium ions) and second electrode according to the process described in Figure 2.6. All optical and electrochemical measurements presented below were performed *in-situ* in so encapsulated devices. Application of voltage drives the ions into *a*-WO_3/TiO_2/WO_X film, where they are intercalated causing the chromatic effect. Reversing the voltage returns them to the electrolyte, which also serves as ion storage. Cathodic polarization irreversibly reduced the peroxo complexes to *a*-WO_3 which is typical for PTA precursor regardless of the deposition method. This process was manifested by poor initial responses which improved and stabilized after few cycles.

The contour plot on a trilinear coordinate scale was used to present predictions of experimental results obtained *via* multiple regression fitting discussed in Section 2.3.1. This graphical methodology provides an easy way to demonstrate the efficacy of the enhanced performance of printed EC films. Ternary plots were generated as a function of TiO_2/WO_X nanocrystalline content, while the concentrations of other components (PTA, OAD) were kept constant (see Figure 3.7, Figure 3.8, Figure 3.9 and Figure 3.15). The third axis stood for pure alcoholic aqueous solvent in order to quantify amount of nanocrystals dispersed in the ink and afterwards transferred to the printed films. Comparison between corresponding surface responses plotted for different WO_X stoichiometry ($WO_{2.9}$ and WO_3) provides information regarding the role of oxygen content in nanocrystalline phase. In the whole range of studied concentration, films containing WO_3 nanoparticles outperform their $WO_{2.9}$ analogues, while both represent similar relationships between factors and responses. Such a dual-phase *a*-WO_3/TiO_2/WO_X microstructure aided ion movement manifested in coloration/bleach kinetics, optical density and coloration efficiency faster and higher than previously reported sol-gel derived WO_3 films. The application of a negative potential causes the active film to turn deep blue over τ_{col} (see Figure 3.7a) and the initial bleached state can be restored by applying reverse potential within τ_{bl} value (see Figure 3.7b).

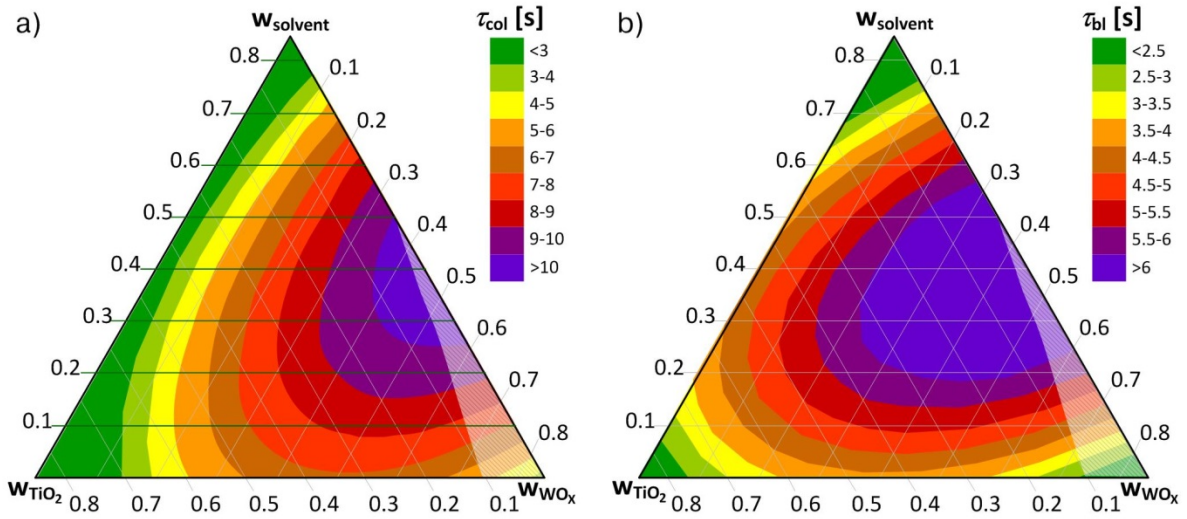

Figure 3.7. Response contour plots presenting variation in a) coloration and b) bleaching time as the weight fractions of TiO_2 and WO_X dispersions are varied (w_{PTA} = 0.01, w_{OAD} = 0, X = 3{*yellow*}); the faded region indicates unreliable measurements due to the low optical modulation; please, note that these plots differ from the ones presented in Figure 2.8, due to the different OAD content

Those parameters were defined as the requisite time for the transmittance change by 80 % of the total difference between final states (see Section 2.5.5 for detailed definitions of parameters). The highest measured coloring and bleaching time values do not exceed 14 and 12 seconds, respectively. A substantial reduction in coloration and bleaching time is observed when increasing the nanocrystalline TiO_2 content, reaching more than three times lower values ($\tau_{col} < 3$ and $\tau_{bl} < 2.5$). Coloration kinetics is observed to be slower than bleaching kinetics for all the films under investigation, which stays in agreement with the well-defined, but different mechanism governing the two processes. While the exchange of current density at the EC film-electrolyte interface controls coloration kinetics, the space charge-limited Li^+ ion diffusion current governs the bleaching time [63].

As a consequence of dual-phase microstructure, there is a large interface between the oxide layer and gel electrolyte, which promotes ion diffusion through the porous film. In order to evaluate the difference in electrochemical properties, one needs to refer the values of the total charge inserted during coloration cycle (Q_{INS}). Our findings allowed us to estimate Q_{INS} values and demonstrate them in ternary plot as a function of TiO_2/WO_X nanocrystalline content (see Figure 3.8a). The contradiction between results and the postulated microstructure-dependent mechanism for films with high nanoparticle loading is due to the film discontinuity which causes overestimation of surface area. In order to mark these concentrations for further considerations, ternary plots which present parameters by definition calculated per unit area and current flowing through EC device contain faded rounded regions. The Q_{INS} higher than 1.4 mC cm^{-2} were measured for films containing high amount of WO_X

nanoparticles implying a higher anodic current flow though the crystalline fraction and higher Li^+ ion mobility of the film.

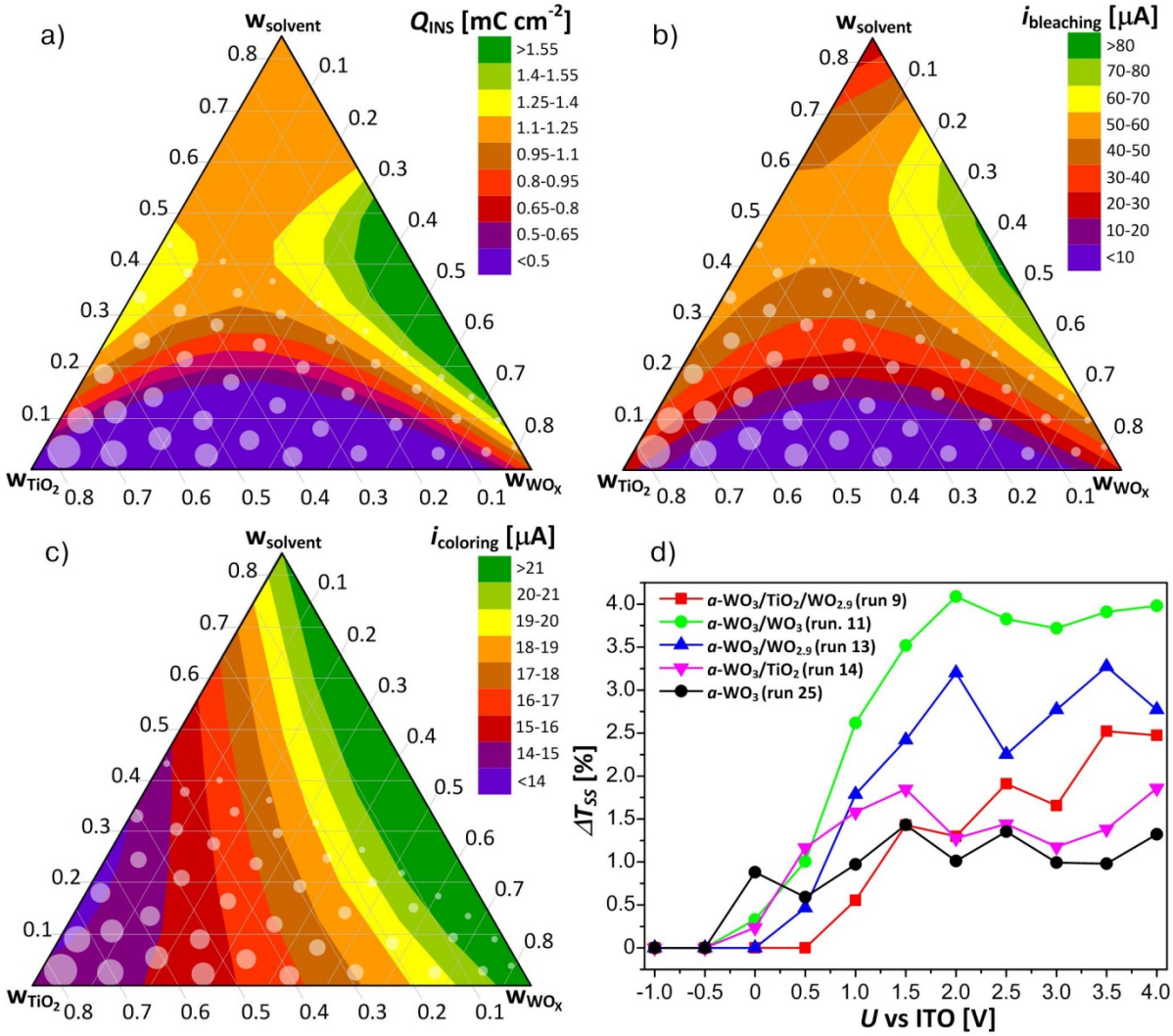

Figure 3.8. Response contour plots showing variation in a) charge densities, b) bleaching current maximum peak and c) coloration current maximum peak as the weight fractions of TiO_2 and WO_X dispersions are varied (w_{PTA} = 0.01, w_{OAD} = 0, X = 3{*yellow*}); the green contour shows the concentrations of highest electrical response; the region of rounded faded marks indicates concentrations for which discontinuous patterns were obtained; d) site saturation effect as a function of operating voltage; the ΔT_{SS} is defined as the difference in transmittance of the bleached films to its value before coloration for particular operating voltage (ΔT_{SS} = 0 for fully reversible optical effect)

Very well-defined anodic (bleaching) peak ($i_{bleaching}$) for those films (see Figure 3.8b) is the evidence of improved kinetic performance caused by the highly porous nanocrystalline structure that greatly reduces the diffusion length of lithium ions. On the other hand, these films manifest high values of reduction (coloring) peak maxima ($i_{coloring}$), which may indicate that Li^+ ion insertion/extraction is not completely reversible (see Figure 3.8c). The value of $i_{coloring}$ decreases significantly with increase of

TiO_2 particle loading. By enhancing the operating voltage, the change in transmittance between colored and bleached state is becoming increasingly evident. When the voltage exceeds a certain value, the transmittance of the bleached films is markedly lower than its value before coloration which means that the device does not bleach completely.

This specific value of coloring voltage called optimum voltage [65] (V_{opt}) lies in the range of -1.5V to -1V for *a*-WO_3, -1V to 0V for *a*-WO_3/WO_X and 0V to 0.5V for *a*-WO_3/TiO_2 films (see Section 3.5.3 for more details) . Color-bleached characteristics recorded at 900 nm, shows that the EC effect was fully reversible for operating voltages lower than V_{opt}, while after applying a higher voltage the film did not bleach completely, due to the intensive charge trapping particularly evident for films containing nanocrystalline WO_X phase. Increasing the WO_X nanocrystals concentration in the film, increases the volume of the grain boundaries, which contributes to more trapping of free charge carriers. In addition, lattice strain and crystal distortion can also affect the Li^+ ion insertion/extraction, causing reversible deterioration. It has been also reported before, that while increasing TiO_2 doping concentration the amount of residual charges in the WO_3 based film decreases due to the enhancement in reversibility of redox process [66]. Positive impact of TiO_2 nanoparticles on reversibility of printed EC films is demonstrated in Figure 3.8d, which represents so called site saturation effect [67].

As a merit of optical performance, values of optical density change (ΔOD) and quantitative coloration efficiency (CE) are given as surface responses shown in Figure 3.9. The ΔOD values are calculated as a natural logarithm of the ratio of transmittance in the bleach state to the transmittance in colored state of the films taken at a certain wavelength [61] (see Section 2.5.5 for detailed definitions of parameters). The ΔOD surface response shown in the Figure 3.9a indicates that films containing large amount of TiO_2 nanoparticles with a smaller share of WO_X content in amorphous matrix exhibit the highest transmission modulation due to the modification of internal film structure. The Li^+ conductive network of interconnected TiO_2 nanoparticles facilitates ionic transport into the EC layer. At the same time, mesoscopic TiO_2 structure significantly increases surface area of *a*-WO_3 matrix. As both TiO_2 and WO_X nanoparticles are hydrophilic, films with high nanocrystalline content become more hydrated. Such physisorbed water gives the significant enhancement in ion dynamics through an amorphous phase [63], consequently leading to increase in ΔOD up to 0.82. The overall device performance expressed by CE is defined as a ratio between ΔOD and injected/ejected charge measured for specified film area [61]. According to this definition, an ideal coating would exhibit a large optical modulation with a small amount of operating charge, giving rise to a large CE values. This is a very convenient performance indicator, however its measurement methods vary between research groups, making difficulties in comparison between various deposition systems. The application of IPT brings additional complications in this topic due to the printed film discontinuity. CE should be then redefined in order to describe not only continuous films, but also inhomogeneous printed patterns, in which the sizes of electrochemically active islands and distances between them are

comparable. Such extended definition would refer to the active area of the EC device measured in device length scale instead of microscale as it is commonly practiced.

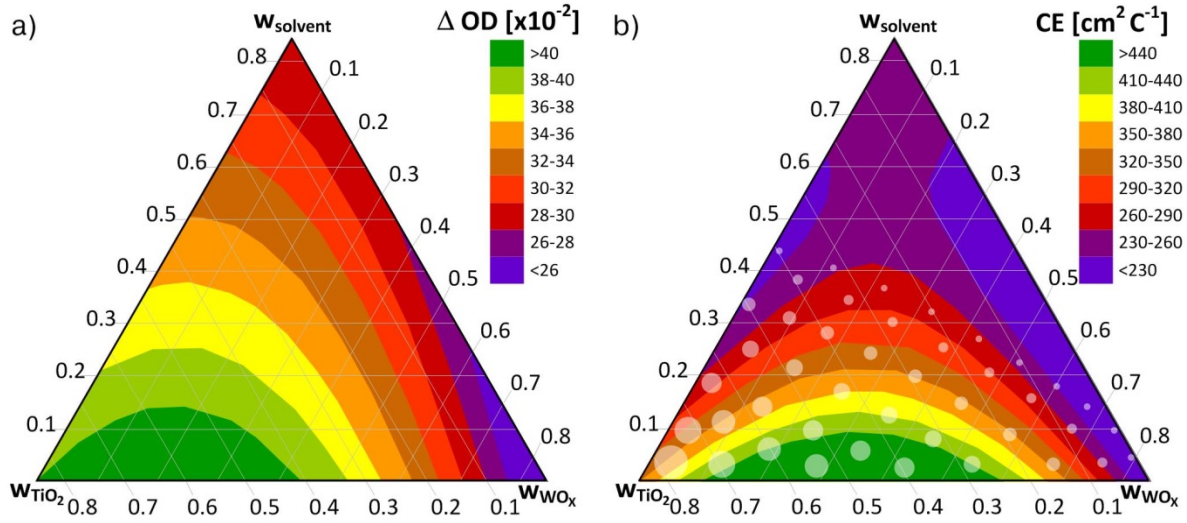

Figure 3.9. Response contour plots presenting variation in a) optical density and b) coloration efficiency as the weight fractions of TiO_2 and WO_X dispersions are varied (w_{PTA} = 0.01, w_{OAD} = 0, X = 3{*yellow*}); the region of rounded faded marks indicates concentrations for which discontinuous patterns were obtained; please, note that these plots differ from the ones presented in Figure 2.8, due to the different OAD content

Inkjet printed EC devices irrespective of the composition exhibit higher CEs than sol-gel derived WO_3 films deposited *via* standard wet methods. The CE values calculated according to redefined formula for printed amorphous films which are observed to be continuous vary between 230 and 260 cm^2 C^{-1} while patterns containing high amount of TiO_2/WO_X nanoparticles exhibit high efficiency of 440 to 470 cm^2 C^{-1} (Figure 3.9b). Although, the accuracy of CE is affected by the method in which optical and electrochemical measurements were not performed in the same time, these values reflect the real EC performance of printed devices. It should be also noted that EC performance of presented devices could be increased by applying counter electrode with higher charge capacity than ITO [68]. In such system, maximal value of charge that can be reversibly shuttled between counter electrode and active film would be higher resulting in increased coloration.

Moreover, CV characteristics (not shown here) indicate that dual-phase *a*-WO_3/WO_X microstructure is most favorable for a rapid ion insertion-extraction process, as these printed films exhibit very well-defined anodic peak and higher charge densities. In addition to the microstructure, amount of dopant, namely TiO_2, plays an important role manifested in decreased charge trapping effect as well as in enhanced optical modulation.

Triton X-100 as non-ionic surfactant has been used in order to adjust the ink surface tension to the value acceptable for printing system (30 - 40 dyne cm^{-1}). The choice of this organic compound was

dictated by two reasons. Firstly, the cationic surfactants are unsuitable for PTA precursor, because their molecules precipitate Keggin-like PTA polyanions, which prevents the synthesis of a stable coating solution [69]. Secondly, Triton X-100 is a well-known surfactant often used with success for inkjet printable inorganic dispersions [70]. It is noteworthy that non-ionic surfactants play also a key role in the formation of WO_3 mesostructures in organic template sol-gel method [71–73]. As the coating solutions presented in those studies are similar to our sol-gel printable precursor, we can expect that printed hybrid films, annealed at 120 ºC may also exhibit a mesostructure. However, this phenomenon has not been investigated and its influence on the EC performance of printed *a*-WO_3/TiO_2/WO_X is not known yet.

3.4. Conclusions

Tungsten oxide is the most extensively studied inorganic EC material due to its interesting electrochemical and physical properties observed for films developed *via* vacuum as well as wet techniques. However, for use in practical high performance EC devices, WO_3 based systems require further improvement in film composition and processing. In order to augment EC properties, dual-phase *a*-WO_3/TiO_2/WO_X deposited *via* IPT using various ink formulations has been investigated. It was indeed surprising to observe that in spite of employing for IPT the same WO_3 sol-gel precursor known from former wet deposition techniques either with nanoparticles or without them, the EC performance of resulting films exhibit dramatic differences to those described in the state-of-the-art, which is indicative of the major role played by the deposition technique.

As-deposited inkjet printed amorphous *a*-WO_3 films prepared from PTA printable precursor and dual-phase *a*-WO_3/TiO_2/WO_X prepared from WO_X and TiO_2 nanoparticles dispersed in the same precursor transform into chemically stable films upon annealing at 120 ºC. The grain size, crystallinity and stoichiometry of those particles are dependent only on the origin of those crystals and are defined at the ink formulation stage. This flexibility in material selection not only endows printed devices with a better chemical stability, but is also responsible for the superior EC performance reflected by high optical density (*i.e.* $\Delta OD \sim 0.82$), enhanced coloration efficiency (*i.e.* $CE > 400$ cm^2 C^{-1} at $\lambda = 900$ nm) and fast color-bleach kinetics (*i.e.* $\tau_{col} < 3$ sec and $\tau_{bl} < 2.5$). Furthermore, inkjet printed EC devices exhibits peak power consumption on the level of 10 μW cm^{-2} in the switching process, which is 40 times lower value when compared to commercial SAGE Electrochromic's window [74] developed by physical route.

Considering just the main effects of each variable in Equation 2.8, it is clear that the amount of WO_X and TiO_2 nanoparticles and WO_3 sol-gel precursor (PTA) have the highest impact on EC performance expressed by τ_{col}, τ_{bl}, ΔOD and CE, while impact of OAD is negligible. Besides, the first order

interactions also occurred between WO_X, TiO_2 and PTA factors justifying the validity of applied first order polynomial model.

Interconnected TiO_2/WO_X nanocrystals of printed dual-phase films lead to higher values of transmission modulation and coloration efficiency over the visible and solar regions as compared to the poor EC performance of *a*-WO_3 films owing to its amorphous structure (see Section 3.5.2 for optical response spectra). With increase in TiO_2 nanoparticle loading, kinetics of intercalation and deintercalation mechanisms improves and significantly reduces the deleterious site saturation effect. The Li^+ conductive network of interconnected TiO_2 nanoparticles facilitates ionic transport into the EC layer and increases significantly active surface area of *a*-WO_3 component. These results demonstrate that IPT is an excellent method for the production of inorganic chromogenic films with controlled composition and dual-phase microstructure for a low temperature, direct-write fabrication of high-performance EC devices. The presented data provide strong support of the general paradigm that to achieve best EC performance an amorphous phase must be combined with nanocrystalline content in light and easily penetrable for cations structure.

Furthermore, this work demonstrated that combination of IPT as a novel deposition technique and DOE methodology provided an effective means to explore and predict the behavior of high performance EC devices. The use of D-optimal mixture design with one no-mixture component could reduce the total number of experimental trials, while still maintaining high accuracy of analysis. The identification of the critical process factors *via* screening experiment was essential for method optimization and resulted in reduced number of system components greatly simplifying technological process.

3.5. Supporting information

In this section, XRD difractograms of raw components of the ink are provided for more detailed description of resulting dual-phase films. The VIS-NIR transmittance spectra of selected films are also presented, and differences between them are discussed. It also provides surface response of V_{opt} parameter.

3.5.1. XRD spectra of raw materials and printed films

XRD data of WO_X powders presented in Figure 3.10 were collected using Brucker D8 Focus Advance diffractometer. Both samples represent monoclinic polymorph but differ in stoichiometry. Detailed crystallographic data are summarized in Table 3.1.

Table 3.1. Crystallographic parameters of WO_X powders according to ICDD PDF 4+ (2009) database

Crystallographic parameters	***yellow***	***blue***
ICDD PDF 4+ (2009) reference	04-005-4272 (I)	04-008-1962 (C)
chemical formula	WO_3	$WO_{2.9991}$
crystal system	monoclinic	monoclinic
space group	P21/n (14)	P21/c (14)
a (Å)	7.29700	7.32000
b (Å)	7.53900	7.54000
c (Å)	7.68800	10.55700
Alpha (°)	90.000	90.000
Beta (°)	90.910	133.093
Gamma (°)	90.000	90.000

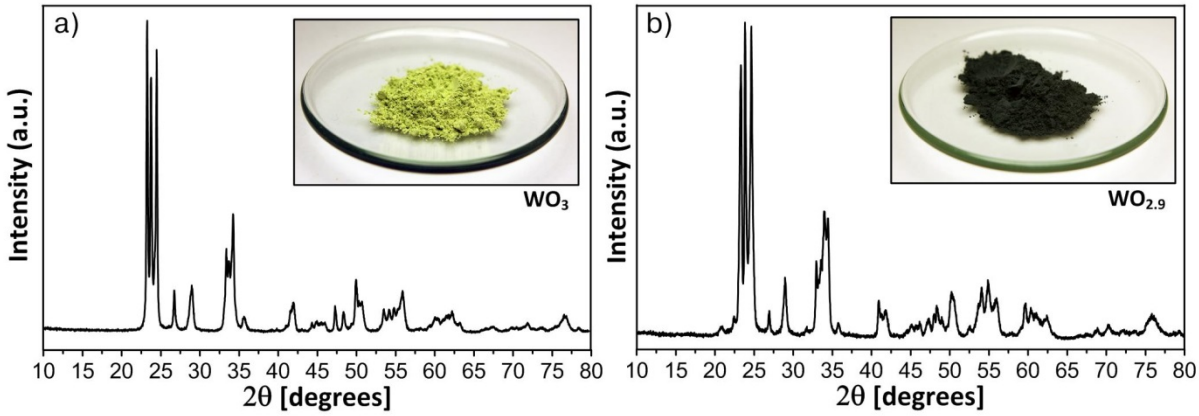

Figure 3.10. The XRD patterns recorded for WO_X powder for a) X = 3{*yellow*} and b) 2.9{*blue*}; insets: photographs of the powder sample

XRD data of mesoporous TiO_2 film (see Figure 3.11a), PTA powder (see Figure 3.11b), OAD powder (see Figure 3.11c) and inkjet printed films (see Figure 3.12) were measured using XPert PRO diffractometer (PANalytical). XRD measurements of mesoporous TiO_2 film deposited by drop-casting of commercial titania paste used in formulation of inks, revealed anatase phase of dispersed NPs.

The XRD observation of PTA dry powder (see Figure 3.11b) confirmed its amorphous structure, which ensures full solubility in aqueous solvent. XRD spectrum of colorless solid OAD shown in Figure 3.11c indicates crystalline structure of this component. However, OAD crystals are fully soluble in water.

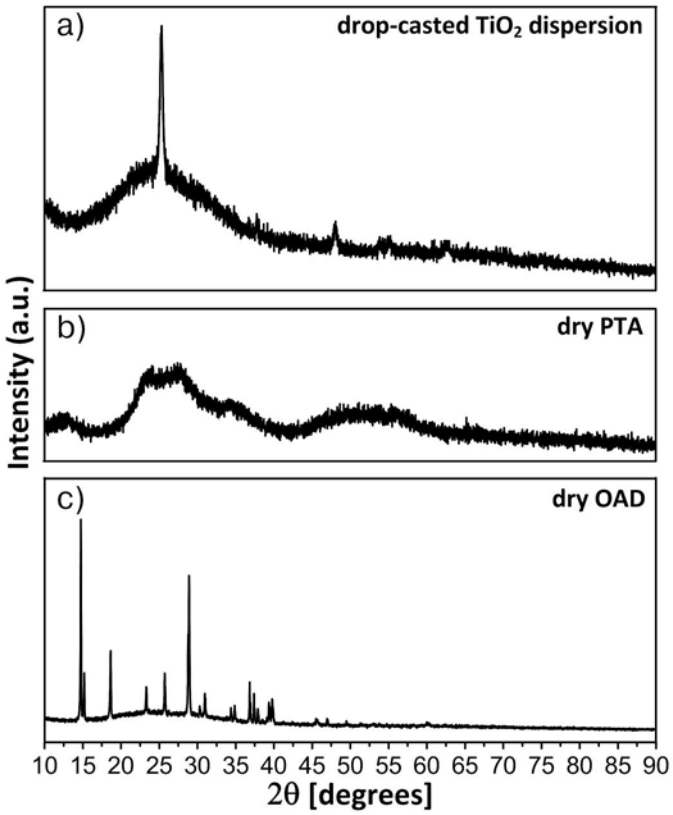

Figure 3.11. The XRD pattern recorded for a) TiO_2 NPs film deposited by drop-casting from titania paste, b) PTA dry powder and c) OAD dry powder

Figure 3.12 shows XRD pattern for three inkjet printed films with different formulation, dried in air for 24h and annealed at 120 °C for 1h. First example (*i.e.* Figure 3.12a) shows spectrum of film containing no MO_X NPs. Amorphous character of this film confirms that soft post-treatment conditions applied in this work are insufficient to induce crystallinity, which stays in agreement with the state-of-the-art. Therefore, the only sources of crystallinity are TiO_2 and WO_X NPs incorporated to the ink at formulation stage, as it is shown in Figure 3.12b and Figure 3.12c. Moreover, spectra shown in Figure 3.12b and Figure 3.12c do not contain peaks from OAD, which means that this component does not recrystallize when the solvent is removed.

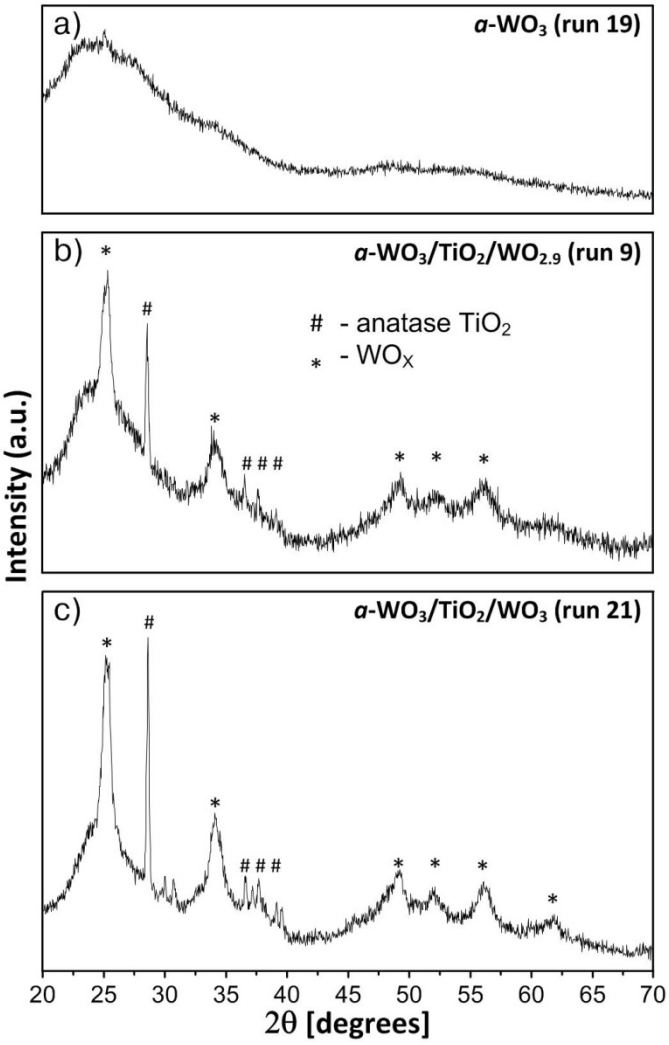

Figure 3.12. The XRD pattern of inkjet printed film developed at run a) 19 ($w_{solvent}$ = 0.866, w_{PTA} = 0.109, w_{OAD} = 0.025, w_{TiO_2} = 0, w_{WO_X} = 0), b) 9 ($w_{solvent}$ = 0, w_{PTA} = 0.01, w_{OAD} = 0, w_{TiO_2} = 0.498, w_{WO_X} = 0.492, X = 2.9{*blue*}) and c) 21 ($w_{solvent}$ = 0, w_{PTA} = 0.081, w_{OAD} = 0.024, w_{TiO_2} = 0.445, w_{WO_X} = 0.451, X = 3{*yellow*})

3.5.2. Optical response spectra of selected films

Optical spectra of various printed films at colored and bleached states are presented in Figure 3.13. The selection of samples aims at showing optical behavior of the material at the edges of the experimental design area, according to Figure 3.14.

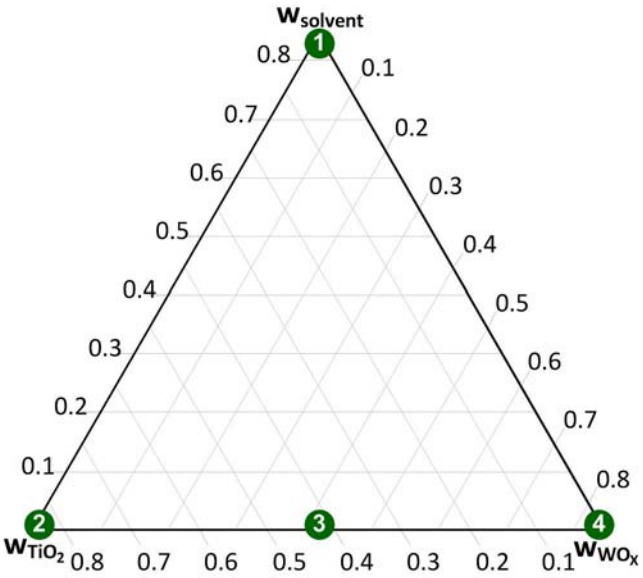

Figure 3.13. Transmittance spectra of EC films derived from four selected ink formulations: a) *a*-WO_3 film (run 25), b) *a*-WO_3/TiO_2 (run 14), c) *a*-$WO_3/TiO_2/WO_X$ (run 9) and d) *a*-WO_3/WO_X (run 11), while $w_{PTA} = 0.01$, $w_{OAD} = 0$ and X = 3 {*yellow*}

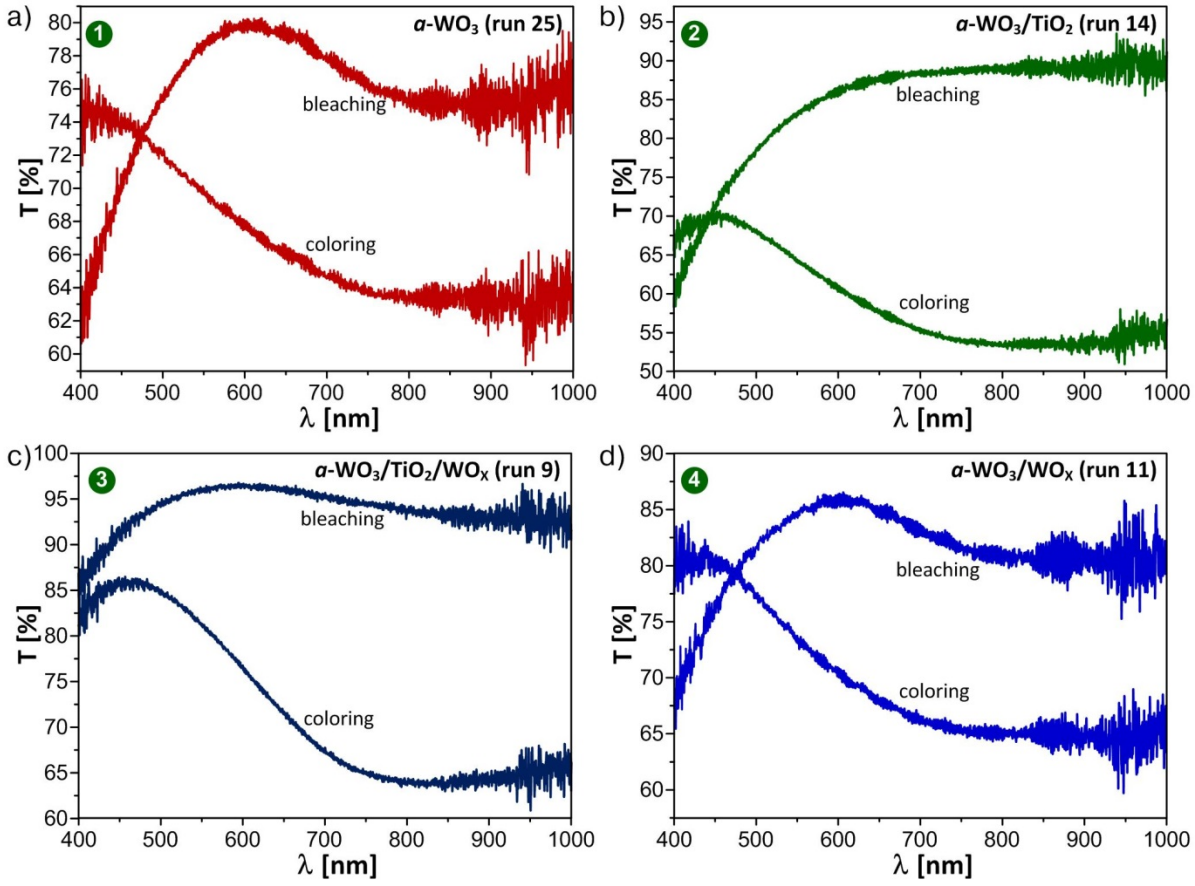

Figure 3.14. A ternary plot showing formulation of inks for development of selected films (w_{PTA} = 0.01, w_{OAD} = 0, X = 3 {*yellow*}); corresponding transmittance spectra are shown in Figure 3.13

The main difference obvious at a glance is a very high transmittance of *a*-WO_3/TiO_2 film at NIR region of electromagnetic radiation (see Figure 3.13b), while *a*-WO_3 and *a*-WO_3/WO_X films (Figure 3.13a and Figure 3.13d, respectively) are suppressing the light in this part of the spectra. Such behavior is typical for TiO_2 films, making them especially attractive for energy harvesting applications. However, EC windows are supposed to cut-off longer wavelength light which consists of unnecessary radiation, including thermal radiation and hazardous electromagnetic fields, in order to create an amenable environment. From the other hand, films containing TiO_2 exhibit the highest optical modulation.

3.5.3. Optimal operational conditions

By increasing the operational voltage, the transmittance of the colored films decreased and the rate of the coloration increased. However, when the coloring voltage exceeds the value of V_{opt}, the EC film is becoming irreversible. Specific values of V_{opt} depending on composition are presented in Figure 3.15. In order to ensure proper performance of EC devices and their long-lasting use, the operational voltage should be lower than V_{opt}. Films loaded with TiO_2 exhibit the highest value of V_{opt}, which means that they can be operated in a wide range of potentials, *i.e.* from -4 up to 0.5 V (bleached to colored) with negligible losses in transmittance. Films developed based solely on tungsten oxide having $V_{opt} < 0$ V, even when operated with low positive voltage, will progressively lower their transmittance in a bleached state. This seemingly small difference may lead to substantial improvement in contrast and switching time.

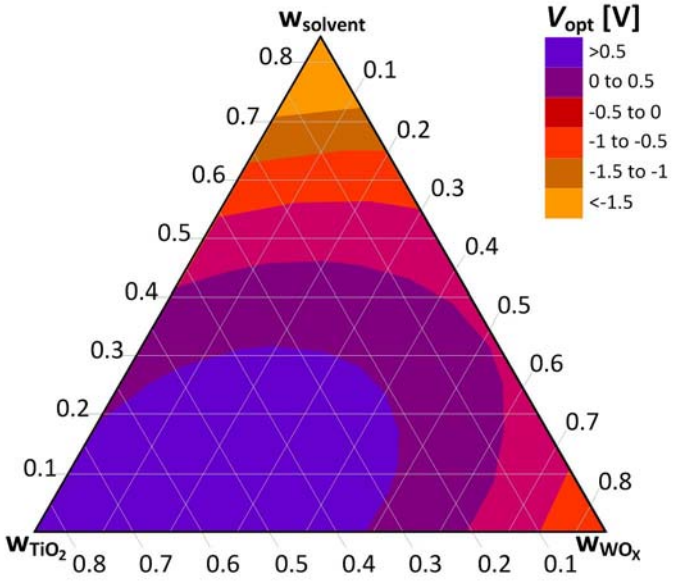

Figure 3.15. Response contour plots presenting variations in V_{opt} as the weight fractions of TiO_2 and WO_X dispersions are varied (w_{PTA} = 0.01, w_{OAD} = 0, X = 3 {*yellow*})

Chapter 4

Metal-oxide nanoparticle engineering for printed electrochemically active films

This chapter is written based on:

Wojcik, P.J., Pereira, L., Martins, R., Fortunato, E.: Metal Oxide Nanoparticle Engineering for Printed Electrochemical Applications. In: Nano-Electrochemistry: Electrochemical Synthesis Methods, Properties and Characterization Techniques. Handbook of Springer **– in press.**

Chapter 4. Metal-oxide nanoparticle engineering for printed electrochemically active films

Chapter 4. Metal-oxide nanoparticle engineering for printed electrochemically active films

Summary

Engineering procedures governing the selection or development of printable nanostructured MO_X NPs for chromic, photovoltaic, photocatalytic, sensing, electrolyte gated TFTs and power storage applications are established in this chapter. The main focus is given on how to perform the material selection and formulation of printable dispersion in order to develop functional films for electrochemical applications.

This chapter is divided into four main parts. Firstly, a brief introduction on electrochemically active nanocrystalline MO_X films developed *via* printing techniques is given. This is followed by the description of the film morphology, structure and required functionality. A theoretical approach to understand the impact of size and shape of NPs on a printable mixture formulation and electrochemical performance being the subject of the third section provides a greater control over the material selection. It was the intention of the author to describe these properties and show that for a given material, the geometry and size of the NPs have a major influence on the electrochemical reactivity and response time. This gives the ability to tune the performance of the film simply by varying the morphology of incorporated nanostructures. This section is completed by the recommendations on each major step of a printable mixture formulation, together with imposed critical constraints concerning the fluid control.

By providing such a rather systematic survey, the author aim to stress the importance of proper design strategy that would result in both, improved physicochemical properties of NPs loaded mixtures and enhanced electrochemical performance of printed functional films.

4.1. Introduction

4.1.1. Nanoparticles for electrochemical applications

One of the most active trends in applied electrochemistry is the development of MO_X NPs with structural, electrical and optical properties tailored to the specific application such as chromic devices [75–77], photovoltaic cells [78], photocatalytic systems [79–82], energy storage devices [83–87], electrolyte-gated TFTs [27, 28], gas sensors [88–90] and electrocatalytic biosensors [91, 92]. Features of those nanostructures are equally as important as their processability, enabling thin film formation with desired functionality [93, 94]. The combination of these two requirements implies a need for a set of engineering rules combining selection/synthesis of the nanocrystalline material and technologically oriented aspects of printing methods into one consistent theory.

Many attempts have been made to deposit previously synthesized MO_X NPs in order to form an electrochemically active nanocrystalline film *via* drop-casting [76], dip-coating [95] or electrophoretic deposition [96, 97]. In other studies, MO_X nanostructures were grown directly on TCO coated glass substrate by crystal-seed-assisted hydrothermal synthesis [75, 98]. However, obtaining a uniform nanocrystalline film with good adhesion to the substrate and desired functionality still remains a challenge. The advent of printing deposition techniques has led to new possibilities in a field of thin solid films based on MO_X NPs. Printing techniques apart from being widely use in graphics, are promising and attractive fabrication methods for a cost-efficient "low end" electronics. An innovative and dynamic research in this area results in new materials and devices, demonstrating their potential to cope with ever-changing requirements and challenges of the electronic market. It was demonstrated that the application of IPT for deposition of MO_X dispersion provides an excellent method for the production of inorganic thin films with controlled composition and microstructure for electrochemical devices such as dye-sensitized solar cells (DSSCs) [70] and electrochromic (EC) windows/displays [60] (see also Chapters 2 and 3). The use of printing techniques is particularly promising for electrochemically active film development, because of its merits of low processing energy, precise patterning with reduced raw material waste, high throughput and flexibility in deposited film composition.

To make genuine progress in development of printed electrochemical devices, it is necessary to take the time to study the problem for which an engineering solution is desired in a broad and interdisciplinary context. In order to define a strategy for MO_X NPs based printed devices, one must consider the requirements and characteristics of electrochemically active material. Studies described in Chapters 2 and 3 have shown, that MO_X NPs content strongly influence the final performance of inkjet printed electrochemically active films, underlying the demand to understand the role of the NPs properties, along all stages of their development and processing. Therefore, the selected strategy is based on a correlation between NPs properties and further technological steps that lead to the development of a functional film for an electrochemical device. These technologically oriented aspects of printing methods consist of the following:

a) Formulation of the MO_X NPs dispersion according to the objectives related to chemical composition and fluid flow aspects.
b) Film deposition with regard to the fluid properties, selected printing technique and substrate.
c) Post-treatment process in which printed layer is subjected to external factors (usually highly energetic process), in order to set the required functionality.
d) Film validation in terms of physical aspects and electrochemical performance.

This chapter shows a general view on how to perform both, the MO_X NPs selection and formulation of printable dispersions in order to develop functional films for electrochemical applications. The

grain size, shape, crystallinity and stoichiometry of MO_X NPs incorporated into the printed film are dependent only on the origin of those crystals and are defined at the printable mixture formulation stage. This flexibility in material selection not only endows printed electrochemical devices with a better chemical stability, but is also responsible for the superior performance *e.g.* shorter response time or higher reactivity. Therefore, the versatility of this method makes it an ideal tool for creating materials with predictable and controlled properties, while maintaining their good processability *via* printing techniques.

To assure the desired electrochemical performance and processability, the criteria for MO_X NPs size, shape, crystallinity as well as the uniformity and agglomeration mechanism are established in following subsections.

4.1.2. Morphology of printed films

Nanocrystalline film is a special category assigned to polycrystalline layers of NPs. Furthermore, the NPs forming the film can be either sintered (mesoporous) or embedded in an amorphous matrix (dual-phase). Figure 4.1 gives a generalized overview presenting both kinds of NPs loaded printed films for electrochemical applications. From the broad range of available film morphologies used typically in electrochemical applications [99], only these two are so far feasible in a printing process. Due to the technological limitations, development of *e.g.* vertically aligned ordered nanostructures or nanoarrays is not possible *via* printing process. Printed mesoporous film shown in Figure 4.1a is developed using NPs loaded dispersion, usually stabilized by polymeric additives. Once the dispersion is deposited on a substrate, its liquid components *i.e.* solvents, NPs stabilizers, thickeners, wetting agents and surfactants are no longer needed. Unfortunately, additives typically used to stabilize dispersions of MO_X NPs in a liquid medium are long chain molecules with high evaporation temperatures, which are difficult to eliminate and usually requires high energy to be applied. Such additives may deteriorate or even inhibit electrochemical reaction. The post-treatment process which may include application of elevated temperature or more specific techniques such as photonic pulse curing or UV irradiation is performed in order to form and dry the film, organic burn-out or sintering of NPs. On the other hand, high temperature may affect morphology and microstructure of NPs, due to their thermal instability [100].

As an alternative to energy requiring methods, a dual-phase composition of the film shown in Figure 4.1b can be induced by mixing NPs with liquid sol-gel precursor, or overprinting the NPs film by sol-gel precursor. Resulting film contains randomly dispersed nanocrystals in a continuous amorphous matrix of the same MO_X, which provides conductive medium for electrons and ions and physically bond the NPs to the surface of the substrate. This approach was successfully applied in development of printed EC films based on sol-gel precursor and NPs of WO_X (see Chapters 2 and 3). The sol-gel

precursor of WO_3 formulated from peroxopolytungstic acid requires relatively low temperature of 120 °C for 1 h in order to condensate and densify, resulting in a non-soluble film [43]. However, formation of other MO_X, such as ternary $M_x^1M_y^2O_z$ films (where M^1 and M^2 are metals such as In, Ga, Sn or Zn) by standard sol-gel route requires an annealing step at relatively high temperature (>250 °C) [101]. In order to overcome this issue, a photochemical activation by deep-UV irradiation at low temperature should be applied to provide an amorphous MO_X matrix [102]. In this method, photo-induced condensation and densification of the wet gel film resulted in device with excellent electronic performance.

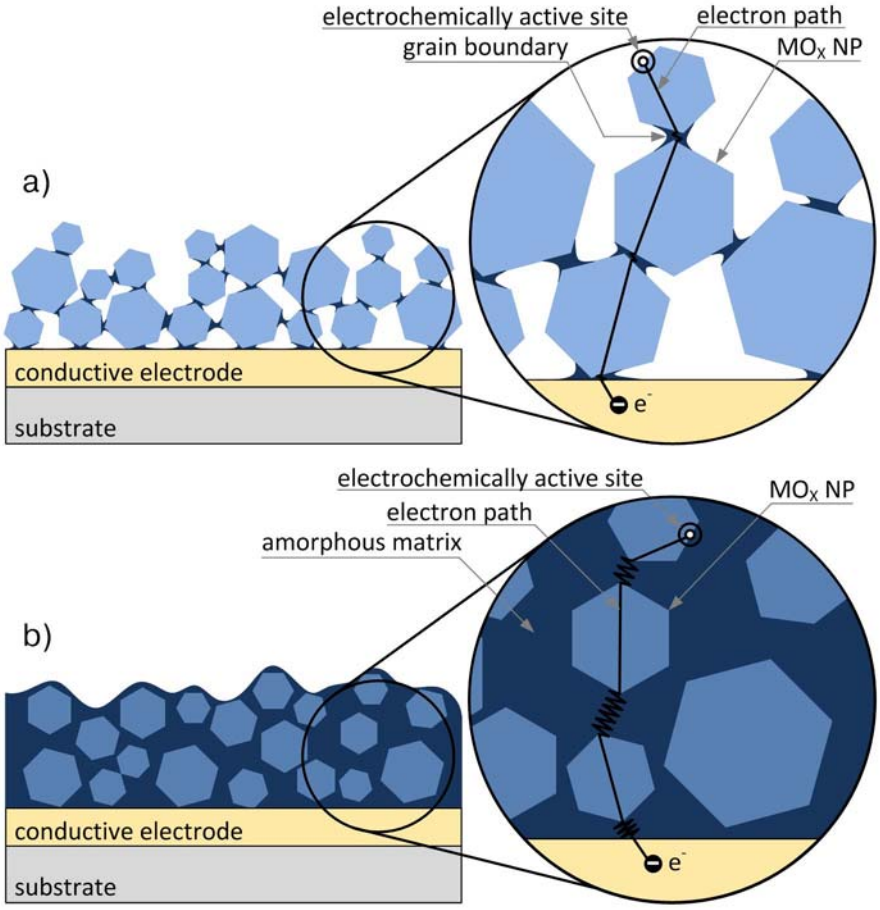

Figure 4.1. Schematically presented nanocrystalline material for electrochemical applications as a) mesoporous and b) dual-phase films; the electron paths were drawn with respect to their electrical transport properties

The main difference between mesoporous and dual-phase film microstructure lies in character of interconnections between NPs. Randomly oriented NPs are separated by grain boundaries in case of nanocrystalline films or interfacial amorphous regions in dual-phase counterpart. Also the thickness of the printed nanocrystalline electrodes depends of the film morphology. Too thick mesoporous electrode leads to the higher resistance and thus reduction in the efficiency of electrochemical process (*e.g.* conversion efficiency of DSSC). In case of dual-phase morphology used in EC devices, two

thick films prevent EC action to take place. The optimum thickness is typically around 10 μm in mesoporous TiO_2 film in DSSCs and 1 μm in dual-phase *a*-WO_3/WO_X film in EC devices.

This generalized overview shows nanocrystalline material with length scale in all three dimensions which corresponds to quasi-spherical NPs. However, restriction of nanocrystalline regions to one or two dimensions (rod-shaped or layered NPs, respectively) results in an anisotropic charge transport, which is beneficial from electrochemical point of view. Electron transport in elongated shape NPs is much faster than percolation through a network of quasi-spherical crystals [78].

Another aspect is related to the disorder at the interface between neighboring NPs. Regardless of the film morphology, one particular weakness is the presence of a massive number of interfacial boundaries acting as trap sites for electron transport. Such trap limited diffusion lowers overall efficiency of electrochemical device. Grain boundaries in mesoporous films have smaller disorder when comparing with amorphous interface in dual-phase film. However in the second variant, by reducing the NPs size and increasing solid content, the volume fraction of interfacial regions can be significantly reduced.

4.1.3. Required functionality

Printed nanocrystalline films described previously can be used interchangeably, unless a technological step exists in a device development which is not compatible with a given film morphology. A typical example is dye molecules anchoring on a surface of MO_X NPs, as an integral step in DSSCs development. The mesoporous structure can be easily penetrated by a solution of dye, while in case of dual-phase film the dye is able to anchor only on the surface of the amorphous layer. Similarly, in electrocatalytic biosensors where immobilization of enzymes on the specific surface area requires proper wetting of the mesoporous structure. Therefore, the application of dual-phase film in DSSCs, and catalytic biosensors is very limited. In other electrochemical devices based on MO_X films such as electrolyte-gated TFTs, EC displays/windows or energy storage devices, the application of dual-phase films seems to be less restricted.

Another aspect is related to the post-treatment of the mesoporous film, which is necessary in order to sinter NPs and provide electron percolation paths. The application of elevated temperature to sinter nanocrystalline film deposited on flexible substrates is limited due to the heat sensitivity of those materials. Maximum processing temperature is 90 °C for regular paper, 130 °C for PET, 160 °C for PEN and 250 °C for PI, which irrespectively of the NPs size is not sufficient to sinter most of MO_X materials.

As a summary of this section, some basic requirements can be pointed out, which should be fulfilled in order to obtain well performing nanocrystalline film. From the electrochemical point of view the film must:

a) provide high surface area for electrochemical reaction (*e.g.* large surface area for dye absorption in DSSC);
b) allow effective diffusion of electrolyte ions into the interface/surface;
c) provide sufficient electronic conductivity (*e.g.* fast charge compensation in EC device, low recombination rates in DSSC);
d) be mechanically stable having good adhesion to the substrate;
e) assure negligible deviation from the reversibility according to the application requirements;
f) provide other specific functionalities if required, such as high transparency in a visible range (in case of *i.e.* EC and DSSC); and
g) be compatible with device processing (*e.g.* enables dye absorption on MO_X NPs, low processing temperature for film deposited on heat sensitive substrates).

4.1.4. Impact of ionic and electronic conductivity

The nature of electrochemical reaction depends of a distinct mechanism governing the interaction between MO_X and ions. In some materials (*e.g.* SnO_2 or PbO_2) alloying/dealloying processes are responsible for reversible reaction with ions [103]. In other MO_X (*e.g.* TiO_2 or WO_X) ions are inserted/deinserted into/out of the crystal network [104]. In transition MO_X (*e.g.* Fe_XO_Y, Ni_XO_Y, Co_XO_Y, RuO_2, IrO_2 or MoO_3) reaction with ions is conducted through an unusual conversion reaction [105]. In many other MO_X (*e.g.* ZnO, In_2O_3 or ternary and quaternary oxide systems such as indium zinc oxide - IZO, zinc tin oxide - ZTO, indium zinc tin oxide - IZTO or indium gallium zinc oxide - IGZO) the reaction with ions is surface limited, inducing field effect in the NPs volume [28].

Ion-intercalation reaction is strongly dependent of chemical and crystallographic structure of MO_X, while ion diffusion coefficient and the length of diffusion path depends on NPs microstructure [106, 107]. High electronic conductivity of crystalline phase leads to the enhancement in lithium ion diffusion rate. As an example, the electronic conductivity of stable WO_X NPs was reported to be the highest for orthorhombic hydrate (*ortho*-$WO_3 \cdot 0.33H_2O$) and gradually smaller for sub-stoichiometric (WO_{3-y} where $0 \leq y \leq 3$), monoclinic (*m*-WO_3) and hexagonal (*h*-WO_3) structure, respectively [108]. The high charge carrier concentration in anhydrate WO_{3-y} ($0 \leq y \leq 3$) is explained by non-stoichiometry, where the free electrons are balanced by much less mobile oxygen vacancies. Better electron transport is also a product of an internal electric field which separates the electrons from the surrounding electrolyte, and sweeps them towards the collection electrode (*e.g.* in DSSCs) or active

site (*e.g.* in EC device). However, in order to support such radial electric field (depletion layer) the minor axis width of the 1D or 2D NP should be big enough (higher than Debye-Hückle screening length) in regard to carrier concentration in a given MO_X.

Fast insertion/extraction of ions in EC and energy storage devices may be achieved by short diffusion length typical for 1D or 2D shapes, and NPs of small size. The smaller NPs dimensions, the shorter diffusion path length. In case of storage devices such as thin film batteries or super capacitors, the charge-discharge capacity was found to be inversely proportional to the NPs size [87]. The insertion/extraction dynamics is related to the energy barrier for diffusion (preferred crystallographic orientation of the facets exposed to the electrolyte) [83]. Electrochemical properties of the MO_X NPs are particularly sensitive to atomic surface structure also in other devices. As an example, anatase TiO_2 has been proved to show the highest photo-electrochemical performance among all possible crystallographic phases of this MO_X [109]. Moreover, the crystallographic orientation of exposed facets, have been demonstrated to play the major role in defining its intrinsic properties, and thus its catalytic activity [79, 83].The wide band gap semiconductors such as TiO_2 becomes one of the best choice to form mesoporous layer in DSSCs. However, ZnO was found to be a promising alternative to TiO_2, mainly due to the much higher electronic mobility [110–114], which improves the electron transport and reduces recombination loses [115, 116].

These conduction phenomena assure efficient charge compensation during the redox process and hence improve the response time of the films in EC devices and electron collection in DSSCs. When the size of NPs dispersed in a film decreases, the trapping and scattering effect of free charge carriers on grain boundaries result in increased film resistivity. If the size of NPs is smaller than electron mean free path, the scattering on grain boundaries dominates and the advantage of nanocrystalline composition is becoming negligible. Design of NPs with proper dimensions while maintaining optimal crystallographic structure, lead to fast response kinetics and enhanced overall performance.

4.2. Materials and methods

Methods presented in this section were developed entirely by the author of this thesis. Presented solutions aim at revealing the impact of particle shape and size on the overall electrochemical performance of selected regular shaped NPs.

4.2.1. Crystallographic modeling of clusters

Crystallographic model of small MO_X cluster was generated using CrystalMaker® for Windows ver. 2.3.0, according to generalized algorithm presented in Figure 4.2. The cluster is built starting from a single metal atom which determines the center of the coordinate system up to the set value of outer

radius (r_h). In such cluster the surface of interaction with ions is a hollow sphere with thickness denoted as d_h (see Figure 4.3a).

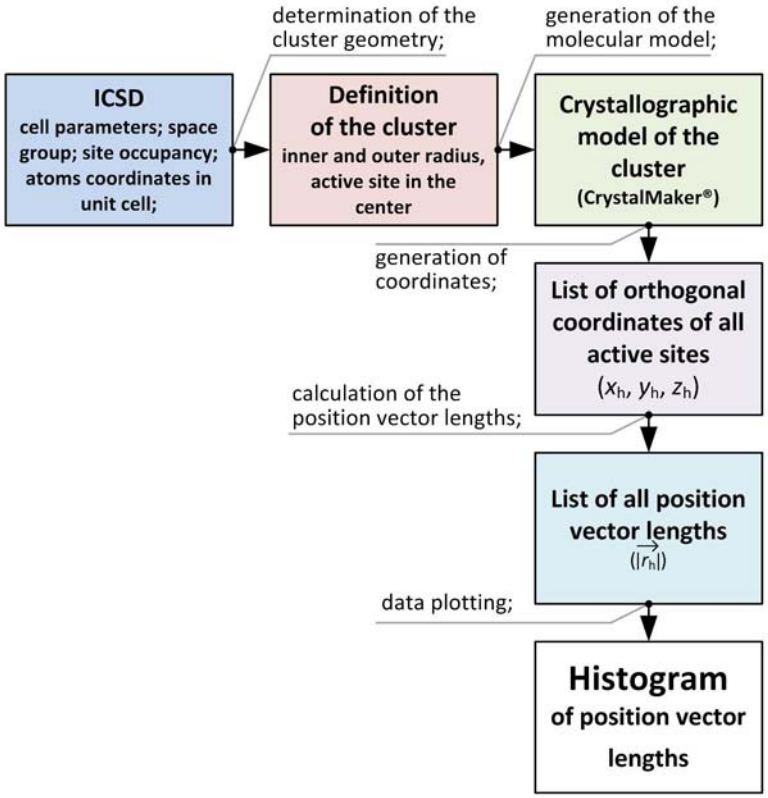

Figure 4.2. Generalized schematic diagram presenting consecutive steps of MO_X cluster modeling; the main outcome of such simulation is the histogram of position vector lengths of all active sites

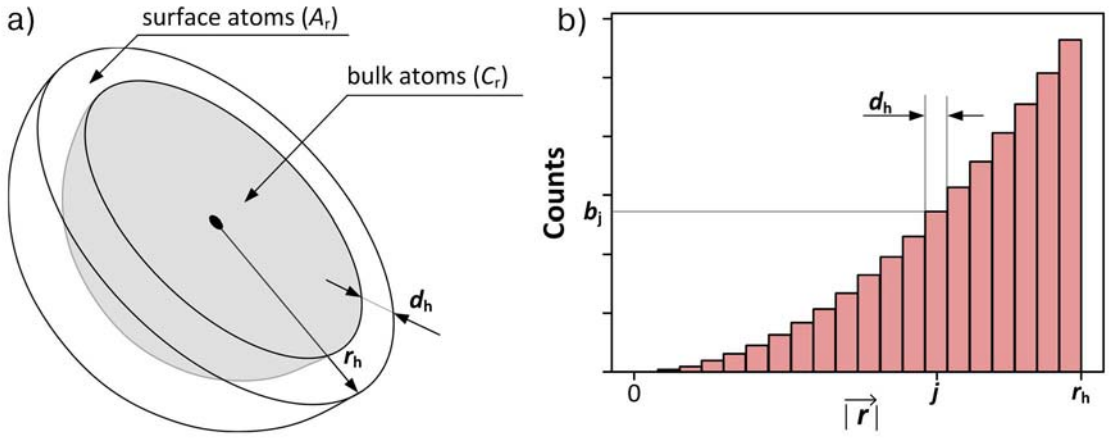

Figure 4.3. Elements of crystallographic modeling shown schematically as a) a cross-section of the modeled cluster and b) corresponding histogram of position vector lengths

When the model of the cluster is completed, CrystalMaker® lists the orthogonal coordinates of all atoms (x_h, y_h, z_h) which are exported to data analysis software (*e.g.* OriginPro or MS Excel). The position vector length ($|\vec{r}|$) of each active site is calculated according to Equation 4.1.

$$|\vec{r}| = \sqrt{x_{\mathrm{h}}^2 + y_{\mathrm{h}}^2 + z_{\mathrm{h}}^2} \tag{4.1}$$

Resulted values are plotted as a histogram shown in Figure 4.3b, in which d_{h} corresponds to the bin size, defining total number of bins (i_{h}) according to Equation 4.2.

$$i_{\mathrm{h}} = \frac{r_{\mathrm{h}}}{d_{\mathrm{h}}} \tag{4.2}$$

Each *j*-th bin contains the number of counts denoted as b_{j}(where $1 < j < i_{\mathrm{h}}$).

The number of surface active centers (A_{r}) of a spherical cluster with radius r_{h} is given by Equation 4.3. Total number of active centers (B_{r}) of a spherical cluster with radius r_{h} is given by Equation 4.4. Number of active centers in the bulk (C_{r}) of a spherical cluster with radius r_{h} is given by Equation 4.5.

$$A_{\mathrm{r}} = \begin{cases} b_{\mathrm{j}} - 1, \text{for } j = 1 \\ b_{\mathrm{j}}, \text{for } j > 1 \end{cases} \tag{4.3}$$

$$B_{\mathrm{r}} = \sum_1^{i_{\mathrm{h}}} b_{\mathrm{j}} \tag{4.4}$$

$$C_{\mathrm{r}} = B_{\mathrm{r}} - A_{\mathrm{r}} + 1 \tag{4.5}$$

Therefore, the surface-to-volume atomic ratio (SA:V$^{(a)}$) is defined as the number of surface atoms to the number of bulk atoms according to Equation 4.6

$$\mathrm{SA{:}\,V}^{(a)} = \frac{A_{\mathrm{r}}}{C_{\mathrm{r}}} \tag{4.6}$$

Percentage of surface ($A_{\mathrm{r}}\,[\%]$) and bulk ($C_{\mathrm{r}}\,[\%]$) active centers can be calculated according to Equations 4.7 and 4.8

$$A_{\mathrm{r}}\,[\%] = \frac{A_{\mathrm{r}}}{B_{\mathrm{r}}} 100\% \tag{4.7}$$

$$C_{\mathrm{r}}\,[\%] = \frac{C_{\mathrm{r}}}{B_{\mathrm{r}}} 100\% \tag{4.8}$$

Results of crystallographic modeling shown in Section 4.3.1.1 were obtain for monoclinic tungsten oxide (*m*-WO_3), modeled according to ICSD: 98-009-1587 with following cell parameters and crystal structure (X, Y, Z): space group P 1 21/c 1; space group number 14; a = 7.2973 Å; b = 7.5390 Å; c = 10.5150 Å; $\alpha = 90°$; $\beta = 133.0250°$; $\gamma = 90°$; W_1 = (0.03400, 0.47700, 0.28400); W_2 = (0.52800, 0.03700, 0.28200); O_1 = (0.21400, 0.01300, 0.49300); O_2 = (0.21600, 0.04300, 0.00800); O_3 = (0.01900, 0.24100, 0.23000); O_4 = (0.49800, 0.26200, 0.28600); O_5 = (0.72500, 0.47400, 0.21800); O_6 = (0.29400, 0.54200, 0.28900). Following input parameters were implemented in the model: $r_{\mathrm{h}} = 100$Å and $d_{\mathrm{h}} = 5$Å.

4.2.2. Models of shaped nanocrystals

Simulations of selected single nanocrystals were conducted on primary and regular shapes drawn in Figure 4.4.

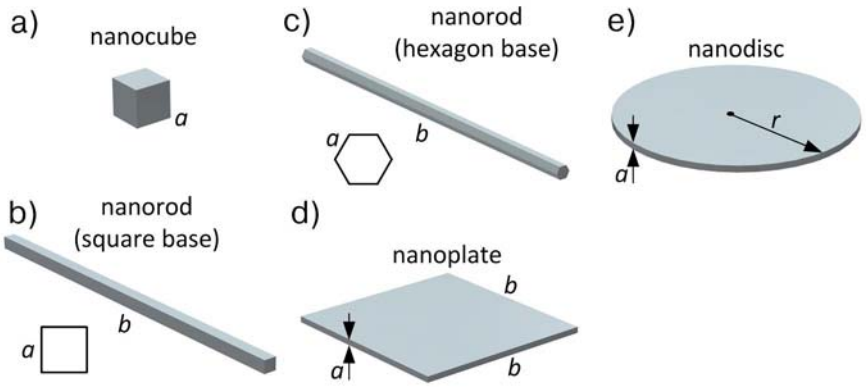

Figure 4.4. Theoretical examples of various regular shaped NPs: a) nanocube (3D), b) square base nanorod (1D), c) hexagon base nanorod (1D), d) nanoplate (2D) and e) nanodisc (2D)

The AR and SA:V parameters for these regular shaped NPs were calculated using equations presented in Table 4.1. Accordingly, sphere and cube are characterized by AR= 1. Please note, that considerations presented in Section 4.3.1.2 are valid as long as an ideal dispersion of NPs is concerned. This means that we consider the products of a synthesis which consists of separated nanocrystals with equal volume and shape.

Table 4.1. Relations between AR and SA:V derived for various regular shaped NPs

shape	**AR**	**SA: V = f(AR)**
nanorod (square base)	$\frac{b}{a}$	$\frac{2a}{b^2}AR + \frac{4}{b}AR$
nanorod (hexagon base)	$\frac{b}{a\sqrt{3}}$	$\frac{2a\sqrt{3}}{b^2}AR + \frac{4}{b}AR$
nanoplate	$\frac{b}{a}$	$\frac{2}{b}AR + \frac{4a}{b^2}AR$
nanodisc	$\frac{2r}{a}$	$\frac{1}{r}AR + \frac{a}{r^2}AR$

4.2.3. Model of agglomeration

A simple agglomeration model shown in Figure 4.5 was used in order to simulate the relation between SA:V and number of agglomerated particles.

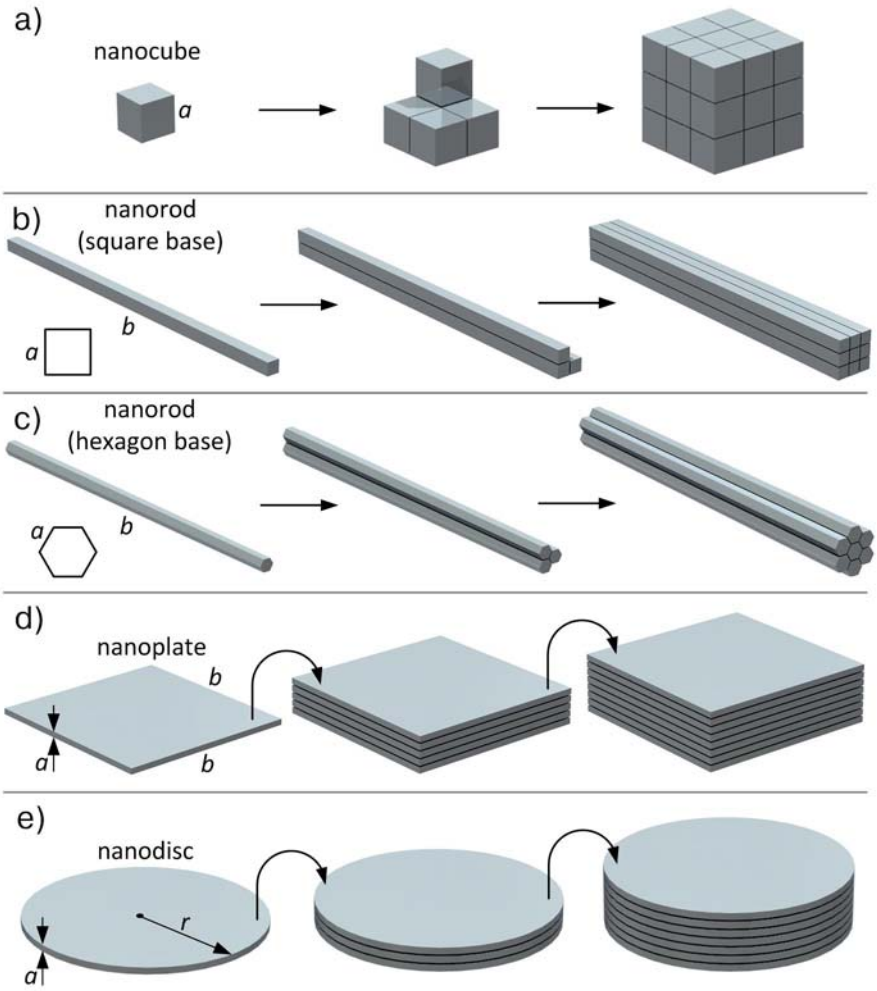

Figure 4.5. Basic agglomeration model for various regular shaped NPs: a) nanocubes (3D), b) square base nanorods (1D), c) hexagon base nanorods (1D), d) nanoplates (2D) and e) nanodiscs (2D)

NPs of various shapes are described with simple assumption that the volume of all individual particles is equal. Particles presented in such simulation have primary and regular shapes with unit volume.

4.3. Results and Discussion

4.3.1. Size–shape impact: from small clusters to massive agglomerates

When the dimensions of a material system are reduced below a certain length, typically tens of nanometers, the physical properties, which are associated with this length, may drastically change. Then, material properties are no longer solely given by its chemical composition, but also by the size and shape of its nanoscale constituents [117, 118]. The following section attempts to describe these properties, and show that for a given material, geometry (shape) and particle size have a major influence on the overall electrochemical properties of a printed film. The size, as well as the shape of the NPs determines physical and chemical properties of the material. The laws of quantum chemistry

govern the smallest particles with sizes ranging from less than a nanometer up to several nanometers. For particles with sizes higher than tens of nanometers, the laws of solid-state physics hold. For the intermediate sizes ranging from several to tens of nanometers, chemical and physical properties do not comply strictly with any of those theories [119]. In the following section, an electrochemical performance of NPs loaded films (*i.e.* reactivity and response time) is correlated with geometrical properties of NPs.

In the large range between molecules and massive agglomerates of particles, three size-shape regimes can be distinguished in which electrochemical properties are mainly related to: distribution of atoms on the surface and in the bulk (regime I), geometry of nanocrystals (regime II) and agglomeration process (regime III). In order to transform the shape into mathematical form that still would contain its geometrical description, let's use the aspect ratio (AR). This parameter is defined as the length of the major axis (*b*) divided by the width of the minor axis (*a*) [120]. Using size-shape coordinate system, all three regimes can be schematically presented as it is shown in Figure 4.6. The highest values of AR correspond to 1D morphologies such as nanowires and nanorods. Medium values are typical for 2D morphologies such as nanolamellas, nanoplates and nanodiscs, while the lowest values are the domain of 3D morphologies such as nanocubes or nanospheres.

In the following sub-sections a deeper consideration on size–shape impact on electrochemical performance of MO_X NPs is provided. It is deduced that the minimum response time of those nanostructured systems can be achieved in a first regime of the size–shape space. On the other hand, the electrochemical reactivity is attributed mainly to the shape of the NPs and can be maximized in the second regime with increase in active surface area. When the NPs are becoming larger entering the third regime, the agglomeration processed causing properties deterioration, and hence lowering the electrochemical performance of the material.

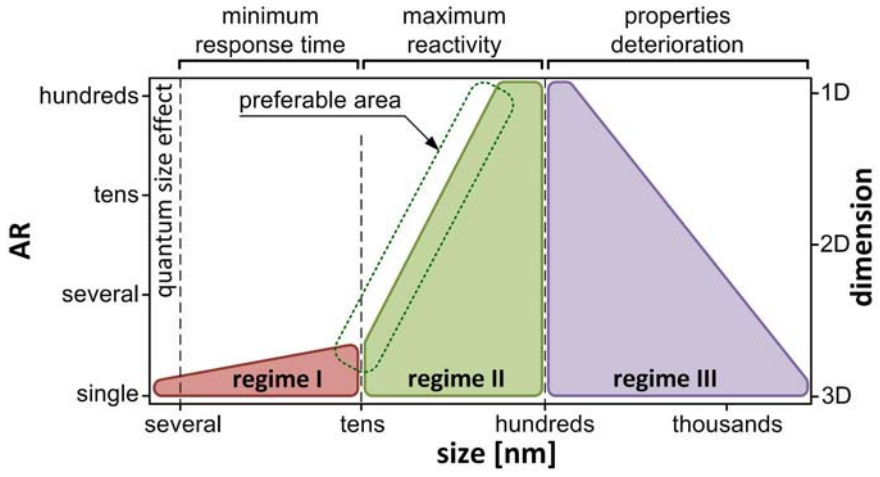

Figure 4.6. Electrochemical properties of MO_X NPs in the size–shape coordinating system

4.3.1.1. Small clusters

Irrespectively of the size, an important factor for electrochemical reactivity, that is, the rate at which the electrochemical reaction will proceed is the area/volume ratio of the nano-sized object. In the first size regime, in which NPs are larger than molecules and smaller than tens of nanometers, electrochemical properties are strongly dependent on $SA:V^{(a)}$ [121, 122]. It should be noted that by the number of atoms in case of MO_X, we understand the number of electrochemically active sites, which means the number of metal atoms. Therefore, let's consider spherical WO_3 cluster in which each tungsten atom serves as potential electrochemically active center changing from transparent state to a colored state. A schematic drawing of the cross-section of *m*-WO_3 spherical cluster with diameter of 5 nm is presented in Figure 4.7.

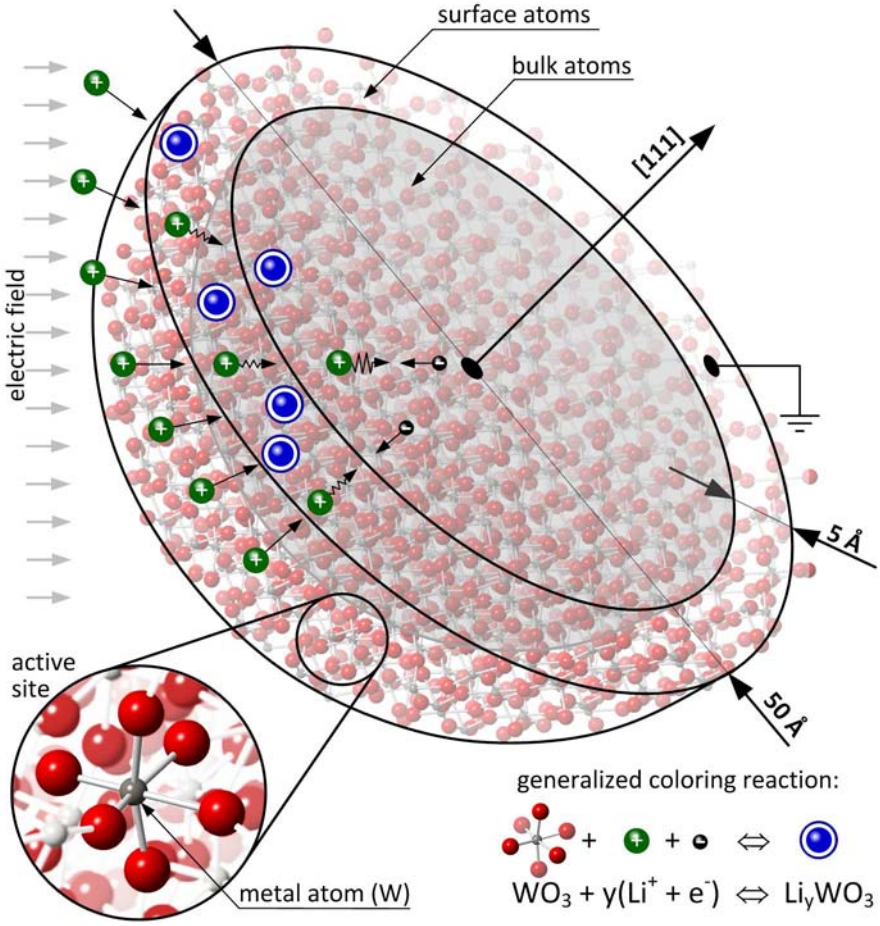

Figure 4.7. Schematic drawing of the cross-section (along [111] plane) of *m*-WO_3 spherical cluster with diameter of 5 nm; in this case tungsten atoms are distributed equally, 50% in the surface hollow sphere and 50 % in the bulk ball which gives $SA:V^{(a)}$ = 1; an equation represents generalized mechanism of electrochemical reaction for coloring action

According to calculations for such cluster (see Figure 4.8), high percentage of electrochemically active sites at the surface of NP (let's assume a hollow sphere with thickness of 0.5 nm), being in contact with electrolyte is characteristic for nanostructures with mean particle size ranging in the first

regime. In the cluster of around 2 nm in diameter, 85 % of tungsten atoms are located on the surface ($SA:V^{(a)}$ = 5.7), while in cluster of 5 nm in diameter tungsten atoms are distributed equally in the surface and bulk ($SA:V^{(a)}$ = 1).

According to the electrochromism theory, the mechanism of optical modulation is different in crystalline and amorphous phase. In nanocrystalline WO_X electrochromism arises due to the increasing Drude type (metallic) reflection, observed especially in IR region with increasing free electron/lithium injection [61]. On the other hand, in amorphous phase, the most widely accepted model assumes that the optical modulation upon the double injection occurs through increasing absorption arising from the transfer of localized electrons between W^{5+} and W^{6+} sites, so called small polaron absorption [62, 63, 123].

Figure 4.7 presents generalized mechanism of electrochemical reaction of coloring in a single EC NP. It is assumed that WO_3 NP in transparent state can be switched reversibly to a colored state by both insertion of ions and electrons to form tungsten bronze (*a*-Li_yWO_3, where *y* is the fractional number of sites filled in the WO_3 lattice). Although being an obvious oversimplification, presented schema provide a very convenient background for further discussion. In considered situation WO_3 NP is in contact with ion (Li^+) conductor, which also serves as ion storage, and electron (e^-) conductor as negative charge collector/source. An electric field shuttles ions into and out of the NP causing coloring (Li_yWO_3) and bleaching (WO_3) action. A hollow sphere representing surface atoms is more conductive for ions and less conductive for electrons when comparing with NP's inferior made of bulk atoms. Therefore, the probability of electrochemical reaction (redox) is the highest at the interface between surface and bulk volume, where electrons meet ions leading to the formation of Li_yWO_3. Moreover, high $SA:V^{(a)}$ ratio drastically reduces response time due to the fast charge compensation during the redox process [124].

In the MO_X based electrolyte-gated TFT, external voltage applied to semiconductor/electrolyte interface cause creation of space charge regions which consists of charged immobile donors or acceptors, or by mobile electrons or holes from the conduction and valence bands, respectively. High amount of surface atoms and low sizes result with grains wholly filled by space charge region, improving current switching characteristics. In those NPs, the electrical conduction is no longer controlled by the grain boundaries, but by the grain itself.

Similarly, in MO_X based chemical gas sensors the space charge region extended to the whole NP volume causes significant improvement in the sensitivity. Additionally, much higher concentration of surface defects leads to a higher surface reactivity, when comparing to their hundreds-nanometer sized counterparts. Thus, the use of materials with the mean particle size ranging in the first regime, significantly improves the gas sensing properties [125, 126]. The large active surface area enhances

the material sensitivity, while the faster response is related to short diffusion paths and rapid grain boundary diffusion.

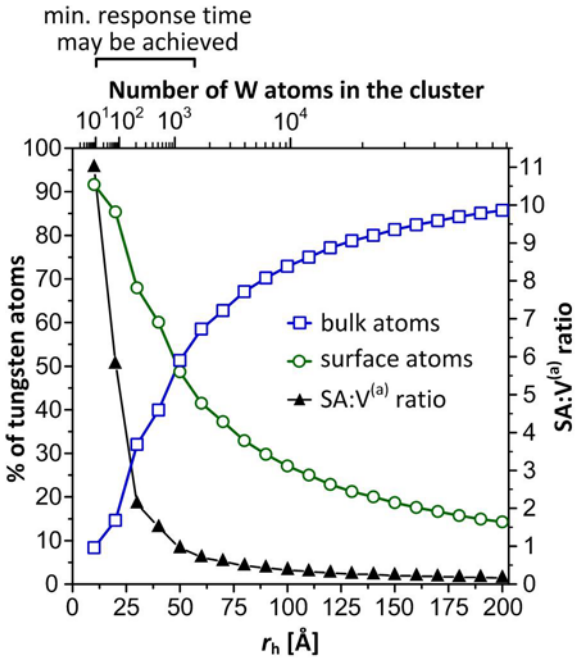

Figure 4.8. Relative numbers of tungsten surface/bulk atoms and SA:$V^{(a)}$ ratio as a function of spherical cluster diameter calculated for *m*-WO_3 (ICSD: 98-009-1587)

4.3.1.2.Shaped nanocrystals

In the second regime of size–shape coordinating system, which comprises NPs higher than tens and lower than several hundreds of nanometers, electrochemical properties are dependent rather on geometric shape than size. Electrochemical properties in this size range are strongly dependent on surface-to-volume ratio (SA:V) defined by means of geometric surface area to the volume of the object. Let's use the aspect ratio (AR) to analyze various NPs with primary and regular shapes. Although, it is very rare in practice to synthesize such ideal shaped nanostructures, by plotting SA:V in a function of AR we can get an idea of how those regular shape may influence electrochemical reactivity. Plots presented in Figure 4.9 indicate that nanoplates and nanodiscs are the most preferable shapes of NPs in terms of SA:V value. Along with enhanced anisotropy of NPs, and thus higher AR value (conventionally for AR > 20), nanoplates, nanodiscs and nanorods transform into nanoribbons, nanomembranes and nanowires, respectively.

Nanostructured MO_X NPs with high SA:V and high AR enhance electrochemical performance of printed nanocrystalline films in two different ways. Firstly, in terms of electrochemical reactivity manifested differently depending of the device functionality. Higher values of optical modulation in EC devices are obtained by increased interaction with lithium ions due to the larger interface between

NPs and amorphous coating or NPs and electrolyte. The EC reaction occurs in electrochemically active sites, and so it will be favored as the number of active sites available at the interface increases. High AR of NPs results in high roughness factor of the film defined as the total film area per unit substrate area [78]. Due to high roughness of the film, it is possible to increase the dye and enzyme loading in DSSC and electrocatalytic biosensors, respectively. In DSSC, high SA:V of MO_X nanocrystalline electrode indicates high area exposed to the sensitizer during the dye absorption, and thus higher number of light sensitive active sites. The sensitivity and response time of electrochemical gas sensors is also highly dependent of the SA:V [127]. Moreover, large surface area is beneficial when placing of selective catalytic dopants is concerned.

Secondly, electronically conductive network of elongated nanostructures enhance conductivity of the film thanks to the anisotropic diffusion of electrons, helping the electrochemical reaction to be completed faster (*e.g.* efficient carrier collection in DSSCs, or decreased switching time in EC devices). Additionally, semiconducting electrode formed of elongated nanostructures provides a more direct path, with less trap sites for electron transport to the collection electrode, and thus, reduces electron percolation deficiency [128]. The application of 1D shaped NPs may also introduce an internal electric field to provide additional driving force and enhance electrochemical reaction.

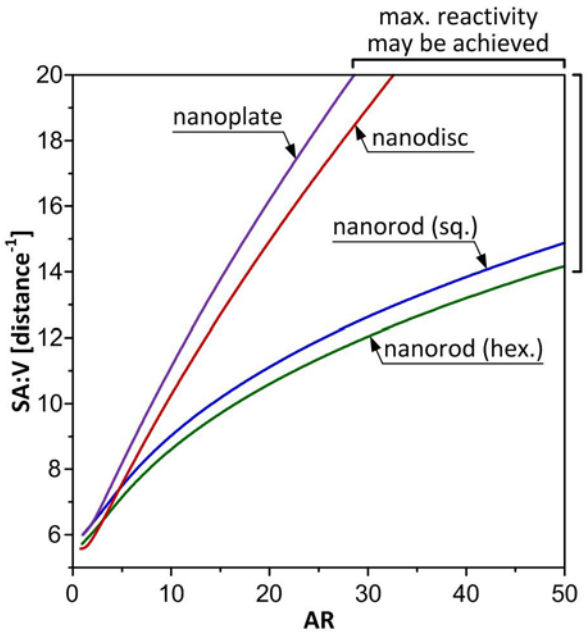

Figure 4.9. Simulation of SA:V as a function of AR for various regular shaped NPs. Variables *a* and *b* were selected according to the simple assumption that the volume of all individual particles is equal.

4.3.1.3.Agglomerates

An unfavorable aspect associated with MO_X NPs from the third regime of size–shape coordinating system is agglomeration which leads to the formation of massive blocks, significantly reducing SA:V.

The relation between SA:V and number of agglomerated particles using a simple agglomeration model presented in Section 4.2.3 are shown in Figure 4.10.

When considering the ideal dispersion of NPs in which agglomeration does not occur, nanoplates and nanodiscs are the most preferable in terms of SA:V value. For agglomerated NPs, high values of SA:V are obtained for agglomerates of nanorods (agglomerates consisting of more than 3 NPs), although their individual specific surface area is not the highest among shapes under consideration. The least favorable seem to be nanocubes in case of which SA:V is small for fine dispersions and significantly drops down with increased number of agglomerated particles. As it is very rare in practice to synthesize not agglomerated NPs, it may be assumed that 1D nanorods are the most desirable products of synthesis as long as their electrochemical application is concerned.

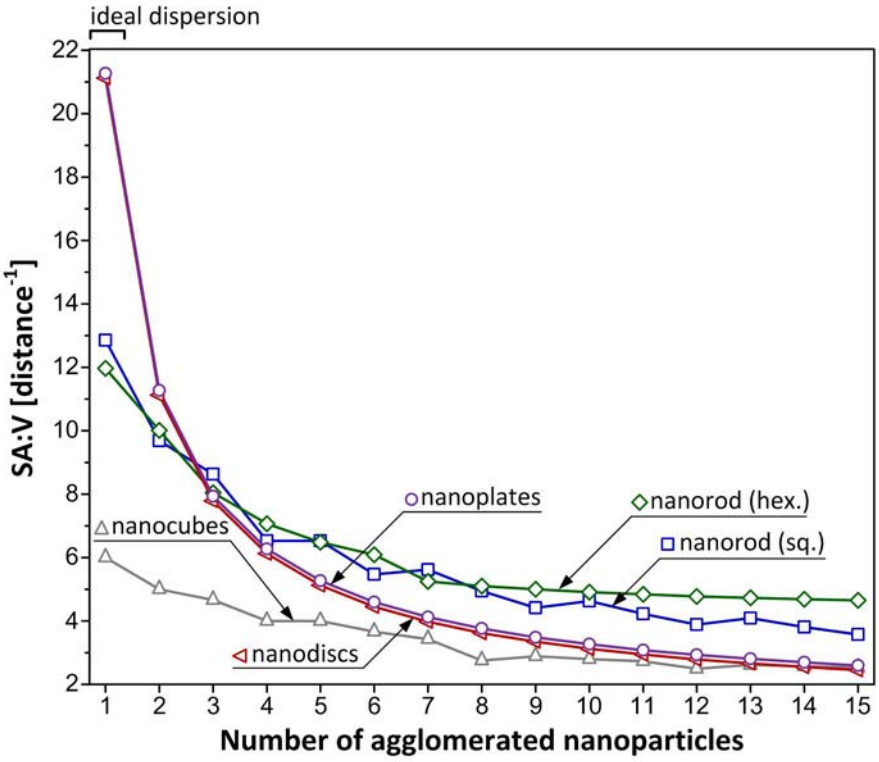

Figure 4.10. Model of agglomeration for various regular shaped NPs; the volume of all individual particles is equal to 1; the term 'ideal dispersion' refers to the situation in which agglomeration does not occur.

In contrast to the agglomerated NPs, hollow and hierarchical nanostructures assembled in a highly periodic and porous manner generally exhibit much higher SA:V [129, 130]. The van der Waals attraction between hierarchical structures is relatively weak due to larger size, which makes them more advantageous in dispersions when comparing to anisotropic NPs. However, the large size of such particles restricts their application in printable dispersions. The synthesis of highly porous, hierarchical MO_X nanostructures with sub-micrometer dimensions, although very promising, is still a challenging issue.

4.3.2. Fluid control of printable dispersions

The development of printable functional MO_X dispersion is strictly reliant on the development of NPs. Thereby, the key issue is to select product with morphology tailored to assure desired physical properties of its dispersion [131]. This section attempts to provide basic recommendations on each major step of printable mixture formulation, and impose critical constraints. The requirements for MO_X NPs loaded mixtures in the area of printed electronics are the following:

a) the dispersion must ensure reliable print under deposition conditions;
b) chemical and physical stability of the dispersion must be provided;
c) printable formulation is not hazardous;
d) printed film must display required functional performance;

In general, printable MO_X dispersions are two phase fluids consisting of a dispersion of NPs in a liquid carrier (aqueous or organic), so-called vehicle. The viscosity of such dispersion varies between 1 and 10^5 cP depending mainly on the vehicle composition, and is tailored for a specific printed technique. However, NPs volume fraction, their shape as well as particle orientation in a fluidic flow, may imply critical consequences on viscosity especially when the Drop-On-Demand (DOD) inkjet printing process is concerned [131]. Typical viscosities of NPs dispersion for basic printing techniques are presented in Figure 4.11.

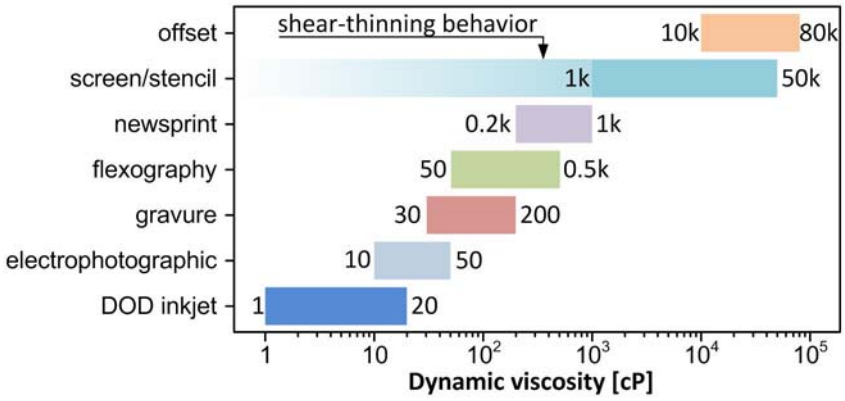

Figure 4.11. Dynamic viscosity values of MO_X NPs dispersions for various printing techniques

The viscosity of the dispersion can be easily increased to the acceptable level without substantially modifying its other properties, by addition of thickening agents. For inorganic solid/liquid mixtures, it can be a low boiling point, viscous and miscible with the vehicle organic solvent or soluble polymer, *e.g.* (for aqueous dispersions) polyethylene glycol (PEG) or polyvinyl alcohol (PVA). However, there is another aspect related to fluid viscoelasticity, which makes NPs loaded fluid control much more complicated [132, 133]. Newtonian character of pure liquid is changing radically with the addition of NPs, due to the increased viscoelasticity of the dispersion [134, 135]. The most drastic consequence may be observed in case of IPT, where the formation of the fluid drops from the nozzle is disrupted

leading to the formation of satellite drops, which deteriorate pattern quality. Non-linear character of the share stress in a function of share rate affects also the droplet behavior on a substrate surface in the moment of impact (deposition, splashing or rebound) and spreading (pattern size) [136]. In R2R processing of creating electronic devices on a flexible substrate, the viscoelasticity of dispersion may significantly limit the printing speed. Therefore, the viscosity of the dispersion should not change with shear stress applied in a broad range of values (10^{-2} – 10^{2} Pa), which means that Newtonian behavior of the fluid is expected [131]. In order to fulfill this requirement, a solid content of the dispersion should be in a relatively low range of 0.01 – 1 wt %. Additionally, an agglomeration phenomenon among NPs is not desirable, especially in case of low viscosity dispersion, in which stability is the main issue. Therefore, a narrow particle size distribution is recommended.

An exception among printing techniques under consideration is screen printing in which shear-thinning behavior (viscosity decrease with applied shear stress) is necessary to transfer the NPs loaded paste through printing mesh.

The surface tension value for typical low viscosity inks is between 30 and 40 mN m^{-1}. In order to adjust this parameter to acceptable range, the nonionic surfactant such as *e.g.* Triton X-100 or Triton X-45 can be added in amount of 0.1 - 0.5 wt%. It is worth mentioning that, the spontaneous movement of NPs toward the ink/air interface may affect the surface tension. However, imposed changes usually do not affect the printing process significantly, as long as proper ink rheology is maintained.

In order to effectively disperse nanomaterial powder in a vehicle, breaking of NPs agglomerates and stabilization by pH modification, additions of surfactants or polymers are required. However, liquid medium complexity may significantly deteriorate electrical performance of final printed films. Therefore, in a perfect situation, NPs are dispersed in a pure water or aqueous alcoholic solution with no other organic additives, which allows for low post-treatment temperature. Moreover, it is crucial that the dispersion components are chemically compatible with the substrate they will be printed on.

Selected or synthesized NPs must comply with important size limitation in order to allow its usage in printing system. The most drastic restrictions are applied in formulation of inkjet printable ink. It can be assumed (with some exceptions *e.g.* nanorods alignment in a microfluidic flow [137, 138]) that the maximum particle size should be at least 50 times smaller than nozzle diameter. If NPs are too large, the nozzle may clog and printing will simply stop. Moreover, larger NPs also increase probability that the dispersion will suffer from particles precipitation and agglomeration, unless the mixture is constantly agitated or special additives are included to the large particles in dispersion.

4.3.3. Design rules outline

Engineering rules presented in Figure 4.12 have been developed as a summary of the previous section existing in this chapter. In order to determine preferable regime for printed electrochemical applications, each alternative was studied until the choice is clear, rational and optimal according to existing knowledge and common practice. By following the diagram one can formulate MO_X NPs loaded printable mixture which assures good printing processability and enhancement in electrochemical performance. Such design rules outline is an approach to proper arrangement of various factors including structural, morphological, electrical and rheological properties while taking into account post-treatment conditions. However, those eleven parameters do not restrict the scope of research in this area. Many other factors may be considered as relevant, depending on the studies complexity.

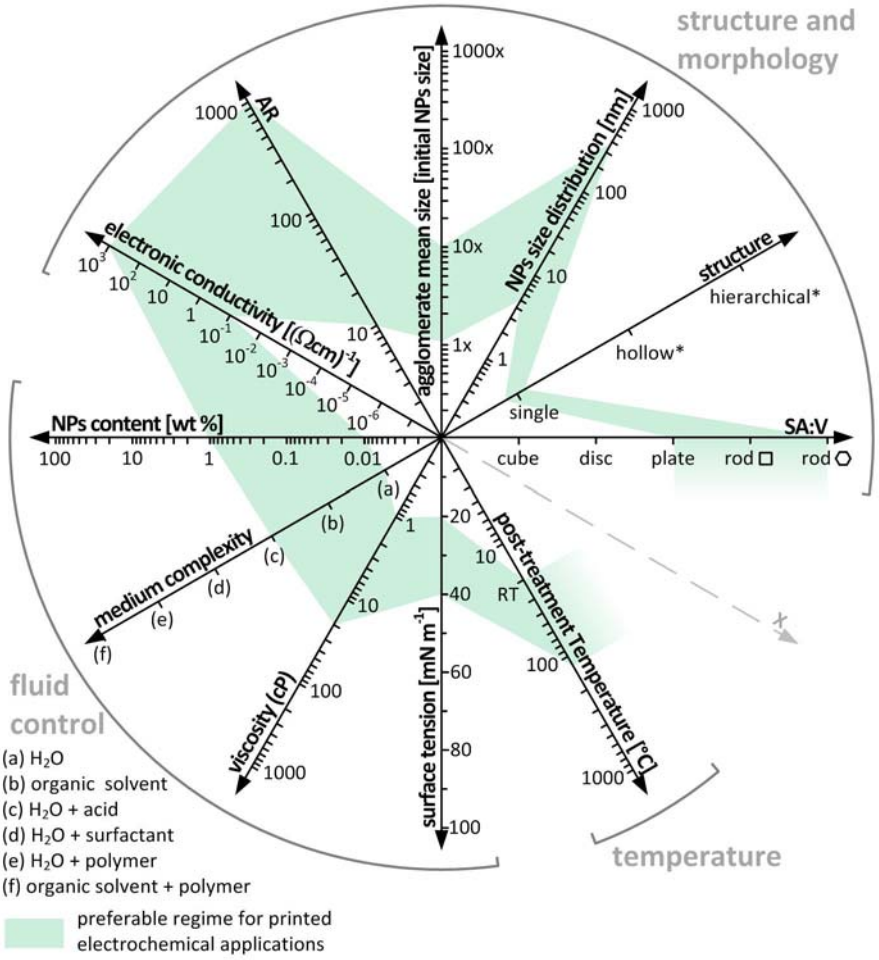

Figure 4.12. The design rules outline for the formulation of MO_X NPs loaded printable dispersions for development of electrochemically active films; preferable regime for electrochemical applications based on inkjet printed inorganic film is indicated

Presented here engineering rules for NPs selection and printable mixture formulation have to a large extent, universal character and may be implemented to create a variety of new inkjet printable

nanostructured MO_X materials for chromic, photovoltaic, photo- and electro catalytic, sensing, power storage and basic electronic devices. It can be also expanded to other printing techniques by establishing appropriate physical and chemical constrains.

4.4. Conclusions

Nowadays, printable films based on MO_X NPs attract growing attention as a convenient and scalable to mass production way of producing electrochemically active thin films. The process has developed as means of depositing light and easily ion-penetrable films from the dispersions on NPs on a variety of substrates, including flexible and heat sensitive materials such as plastic foil (PET, PEN, PI) or paper.

The reasonable theoretical explanation of the dependence between morphology of NPs and electrochemical performance *i.e.* response time and reactivity, have been provided in this chapter. Based on performed modeling, it was deduced that the minimum response time can be achieved when small (several nanometers) NPs are incorporated to the printed film. On the other hand, the electrochemical reactivity can be enhanced by selection of NPs with high aspect ratio and thus high specific surface area. We have also considered agglomeration phenomenon which causes lowering of electrochemical performance. Basic simulations have shown that an effective way to limit the deterioration of material properties *via* agglomeration is to select 1D morphologies such as nanowires and nanorods.

This chapter contains also basic rules governing selection or development of a variety of nanostructured MO_X based materials for inkjet printed electrochemical applications. Proposed engineering rules can be expanded to other printing techniques by establishing appropriate physical and chemical constraints. The versatility of this outline makes it a useful guide not only in the selection of MO_X NPs for high performance applications but also meets the challenges encountered when using those materials in a printing process. This outline was applied in development of films containing synthesized WO_X NPs, which is the subject of the Chapter 5.

Chapter 5

Tungsten oxide nanoparticles for inkjet printed electrochromic devices

This chapter is written based on:

Wojcik, P.J., Santos, L., Pereira, L., Martins, R., Fortunato, E.: Tungsten Oxide Nanoparticle Engineering for Inkjet Printed Electrochromic Devices **– under submission.**

Wojcik, P.J., Santos, L., Pereira, L., Martins, R., Fortunato, E.: Formation mechanism and electrochromic response of WO_X nanoparticles synthesized *via* hydrothermal process **– under preparation.**

Contributions of Co-Authors:

L. Santos performed syntheses of nanopowder, film deposition and characterization, delivering raw data for analysis.

L. Pereira performed SEM characterization.

Chapter 5. Tungsten oxide nanoparticles for inkjet printed electrochromic devices

Chapter 5. Tungsten oxide nanoparticles for inkjet printed electrochromic devices

Summary

Engineering procedures governing the development of inkjet printable nanostructured MO_X NPs for electrochemical applications were established in previous chapter. In the present chapter, proposed scheme was applied to synthesize WO_X NPs in a hydrothermal process and formulate inkjet printable inks. Consequently, nanostructured tungsten oxide particles in monoclinic (*m*-WO_3) and orthorhombic hydrate (*ortho*-$WO_3 \cdot 0.33H_2O$) polymorphic phases were successfully synthesized from pure or acidified aqueous sol-gel precursor. The structure and morphology of nanoparticles were tailored to assure their desired performance and printability. The effect of various reaction parameters on nanoparticles properties leading to variations in electrochromic performance of dual-phase films is the main topic of the discussion.

The results presented in this chapter concern three aspects of NPs engineering. Firstly, a mechanism of nanostructured WO_X NPs growth under hydrothermal conditions is proposed. Secondly, the printability of synthesized product is discussed in terms of its structure and morphology. Finally, this chapter is completed with discussion on electrochromic performance of dual-phase films loaded with *m*-WO_3 and *ortho*-$WO_3 \cdot 0.33H_2O$ NPs.

5.1. Introduction

5.1.1. Tungsten oxide nanoparticles for electrochromic application

Nanostructured WO_X and its hydrates ($WO_X \cdot aH_2O$, $a \in \{1, 1/3, 2\}$) are an important class of materials due to their electrochromic [75, 76], photochromic [77], photochemical [80], energy storage [84] and sensing [88–90] properties. Many different approaches have been implemented in order to develop these material using physical vapor deposition (PVD) and wet chemical methods [64]. In recent years, there has been an increasing interest in developing solution-based methods as they offer better control of material morphology while being much less expensive in implementation. From the vast number of existing wet chemical synthesis routes, hydrolysis, condensation, etching and oxidation are the four most relevant [64]. Products of these syntheses which form WO_X polymorphs such as monoclinic [139], orthorhombic [95], cubic [140] and hexagonal [141, 142] have been reported to exist in various morphological structures depending on precursor composition and process parameters. The main activity in this field has been focused on the structure and morphology control, in order to increase their performance in technological applications. The impact of crystallographic structure and morphology of WO_X NPs on electrochromic performance has been identified as relevant due to the significant improvement in charge density, coloration efficiency and switching time compared to their

amorphous and crystalline counterparts [143]. Size reduction in nanoscale regime also improves chemical, physical, optical and electrical properties due to their large surface area, strong surface adsorption and enhanced band gap.

Among all wet chemical syntheses, hydrothermal treatment seems to be the most facile, cost-effective and well-studied technique, which additionally offers flexibility in possible nanomorphologies. In most studies, precursor for nanostructured WO_X hydrothermal synthesis contain peroxopolytungstic acid (PTA) [144, 145], tungstic acid (H_2WO_4) [146], sodium tungstate (Na_2WO_4) [88, 140, 147], ammonium metatungstate ($(NH_4)_6H_2W_{12}O_{40}$) [80, 142] or tungsten hexachloride (WCl_6) [89, 90] as a source of tungsten dissolved in aqueous solution, often accompanied by structure directing agent (mainly sulphate based). The acidity of the precursor, and hence the H^+ ions concentration value, was also found to affect crystal WO_X growth during hydrothermal synthesis [76]. Selected precursor is then subjected to hydrothermal conditions, which by definition imply elevated temperature (typically ranging from 120 up to 200 °C) and high vapor pressure (between 0.21 and 1.73 MPa, respectively) for a certain period of time enabling nucleation and growth of crystallites. Besides conventional hydrothermal synthesis in Teflon-lined stainless-steal autoclave, a microwave-assisted variant exists [141].

Hydrothermal synthesis of water soluble PTA precursor has been reported to result in NPs of various shapes, varying from flat plates and long rods to round or cubic blocs [144]. It has been proved that process parameters, such as pH value, and residual metal ions have great effect in the crystal size, crystallinity and crystal structure of the obtained product, while the temperature (100 - 200 °C) and precursor concentration are of secondary importance [95, 140]. Although the hydrothermal synthesis of WO_X NPs has been widely reported, to the best knowledge of the author, no attempt has been made to deposit those products in a form of printable dispersion *via* IPT.

Likewise, PTA solutions are the most widely used precursors in WO_3 sol-gel film deposition due to their low cost and relatively high stability in an ambient environment. Deposition methods based on sol-gel (PTA) processed electrochromic WO_X such as dip-coating [50], spin-coating [10], electrodeposition [53, 54] and IPT (see Chapters 2 and 3) offer several advantages over conventional vacuum processed techniques. However, particular attention should be paid to the composition of precursor and processing conditions to get desired microstructure, which would guarantee good performance of electrochromic films.

Taking under account existing state-of-the-art and own observations presented in Chapters 2 and 3, it is expected that the incorporation of WO_X NPs synthesized in external process into the amorphous matrix of the same metal oxide, would provide better control of film microstructure and morphology, reflected in enhanced electrochromic performance. Accordingly, in this chapter, a facile synthesis of WO_X NPs based on sol-gel precursor with controlled morphology evolution and phase transition

under hydrothermal conditions is reported. The structure and morphology of obtained NPs were engineered for their application in IPT and applied in electrochromic device development. The effect of various reaction parameters on crystalline structure, morphology, size, shape, uniformity and agglomeration of NPs leading to variations in electrochromic performance is also described.

5.1.2. Process description

The strategy selected in this study is based on correlation of the NPs synthesis parameters with further technological steps for ink formulation, film deposition, post-treatment and resulting film performance, as it is schematically presented in Figure 5.1. In order to enhance electrochromic performance and ensure processability, the criteria for NPs structure and morphology described in Chapter 4 are going to be applied in following sections.

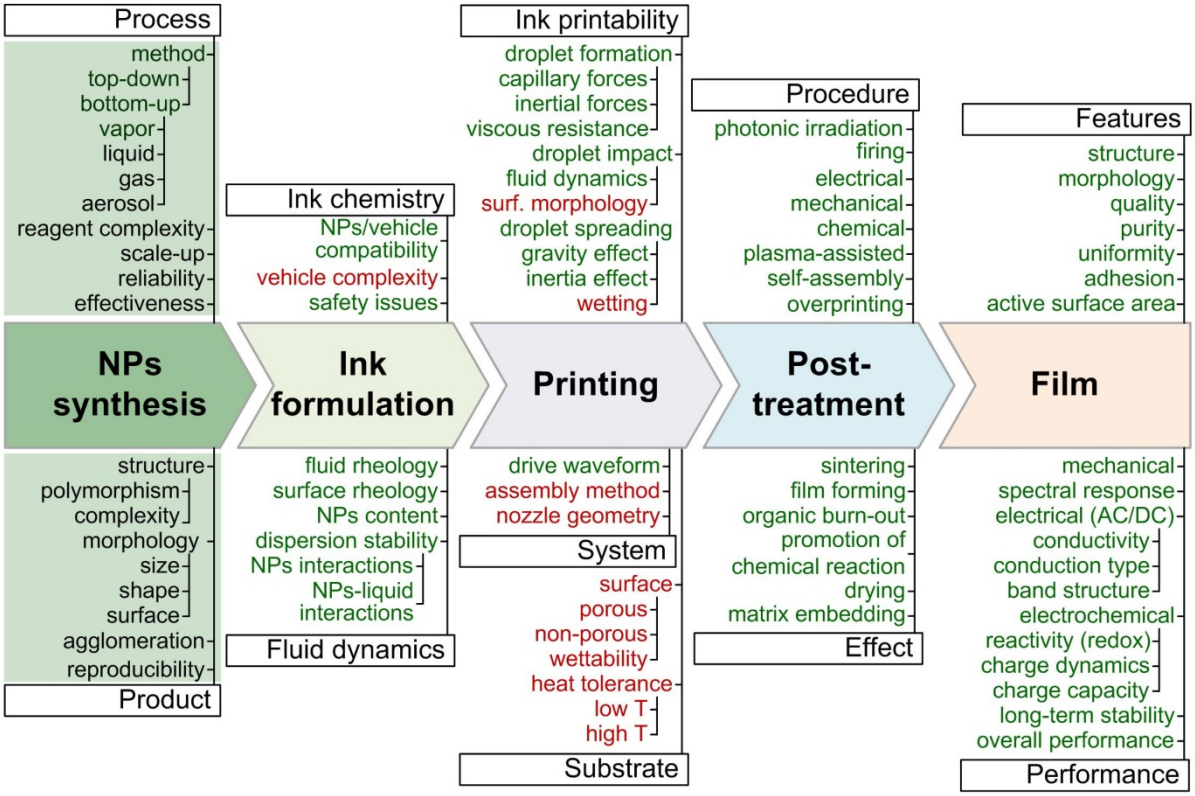

Figure 5.1. Simplified NPs process flow diagram for printed electrochemically active films; factors closely associated with NPs properties were colored in green

To make genuine progress in development of inkjet printed electrochemical devices, it is absolutely necessary to take the time to study the problem for which an engineering solution is desired in as broad an interdisciplinary context as the problem requires. In order to define a strategy for NPs based printed devices, let's consider such system to be designed as a field of requirements and characteristics of electrochemically active material. Studies presented in Chapters 2 and 3 have shown that inorganic nanocrystalline content strongly influence the final performance of inkjet printed

electrochromic film, underlying the demand to understand the role of the NPs properties, at all stages of their development and processing. This means understanding and describing the desired nanomaterial performance, as well as its technological and environmental requirements related to this topic.

5.2. Materials and methods

5.2.1. Synthesis of WO_X sol-gel precursor

Peroxopolytungstic acid (PTA) was synthesized based on the procedure reported by Tetsuichi Kudo *et al.* [43]. The tungsten metal monocrystalline powder (99.9 %, 0.6-1μm, Aldrich) was carefully added to 50 ml mixture (50:50) of distilled water (Millipore) and hydrogen peroxide (30 %, Sigma-Aldrich). The cooling was employed and the solution was kept slowly stirring in a refrigerator to prevent thermal changes due to the strong exothermic nature of reaction. The excess of tungsten powder was then removed by filtration (0.45 μm syringe filter, Roth) leading to a transparent solution. In order to remove the excess of the hydrogen peroxide, the solution was dried at 65 ºC and washed several times with distilled water. After drying, a water soluble $WO_3 \cdot aH_2O_2 \cdot bH_2O$ orange crystal powder was obtained as final WO_X precursor. The process was optimized to provide high quality of the product and to assure its repeatability by implementation of a very detailed protocol. Additionally in order to unify the input material for an ink formulation, products of many syntheses were mixed and grinded together. As the PTA crystals are known for their instability, the final product was stored at low temperature (-18 °C).

5.2.2. Hydrothermal synthesis of WO_X NPs

For the hydrothermal synthesis, 0.4 g of previously synthesized PTA was dissolved in HCl (37%, Merck) aqueous solution. The final solution was transferred to 23 ml PTFE chamber, set inside a stainless steel autoclave (4745 general purpose vessel, Parr) and installed in the oven (L3/11/B170, Nabertherm) at 180 °C. Approximate value of pressure inside the autoclave during the hydrothermal synthesis is ~1.1 MPa (see Section 5.5.1 for more details on hydrothermal conditions). The HCl concentration (0 M, 0.3 M and 3 M) and the reaction time (2 h, 4 h and 6 h) were selected for each experiment according to determined processes parameters. The product of synthesis was collected by centrifugation at 3000 rpm for 2 min (F140, Focus instruments) and washed three times with water.

5.2.3. Ink formulation

The fabrication of dual-phase *a*-WO_3/WO_X films were performed in two separate depositions. Firstly, nanostructured WO_X was used in a form of aqueous (Millipore) alcohol (ethanol 96%, Aga) dispersions in a fixed proportion of 1:1 with a solid content of 0.03 wt%, followed by ultrasonic treatment (UP400S, Hielscher, see Section 5.5.3 for detailed procedure description) and filtering (Roth, 0.45 μm syringe filter). The inks composition results in the viscosity and the surface tension values of 1.5 – 1.75 cP and 20 - 40 mN m^{-1}, respectively, acceptable for conventional office printer. Individual layers (1 cm^2) were repeatedly printed (20-80 passes) using conventional desktop printer (Canon PIXMA IP4850, see Section 1.4.3.1 for detailed printing system description) in regular intervals of around 1 min while being exposed to a relative humidity of 50 %, at 28 ºC on ITO PET substrates (Sigma-Aldrich, 1000 Å of ITO, 60 Ω/sq, T > 75 % at 550 nm, see Section 5.5.2 for more details concerning substrate preparation). Variable numbers of passes depending on the solid content nature were adjusted separately in order to obtain uniform coverage. All films were dried at room temperature for several hours. Secondly, 0.16 g of PTA was dissolved in 0.92 g of water and 0.92 g of alcohol (ethanol 96%, Aga). The solution was stirred for 15 minutes, 150 rpm at 60 °C and filtered (Roth, 0.45 μm syringe filter). Individual layers (1 cm^2) were printed only once under equal environmental conditions on top of the previously deposited NPs. All films were dried at room temperature for 24 h and annealed in air at 120 °C (EHRET, TK4067, Germany) for 1 h.

5.2.4. Film forming

The fabrication of inkjet printed EC films were performed *via* two separate depositions, according to the diagram presented in Figure 5.2. Firstly, printable WO_X dispersion was deposited on the substrate and dried. Secondly, such nanocrystalline film was coated with printable sol, containing precursor of WO_3, resulting in dual phase *a*-WO_3/WO_X film. Depending of the NPs incorporated to the dispersion in the first deposition step, dual-phase *a*-WO_3/*m*-WO_3, *a*-WO_3/*ortho*-$WO_3 \cdot 0.33H_2O$ or *a*-WO_3/(*m*-WO_3 + *ortho*-$WO_3 \cdot 0.33H_2O$) compositions were obtained. The existence of amorphous phase (*a*-WO_3) in each film under investigation provides compact mechanical structure of the film and guarantees EC effect, by allowing electronic conduction to take place in the structure processed at low temperature. The use of PTA as the precursor for NPs synthesis and *a*-WO_3 coating show convergence of the technologies.

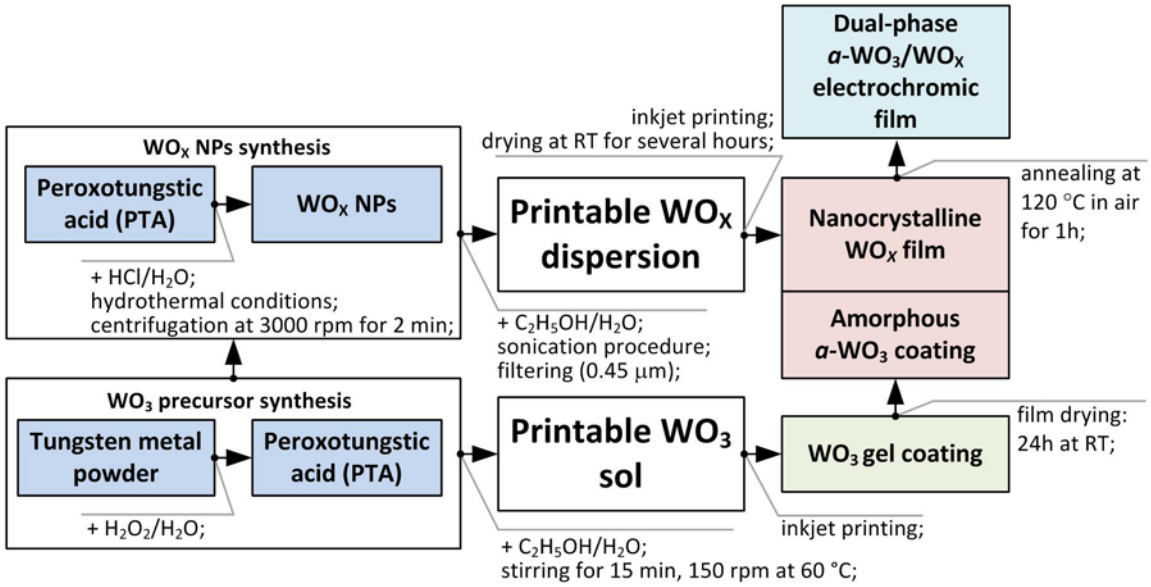

Figure 5.2. Dual-phase *a*-WO_3/WO_X electrochromic film in a) a schematic diagram representing the elements of the studied material system with corresponding technological steps

A uniform coverage of nanocrystals by amorphous coating was confirmed by SEM micrograph presented in Figure 5.3 in which nanorods are randomly dispersed in a single level pattern embedded in continuous amorphous film.

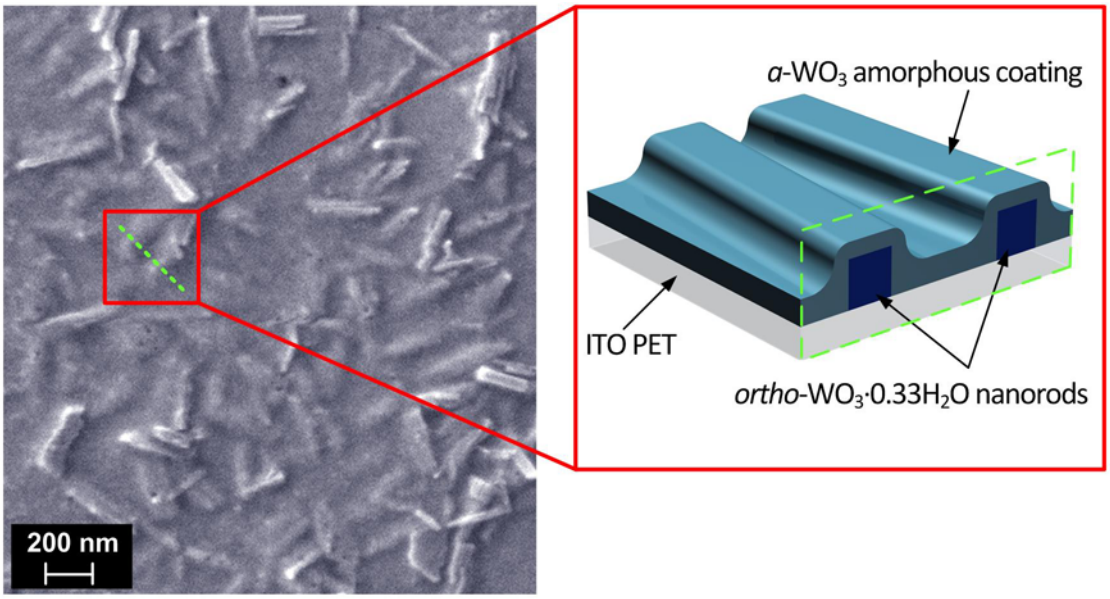

Figure 5.3. SEM image of *a*-WO_3/*ortho*-$WO_3 \cdot 0.33H_2O$ on ITO PET substrate (inset: schematic representation)

5.2.5. Characterization

The morphological and structural characterization of WO_X NPs was performed by SEM (Auriga SEM-FIB, Zeiss) and XRD (XPert PRO, PANalytical). Supplementary structural characterization of WO_X NPs was performed by FT-IR (Nicolet 6700, Thermo Electron Corporation).

Thermal analysis of NPs was performed by Thermogravimetric Analyzer (STA 449 F3 Jupiter, Netzsch) in air with a heating ramp of 5 °C/min starting from RT up to 600 °C.

Intrinsic viscosity of an ink vehicle and genuine CANON inks was measured by glass capillary viscometer (CANNON-UBBELOHDE, 9721-K53 CUC Series). Surface tension was measured with glass stalagmometer (Rohr A, NEUBERT-GLAS).

Optical measurements of printed dual-phase films were performed *in-situ* using a spectrometer setup consist of HR4000 High-Resolution Spectrometer (Ocean Optics), Halogen Light Source HL-2000-FHSA (Mikropack) in range of 450-850 nm. The electrochemical cell consisting of working electrode (dual-phase EC film) and platinum wire used as counter electrode was filled with lithium based gel electrolyte prepared according to the recipe described elsewhere [47]. Resulting cell was driven by High Current Source Measure Unit (KEITHLEY 238) in order to induce electrochromic action in square wave (±2 V, 30 s per pulse) and linear stair pulse (from -2 V up to 2 V in a 0.5 V step, -2 V of bias, 30 s per pulse) modes. Spectra were recorded in reference to the uncoated substrate under equal conditions.

Electrochemical measurements were performed using Gamry Reference 600 Potentiostat (Gamry Instruments) in two-electrode configuration setup (see Section 5.5.4 for detailed system description).

5.2.6. 3D modeling of NPs

Method for 3D modeling of NPs presented in this section was developed by the author of this thesis. Presented solution was used to develop a mathematical representation of synthesized nanocrystals, revealing crystallographic orientations of surface planes, and their evolution during the synthesis. The process of transforming XRD spectra into 3D object shown in Figure 5.4, involves application of specific software such as CrystalMaker® and CrystalDiffract® (CrystalMaker Software Ltd., version 2.3.0), X'Pert HighScore Plus (PANalytical B.V., version 2.2.5) and KrystalShaper (©JCrystalSoft, version 1.3.1).

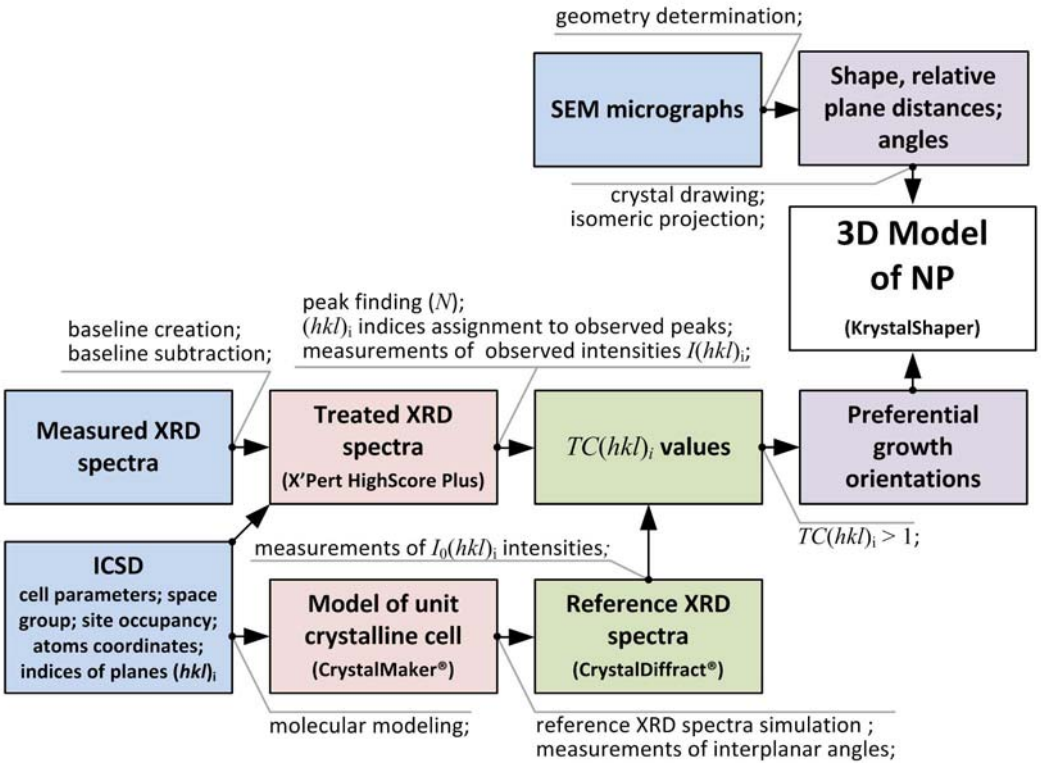

Figure 5.4. Schematic diagram of 3D NP modeling process based on information obtained from the analysis of preferential growth and SEM observations

Quantitative information concerning the preferential crystalline orientation (see Figure 5.5) was obtained on a basis of texture coefficient denoted as $TC(hkl)_{\mathrm{i}}$ and expressed by Equation 5.1 [148].

$$TC(hkl)_{\mathrm{i}} = \frac{\frac{I(hkl)_{\mathrm{i}}}{I_0(hkl)_{\mathrm{i}}}}{\frac{1}{N}\sum_{\mathrm{n}}\frac{I(hkl)_{\mathrm{n}}}{I_0(hkl)_{\mathrm{n}}}} \tag{5.1}$$

where: $I(hkl)_{\mathrm{i}}$ is the observed intensity of $(hkl)_{\mathrm{i}}$ plane, $I_0(hkl)_{\mathrm{i}}$ is the intensity of $(hkl)_{\mathrm{i}}$ reflection of a polycrystalline sample, *N* is the total number of reflections taken into account, and (hkl) denotes the Miller indices of the lattice planes of a given signal.

By using Equation 5.1, the preferential orientation of the facets can be reviled. The $TC(hkl)_{\mathrm{i}}$ values of facets of *m*-WO_3 and *ortho*-$WO_3 \cdot 0.33H_2O$ NPs synthesized under all conditions are presented in Figure 5.5. The $TC(hkl)_{\mathrm{i}}$ values larger than 1 indicate a preferred orientation of the crystals/grains in the samples. The $TC(hkl)_{\mathrm{i}}$ is expected to be unity for facets which does not have preferential orientation. If $TC(hkl)_{\mathrm{i}}$ is higher than unity, it is a preferentially grown facet.

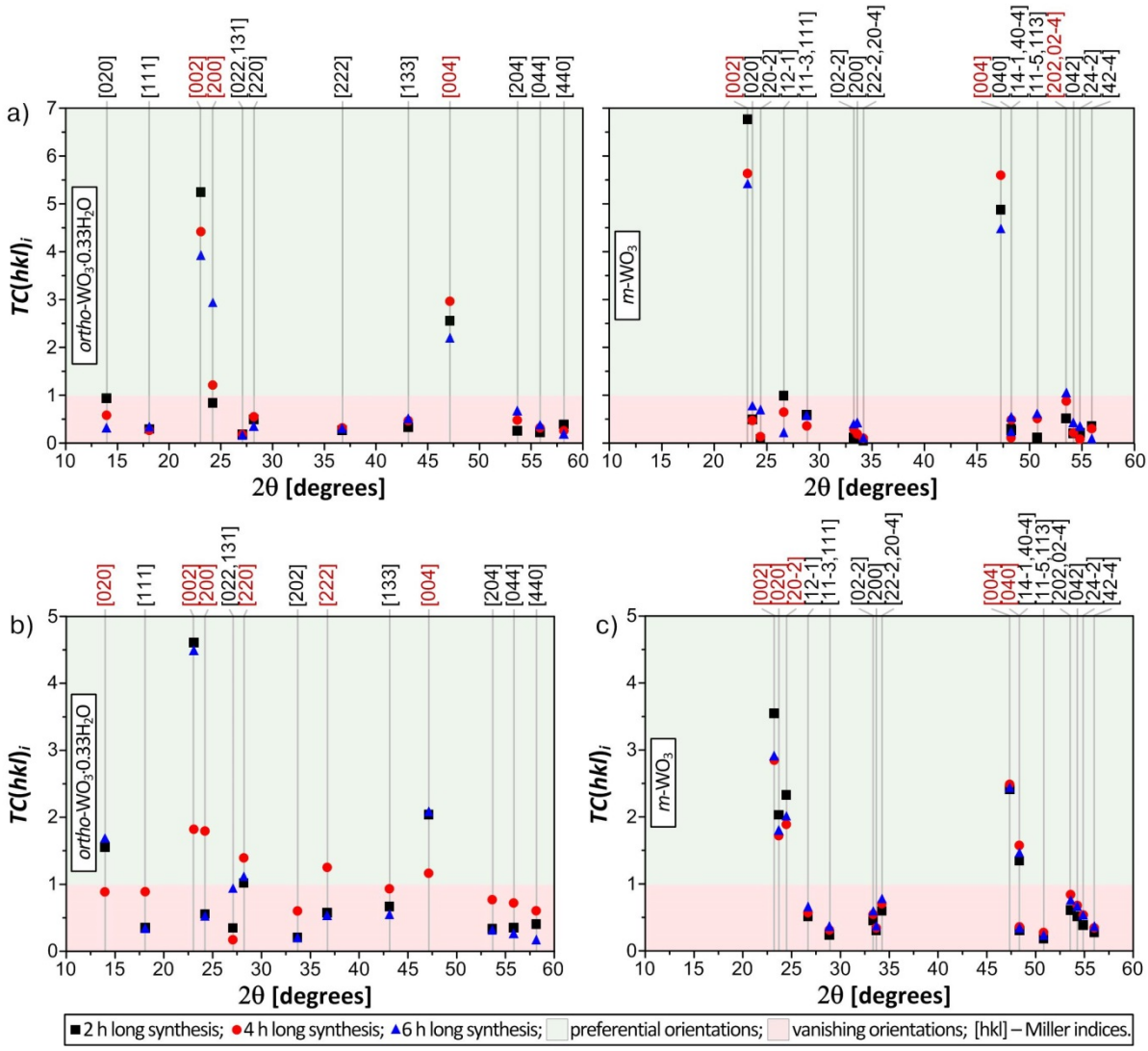

Figure 5.5. Texture coefficient spectra calculated for nanopowders obtained *via* hydrothermal syntheses performed from a) non-acetified precursor, precursor dissolved in a) 0.3 M HCl and b) 3 M HCl solution after 2 h, 4 h and 6 h; Miller indices of preferential orientations were highlighted by red color

An important input for 3D modeling of NPs concerning shape, relative plane distances and estimation of interplanar angles were obtained from SEM micrographs as it is presented in example shown in Figure 5.6.

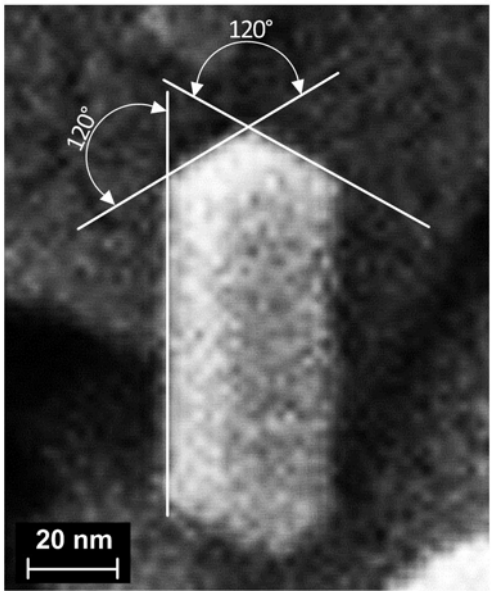

Figure 5.6. SEM image of a single *ortho*-$WO_3 \cdot 0.33H_2O$ NP obtained *via* hydrothermal synthesis performed from precursor dissolved in 0.3 M HCl after 6 h; white lines were drawn along the edges of the surfaces in order to estimate values of interplanar angles

5.3. Results and Discussion

5.3.1. Mechanism of nanoparticle growth

PTA based aqueous precursors contain various species which can be generally described as anions without peroxo substitutions $[X1(O)_mX2]^{k-}$ and peroxo $[X1(O_2)_mX2]^{k-}$ complexes, where the subunit *X1* contains W^{VI} ions complexed by chelating $[O]^{2-}$ or $[O_2]^{2-}$ ligands, while *X2* is denoted as water molecules which occur in hydrated form of complexes. Among these species, monomeric tungstate anion WO_4^{2-}, monomeric peroxo anion $[W(O_2)_4]^{2-}$, dimeric peroxo anion $[W_2O_3(O_2)_4(H_2O)_2]^{2-}$, tetraperoxotetratungstate anion $[W_4(O_9)(O_2)_4(H_2O)_2]^{2-}$ and higher-order peroxo anions such as $[W_7O_{23}(O_2)]^{6-}$ and $[W_7O_{22}(O_2)]^{6-}$ were identified as the most evident [45, 46, 149, 150]. The concentrations of individual peroxotungstate species depend of the pH value leading to formation of ions with different W to $[O_2]^{2-}$ ratio. Moreover, at lower pH the chemical union of homogenous ions becomes possible as it is shown in example described by chemical reaction in Equation 5.2.

$$2[W(O_2)_4]^{2-} + 2H^+ + 5H_2O \rightarrow [W_2O_3(O_2)_4(H_2O)_2]^{2-} + 4H_2O + 2O_2 \uparrow \qquad (5.2)$$

The complexing behavior of peroxo ligands prevents condensation, however all peroxo tungsten compounds are considered as unstable. The degree of instability decreases by lowering the pH as the number of $[O_2]^{2-}$ ligands per each W atom (*n*) is decreasing.

Accordingly, a new growth mechanism is proposed here, in which creation of nanostructured WO_X NPs at aqueous PTA precursor can be described by following reactions (Equations 5.3, 5.4 and 5.5):

$$WO_X \cdot aH_2O_2 \cdot bH_2O + H_2O \xrightarrow{pH,RT} [X1(O)_mX2]^{k-} + [X1(O_2)_nX2]^{k-} + H_20 + O_2 \uparrow \quad (5.3)$$

$$\begin{cases} [X1(O)_mX2]^{k-} \\ [X1(O_2)_nX2]^{k-} \end{cases} + H_20 \xrightarrow{H_2O,180^oC} WO_X^{(nucleus)} + WO_X \cdot H_2O^{(nucleus)} + H_2O + O_2 \uparrow \quad (5.4)$$

$$\begin{cases} WO_X \cdot H_2O^{(nucleus)} \\ WO_X^{(nucleus)} \end{cases} \xrightarrow{H_2O,180^oC} \begin{cases} WO_X \cdot H_2O^{(nP)} \\ WO_X^{(nP)} \end{cases} \downarrow \quad (5.5)$$

According to the reaction Equation 5.3, various $[X1(O)_mX2]^{k-}$ and $[X1(O_2)_nX2]^{k-}$ anions appear simultaneously during PTA reaction with water at certain pH [150]. This explains coexistence of hydrated and anhydrous phase synthesized from non-acetified precursor. By dissolving PTA in 0.3 M or 3 M HCl, and hence lowering the pH, particular kind of peroxo anions is highly predominant. The lower the pH, the more uniform peroxo anions are formed as their stability is enhanced by decreased number of $[O_2]^{2-}$ ligands per each W atom leading to sequential creation of tatra-, tri-, di- and mono-peroxo complexes. When the reaction temperature exceeds decomposition temperature of precursor at a given pressure, the nucleation process begins according to Equation 5.4, as the sufficient energy is provided by hydrothermal system. The energy required to form a nucleus is strongly dependent on surface energy and the supersaturation. The nucleation rate, in turn, increases strongly with decreasing surface energy and increasing supersaturation [151]. All existing peroxo complexes undergo condensation and their contribution to the final product depends of their stability and initial amount as supersaturation is the driving force for nucleus formation. Complex peroxo ions with high number of $[O_2]^{2-}$ ligands per each W atom condensate into *ortho*-$WO_3 \cdot 0.33H_2O$ nuclei phase, while mono-peroxo complexes condensate into *m*-WO_3 nuclei. Subsequently, under hydrothermal conditions the nuclei combines into particles in order to minimize their energy as shown in Equation 5.5. A slow subsequent growth starts when the supersaturation drops down to low level. Crystalline solids are then precipitated from the precursor solution under hydrothermal conditions and the crystallinity of the product is a direct consequence of acidity. Over reaction time, the structure of unprivileged phase, if one exists, tends to break and transform to majority phase as it was described in structural analysis for non-acetified precursor.

Hydrothermal synthesis performed from PTA precursor solutions at various pH results in formation nanorods (1D) and rectangular nanoslabs (2D) identified by XRD analysis as *ortho*-$WO_3 \cdot 0.33H_2O$ and *m*-WO_3 tungsten oxide polymorphs, respectively. The crystal nucleus growth in 1D and 2D is due to the varied growth rates of each crystal facet cause by their atomic densities, according to Bravais law.

The nanostructured product obtained in the present study differs from the ones presented by other authors [144] in terms of morphology evolution. By analyzing these reports, the main difference was identified in PTA precursor preparation in which H_2O_2 content (expressed by number *x* in empirical formula $WO_3 \cdot xH_2O_2 \cdot yH_2O$ of PTA) depends of the applied evaporation procedure (hot plate, N_2

bubbling or rotary evaporation) in precursor synthesis [45, 46]. Slow evaporation of the solvent after metallic tungsten etching by aqueous hydrogen peroxide results in a white crystalline powder, while accelerated evaporation under air extraction and elevated temperature (65º C) results in transparent yellow crystals. In order to remove the excess of hydrogen peroxide, in the present studies the solution was repeatedly washed with distilled water and dried at 65º C, till deep yellow and transparent crystals occurs. Such PTA gives pale yellow liquid when dissolved in water. The variable amount of cheating peroxo groups $[O_2]^{2-}$ affects morphological evolution during hydrothermal synthesis, therefore obtaining reproducible products in different laboratories is difficult. Similar conclusion was also formulated by Zhou *et al.* while studding influence of H_2O_2 addition to precursor in hydrothermal synthesis [95]. Moreover, when the solubility of metal oxide precursor increases, the supersaturation decreases, thus the precursor properties have a strong influence on the nucleation rate [151]. The commercialization of PTA with consistent performance further optimized for electrochromic application could be a reasonable solution, particularly appreciated by industrial users. In fact, widespread availability of certified precursors is vital for the further commercialization of nanostructured WO_X based electrochemical devices.

5.3.2. Structure and morphology

There are only few studies reported in literature wherein the effect of various reaction parameters on crystalline structure and morphology of NPs leading to variations in electrochromic performance have been described [75, 76]. Figure 5.7 shows the XRD patterns of the as-synthesized WO_X nanopowders prepared at various acidities and reaction time with corresponding Inorganic Crystal Structure Database (ICSD) references. The products of syntheses performed from non-acetified precursor solution indicate the coexistence of two WO_X polymorphs, namely monoclinic (*m*-WO_3) and orthorhombic tungsten oxide hydrate (*ortho*-$WO_3 \cdot 0.33H_2O$).

Lowering acidity of precursor by dissolving PTA in 0.3 M HCl and 3 M HCl causes phase unification to *ortho*-$WO_3 \cdot 0.33H_2O$ and *m*-WO_3, respectively. The enhancement in lithium ion diffusion rate, and hence shorter electrochemical response is expected for films containing orthorhombic hydrate (*ortho*-$WO_3 \cdot 0.33H_2O$) NPs due to the higher electronic conductivity of this phase when comparing to monoclinic (*m*-WO_3) nanocrystals [108]. Therefore, the product of synthesis from PTA dissolved in 0.3 M HCl seems to be the most desirable, as long as the crystallinity is concerned.

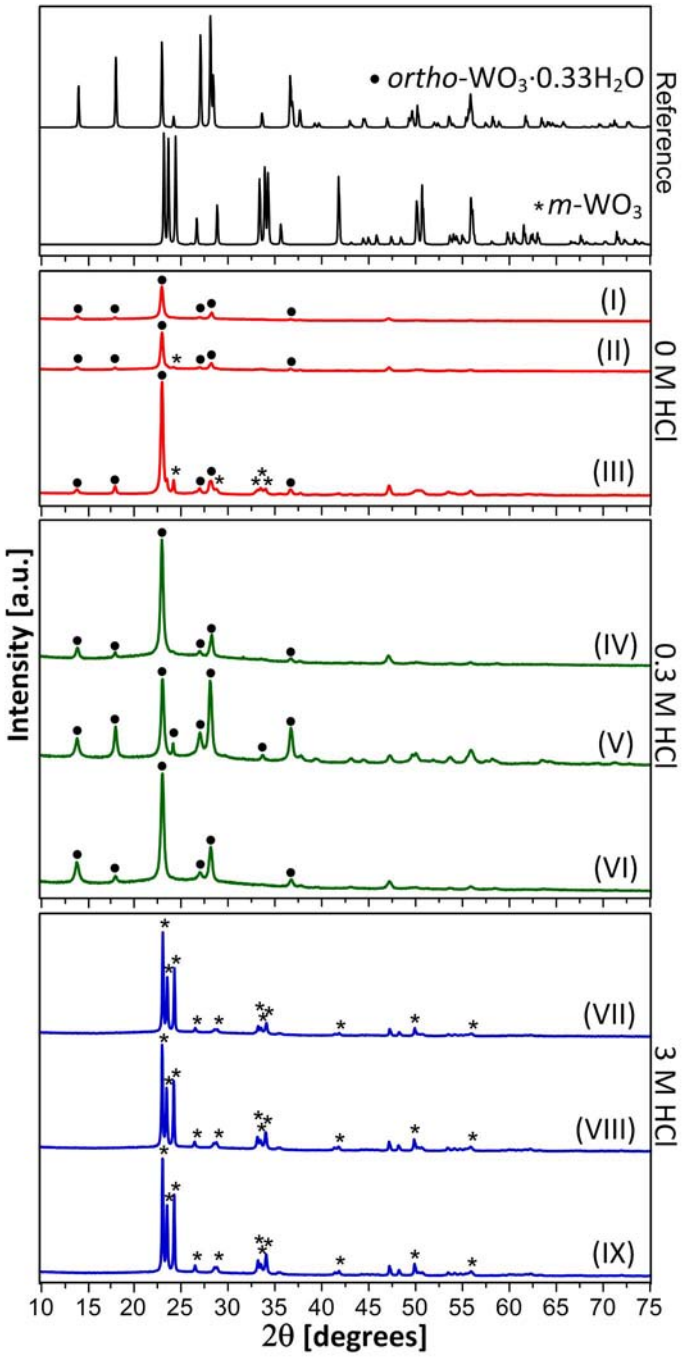

Figure 5.7. XRD difractograms of nanopowders obtained *via* hydrothermal syntheses performed from (I) non-acetified precursor solution after 2 h, (II) 4 h and (III) 6 h; (IV) precursor dissolved in 0.3 M HCl after 2 h, (V) 4 h and (VI) 6 h; (VII) precursor dissolved in 3 M HCl after 2 h, (VIII) 4 h and (IX) 6 h; reference spectra for *ortho*-$WO_3 \cdot 0.33H_2O$ (ICSD: 98-003-7822) and *m*-WO_3 (ICSD: 98-009-1587) have been placed above;

Transmittance spectra recorded by FT-IR (see Figure 5.8) were studied in order to identify coordinated water molecules in $WO_5(H_2O)$ octahedron and vibrations in WO_6 octahedron in accordance to the state of the art [152]. The broad absorption band at 3470 cm^{-1} (-OH stretching) and sharp band at 1610 cm^{-1} (-OH in plane bending) have been observed in the powder synthesized from

non-acetified precursor and precursor dissolved in 0.3 M HCl indicating high amount of water molecules in the powder. No indicators of water have been detected in the powder synthesized from the precursor dissolved in 3 M HCl revealing its anhydrous nature. The same samples exhibit also strong absorption band at 970 cm^{-1} and 1000 cm^{-1} corresponding to the W-O stretching in WO_6 octahedron. The broad band between 640 cm^{-1} and 955 cm^{-1} observed in all analyzed samples has been assigned to the W-O-W triplet stretching.

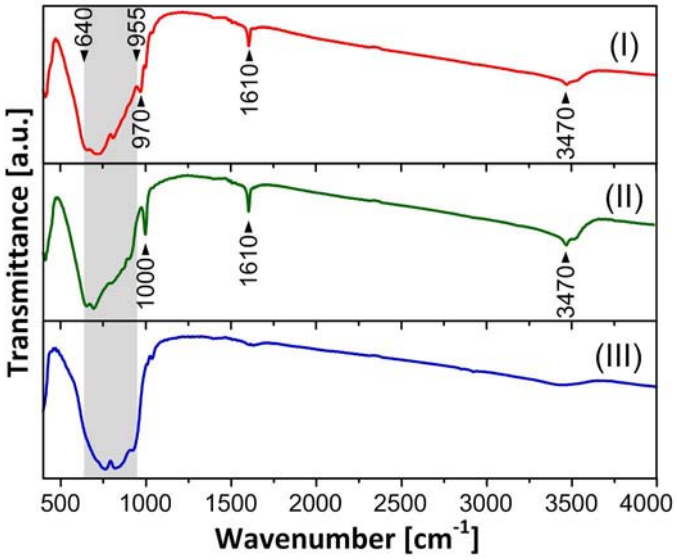

Figure 5.8. FTIR transmittance spectra of nanostructured products obtained from (I) non-acetified precursor solution, (II) precursor dissolved in 0.3 M HCl and (III) precursor dissolved in 3 M HCl after 6 h of hydrothermal synthesis.

The TG spectra presented in Figure 5.9a show distinct responses to increasing temperature in air atmosphere. The total weight loss observed up to 600 °C for NPs produced from non-acetified 0.3 M HCl and 3 M HCl precursor was 2.37 wt% (*m*-WO_3/*ortho*-$WO_3 \cdot 0.33H_2O$), 4.1 wt% (*ortho*-$WO_3 \cdot 0.33H_2O$) and 0.5 wt% (*m*-WO_3), respectively. The weight loss of *ortho*-$WO_3 \cdot 0.33H_2O$ is almost double of theoretically calculated value of 2.58% for structurally coordinated water. Higher value suggests the influence of physisorbed water on total weight loss, which can be confirmed by weight loss observation even below 100 °C.

The DSC curves (see Figure 5.9b) of NPs produced from non-acetified and 0.3 M HCl precursor exhibit sharp exothermic peak at 315 and 325 °C which correspond to removal of structurally coordinated water and formation of crystalline WO_3. No peaks were detected in DSC spectra of the dehydrated *m*-WO_3 synthesized from 3 M HCl precursor confirming the water absence suggested by FTIR data.

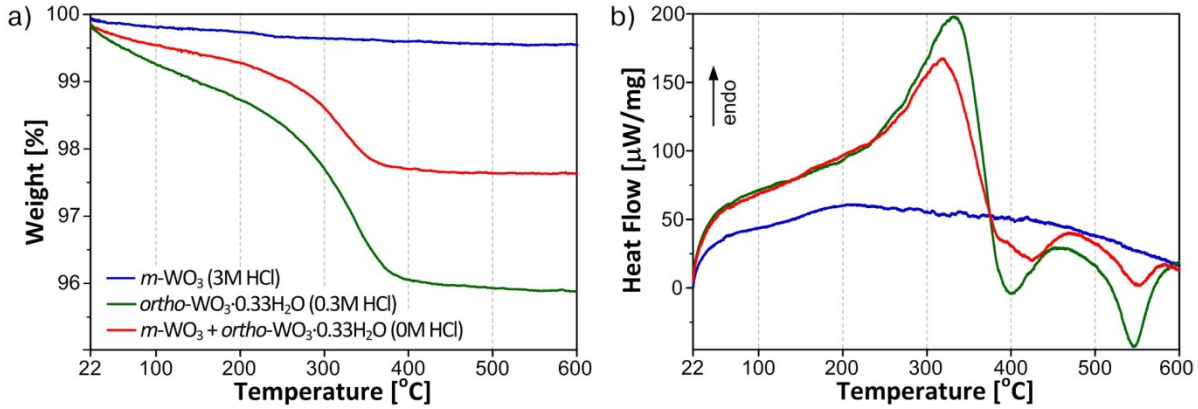

Figure 5.9. Results of thermal analysis consisting of a) TG and b) DSC spectra of nanostructured products obtained from non-acetified precursor solution, precursor dissolved in 0.3 M and precursor dissolved in 3 M HCl after 6 h of hydrothermal synthesis

SEM micrographs of the as-synthesized WOx NPs prepared at different acidity and reaction time are shown in Figure 5.10. The imminent difference obvious at a glance between the morphological characteristics of WO_X NPs synthesized at various precursor acidities is a distribution and shape of nanostructured particles in a form of nanoslabs and nanorods. According to micrograph presented in Figure 5.10a-c, the syntheses performed from non-acetified precursor solution result in a mixture of agglomerated nanorods and rectangular nanoslabs previously identified by XRD analysis as *ortho*-$WO_3 \cdot 0.33H_2O$ and *m*-WO_3 tungsten oxide polymorphs, respectively. The agglomeration of *m*-WO_3 nanoslabs is ordered in multilayer stacks and proceeds with time, while the agglomeration of *ortho*-$WO_3 \cdot 0.33H_2O$ NPs seems to be limited by decreasing quantity of this phase with elapsed reaction time. Such phase transition from orthorhombic to monoclinic under similar conditions was observed also by Jiayin *et al.* [45]. Powders prepared from PTA dissolved in 0.3 M HCl shown in Figure 5.10d-f are composed of *ortho*-$WO_3 \cdot 0.33H_2O$ well defined cubic nanorods with slight but progressive agglomeration which is privileged along the rod's faces of larger area. It is therefore an argument to challenge common opinion [153] saying that sulfates are necessary as directing agents for the formation of 1D WO_3 nanostructures. Powders prepared from PTA dissolved in 3 M HCl shown in Figure 5.10g-i are composed of *m*-WO_3 nanoslabs which agglomerate with the reaction time to multilayer stacks leading to formation of cubic structures. The resulting polyhedrons, despite big differences in dimensions, own smooth surfaces and well defined corners of 90 °.

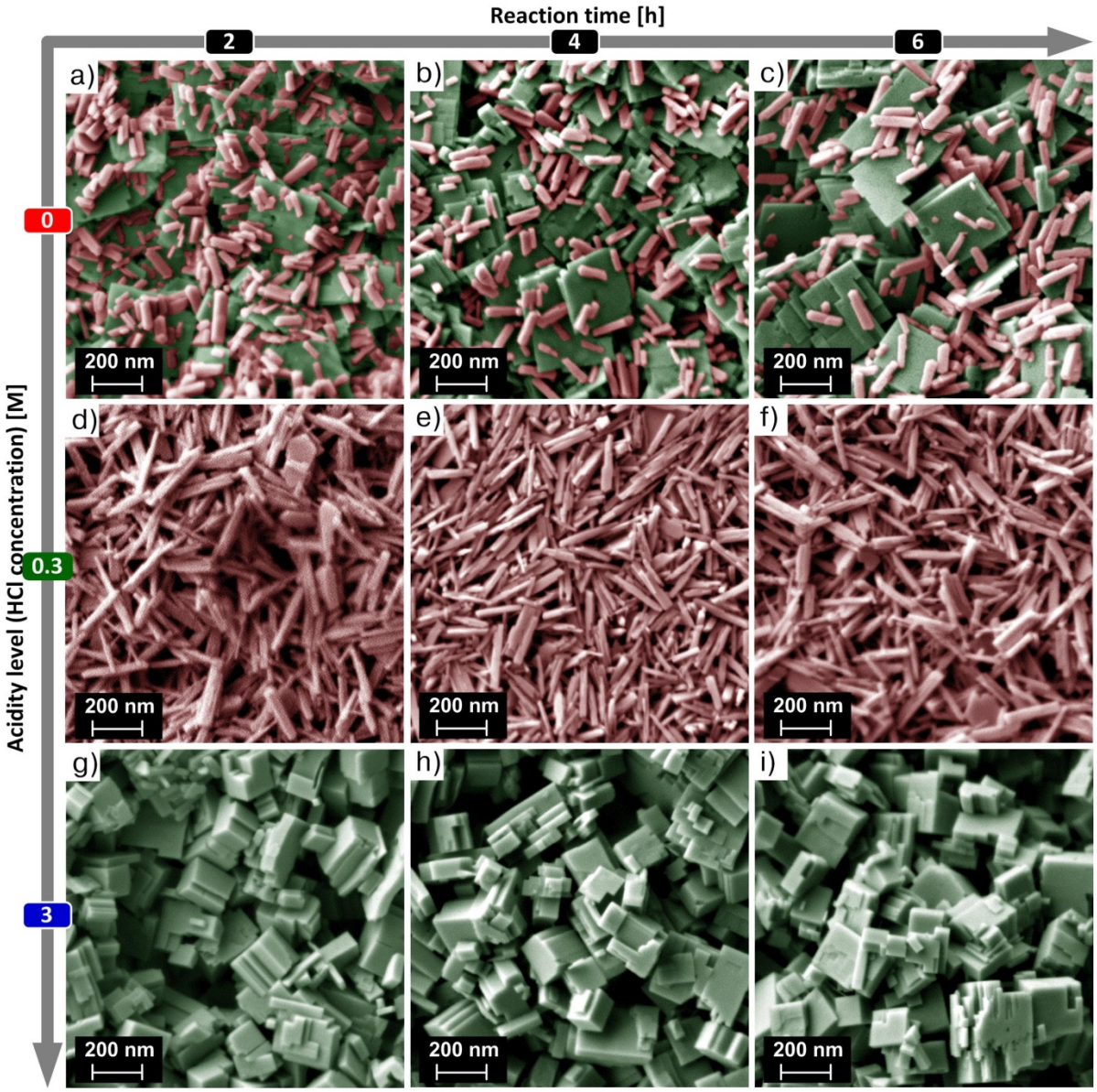

Figure 5.10. SEM images of nanostructured products obtained *via* hydrothermal syntheses performed from a) non-acetified precursor solution after 2 h, b) 4 h and c) 6 h; d) precursor dissolved in 0.3 M HCl after 2 h, e) 4 h and f) 6 h; g) precursor dissolved in 3 M HCl after 2 h, h) 4 h and i) 6 h; micrographs were false colored for enhancing visual illustration.

3D projections of orthorhombic tungsten oxide hydrate NPs presented in Figure 5.11a and Figure 5.11b, and monoclinic tungsten oxide NP presented in Figure 5.11c were drawn using quantitative information concerning the preferential crystalline orientation obtained on a basis of texture coefficient, and SEM observations (see Section 5.2.6 for description of the method). Schemes of both *ortho*-$WO_3 \cdot 0.33H_2O$ nanorods are oriented in the same way. However, facets (220), (-220), (2-20) and (-2-20) do not constitute the shape of NP synthesized from precursor dissolved in 0.3 M HCl. These facets disappear due to the dominant growth of NP in [200] and [-200] directions, whilst slower growth along [020] and [0-20].

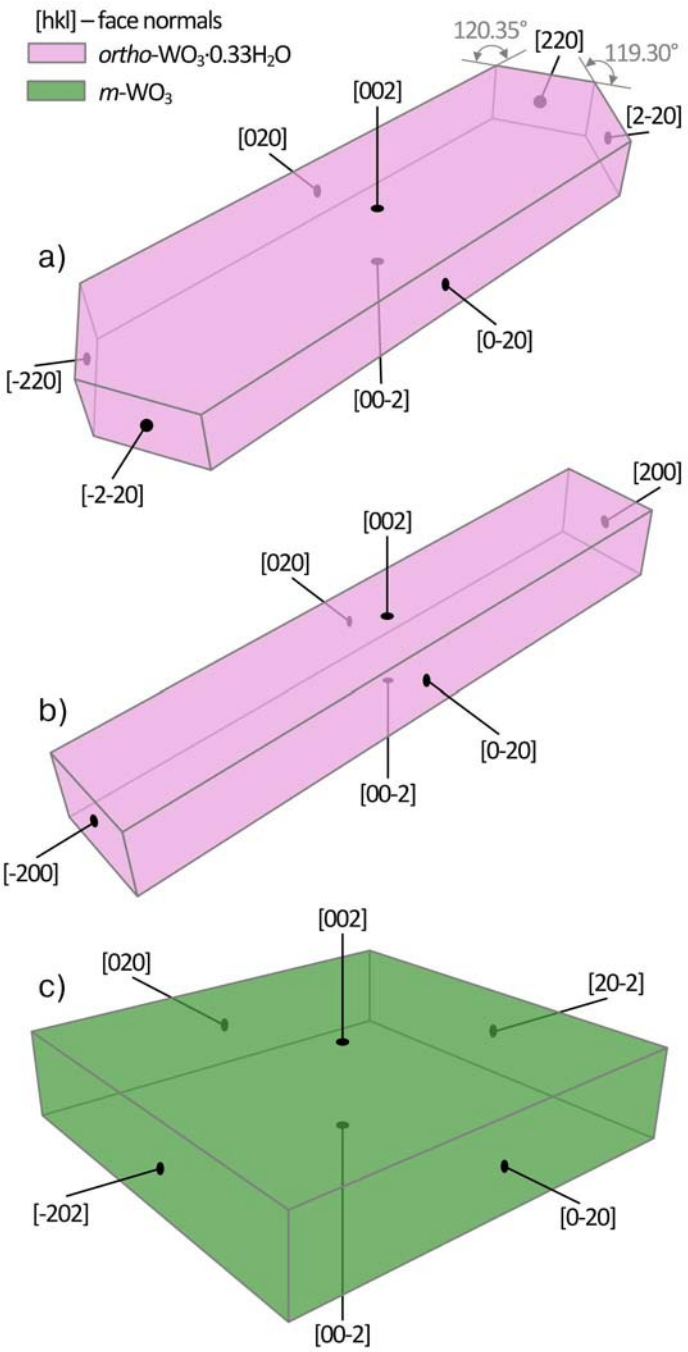

Figure 5.11. 3D models (isomeric projections) of a), b) *ortho*-$WO_3 \cdot 0.33H_2O$ nanorods and c) *m*-WO_3 nanoslabs developed based on quantitative information concerning the preferential crystalline orientation (texture coefficient) and SEM observations

In order to reduce the complex visual information contained in SEM images to easily interpretable quantitative information, the micrographs shown in Figure 5.10 can be presented in a form of simple plots as shown in Figure 5.12. The dimensions were estimated by measuring the size (length) of randomly selected particles in enlarged SEM images. Such analysis of the SEM micrographs revealed

discrete histograms shown in Figure 5.12, to which Gaussian curves were fitted to present continuous particle size distribution.

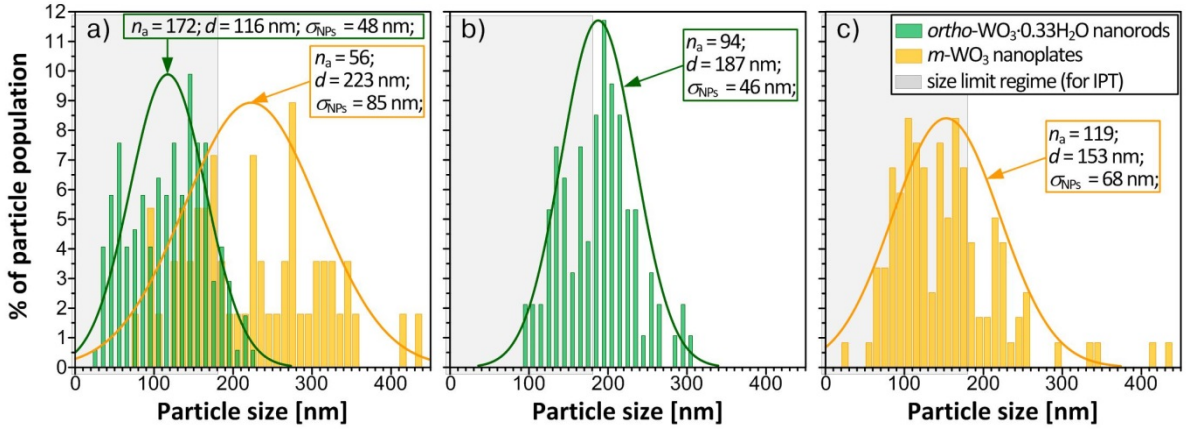

Figure 5.12. Discrete (histogram) with continuous (Gaussian) particle size distribution for products of 6 hours long syntheses performed from a) non-acetified precursor solution, b) precursor dissolved in 0.3 M HCl and c) precursor dissolved in 3 M HCl; particle size was defined as the largest dimension measured along the NP; parameters n_a, d and σ_{NPs} stand for number of NPs in a population, arithmetic mean particle size and standard deviation, respectively

The *ortho*-$WO_3 \cdot 0.33H_2O$ nanorods synthesized from non-acetified precursor solution (Figure 5.12a) are 116 ± 48 nm long, ~40 nm wide and ~20 nm thick (AR = 5.8 ± 2.4). Rectangular *m*-WO_3 nanoslabs fraction of the same product have uniform thickness of ~12 nm, while other dimensions vary in size of 223 ± 85 nm (AR = 18.6 ± 7.1). The *ortho*-$WO_3 \cdot 0.33H_2O$ nanorods prepared from PTA dissolved in 0.3 M HCl (Figure 5.12b) are 187 ± 46 nm long, having well-defined square cross-section with a side length of ~12 nm. The *m*-WO_3 cubic structures prepared from PTA dissolved in 3 M HCl (Figure 5.12c) are agglomerates of rectangular nanoslabs with uniform thickness of ~20 nm while other dimensions vary in size of 153 ± 68 nm (AR = 7.7 ± 3.4).

Size distributions of synthesized products were used also to estimate SA:V as a function of agglomerate size, shown in Figure 5.13. The highest values of SA:V were obtained for agglomerates of *ortho*-$WO_3 \cdot 0.33H_2O$ nanorods prepared from PTA dissolved in 0.3 M HCl. Their individual specific surface area is also the highest among synthesized products. The least favorable in terms of SA:V are *m*-WO_3 nanoslabs synthesized from PTA dissolved in 3 M HCl, irrespectively of the agglomerate size. Obtained SA:V estimations stay in agreement with theoretical considerations described in Chapter 4 which results were plotted in Figure 4.10. Therefore, synthesized *ortho*-$WO_3 \cdot 0.33H_2O$ nanorods are the most desirable products in terms of SA:V, as long as their electrochemical application is concerned.

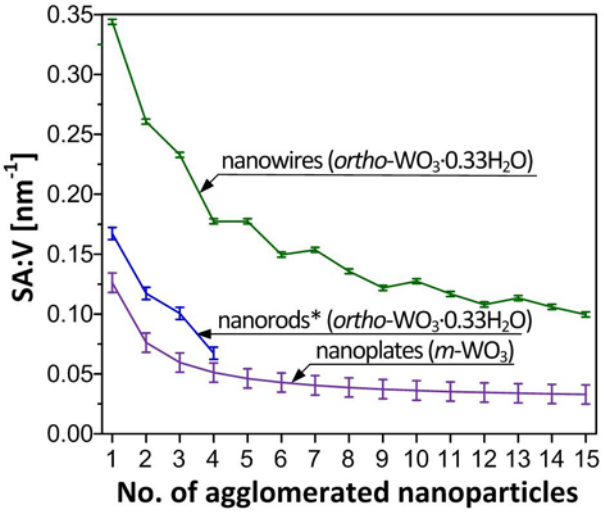

Figure 5.13. Estimation of SA:V as a function of agglomerate size, based on particle size distribution and basic agglomeration model; y-axis error bars reflect standard deviation of a mean particle size; *agglomerates of nanorods (synthesized from PTA dissolved in 0M HCl) with number of NPs higher than four were not observed;

5.3.3. Printability

According to the print-head specification (Canon Thermal DOD FINE^{TM}) used in Canon PIXMA IP4850 printer, the nozzle diameter is 9 μm. Therefore, not all nanostructured products obtained in experiments comply with size limitations (particle size ≤ 180 nm), even when assuming that agglomeration does not occur. Based on plots shown in Figure 5.14 it is possible to conclude that nanorods synthesized from non-acidified precursor and PTA dissolved in 0.3 M HCl are printable in 100 % and 48 %, respectively (under assumption of uniform size distribution of agglomerates, and cluster size not exceeding 15 NPs). Nanoplates synthesized from non-acidified precursor are not printable at all, and only 17 % of the ones synthesized from PTA dissolved in 3 M HCl are capable to pass the nozzle. Therefore, NPs agglomeration has dramatic influence on nanostructure printability in case of nanoslabs, while in case of nanorods seems to not be that relevant. Therefore, the major concern is associated with the nanoplates, as they are relatively large in size and tend to agglomerate significantly exceeding size limitation for this particular Canon printing system.

Irrespectively of the complexity of an ink vehicle, controllable and reproducible deposition of NPs-loaded inks encompasses some challenges. In standard desktop printers, such as CANON PIXMA IP4850 used in present studies, the jetting parameters can be controlled only by proper adjustment of ink fluid parameters, as there is no direct access to the print-head's driver.

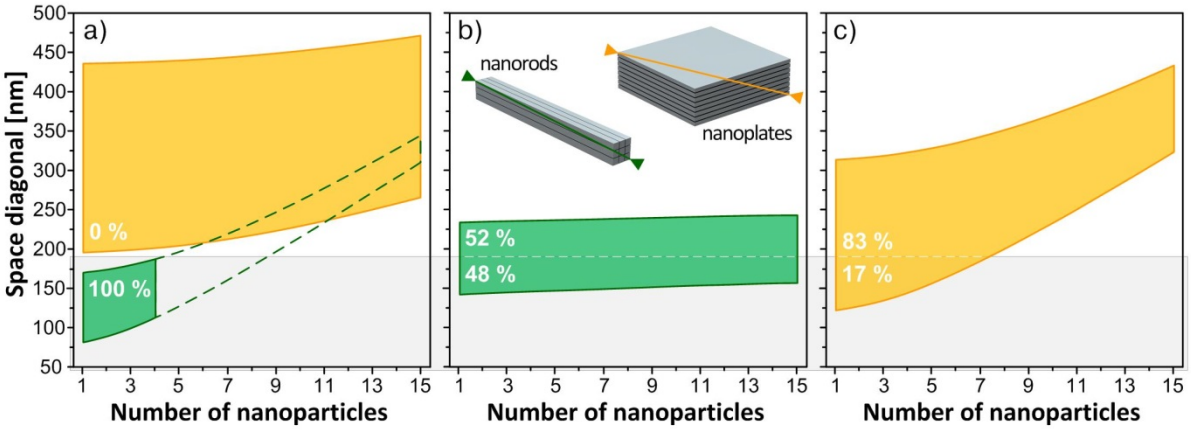

Figure 5.14. Agglomerate size estimation for products of 6 hours long syntheses performed from a) non-acetified precursor solution (agglomerates of nanorods with number of NPs higher than four were not observed), b) precursor dissolved in 0.3 M HCl and c) precursor dissolved in 3 M HCl; agglomerate size is defined as its space diagonal and uniform size distribution of agglomerates is assumed

To assure proper droplets formulation, the custom ink should have similar rheology to the genuine CANON inks (indicated in Figure 5.15). In the same time it should be water-based ink as most of the organic solvents may dissolve printhead structure. Such water-based ink offers several advantages:

a) reduced volatility;
b) low reactivity with the substrate and print-head elements;
c) fewer restrictions in terms of safe handling when comparing with organic solvents based counterparts;

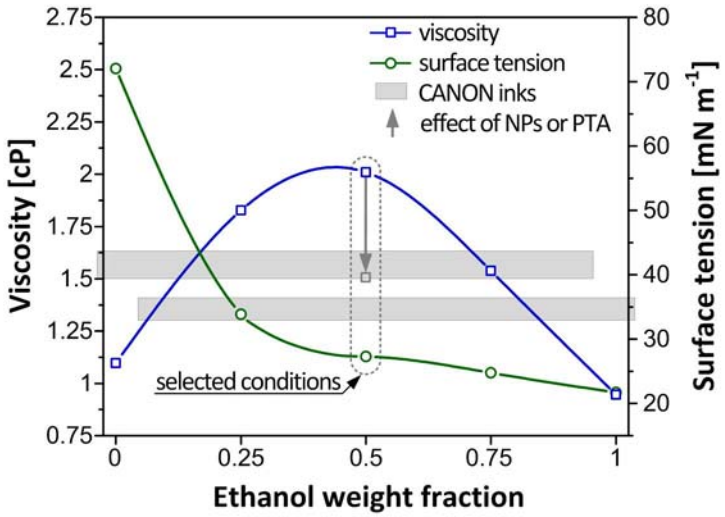

Figure 5.15. Viscosity and surface tension of an alcohol aqueous ink vehicle as a function of alcohol (*i.e.* ethanol) weight fraction; the regime of genuine CANON inks (CLI-526 cyan, magenta and yellow) is shown in grey

In order to adjust the viscosity and surface tension to the range within which the printer operates, the ethanol weight fraction was selected as 0.5, according to the plot shown in a Figure 5.15, resulting in values of 2 cP and 27 mN m^{-1}, respectively. The viscosity of obtained vehicle is too high when comparing with genuine CANON inks, but addition of NPs in amount of 0.03 wt%, or 8.7 wt% of PTA transfers the viscosity value into CANON inks regime. Thus, the viscosity and the surface tension of both, NPs dispersion and WO_3 sol assure expected printability.

5.3.4. Electrochromic response of inkjet printed films

According to the electrochromism theory, the mechanism of optical modulation is different in crystalline and amorphous phase. In nanocrystalline WO_X electrochromism arises due to the increasing Drude type (metallic) reflection, observed especially in IR region with increasing free electron/lithium injection [61]. On the other hand, in amorphous phase, the most widely accepted model assumes that the optical modulation upon the double injection occurs through increasing absorption arising from the transfer of localized electrons between W^{5+} and W^{6+} sites, so called small polaron absorption [62, 63, 123]. Figure 5.16a and Figure 5.16b show generalized mechanism of electrochemical reaction in EC device based on dual-phase film for coloring and bleaching, respectively.

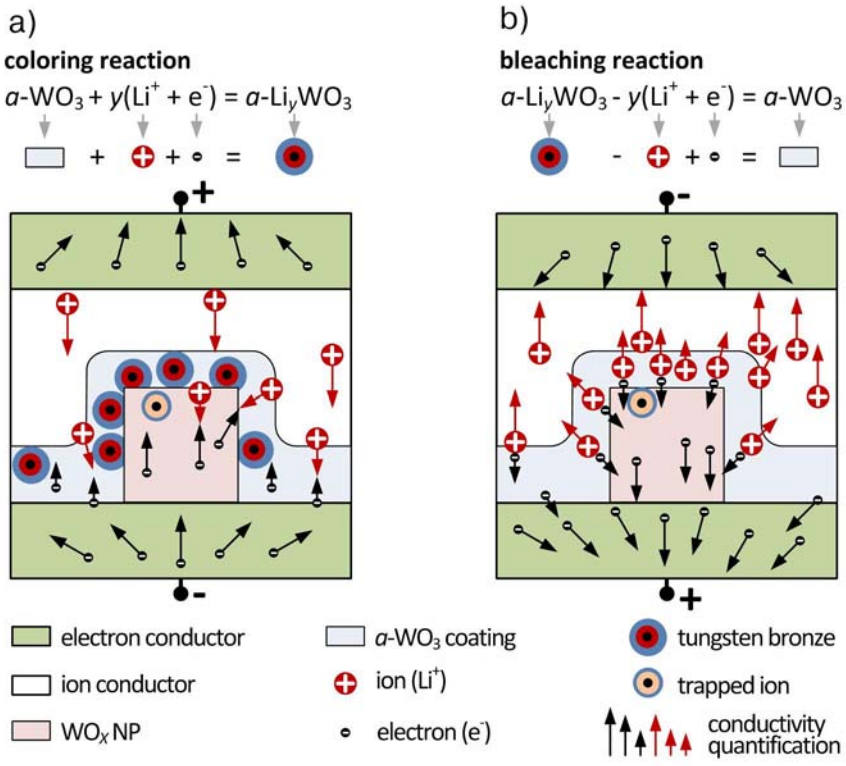

Figure 5.16. Schematic illustration of a) coloring and b) bleaching reaction under operational conditions in inkjet printed dual phase *a*-WO_3/WO_X film

It is assumed that EC WO_3 film in transparent state can be switched reversibly to a colored state by both insertion of ions and electrons to form tungsten bronze (a-Li_yWO_3, where y stands for the fractional number of sites filled in the WO_3 lattice). Although being an obvious oversimplification, presented schemas provide very convenient background for further discussion on a-WO_3/WO_X electrochemical performance. In considered device structure, an EC film is in contact with ion (Li^+) conductor, which also serves as ion storage. Two electron (e^-) conductors serve for setting up the distributed electric field. Operational voltage shuttles ions into and out of the film causing coloring (a-Li_yWO_3) and bleaching (a-WO_3) action, respectively. Nanostructured WO_X is more conductive for e^- and less conductive for Li^+ ions when comparing to a-WO_3. Therefore, the highest density of optically active centers is in the interface between WO_X and a-WO_3, where electrons meet ions leading to the formation of a-Li_yWO_3. Despite slower Li^+ diffusion in crystalline medium, some ions cross the grain boundary and get trapped into the crystalline structure of NP, due to the existence of imperfections.

Quantitative EC response analysis is based on CA technique which is a square-wave potential step method coupled with optical spectroscopy used for analysis of switching kinetics and contrast of the film. The electrochemical cell consisting of working electrode (printed film on ITO PET substrate) and platinum wire used as counter electrode was filled with lithium based gel electrolyte prepared according to the recipe described elsewhere [47]. Resulting cell was driven by power supply in order to induce EC action in a linear stair pulse mode (from -2 V up to 2 V in a 0.5 V step, -2 V of bias, 30 s per pulse). Spectra were recorded in reference to the uncoated substrate under equal conditions. The main output is confined to the basic performance indicators defined in Section 5.5.5, consisting of ΔOD, τ_{col}, τ_{bl} and ΔT_{SS}. Comparison between corresponding changes in optical densities of dual-phase films in reference to the response of pure amorphous film is shown in Figure 5.17. Such presentation of the optical modulation provides the information regarding the role of NPs content selectively, in EC mechanism.

Films which contain either *ortho*-$WO_3 \cdot 0.33H_2O$ or m-WO_3 NPs, outperform their amorphous analogs in term of optical modulation (see Section 5.5.7 for corresponding spectral responses). It is a consequence of dual-phase microstructure which provides large interfaces between dual-phase film and gel electrolyte, as well as between amorphous and nanocrystalline phases itself. Such microstructure promotes ion diffusion through the porous film. The highest ΔOD values were recorded for film containing *ortho*-$WO_3 \cdot 0.33H_2O$ nanowires, which is a direct repercussion of the highest value of SA:V for those NPs, even in spite of progressing agglomeration. It should be noted that the performance of EC films either amorphous, nanocrystalline or dual-phase, in particular ΔOD, is ultimately governed not only by the film composition but also by the thickness (see Section 5.5.6 for details concerning dependence between film thickness and electrochromic response).

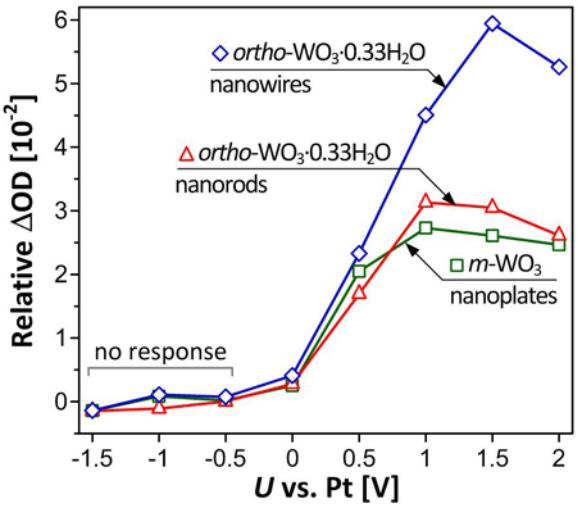

Figure 5.17. Change in optical density (ΔOD) as a function of operating voltage for dual-phase inkjet printed films containing different types of NPs; relative values represent the difference between ΔOD of dual-phase film and ΔOD of pure amorphous analog (reference)

Differences in switching dynamics of dual-phase and amorphous films shown in Figure 5.18 and Figure 5.19, provide an information regarding the role of NPs in the dynamics of the EC reaction. Low potentials applied between electrodes (0.5 V and 1 V) cause slow but apparent transition between bleached and colored state. However, the rate of the electrochemical reaction is lower when comparing with pure amorphous phase (see Figure 5.18). Operation with the higher voltage level (1.5 V and 2 V) results in improved coloration time (< 3 s for 2 V) of all films containing NPs in comparison with pure amorphous film (~5 s).

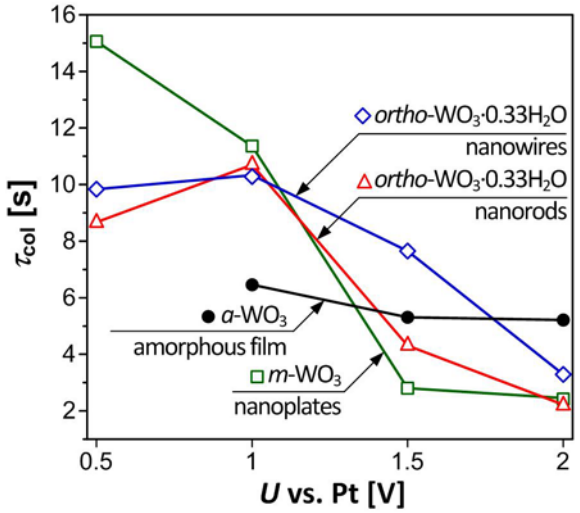

Figure 5.18. Variation in coloring time as a function of operating voltage for dual-phase inkjet printed films containing different types of NPs; amorphous film is presented for comparison.

The application of a reverse potential (-2 V) restores the film to its bleached state over a short period of time denoted as τ_{bl}. The switching dynamics from colored to bleached state depends on the voltage

level at which coloration was induced. According to Figure 5.19, when restoring the pure amorphous film after coloration at low potential (1 V), the optical change proceeds very slowly (~8.5 s). However, bleaching period is much shorter in case of dual-phase films. Films containing *ortho*-$WO_3 \cdot 0.33H_2O$ nanowires bleach within time lower than 1.9 s, irrespectively of the level of the operational voltage which induced coloring state, owed to high electronic conductivity of those nanostructures. For other films, NPs content is beneficial especially when low voltage levels are used to supply the device.

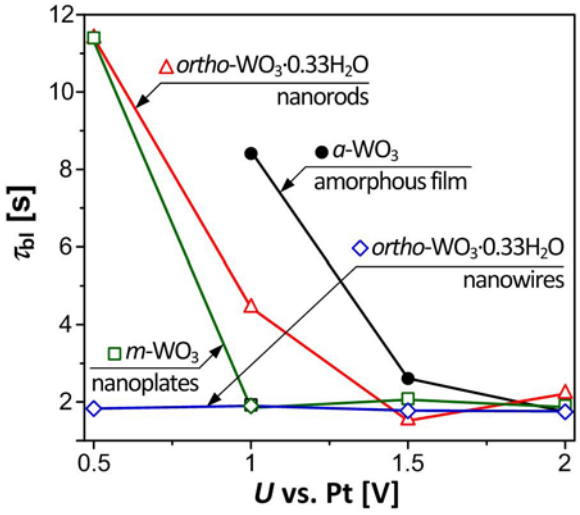

Figure 5.19. Variation in bleaching time for dual-phase inkjet printed films containing different types of NPs; bleached state was restored by supplying -2 V, after coloring under operational voltage (an abscissa); amorphous film is presented for comparison.

The coloration kinetics is observed to be slower than bleaching kinetics for all the films under investigation, which stays in agreement with the well-defined, but different mechanism governing the two processes. While the exchange of the current density at the EC film-electrolyte interface controls coloration kinetics, the space charge-limited Li^+ ion diffusion current governs the bleaching time [63].

Presented results clearly shows beneficial impact of WO_X NPs on electrochromic performance of printed films, reflected in 2.5 times higher optical modulation, and 2 times faster coloration time, when comparing with pure amorphous film. Such improvement is mainly attributed to higher interface between amorphous and nanocrystalline phase, as well as between MO_X layer and ion conductor.

The impact of NPs selection on reversibility of printed dual-phase EC films is demonstrated in Figure 5.20, which represents so called site saturation effect [67].

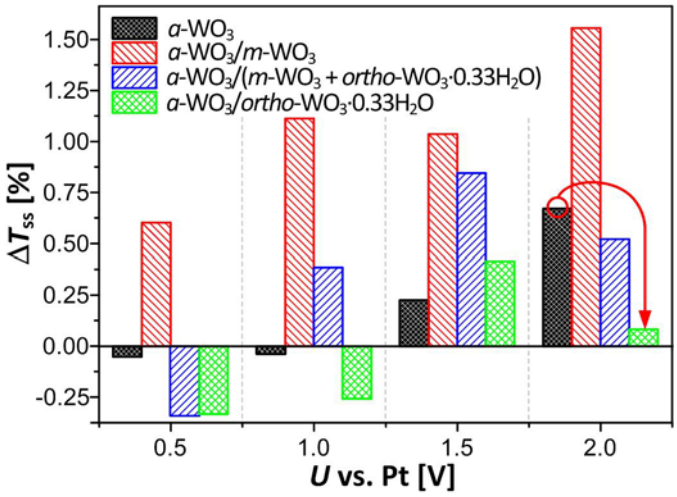

Figure 5.20. Response plots presenting variation in site saturation effect (defined as ΔT_{SS}) as a function of operating voltage for dual-phase inkjet printed films containing NPs synthesized in 6 h long process; $\Delta T_{SS} = 0$ for fully reversible optical effect

When the operational voltage exceeds a certain value, the transmittance of the bleached films is markedly lower than its value before coloration which means that the device does not bleach completely ($\Delta T_{ss} > 0$). The EC action was fully reversible for films containing *ortho*-$WO_3 \cdot 0.33H_2O$ NPs, while films with other phases did not bleach completely due to the intensive charge trapping particularly evident for films containing *m*-WO_3 phase. This irreversible deterioration in *m*-WO_3 phase may be caused by lattice strain and possible crystal distortion which affect the Li^+ ion insertion/extraction. It was also observed that the addition of *ortho*-$WO_3 \cdot 0.33H_2O$ NPs to the film lowers the charge trapping effect in the amorphous phase due to increased surface area of *a*-WO_3 matrix. Moreover, *ortho*-$WO_3 \cdot 0.33H_2O$ NPs contain coordinated water and are also hydrophilic, what makes the films with high nanocrystalline content more hydrated. Such physisorbed water gives the significant enhancement in ion dynamics through an amorphous phase [63].

5.3.5. Design rule outline

Figure 5.21 summarizes engineering rules applied in WO_X NPs synthesis and ink formulation. Following the indications marked as preferable area, assures good printing processability and enhancement in performance of *a*-WO_3/WO_X film when comparing to pure amorphous microstructure. In order to determine such preferable regime for EC applications, each alternative was studied until the choice is clear, rational and optimal according to existing knowledge.

Such design rules outline is an approach to proper arrangement of various factors including structural, morphological, electrical and rheological properties while taking into account post-treatment

conditions. However, those eleven parameters do not restrict the scope of research in this area. Many other factors may be considered as relevant, depending on the studies complexity.

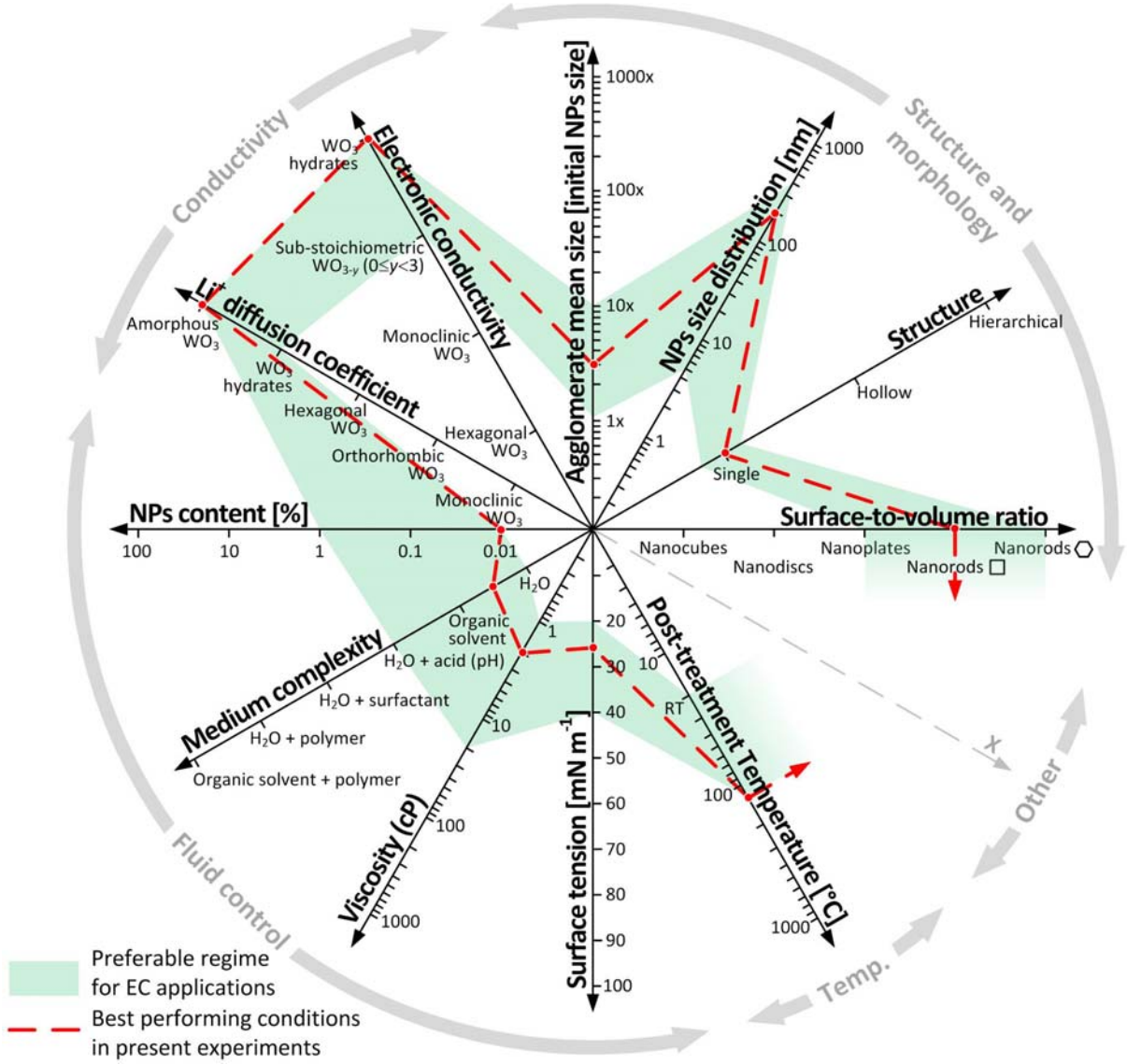

Figure 5.21. The design rules outline for WO_X NPs synthesis and ink formulation process; preferable regime for EC applications based on inkjet printed inorganic films and factors for best performing material in present studies were also plotted

The rules formulated in this section relate to the outline determined in Chapter 4 (see Section 4.3.3), which shows a view on printed electrochemical applications at large. However, here the considerations are restricted to the specific material system (*i.e.* WO_X NPs) and particular printing deposition technique (*i.e.* IPT).

5.4. Conclusions

In the presented study, the morphology evolution of WO_X NPs has been successfully controlled by acidity level of sol-gel precursor under hydrothermal conditions. In order to evaluate EC properties of developed NPs, dual-phase films deposited *via* IPT has been investigated showing higher values of transmission modulation over the visible and solar regions as compared to the poor EC performance of amorphous films. Films containing synthesized NPs exhibit 2.5 times higher optical modulation, and 2 times faster coloration time, when comparing with pure amorphous film. Such improvement is mainly attributed to the increased hydration of the structure, and higher interface between amorphous and nanocrystalline phase, as well as between metal oxide layer and ion conductor. Moreover, the presence of orthorhombic NPs improves kinetics of intercalation and deintercalation mechanisms and significantly reduces the deleterious site saturation effect improving reversibility of electrochromic action. The conductive network of interconnected WO_X NPs facilitates charge transport in the EC layer and increases significantly the active surface area of the amorphous matrix. Therefore, the impact of synthesized NPs structure and morphology on electrochromic performance has been identified as crucial. These results demonstrate that combination of IPT with controlled synthesis of NPs provide an excellent method for the production of inorganic chromogenic films with controlled composition and dual-phase microstructure for a low temperature, direct-write fabrication of high-performance EC devices. It is evident that described approach not only leads to a significant improvement in EC performance, but also meets the challenges encountered when using synthesized metal oxide NPs in a printing process. By following the presented strategy for electrochromic tungsten oxide, it is possible to correlate the synthesis parameters with further technological processes leading to the application of those nanomaterials in high-performance electrochemical devices.

5.5. Supporting information

In this section, several diagrams, pictures and plots are provided for more detailed description of the methodology, arguments and conclusions presented in above chapter. It provides information about synthesis, sample dimension, ink formulation, opto-electrochemical measurements setup, definitions of parameters (responses) and spectral response of printed films.

5.5.1. Hydrothermal synthesis details

The hydrothermal synthesis was performed using Teflon-lined stainless steel autoclave (4745 general purpose vessel, Parr) and laboratory furnace with settable temperature profile (L3/11/B170, Nabertherm) as it is presented in Figure 5.22.

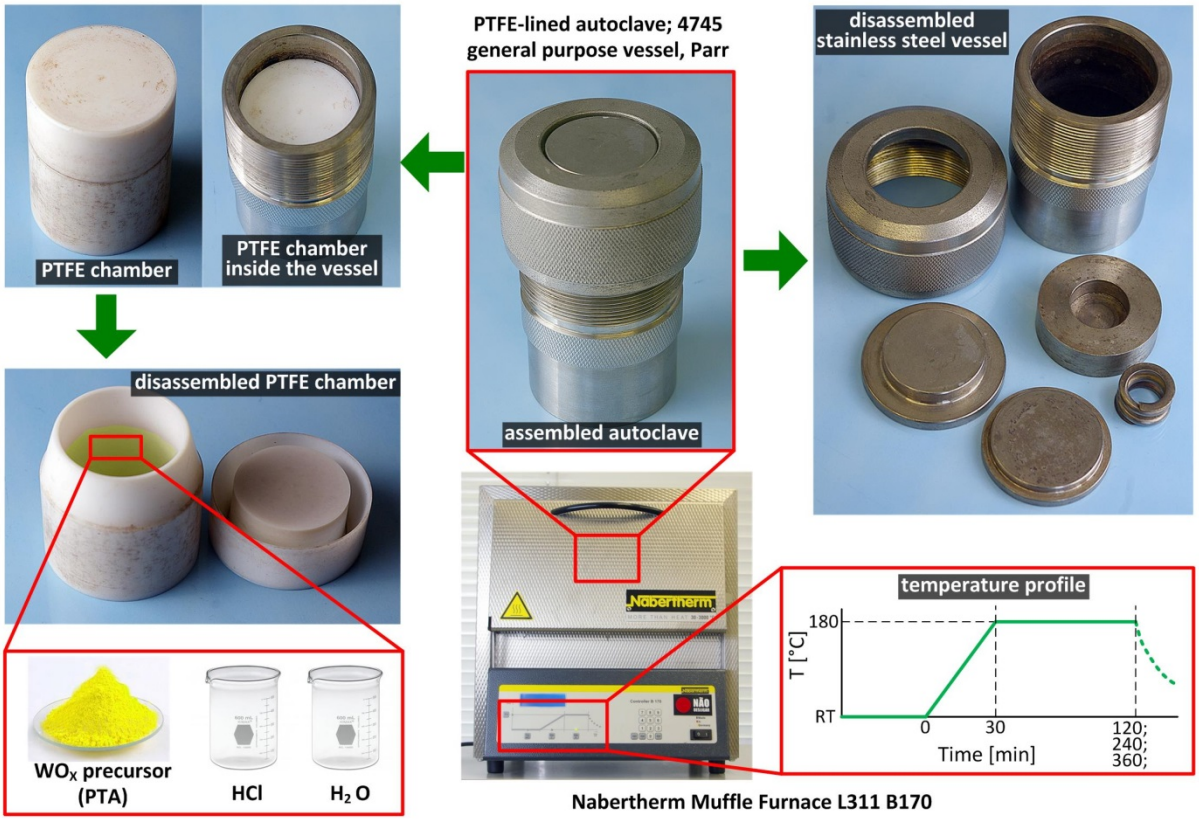

Figure 5.22. Hydrothermal synthesis setup

The starting material for WO_X NPs synthesis consisted of previously synthesized PTA dissolved in HCl aqueous solution just before use. Prepared solution was transferred into PTFE chamber, set inside the stainless steel autoclave and installed in the oven with temperature rising from RT up to 180 °C, ramp rate ~ 5 °C/min, for selected time of 120, 240 or 360 min.

The hydrothermal conditions plotted in Figure 5.23 for water based precursor can be approximated using well known August-Roche-Magnus empirical formula expressed by Equation 5.6.

$$p(T) = p_0 e^{\left(\frac{17.625T}{T+243.04}\right)} \tag{5.6}$$

where: p is saturation water vapor pressure in hPa, T is temperature in °C, p_0 is saturation water pressure at T = 0 °C (p_0 = 6.1094 hPa). The plot of water vapor pressure in function of temperature in a range of RT-220 °C is presented in Figure 5.23.

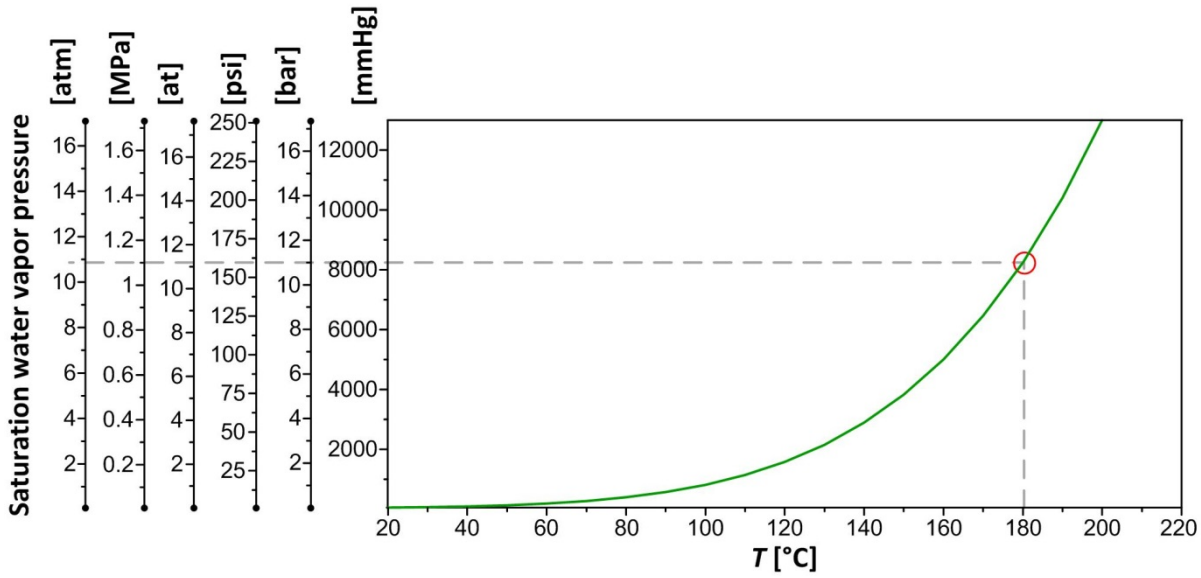

Figure 5.23. Saturation water vapor pressure in function of temperature as an approximation of conditions during hydrothermal synthesis

5.5.2. Sample dimensions and substrate cleaning procedure

Optically active *a*-WO_3/WO_X films with area of 1 cm^2 were printed in ITO PET stripes with dimensions shown in Figure 5.24.

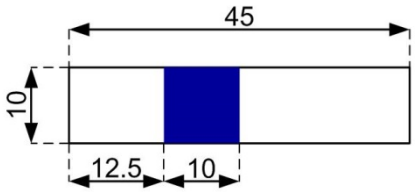

Figure 5.24. Sample dimensions

Following procedure was applied for ITO PET substrates cleaning:

a) Protection foil is removed from ITO PET surface just before cleaning procedure.
b) Both surfaces of ITO PET substrate are cleaned with lint free tissues and isopropyl alcohol.
c) First ultrasonic cleaning of substrates is performed in deionized water with 3% glass detergent (Cleaner concentrate for cuvette washing, *Fluka*) for 10 minutes at 60ºC.
d) Substrates are thoroughly rinsed with deionized water.
e) Second ultrasonic cleaning is performed in deionized water for 10 minutes at 60 ºC.
f) Substrates are thoroughly rinsed with deionized water.
g) Third ultrasonic cleaning is performed in ethanol for 5 minutes at 60 ºC.
h) Substrates are thoroughly rinsed with deionized water.

i) The last step of ultrasonic cleaning is performed in isopropyl alcohol for 5 minutes at 60 ºC. If necessary, substrates can be stored in isopropyl alcohol.

j) Just before use substrates are dried by nitrogen flow.

5.5.3. Ink formulation details

The WO_X NPs loaded dispersions based on aqueous ethanol vehicle were subjected to ultrasonic treatment using ultrasonic stand mounted homogenizer (Ultrasonic Compact Hielscher UP400S) applied in ice cooled batch, as shown in Figure 5.25a. Sonication amplitude was applied according to the profile shown in Figure 5.25b.

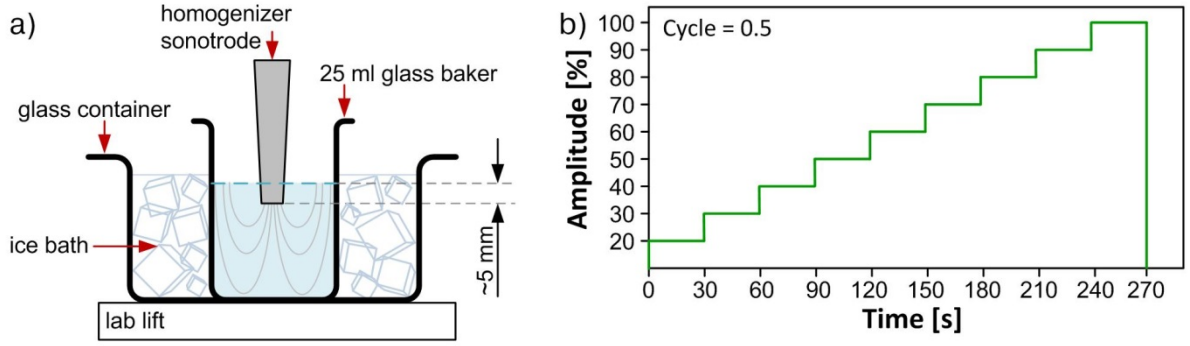

Figure 5.25. Ultrasonic procedure shown as a) schematic drawing and b) amplitude profile; 100 % amplitude corresponds to 400 W ultrasonic (24 kHz, automatically tuned frequency) power; cycle parameter was set as 0.5

Homogenizer was equipped with titanium sonotrode (dispersing tools) with tip diameter 3 mm, length 100 mm and male thread M10×1 designed for samples ranging from 5 up to 200 ml.

5.5.4. Opto-electrochemical measurement setup

Optical and electrochemical measurements were performed simultaneously using specially designed transparent opto-electrochemical cell, presented in Figure 1.11, Section 1.4.3.3. The electrochemical responses of the films were measured in two-electrode configuration cell shown in Figure 5.26. *Working electrode* consists of ITO PET substrates coated with optically active *a*-WO_3/WO_X electrode, while platinum wire serves as *reference* and *counter* electrode. Both electrodes are immersed in liquid/gel electrolyte.

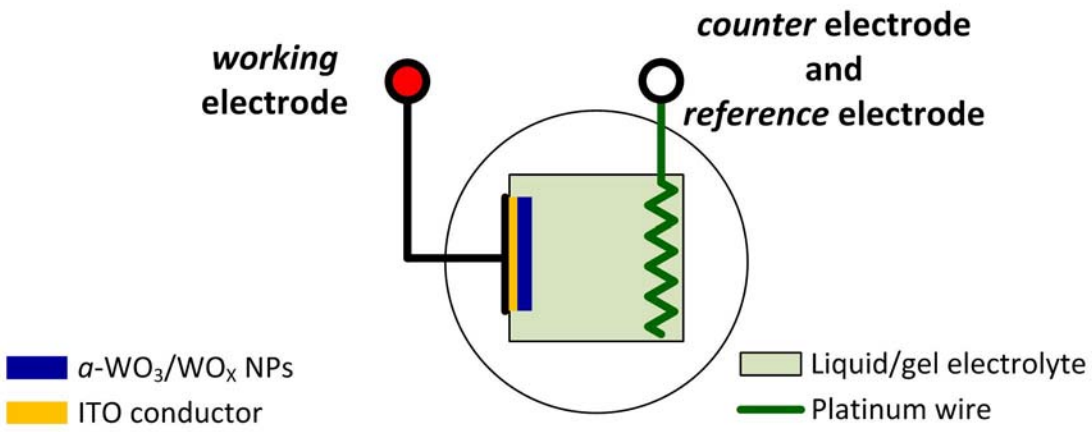

Figure 5.26. Schematic representation of two-electrode electrochemical cell setup

Optical measurements were performed using spectrometer setup shown in Figure 5.27. Main elements of this system are: UV-Vis spectrometer (HR4000 High-Resolution Spectrometer, Ocean Optics), light source (HL-2000-FHSA Halogen Light Source, Mikropack), power supply (High Current Source Measure Unit, KEITHLEY 238) and optical fibers (QP600-2-SR/BX, type – SR, core diameter - 600 μm, connector – QSMA, jacketing – BX).

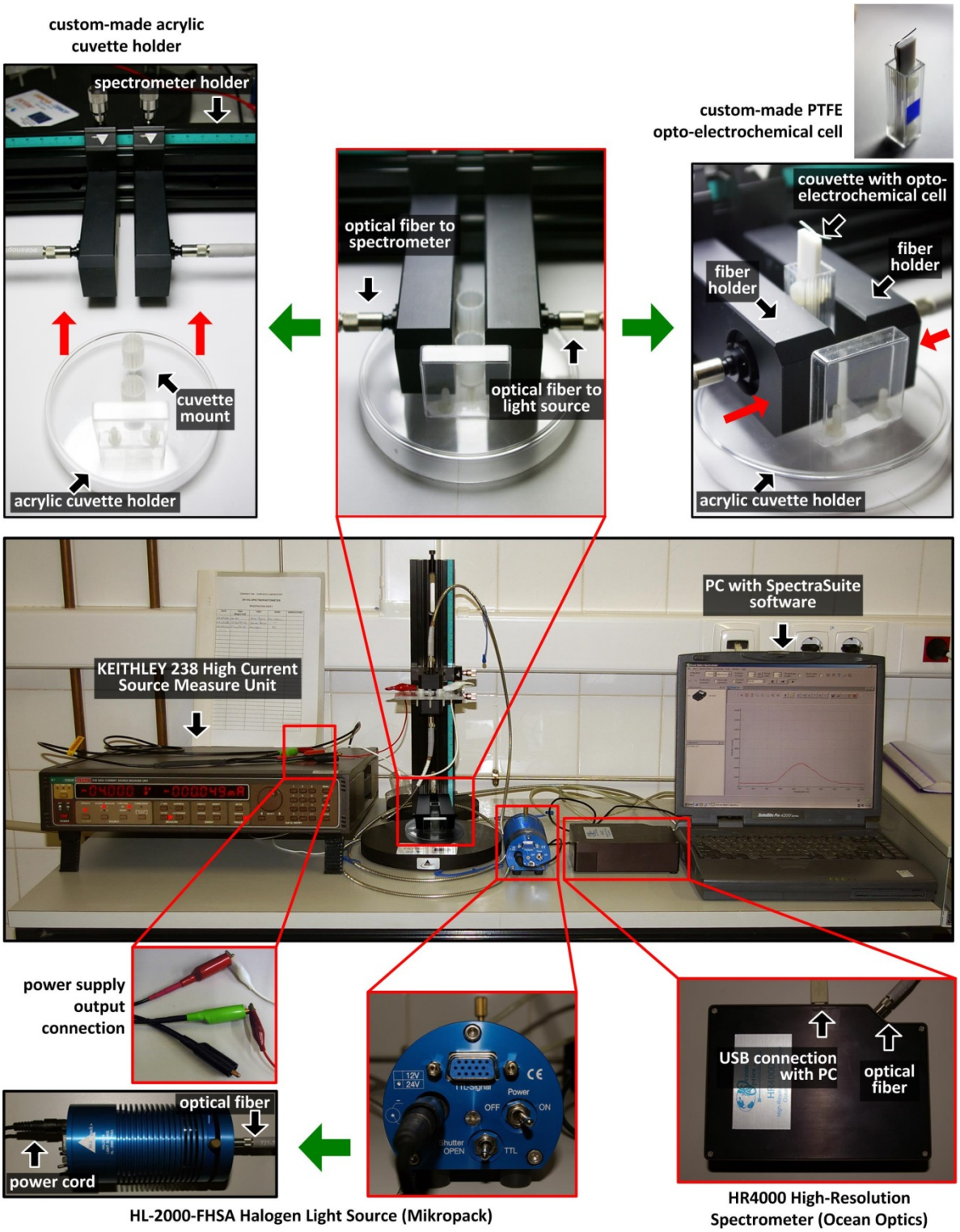

Figure 5.27. Opto-electrochemical measurement setup

5.5.5. Definitions of parameters

Optical measurements are based on chronoabsorptometry (CAbs) technique which is a square-wave potential step (see Figure 5.28a) method coupled with optical spectroscopy used for analysis of switching kinetics and contrast of the film.

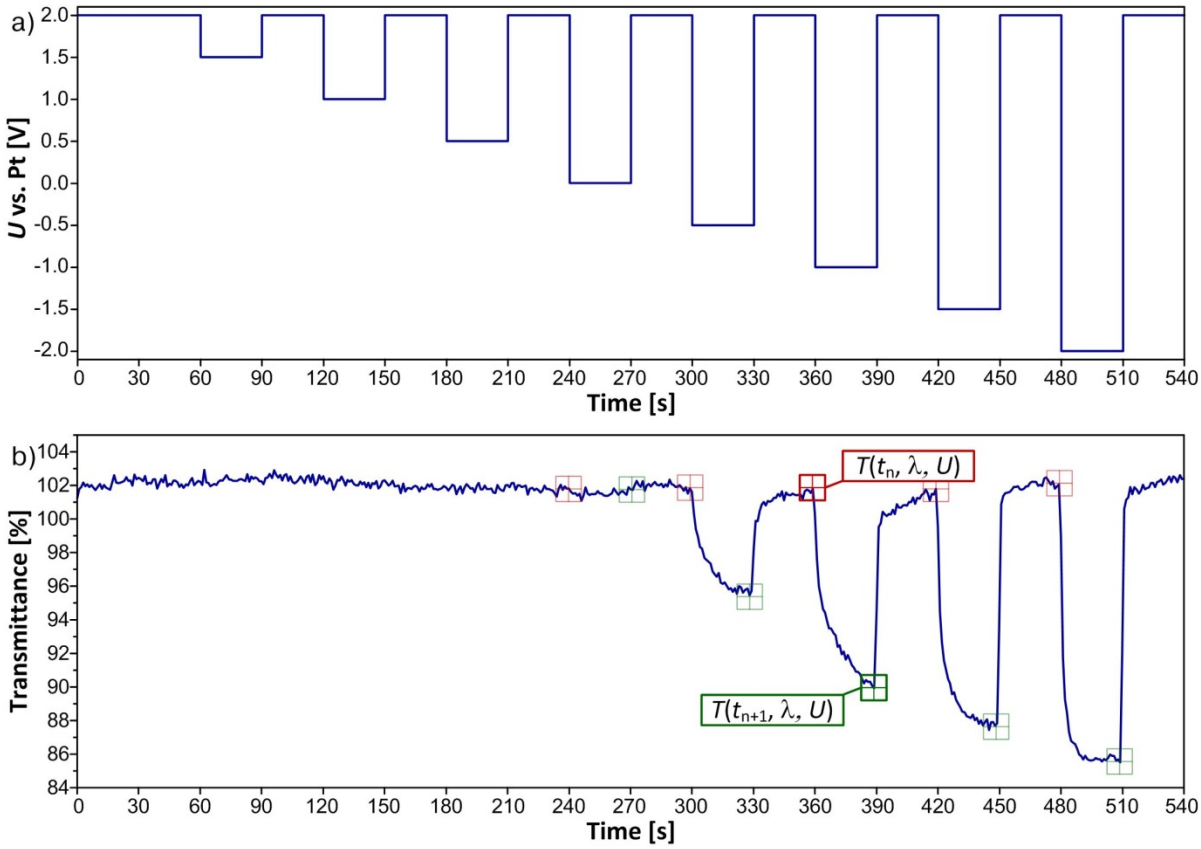

Figure 5.28. Determination of ΔOD as a function of operational voltage based on chronoabsorptometry technique in which a) linear stair pulse wave form is supplied to the film and its b) optical response at λ = 800 nm is recorded showing change in transmittance depending of the level of supplied voltage; an example shows optical response of a *a*-WO_3/WO_X film based on a products of 4 hours long synthesis performed from the PTA precursor dissolved in 0.3 M HCl (*ortho*-$WO_3 \cdot 0.33H_2O$ nanorods)

The electrochromic testing was processed within an appropriate voltage range (-2 V to 2 V), so as to avoid electrolyte oxidation and (eventual) ITO reduction. The main output from CA measurements is the change in optical density (ΔOD), which indicates how much the transmittance of the electrochromic layer is reduced during the coloring process (or increased during bleaching) for various levels of operational voltage. A linear stair pulse wave form shown in Figure 5.28a was used to induce electrochromic action, and the spectral response recorded for λ = 800 nm was analyzed according to Figure 5.28b.

The change in optical density is calculated using Equation 5.7.

$$\Delta \mathrm{OD} = \log_{10}\left(\frac{T(t_n,\lambda)}{T(t_{n+1},\lambda)}\right) \tag{5.7}$$

where: $T(t_n,\lambda)$ and $T(t_{n+1},\lambda)$ are transmittances of the films at λ = 800 nm before (t_n,) and after (t_{n+1}) coloration process, respectively for each level of operational voltage (see also Figure 5.28b).

The impact of WO_X NPs on reversibility of printed dual-phase EC films is measured as ΔT_{SS} which represents so called site saturation effect [67]. The ΔT_{SS} is defined according to Equation 5.8 as the difference in average transmittance ($T(t_0,\lambda)$, λ = 800 nm) of the film bleached by negative voltage to its bleached value after coloration for particular operating voltage (U) (see also Figure 5.29). The ΔT_{SS} is equal to 0 for fully reversible optical effect.

$$\Delta T_{SS} = T(t_0,\lambda) - T(t_m,\lambda,U) \tag{5.8}$$

Site saturation effect is quantified based on the CA results with linear stair pulse wave form shown in Figure 5.28a used to induce electrochromic action.

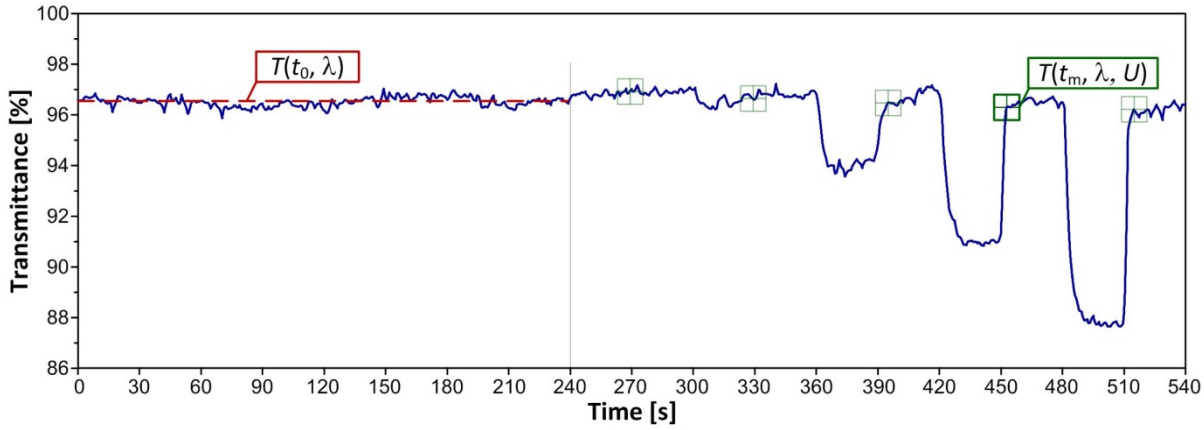

Figure 5.29. Determination of ΔT_{SS} as a function of operational voltage based on recorded optical response at λ = 800 nm; an example shows optical response of a-WO_3 film with no NPs incorporated

Data obtained from CA measurements in which square wave potential (see Figure 5.30a) is applied, enables estimation of the switching time for coloring and bleaching process according to Figure 5.30b. The coloration time (τ_{col}) is defined as the time required for an electrochromic device to change from its bleached to colored state. In present studies the coloration time is defined as the requisite time for reduction of the device's transmittance to 80% of the final reduction according to Equation 5.9 (see also Figure 5.30b).

$$\tau_{\mathrm{col}} = f^{-1}\left(T(t_2,\lambda) + 0.2\big(T(t_1,\lambda) - T(t_2,\lambda)\big)\right) - t_1 \tag{5.9}$$

The bleaching time (τ_{bl}) is defined as the time required for an electrochromic device to change from its colored to bleached state. In these studies the bleaching time is defined as the requisite time for

change of the device's transmittance to 80% of the final bleach level, according to Equation 5.10 (see also Figure 5.30b).

$$\tau_{bl} = f^{-1}\left(T(t'_2,\lambda) - 0.2\left(T(t'_2,\lambda) - T(t'_1,\lambda)\right)\right) - t'_1 \qquad (5.10)$$

The values of τ_{col} and τ_{bl} were determined as average values obtained from 5 consecutive cycles.

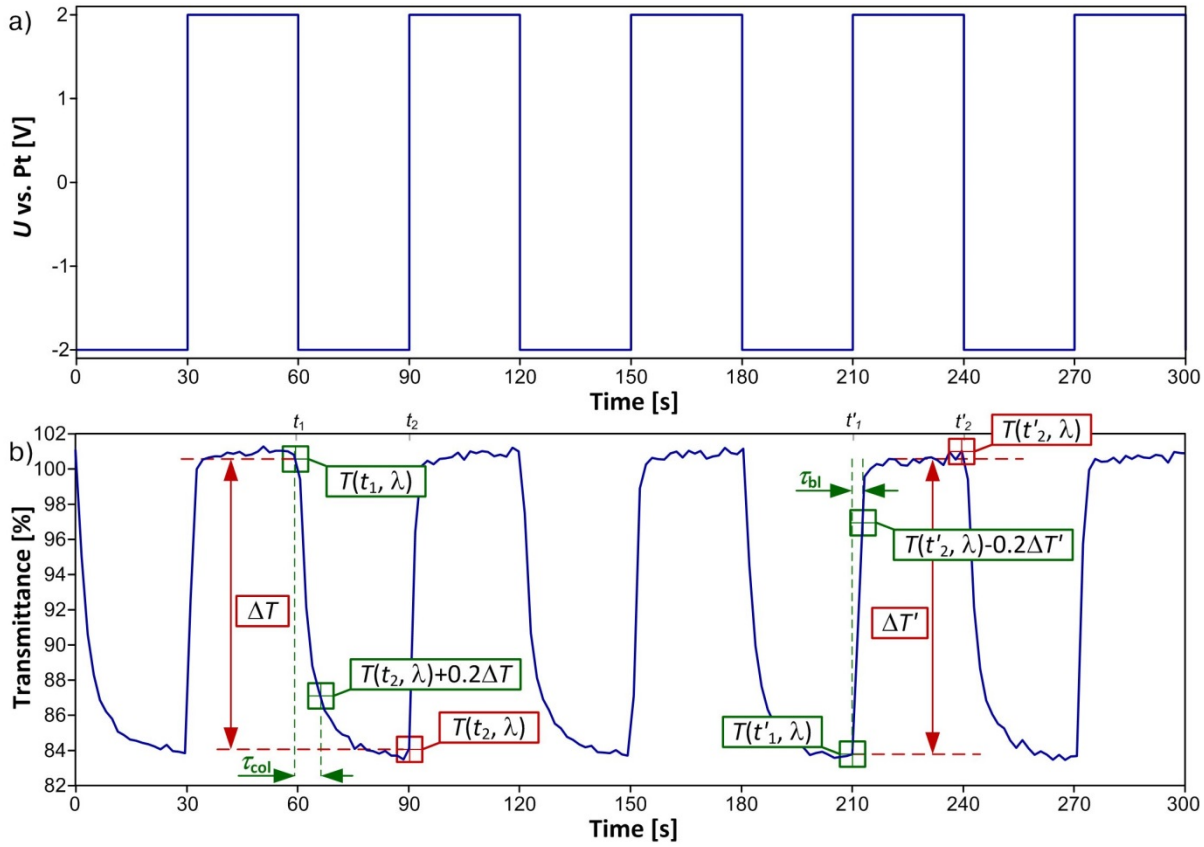

Figure 5.30. Determination of coloration and bleaching time based on chronoabsorptometry technique in which a) square wave form is supplied to the film and its b) optical response at λ = 800 nm is recorded showing change in transmittance; an example shows optical response of a *a*-WO_3/WO_X film based on a products of 4 hours long synthesis performed from the PTA precursor dissolved in 0.3 M HCl (*ortho*-$WO_3 \cdot 0.33H_2O$ nanorods)

5.5.6. Influence of the film thickness on electrochemical response

Influence of the film thickness on ΔOD shown in Figure 5.31 was measured for films with similar composition to the one reported in this chapter. In order to formulate an ink, 0.75 g of PTA was dissolved in 7.5 g of aqueous isopropyl alcohol mixture with weight ratio of 70:30 and addition of oxalic acid in amount of 0.45 g. The solution was stirred for 15 minutes, 150 rpm at 60 °C and filtered (Roth, 0.45 µm syringe filter). Individual layers (1 cm^2) were printed 1, 3 and 5 times under equal

environmental conditions on top of ITO PET substrate (Sigma-Aldrich, 1000 Å of ITO, 60 Ω/sq, T > 75 % at 550 nm). All films were dried at room temperature for 24 h and annealed in air at 120 °C (EHRET, TK4067, Germany) for 1 h. Detailed information on device encapsulation, experimental setup and measurements procedure can be found in Section 2.2 and Section 2.5.

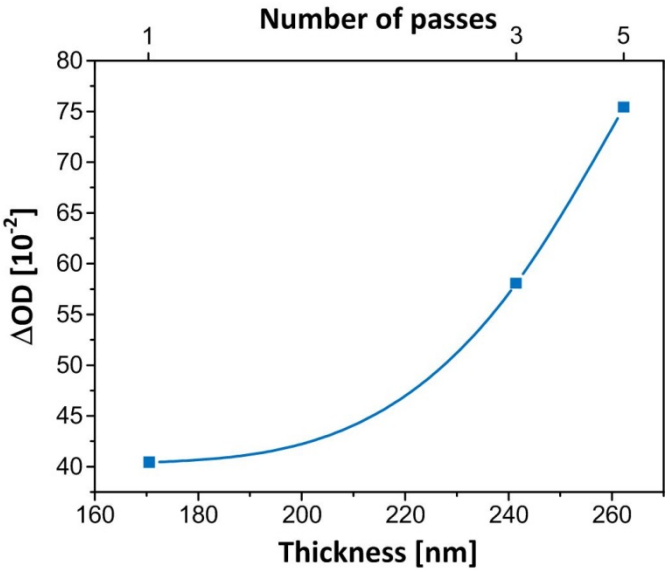

Figure 5.31. Change in optical density in function of the *a*-WO_3 film thickness. The electrochromic action was induced by applying voltage of ±4V

Every successive printing pass causes the layer grow of about 23 nm. Films printed 5 times exhibit change in optical density almost twice higher than films printed with single pass.

5.5.7. Spectral response

Transmittance spectra for dual-phase films containing NPs synthesized in 6 h long process under various precursor acidities in their colored and bleached states are illustrated in Figure 5.32. In the bleached state all samples have high transmittances in a visible region indicating high transparency of the coatings. Under application of a negative voltage (-2 V), all microstructures exhibited observable transmittance modulation performance. The apparent transmittance reduction of *a*-WO_3/(*m*-WO_3 + *ortho*-$WO_3 \cdot 0.33H_2O$) at ~525 nm comes from the existence of both crystalline phases.

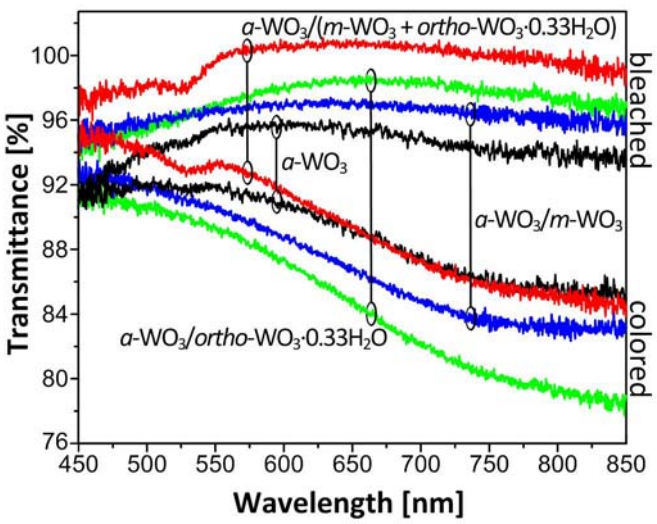

Figure 5.32. UV-vis transmittance of dual-phase inkjet printed films containing NPs synthesized in 6 h long process under various precursor acidities; bleaching and coloring optical states were induced by ±2 V operational voltages

Chapter 6

Thermosetting composite solid electrolyte for electrochromic applications

This chapter is written based on:

Wojcik, P.J., Cruz, A.S., Pereira, L., Martins, R., Fortunato, E.: Resin-based Thermosetting Composite Solid Electrolyte for Electrochromic Applications **– under submission.**

Wojcik, P.J., Santos, L., Pereira, L., Martins, R., Fortunato, E.: Resin-based Thermosetting Composite Solid Electrolyte: New Perspective on Printed Electrochemical Devices **– under preparation.**

Contributions of Co-Authors:

A.S. Cruz performed mechanical strength measurements and provided raw data for analysis.

L. Pereira performed SEM characterization.

Chapter 6. Thermosetting composite solid electrolyte for electrochromic applications

Chapter 6. Thermosetting composite solid-state electrolyte for electrochromic applications

Summary

One of the most active trends in applied electrochemistry is the development of solid ionic conductors with electrical, mechanical and optical properties tailored for a specific functional application. This chapter describes a new concept of solid state electrolyte based on plastic crystal doped with lithium salt, dispersed in a thermosetting polymer resin network. This soft matter electrolyte meets requirements for electrochromic applications, exhibiting ionic conductivities of 10^{-6} - 10^{-4} S cm^{-1} at ambient temperature, Young's Modulus in the range of 0.1 - 1.4 MPa and operational temperature up to 115 °C. The effect of composition on electrolyte performance is comprehensively studied using multi-factorial DOE coupled with Multivariate Analysis.

Results presented in this chapter were obtained *via* two different approaches. Firstly, structural, electrical and mechanical properties of TCSE determined based on standard characterization methods were discussed. Secondly, specific relationships not manifested through experimental data analysis, were revealed by examination of developed mathematical model.

6.1. Introduction

Ion conductive materials are an integral part of any electrochemical device including batteries, EC devices, DSSCs and fuel cells. The replacement of liquid electrolyte by solid-state membranes or thin printed films is mandatory in order to extend a lifetime of electrochemical applications while enhancing their reliability and stability. This seems to be crucial for industrialization and the commercialization of those devices in the near future. Many alternative soft matter quasi-solid and solid state electrolytes have been designed over a decade aiming at high ionic conductivity at room temperature (σ_{RT}), good mechanical properties (expressed usually by Young's Modulus, E) and long-term stability. Two of the most widely employed approaches for solid state electrolyte formulation have been (i) polymer doping with organic or inorganic salt resulting in so called polymer electrolytes and (ii) inclusion of a polymer in a semi-solid conductive matrix based on plastic crystalline material, called composite electrolyte. The mechanical properties of polymer electrolytes decrease the severity of problems that might arise from the encapsulation, size, cost and durability issues. However, the polymer electrolytes that have shown the most promise for use in electrochemical applications exhibit low σ_{RT} values, due to the limited chain mobility above their glass transition temperature [154].

Composite solid state electrolytes are based on a new class of semisolid-state ion conductive matrixes in which lithium salt is dissolved in either molecular or ionic plastic crystals yielding satisfying σ values [155]. Plastic crystals are mesophases characterized by rotational and/or orientational disorder while retaining the long-range translational order resulting in high diffusivity and plasticity. As a consequence, defects are formed inducing fast ion motion and giving plastic mechanical properties to the material. Pure molecular plastic crystals exhibit very low σ values (e. g. Succinonitrile, ~10^{-7} S cm^{-1}) [156]. However, addition of lithium salt (*e.g.* lithium perchlorate, $LiClO_4$) results in a drastic increase in σ value [157, 158], which is particularly important from application perspective.

Plastic crystal phase of highly polar molecules of Succinonitrile (N≡C–CH_2–CH_2–C≡N, SCN) has been recognized as an excellent matrix for the formation of many solid state ionic conductors. The fast ion mobility of mixture consisting of SCN and lithium salt (SCN:Li^+) was attributed to the orientational disorder and the existence of vacancies in the plastic crystal lattice. However, SCN:Li^+ mixture is highly plastic and deforms easily under low stress and due to this limitation it cannot be used as self-standing film. Additionally, those materials were found to be volatile and flammable, due to the presence of large amount of flammable molecular compound [159]. Unsuitable or inconvenient nature of those materials in intended applications initiated studies aimed at enhancing their mechanical strength as well as safety and reliability, in particular by using various additives. The use of polymer network as a mechanical support for ion conducting matrix is clearly important in the developments of all-solid-state electrochemical devices. To dates, previous studies on enhancement of the mechanical properties of composite solid state electrolytes have been limited to the addition of polymers such as polyacrylonitrile (PAN) [160], polyethylene oxide (PEO) [161–163], polyvinylidenefluoride-co-hexafluoropropyle (PVdF-HFP) [161, 162, 164, 165], and recently also very promising cross-linked UV-curable polyethylene glycol dimethacrylate (PEGDMA) [166] or ethoxylated trimethylolpropane triacrylate (ETPTA) [164, 165].

As it is shown in Figure 6.1, state-of-the-art approaches often succeed to achieve satisfactory tensile properties, while maintaining high σ values. However, composite solid state electrolytes formed by those polymers have shown at least one of the disadvantages, which may impede or preclude their application in commercialized electrochemical devices, namely, insufficient thermal stability, poor contact to the electrodes, swelling, solution leaking, propensity to crystallize, sensitivity to ambient atmosphere or high price [160, 163–165]. Solid state electrolyte based on thermosetting polyester resin, which will be introduced in this chapter is located in less favorable range in the plot shown in Figure 6.1. However this new material is free from disadvantages listed above, which makes it particularly interesting from application perspective.

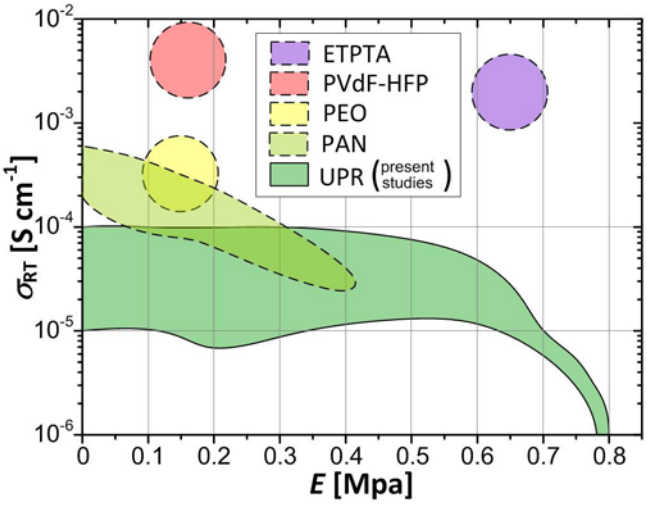

Figure 6.1. Graphical review presenting the σ_{RT} as a function of E for the state-of-the-art polymer reinforced plastic crystal composites based on ETPTA [164, 165], PVdF-HFP [164, 165], PEO [163] and PAN [160] in comparison to UPR used in present studies

An alternative strategy for increasing conductivity and/or tensile properties of composite electrolytes is through the addition of metal oxide NPs, *e.g.* TiO_2, Al_2O_3 or SiO_2 [167, 168]. The achieved improvement was attributed to an increase in the plastic flow of the material and number of mobile defects, which both together constitute to the enhanced charge mobility. However, this effect was found to be not universal, varying with plastic crystal and NPs used. It should be noted that the use of NPs such as TiO_2 turns transparent material into white opaque membrane. This transformation is especially desirable in case of EC displays [10], in which the color contrast between colored EC pattern and white background would be significantly increased when TiO_2 loaded electrolyte is applied.

Semi-solid and solid state composite electrolytes have been investigated in the context of electrochromic applications based on organic chromogenic materials, indicating their compatibility with these materials [169–171]. However, to the author' knowledge, no report on their application with inorganic electrochromic material exists. This chapter describes a new concept of thermosetting composite solid electrolyte (hereinafter, abbreviated as TCSE) based on plastic crystal doped with lithium salt dispersed in a thermosetting resin.

6.2. Materials and methods

6.2.1. Materials used

Following materials were used for formulation of liquid mixtures for TCSE development (pre-TCSE): Succinonitrile (Aldrich), orthophtalic unsaturated polyester resin monomer (UPR, Resipur 9600 - TGR, Resiquimica), benzoyl peroxide (BPO, Merck), N,N – dimethylaniline (DMA, Aldrich),

6% cobalt naphthenate (CoN, Aldrich), lithium perchlorate, ($LiClO_4$, Sigma-Aldrich) and TiO_2 nanoparticles (Aeroxide P25, Degusa). All components were used as received and no prior treatment was provided for water removal. The role of individual elements is the following: UPR – source of monomers for polymer network, BPO – activator (catalyst) of polymerization reaction, DMA and CoN – promoters of polymerization reaction. Low-density polyethylene (LDPE) foil was used for protection of casted membranes.

6.2.2. Design of Experiment

The Design of Experiment and statistical data analysis were performed using JMP 8.0 (S.A.S. Institute Inc., Cary, NC, USA). Ternary contour graphical presentations of the models were generated in JMP 8.0 and processed graphically in Visio 2010 (Microsoft Corp., Redmond, USA) diagraming tool. A screening design method has been selected to characterize TCSE because studied problem involves a large number of input factors. The DOE approach for TCSE studies consists of following phases:

- factors identification that affects the outcome of the experiment and responses that give a measure of the outcome –pre-TCSE components;
- selection of appropriate experimental design for screening/surface modeling;
- generation of design matrix – recipes for pre-TCSE mixtures;
- conducting the experiments – membrane casting;
- data collection – TCSE membrane measurements;
- data fitting and generating mathematical models for each response;
- analysis of significance;
- pre-TCSE mixture optimization;
- drawing conclusions.

Designed mixture of pre-TCSE for membrane casting is described as ternary system consisting of conductive matrix (CM), resin pre-polymer (RPP) and inorganic filler (TiO_2). Those independent factors are proportions of different components of a blend (weight fractions) which must satisfy condition described by Equations 6.1 and 6.2.

$$w_{\mathrm{CM}} + w_{\mathrm{RPP}} + w_{\mathrm{TiO_2}} = 1 \tag{6.1}$$

$$\begin{cases} w_{\mathrm{CM}} = \dfrac{m_{\mathrm{CM}}}{m_t} \\ w_{\mathrm{RPP}} = \dfrac{m_{\mathrm{RPP}}}{m_t} \\ w_{\mathrm{TiO_2}} = \dfrac{m_{\mathrm{TiO_2}}}{m_t} \end{cases} \tag{6.2}$$

Where: w_{CM} stands for weight fraction of conductive matrix consisting of SCN and $LiClO_4$; w_{RPP} is a weight fraction of RPP consisting of resin monomer together with comonomers, activator (BPO), and promoters (DMA and CoN); $w_{\mathrm{TiO_2}}$ is a weight fraction of TiO_2 NPs serving as inorganic filler and m_t is a total mass of the mixture; m_{CM}, m_{RPP} and $m_{\mathrm{TiO_2}}$ denote weights of those components in agreement with Equations 6.3 and 6.4 describing their composition.

$$m_{\mathrm{CM}} = (100 - x_{\mathrm{a}})\%\mathrm{SCN} + x_{\mathrm{a}}\%\mathrm{LiClO_4} \tag{6.3}$$

$$m_{RPP} = (100 - x_{\mathrm{b}} - x_{\mathrm{c}} - x_{\mathrm{d}})\%\mathrm{RPP} + x_{\mathrm{b}}\%\mathrm{BPO} + x_{\mathrm{c}}\%\mathrm{DMA} + x_{\mathrm{d}}\%\mathrm{CoN} \tag{6.4}$$

Where x_{a} stands for a weight percent of lithium salt in a conductive matrix; x_{b}, x_{c} and x_{d} are weight percent of BPO, DMA and CoN in RPP, respectively.

Pre-TCSE mixtures must meet strict quantitative relationships which impose several constrains. In case of UPR used, all samples must contain no more than 25 wt% of conductive matrix, which guarantees (empirically proven) effective curing of resin network. Moreover, a weight percent of lithium salt in a conductive matrix must be not greater that 9% due to the limited solubility of $LiClO_4$ in SCN. Based on imposed restrictions the values of individual weight fraction ranges and weight percent levels of factors were defined as follow: $0.1 \leq w_{\mathrm{CM}} \leq 0.25$, $0.75 \leq w_{\mathrm{RPP}} \leq 0.9$ and $0 \leq w_{\mathrm{TiO_2}} \leq 0.05$, while $5 \leq x_{\mathrm{a}} \leq 9$, $2 \leq x_{\mathrm{b}} \leq 4$, $0.05 \leq x_{\mathrm{c}} \leq 0.1$and $0 \leq x_{\mathrm{d}} \leq 0.1$. Due to the complexity of such constricted experimental area, the application of D-optimal algorithm for experimental design seems to be essential.

The computer aided D-optimal design for seven factors studied shown in Table 6.1, was composed of 28 experiments (minimum) and the order of runs was fully randomized to minimize the effect of uncontrolled factors that could affect the final results. Application of a computer aided D-optimal design successfully reduced the number of overall experimental trials from 2187 defined for three-level full factorial design down to 28 runs in present studies. For each of experimental runs a pre-TCSE mixture and casting mold were freshly prepared just before the use in laboratory experiment.

Due to the limited accuracy of weighting, a real design matrix calculated for each set according to the analytical balance reading was applied in analysis (see Section 6.5.1 for real design matrix).

Table 6.1. The list of experimental trials (design matrix) according to three component mixture design methodology with four additional continuous factors

Run	Factors						
	Mixture			Continuous			
	w_{CM}	w_{RPP}	w_{TiO2}	x_a	x_b	x_c	x_d
1	0.1	0.85	0.05	9	4	0.05	0.1
2	0.25	0.75	0	9	4	0.1	0.1
3	0.159	0.841	0	7	2	0.1	0.05
4	0.25	0.75	0	9	2	0.1	0
5	0.2	0.75	0.05	5	4	0.05	0
6	0.2	0.75	0.05	5	2	0.1	0
7	0.1	0.888	0.012	5	2	0.1	0
8	0.1	0.9	0	9	2	0.05	0
9	0.25	0.75	0	5	4	0.1	0
10	0.1	0.85	0.05	5	2	0.05	0.1
11	0.2	0.75	0.05	7	3	0.075	0.1
12	0.246	0.754	0	5	4	0.05	0.1
13	0.211	0.789	0	5	2	0.05	0
14	0.2	0.75	0.05	9	2	0.05	0
15	0.172	0.828	0	5	3	0.1	0.1
16	0.1	0.9	0	5	4	0.05	0
17	0.1	0.882	0.018	7	3	0.05	0.1
18	0.1	0.9	0	9	4	0.1	0
19	0.25	0.75	0	9	2	0.05	0.1
20	0.2	0.75	0.05	9	4	0.1	0
21	0.1	0.9	0	5	2	0.075	0.1
22	0.164	0.812	0.023	9	2	0.075	0.05
23	0.25	0.75	0	5	3	0.05	0.05
24	0.1	0.85	0.05	5	4	0.1	0.1
25	0.25	0.75	0	9	4	0.05	0
26	0.1	0.85	0.05	7	3	0.075	0
27	0.1	0.85	0.05	9	2	0.1	0.1
28	0.236	0.75	0.014	5	2	0.1	0.1

6.2.3. Pre-TCSE mixture formulation and processing

All formulation steps of pre-TCSE were performed under ambient atmosphere with components being exposed to a relative humidity of ~50 %. Requisite amount of $LiClO_4$ was added to molten SCN and stirred at 60 °C, 250 rpm until homogeneous mixture was obtained (40 min – 2 h). Resin monomer, BPO and TiO_2 (if required) were added and stirred at 60 °C, 250 rpm for 40 min. Dispersion was then cooled down to RT. Requisite amount of resin monomer mixed with 6% Cobalt Naphthenate (50:1) and resin monomer mixed with DMA (50:1) were added to the dispersion and mixed at RT, 100 rpm for 1 min. Viscous liquid mixture was then casted in a custom made stainless steel mold (see Section 1.4.3.2 for more details on mold construction) and left for curing at room temperature for 24h.

Resulting self-standing membrane with dimensions of ~0.5 x 100 x 100 mm was removed from the mold. LDPE foils were applied from both sides of the membrane for surfaces protection. Ageing was performed for 24h at ambient atmosphere in a hot plate heated up to 60 °C.

The water wash-out of TCSE (TCSE*) was performed in a magnetically stirred glass flask filled with water. The process was carried out for several hours at room temperature. The TCSE* membrane was then removed from the bath and dried for several days at room temperature.

6.2.4. Characterization

The structural characterization of ion conductive membranes was performed by XRD (XPert PRO, PANalytical). Supplementary structural characterization of TCSE membranes and pre-TCSE components were performed by FT-IR (Nicolet 6700, Thermo Electron Corporation).

Thermal analysis was performed by Thermogravimetric Analyzer (STA 449 F3 Jupiter, Netzsch) in air with a heating ramp of 5 °C min^{-1} starting from room temperature up to 375 °C.

Conductivity measurements were performed by impedance spectroscopy over the frequency range 1 – 10^6 Hz with amplitude of 200 mV rms using Gamry Reference 600 Potentiostat (Gamry Instruments). Semi-solid $(100 - x)_{wt\%}SCN{:}x_{wt\%}LiClO_4$ mixtures were molten and injected directly into custom-build cylindrical electrochemical cell shown schematically in Figure 6.2.

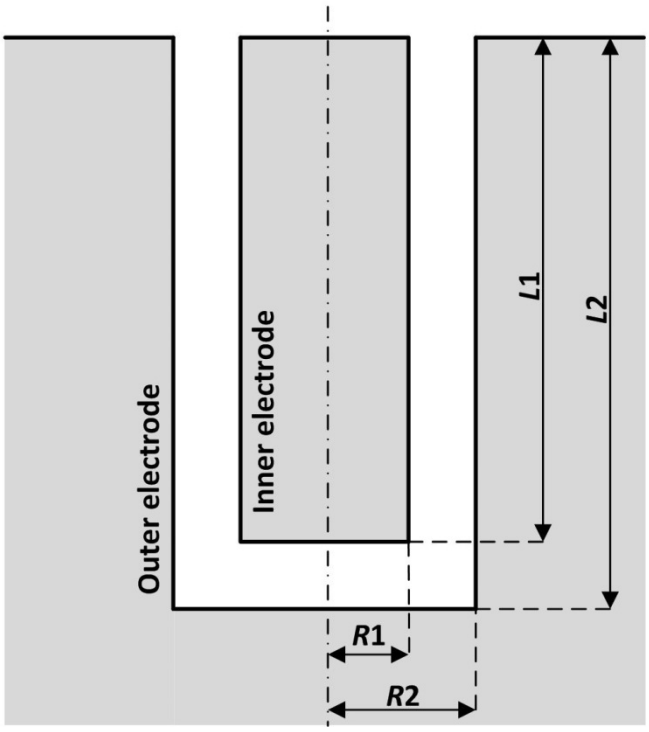

Figure 6.2. Schematic drawing of the cylindrical electrochemical cell for ionic conductivity measurements of liquid/gel samples

Geometric Factor (*GF*) of the electrochemical cell was calculated according to Equation 6.5:

$$GF^{-1} = \pi \int_{L1}^{L2} \int_{R1}^{R2} (2rl + r^2)\, drdl \quad (6.5)$$

Where: r and l stand for variable diameter and length, respectively; $R1$ is the diameter of an inner electrode, $R2$ is the diameter of an outher electrode, $L1$ is the length of upper electrode and $L2$ is the cell depth. For a given values of $L1$ = 17 mm, $L2$ = 18 mm, $R1$ = 2.5 mm and $R2$ = 3.5 mm the GF^{-1}= 114.083π m, which gives GF = 0.279 cm^{-1}.

In case of TCSE membranes, circular disk shaped samples with area of 1 cm^2 were cut and sandwiched in between two stainless steel electrodes, which gives *GF* value equal to the value of the membrane thickness expressed in cm (d_m cm^{-1}). The matrix of those cylindrical or plane capacitors enables for simultaneous electrochemical measurements of 9 liquid/gel or solid ion conducting samples (see Figure 1.13, Figure 1.14 in Section 1.4.3.3 for detailed information on electrochemical setup). The matrix of conductivity cells was assembled with custom-made thermostat system (see Figure 1.15) consisting of Thermoelectric Power Generation Peltier Module (200C, 6.4V, 3.1W, Thermovoltaik), Temperature Controller (TC-XX-PR-59, Supercool AB) and Liquid Cooling System (Bigwater 760is, Thermaltake) inside a nitrogen filled glove-box (Captair Pyramid Glove Bag). Measurements were taken as the temperature was increasing from -10 to 100 °C. The intersection of the spike corresponding to electrode-electrolyte interface with the real impedance axis in Nyquist plot was taken as sample resistance (R_a). Value of σ was calculated according to the following formula $\sigma = GF \cdot R_a^{-1}$. Activation energy ($E_a$) was approximated by Arrhenius formula *via* linear fitting of conductivity data plotted in function of T^{-1} according to Equation 6.6

$$\sigma(T) = Ae^{\frac{-E_a}{k_B T}} \quad (6.6)$$

Where: $\sigma(T)$ is the ionic conductivity at given temperature level (T), k_B – is the Boltzmann's constant and A denotes pre-exponential coefficient which describes all the remaining factors that influence conduction.

Tensile measurements on rectangular shaped samples with dimensions of d_m x 10 x 30 mm were performed using Low-load Horizontal Tensile Test Machine (Minimat 2000) at room temperature and strain rate of 5 mm min^{-1}.

6.3. Results and Discussion

6.3.1. Data Fitting and Factorial Analysis

Electrical, mechanical and optical characterization of developed TCSE membranes brought massive data describing the characteristics of this material as a function of composition. Due to the complexity

of analysis and the number of studied responses, the following considerations are limited to main parameters describing temperature-dependent values of σ, E_a and E. However, these responses were given in a more precise form referring to specific level of temperature in case of σ, and selected temperature range in case of E_a. Thus, following responses were considered: σ at -10 °C ($\log\sigma_{-10}$), 0 °C ($\log\sigma_0$), 20 °C ($\log\sigma_{\mathrm{RT}}$) and 40 °C ($\log\sigma_{40}$); E_a at temperature > 20 °C $\left(E_{\mathrm{a}}^{\mathrm{Zone\ A}}\right)$ and < 20 °C $\left(E_{\mathrm{a}}^{\mathrm{Zone\ B}}\right)$; E at 20 °C (see Table 6.2 for values of measured responses). Mathematical fitting based on multiple regression have been performed for each response using second order polynomial function expressed by Equation 6.7.

$$Y_{\mathrm{k}} = \sum_{\mathrm{i}=1}^{3} \beta_{\mathrm{i}} X_{\mathrm{i}} + \sum_{\mathrm{i}=1}^{7} \sum_{\mathrm{j}=\mathrm{i}+1}^{7} \beta_{\mathrm{ij}} X_{\mathrm{i}} X_{\mathrm{j}} + \sum_{\mathrm{i}=4}^{7} \beta_{\mathrm{ii}} X_{\mathrm{ii}}^2 + \varepsilon \qquad (6.7)$$

Surface responses Y_{k} were determined by three controlled mixture components $X_{\mathrm{i}}(1 \leq i \leq 3)$ and four continuous factors $X_{\mathrm{i}}(4 \leq i \leq 7)$, coefficients of the main factors, the coefficients of the first and second order interactions β_{i}, β_{ij}, β_{ii}, respectively and ε which represent random error of the method. This model was found to be the most appropriate for data fitting within the experimental space. The contour plots on a trilinear coordinate scale shown in following sections were used to present multiple regression fittings of experimental results according to Equation 6.7. These ternary plots were generated as a function of mixture weight fractions *i.e.* w_{CM}, w_{RPP} and $w_{\mathrm{TiO_2}}$ while the weight percentage values of other components (lithium salt, catalyst and promoters) were kept constant. This graphical methodology provides an easy way to demonstrate the efficacy of the enhanced performance of TCSE membranes. Each response is assumed to depend only on the relative proportions of components present in the mixture and not on the amount of the mixture. As D-optimal design enables to include a certain number of experiments from outside the design and consider them during the analysis, the final table contains data of runs in which accuracy of weighting was insufficient to be considered as a part of DOE, but high enough to be included in the analysis (see Table 6.3). Increased number of runs aims at improved prediction ability of the model.

The model optimality was evaluated based on a summary of fit (least square regression). The polynomial responses modeling (Equation 6.7) performed by screening design appeared to be sufficient for all responses under consideration, because of its ability to supply high coefficient of determination values of $R^2_{\mathrm{adj}}(\log\sigma_{-10}) = 0.98$, $R^2_{\mathrm{adj}}(\log\sigma_0) = 0.99$ $R^2_{\mathrm{adj}}(\log\sigma_{RT}) = 0.98$, $R^2_{\mathrm{adj}}(\log\sigma_{40}) = 0.97$, $R^2_{\mathrm{adj}}\left(E_{\mathrm{a}}^{\mathrm{Zone\ A}}\right) = 0.98$, $R^2_{\mathrm{adj}}\left(E_{\mathrm{a}}^{\mathrm{Zone\ B}}\right) = 0.92$ and $R^2_{\mathrm{adj}}(E) = 0.8$, indicating a good correspondence between fitting and the experiments, while simultaneously minimizing the overall number of coefficients. Therefore, a more-complex design-type is not required, and the lower match between real values and prediction in case of E comes from difficulties associated with accurate tensile measurements.

Within tested range of concentrations, no clear dependence between properties of TCSE membranes and absolute amounts of catalyst (BPO) and promoters (DMA and CoN) in pre-TCSE exists. Significance analyses of all effects (factors and interactions) performed using Student's *t*-test statistics (see Section 6.5.2 for detailed analysis) shown amounts of those components to be irrelevant. Therefore, we can assume that low limit of concentrations for BPO and DMA are sufficient for curing, while CoN can be eliminated from the formulation as redundant component. It is worth mentioning that CoN in conjunction with DMA is known to improve hardness and/or shorten the cure time, while having detrimental effect on the chemical resistance performance. However, any of these aspects is considered in present studies.

6.3.2. Structural and Thermal Analysis

The X-ray diffraction patterns of ion conductive membranes in a transparent and opaque form are shown in Figure 6.3a and b respectively, while the pattern of neat SCN is provided for comparison in Figure 6.3c. Neat SCN sample at room temperature exhibits two characteristic peaks at $2\theta = 19.8°$ and $2\theta = 28.1°$, which indicate its plastic crystal phase. Both diffraction patterns of TCSE don't show the presence of the plastic crystal phase material indicating a high degree of structural disorder at molecular scale. In accordance with DSC-TG results, TCSE membranes appear to be completely homogeneous and amorphous materials. SCN crystalline structure deterioration is known to enhance the rate of isomer transition from *gauche* to *trans*, which consequently increases the *trans* conformer concentration and lowers E_a for ion conduction process [156, 172]. Crystallinity observed in opaque TCSE sample was associated to the addition of TiO_2 NPs as inorganic filler.

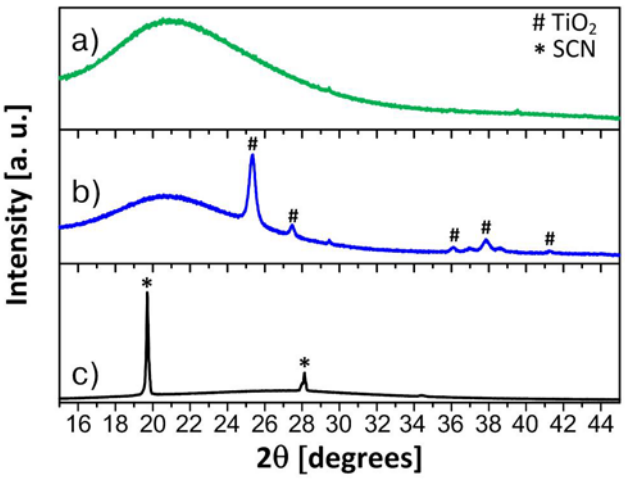

Figure 6.3. Room temperature XRD patterns of a) transparent TCSE membrane (run 2), b) opaque TCSE membrane containing TiO_2 (P25) nanopowder (run 1) and c) neat SCN

ATR FT-IR spectra in the region of 600 – 3700 cm^{-1} of neat SCN, $LiClO_4$, RPP, CM, TCSE membrane (run 4a) and water wash-out TCSE* membrane (run 4a) are presented in Figure 6.4.

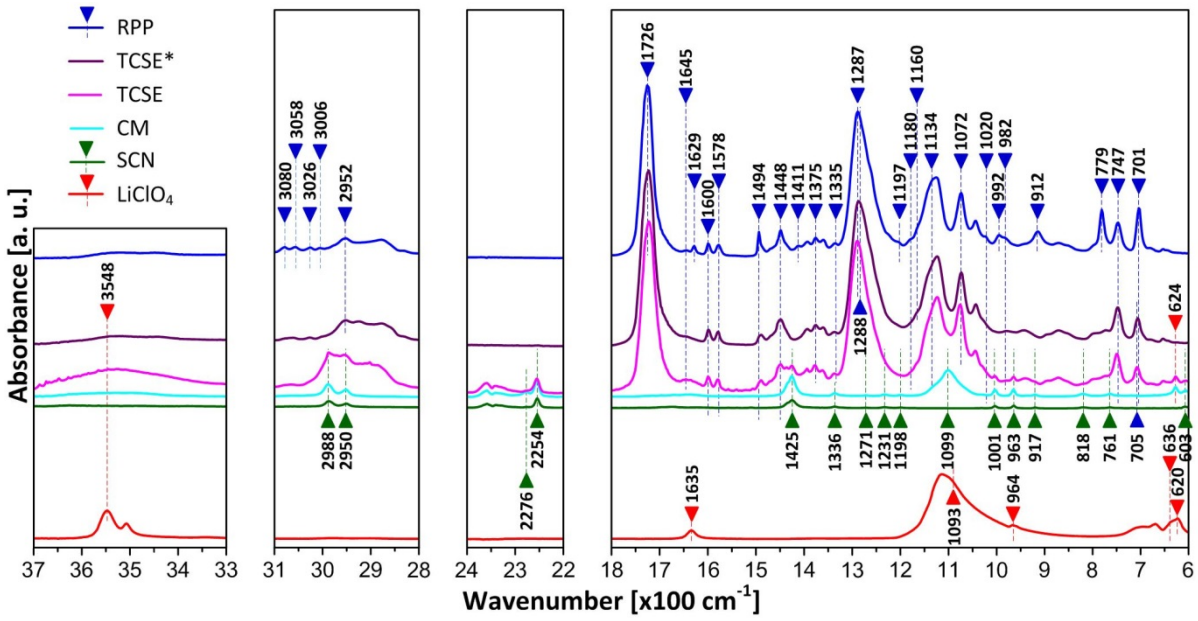

Figure 6.4. ATR FT-IR spectra in the range of 600 – 3700 cm^{-1} of neat SCN, $LiClO_4$, RPP, CM, and TCSE membrane (run 4a, before and after water wash-out)

The SCN, $LiClO_4$ and CM have been in focus of many FT-IR spectroscopic studies [173–177], thus, the band assignments for these two species are well documented. As there are also reported FT-IR studies on UPR [178–181], a complete assignment of the characteristic vibrational wave numbers of neat components and TCSE membranes can be performed. The characteristic fundamental vibrational modes and corresponding wave number collected from ATR FT-IR experimental spectra are listed in Table 6.5 and Table 6.6. ATR FT-IR absorbance spectra of CM and TCSE show correlation between those two samples. This leads to the conclusion the CM dispersed in styrene based RPP and cured at room temperature, retains its molecular structure. Comparison between vibrational modes of TCSE and TCSE* shows that water wash-out process removes entire CM fraction out from the membrane, leaving pure polymer network. This fact is especially interesting when recycling of the TCSE membranes is concerned.

SCN exhibits plastic crystal phase formation at temperatures between -40 and 58 °C, assigned to crystalline/plastic crystal and plastic crystal/liquid phase transitions T_{cp} and T_m, respectively [157]. Figure 6.5 shows the DSC-TG traces of neat SCN, RPP and TCSE membrane.

An endothermic peak in DSC spectra recorded for neat SCN at 58 °C is assigned to the melting point of plastic crystal (mentioned above T_m). TCSE consists of lithium doped SCN dispersed in the resin network which results in morphology changes, implying an increase in concentration of structural defects (*i.e. trans* isomers). It is therefore expected that TCSE still demonstrates plastic crystal behavior, however, characteristic peaks assigned to T_{cp} and T_m are placed below recorded temperature range. The shift of T_m of SCN to lower temperatures reveals deterioration in the crystalline structure. Similar behavior was observed by Ha *et al.*[164], Patel *et al.*[182] and Ryou *et al.*[166] in mixtures of

SCN:Li+ with ETPTA, PAN and PEGDMA, respectively. An endothermic peaks recorded for resin monomer at 143 °C and 256 °C are assigned to the boiling point of styrene in which resin monomers are dispersed and irreversible decomposition of monomers, respectively. Exothermic peak recorded for TCSE membrane at 115 °C indicates softening point of the material. Shortly above this level, slow but progressive irreversible decomposition of membrane starts to proceed.

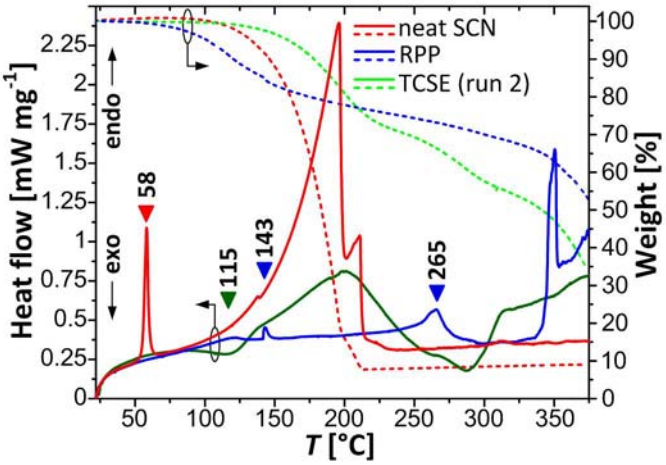

Figure 6.5. DSC-TG traces of neat SCN, RPP and TCSE membrane

TG has been used to investigate the thermal degradation of neat SCN, UPR and TCSE membrane. The weighs loss of neat SCN starts to slowly appear at 75 °C and proceeds dramatically at temperatures above 150 °C, until complete sublimation at 214 °C. Progressive weight loss of resin monomer at the lower temperatures comes from the styrene evaporation till its boiling point is achieved. Further weight loss of this component related to thermal decomposition of monomer, proceeds smoothly. TG curve recorded for TCSE indicates relatively high thermal stability of this material. The weight loss of TCSE starts to appear only near the softening point (~115 °C), which can be determined as maximum operation temperature for TCSE based on this specific resin (UPR). It is worth mentioning that UPR is considered as the one with low softening point when comparing to other thermosetting resins. Therefore, it is expected that the use of resin with higher softening point would extend operational temperature range of resulted TCSE.

6.3.3. Ionic Conductivity Evaluation

The conductivities of SCN:Li^+ mixtures have been already widely discussed in the state-of-the-art [156–158, 172, 175]. Although, the elementary transport mechanism has not been well established, it was proposed that the rotation of the C-C bond of the two -CH_2 moieties of SCN allows the molecule to rotate from *gauche* to *trans* isomer, which acts as an impurity resulting in the enhancement of lattice defects and lowering of E_a for ionic conduction [183].

Figure 6.6 shows σ as a function of temperature between -10 and 100 °C, for the most conductive TCSE sample and $(100 - x)_{wt\%}$SCN:$x_{wt\%}$$LiClO_4$, x={5, 7, 9} mixtures. In a solid plastic phase of $(100 - x)_{wt\%}$SCN:$x_{wt\%}$$LiClO_4$ mixture, both *trans-gauche* isomers and ion electrostatic interaction contribute to E_a, while in molten phase only the second one governs the conduction [156]. In a normal crystalline phase of SCN (below -33 °C), only the *gauche* conformation exists and all rotary motions are frozen [157]. Therefore, the σ value is expected to be significantly lower than in other phases.

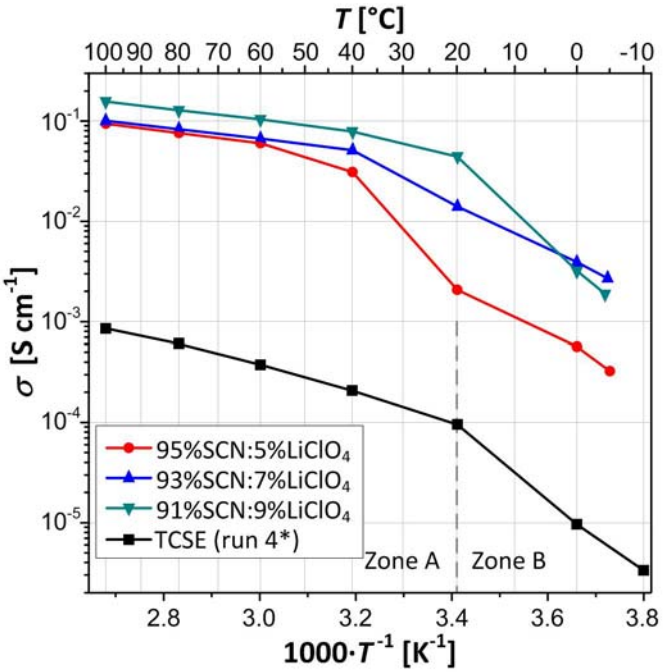

Figure 6.6. The temperature-dependent σ of TCSE (run 4*) in comparison to $(100 - x)_{wt\%}$SCN:$x_{wt\%}$$LiClO_4$, x = {5, 7, 9}

Contrary to other conventional polymer electrolytes in which temperature depended conductivity is fitted as a straight line over the entire range, the same plot for TCSE is separated into two distinctive zones (see Figure 6.6). Upper temperature region denoted as Zone A corresponds to molten phase of SCN:Li^+ mixtures characterized by E_a in the range of 0.1 – 0.25 eV, while lower temperature region denoted as Zone B shows dependence typical for plastic crystalline phase of SCN:Li^+ with E_a in the range of 0.22 – 0.49 eV [156]. Degree of σ_{RT} depends on both, SCN and lithium salt concentrations as it is shown in Figure 6.7a and b, respectively. Low SCN content causes blocking of percolation pathways by resin polymer network. Increased SCN content is beneficial for high σ value, but at the same time deterioration of mechanical properties occurs, which will be demonstrated in the following sections. Similarly, reduction of lithium salt content decreases effective charge carrier concentration. While the σ_{RT} in function of SCN content has nearly linear character in studied range, the dependence between σ_{RT} and $LiClO_4$ content bends at higher concentrations due to the limited salt solubility in the plastic crystal solvent.

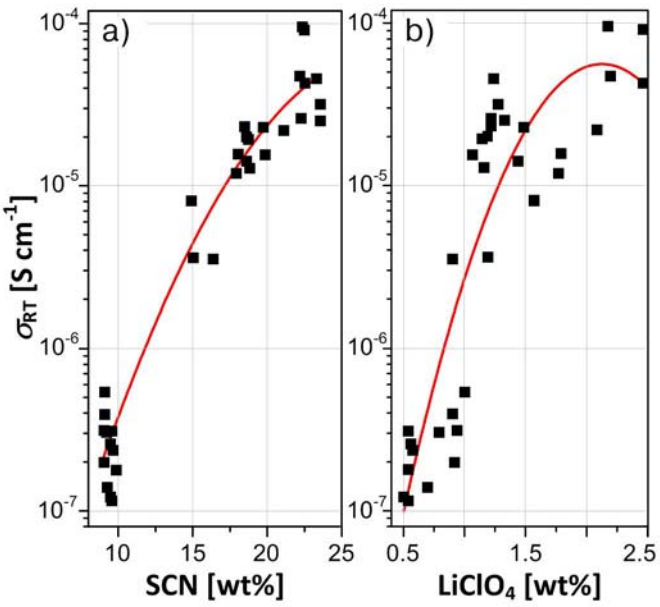

Figure 6.7. The dependence between σ_{RT} a) SCN and b) $LiClO_4$ weight concentrations in total pre-TCSE mixture (red line represents trend estimation) for TCSE membranes

Ternary surface response of σ_{RT} for TCSE presented in Figure 6.8 shows values in range of 10^{-6} - 10^{-4} S cm^{-1} depending on the mixture composition.

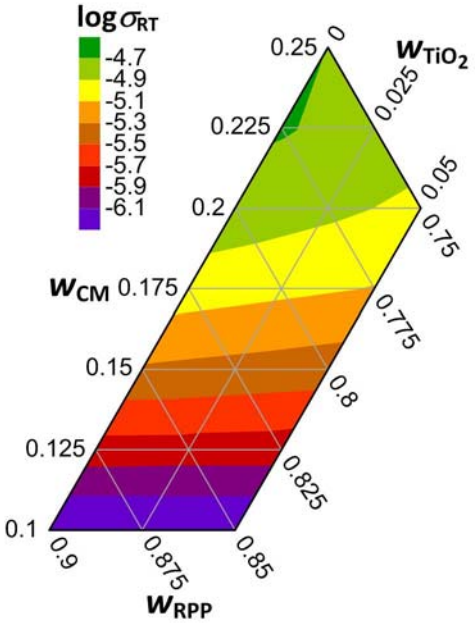

Figure 6.8. Ternary surface response of logσ_{RT} for TCSE mixture composition for x_a = 9, x_b = 2, x_c = 0.05 and x_d = 0

According to this representation, the influence of TiO_2 NPs on electrolyte performance seems to play minor role at ambient temperature, when comparing to SCN and $LiClO_4$. However, the information about the influence of NPs filler on σ values in a full range of operational temperature would be

beneficial for better understanding of this material system. Such considerations have been performed based on mathematical model and are presented in Section 6.3.5.

Semi-solid SCN:$LiClO_4$ mixtures were found to exhibit a three step activation process corresponding to molten, plastic crystalline and crystalline phases [156]. Although, DSC-TG measurements of TCSE do not indicate any phase transition in a temperature range between -10 and 100 °C, the temperature-dependent σ of those membranes is clearly influenced by the physical state of SCN component. The electrical properties of TCSE are rapidly changing depending on the temperature range as it was presented in Figure 6.6. Therefore, the ion conduction process of each TCSE may be described by two E_a values corresponding to molten ($E_a^{\text{Zone A}}$) and plastic crystal ($E_a^{\text{Zone B}}$) phase of SCN component as it is shown in Figure 6.9. The exponential dependence between σ_{RT} and $E_a$makes this relation of utmost importance.

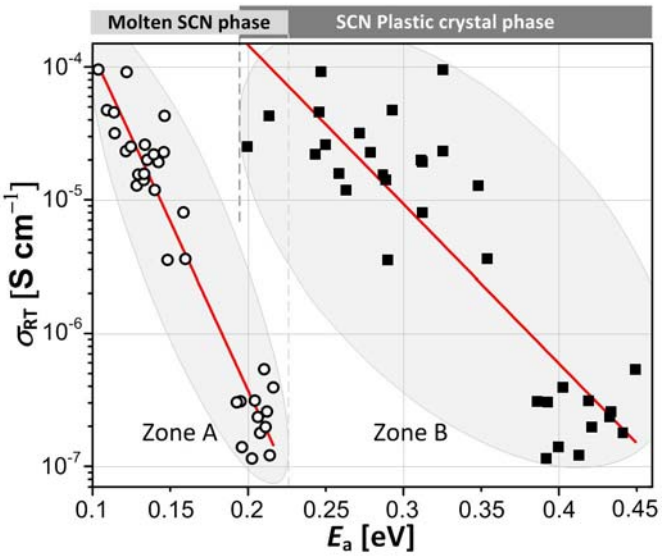

Figure 6.9. The dependence between σ_{RT} and E_a for TCSE in a full range of compositions (red line represents trend estimation); the pre-exponential coefficient *A* in Arrhenius equation is considered as not temperature dependent

Presented in Figure 6.10 a and b ternary surface responses of E_a for TCSE membranes correspond to Zone A and Zone B, respectively. The influence of SCN, RPP and TiO_2 on E_a values follow the same trend as it was in case of $\log\sigma_{RT}$, irrespectively to the temperature range.

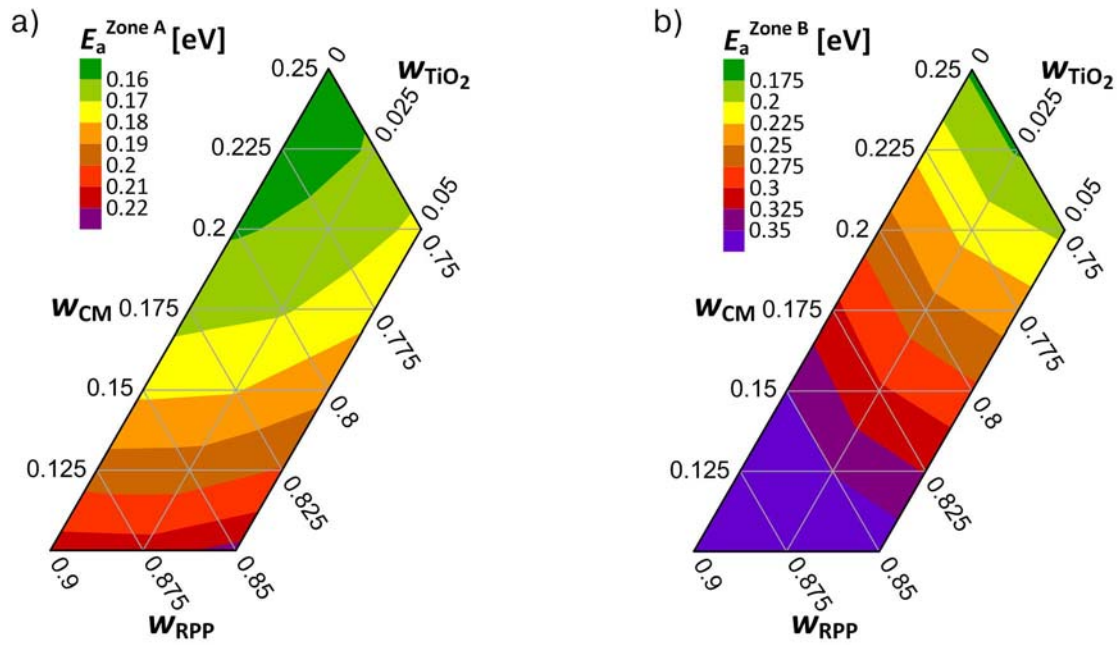

Figure 6.10. Ternary surface responses of E_a for TCSE mixture corresponding to a) molten (Zone A) and b) plastic crystal phase (Zone B) of SCN for $x_a = 9$, $x_b = 2$, $x_c = 0.05$ and $x_d = 0$

6.3.4. Mechanical Properties

The physical appearances of TCSE membranes employing UPR as polymer network are presented in Figure 6.11.

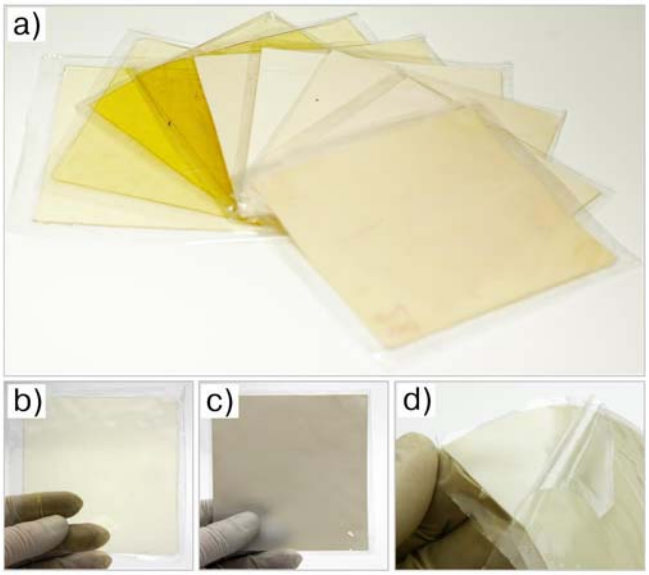

Figure 6.11. Digital camera images of a) ~0.5 x 100 x 100 mm TCSE self-standing b) transparent and c) opaque (TiO_2 loaded) membranes protected by d) LDPE foil

Yellowish color comes from DMA component which is necessary together with BPO for ambient temperature curing. However, the addition of DMA is not required with methyl ethyl ketone peroxide (MEKP) and cumene hydroperoxide (CHP) catalyst systems resulting in colorless product. All samples prepared according to DOE recipes appear to be non-tacky solidified self-standing membranes. No plasticized SCN was smeared out from the membranes during ageing process performed for 24h at ambient atmosphere in a hot plate heated up to 60 °C, which indicates that ion conductive matrix is strongly entrapped in the resin network. Moreover, TCSE membranes are free of SCN dendritic crystal structures which were found to cause bleaching problems in EC applications [170].

The degree of elasticity and plasticity of TCSE depend mainly on the SCN to RPP ratio and to a lesser extend to $LiClO_4$ concentration. It is suggested that high σ values of TCSE at lower E values (0.1 – 0.8 MPa) can be explained by the existence of SCN:Li^+ interconnected channels which provide ionic pathways. Those conductive channels start to break up at certain minimum concentration of SCN into TCSE causing a dramatic decrease in ion transport (2 orders of magnitude in σ_{RT} value), shown in Figure 6.12a.

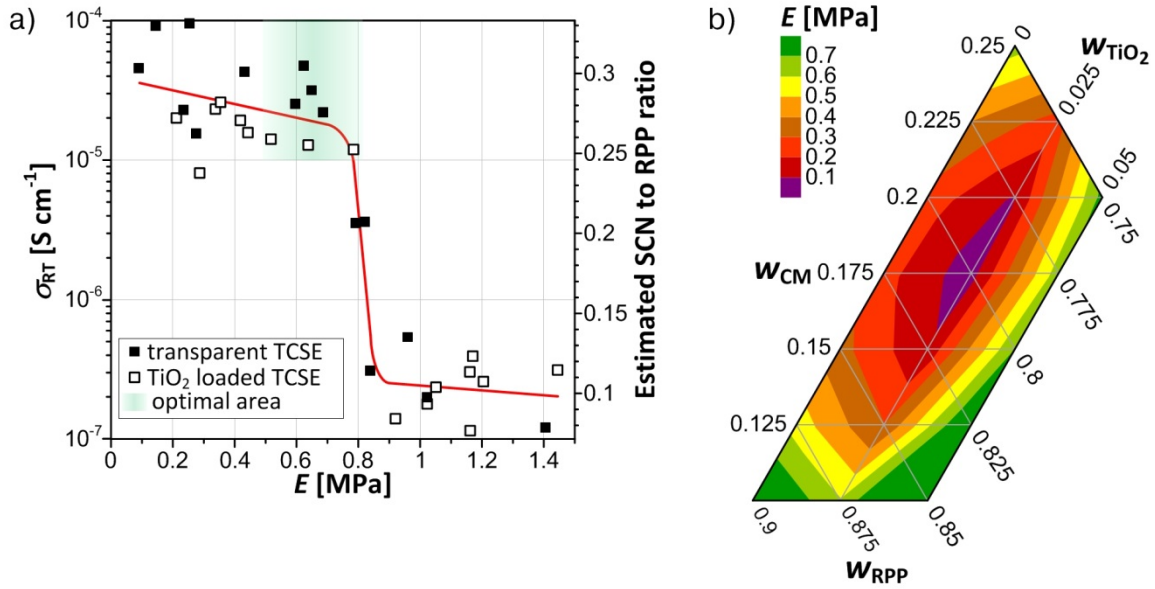

Figure 6.12. Relation between mechanical properties expressed by E and a) logσ_{RT} in a full range of compositions (red line represents a trend estimation), and b) TCSE mixture composition; values of SCN to RPP ratio were estimated based on their near linear relationship with logσ_{RT}; selected area corresponds to the most desirable material which combine both, relatively high E and σ_{RT}; ternary surface response of E is drawn for $x_a = 9$, $x_b = 2$, $x_c = 0.05$ and $x_d = 0$

As it was empirically determined, σ_{RT} values higher than 10^{-5} S cm^{-1} can be achieved when the weight ratio between SCN and RPP is not lower than ~0.25. According to the technical specification of resin monomer used in TCSE formulation, E value of cured pure resin is 14 MPa, while addition of w_{CM}=

0.1 into RPP results in 10 times lower values. It is therefore evident that SCN works as plasticizer in resin network. As long as TCSE is considered for application in electrochemical devices, the ion conducting membrane should provide sufficient plasticity in order to assure a good contact with electrodes. As the broad range of mechanical properties exists for each kind of resin, the selection of UPR was directed to the relatively plastic one. Ternary surface response of *E* for TCSE presented in Figure 6.12b graphically summarizes all conclusions drawn in this section. It shows that *E* values in range between 0.1 and 0.7 MPa can be achieved, depending on pre-TCSE composition.

The method employed here to convert semi-solid SCN:Li^+ material into a solid state membrane *via* dispersion in polyester resin under suitable optimization, may be also extended to other resins such us epoxy, vinyl ester, phenolic polyurethane and acrylic. To the best of the author's knowledge, the new concept of TCSE comprise a rare example among soft matter electrolytes where electrical, optical and mechanical properties can be predictably and easily manipulated *via* variation in source of thermosetting resin applied in formulation. The ion mobility of TCSE based on those resins may be different than in case of orthophtalic unsaturated polyester resin used in present studies due to the different interaction with Li^+ ions, according to chemical structure of resin molecule. Besides medium in which resin monomer is dispersed (e. g. styrene, water or solvent-free), no additional molecular liquid solvent is involved in TCSE preparation, having a huge advantage over typical solid state polymer electrolytes.

6.3.5. Relationships revealed *via* mathematical modeling

Multiple regression provides sophisticated method for revealing relationships among variables in the pre-TCSE composition, allowing to explore material capabilities and to identify settings for factors that yield optimal performance.

Multiple regression model of σ has been examined in order to reveal the impact of TiO_2 NPs loading on TCSE performance. Results of this analysis are presented in Figure 6.13. The model revealed a negative impact of TiO_2 loading across all studied concentrations at temperatures corresponding to Zone A. However, conductivity enhancement is evident in the same samples at lower temperatures denoted as Zone B. Obtained results suggest that the existence of MO_X NPs provide an opportunity for increase of defect concentration in plastic phase and thus, higher conductivities can be achieved. However, the strain associated with NPs does not lead to significant enhancement in conductivity of a molten phase of SCN, as it is already rich in defects. Nanosize TiO_2 filler shows an optimum concentration of about 3 wt%.

The dependence between E and x_a was found to be a linear function in a full range of studied lithium salt doping concentrations, and can be described by slope-intercept form given by Equation 6.8.

$$E(x_a) = mx_a + \text{const} \quad (6.8)$$

The slope of this function (m) shows how strong such dependence is, according to Equation 6.9.

$$m = \frac{\Delta E}{\Delta x_a} \quad (6.9)$$

Values of m in function of SCN to RPP ration showing the impact of $LiClO_4$ concentration on E are presented based on mathematical model in Figure 6.14a. Accordingly to predicted response, 1 wt% increase in $LiClO_4$ concentration causes increase in value of E between 0.03 and 0.08 MPa (for $w_{TiO_2} = 0$), depending on SCN to RPP ratio. The higher the SCN content, the stronger effect observed. Impact of lithium salt on mechanical properties is more evident in TiO_2 loaded membranes ($w_{TiO_2} = 0.05$) where 1 wt% increase in $LiClO_4$ concentration causes increase in E between 0.11 and 0.14 MPa. The impact of lithium salt on tensile properties of ionic conductive membranes has been also observed in other SCN:Li^+ based materials reinforced by polymer inclusion (PAN) [160]. However, in contrary to present observation, an increase in $LiClO_4$ concentration caused lower E values in favor of increased plasticity.

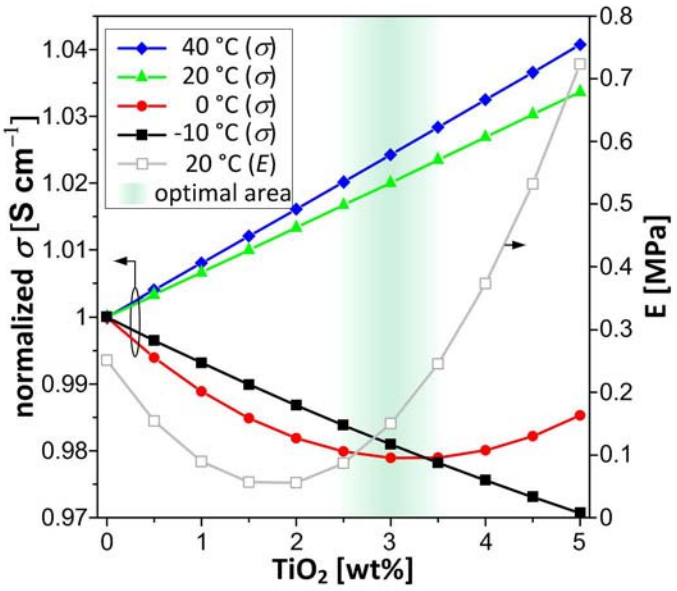

Figure 6.13. Outcomes of the mathematical model analysis showing values of σ (normalized to 1) and E as a function of TiO_2 weight concentration; $w_{CM} = 0.2$, $x_a = 9$, $x_b = 2$, $x_c = 0.05$ and $x_d = 0$

Similarly, the dependence between $\log\sigma_{RT}$ and x_a was found to be a quadratic function given by Equation 6.10.

$$\log\sigma_{RT}(x_a) = ax_a^2 + bx_a + c \quad (6.10)$$

Where a was found to be a constant common to all TCSE samples, equal to 0.0081, while b is the declivity of the parabola. The coefficient a and b together control the axis of symmetry (x_a') of $\log\sigma_{RT} = f(x_a)$ parabola, and hence give the vertex according to Equation 6.11.

$$x'_a = -\frac{b}{2a} \tag{6.11}$$

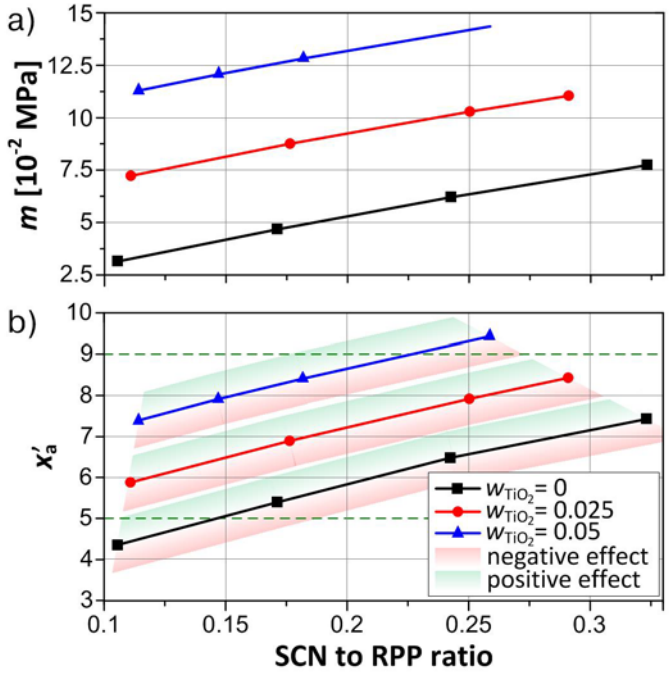

Figure 6.14. Outcome of mathematical model analysis showing values of a) m and b) x'_a as a function of SCN to RPP ratio in a full range of studied lithium salt doping concentrations and various levels of TiO_2 weight fraction

As the coefficient $a > 0$ the vertex is also a minimum point of parabola which monotonically increase to the right or to the left of point x'_a. An increase in $LiClO_4$ concentration (x'_a) has a negative effect on $\log\sigma_{RT}$ when $x_a \in [5, x'_a)$ and a positive effect when $x_a \in (x'_a, 9]$. The position of x'_a within $LiClO_4$ doping range (5 – 9 wt% of a conductive matrix) is presented in Figure 6.14b as a function of SCN to RPP ratio. High $LiClO_4$ content is appropriated in case of transparent TCSE membranes, but it's pointless in case of TiO_2 loaded membranes, especially for high values of SCN to RPP ratio.

6.3.6. Optimization

Response surface maps of experimental regions presented in Figure 6.15 and Figure 6.12 facilitate the decision-making process when determining the most appropriate TCSE for specific application. However, a numerical multi-response optimization described in Section 2.3.4 enables to find the specific point that maximizes the global desirability, and thus, optimal overall performance of the material [49]. In order to find an optimum composition of pre-TCSE mixture, this method was applied also in this study.

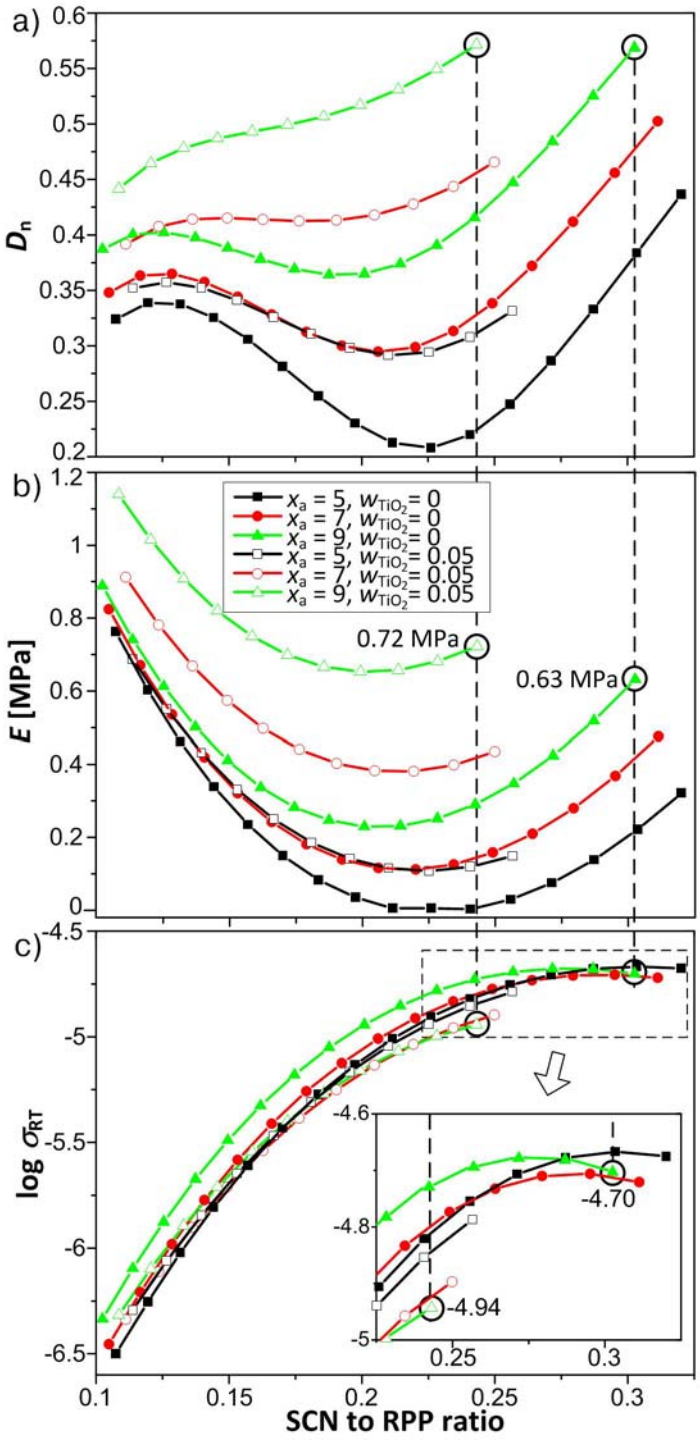

Figure 6.15. Pre-TCSE mixture optimization through a) overall desirability function (D_n) vs. SCN to RPP ratio for transparent and TiO_2 loaded ($w_{TiO_2} = 0.05$) membranes with x_a = {5, 7, 9}, with corresponding b) E and c) σ_{RT} values based on mathematical model for x_b = 2, x_c = 0.05 and x_d = 0 (inset: magnification of the selected range)

In order to determine composition of the best performing TCSE membrane, the optimization goal was defined as the maximum values for both, logσ_{RT} and E_a. Weights and importance values were set as equal (W_k = I_k = 1), while desired response limits (Y_k^{min}, Y_k^{max}) were defined according to

experimental results presented in Table 6.3. The resulting optimum mixture for TCSE is described by following two sets of factors corresponding to both variants, transparent: w_{CM} = 0.25, w_{RPP} = 0.75, $w_{\mathrm{TiO_2}}$= 0, x_{a} = 9, x_{b} = 2, x_{c} = 0.05, x_{d} = 0 and opaque: w_{CM} = 0.2, w_{RPP} = 0.75, $w_{\mathrm{TiO_2}}$= 0.05, x_{a} = 9, x_{b} = 2, x_{c} = 0.05, x_{d} = 0. Maximum overall desirability shown in Figure 6.15a, reached the value of 0.57 for both, transparent and opaque TCSEs. The desirability function plot gives the performance prediction for optimized TCSE composition shown in Figure 6.15b and c in which logσ = -4.70, E = 0.63 MPa for transparent and logσ = -4.94, E = 0.72 MPa for opaque, thereby fulfilling all of the optimization requirements.

6.4. Conclusions

A notable achievement in the TCSE, as compared to the former composite solid state electrolytes based on plastic crystals, is the realization of extremely cheap and mechanically resistive material, while simultaneously affording high ionic conductivity. While dispersion of lithium doped plastic crystals in resin network is directly responsible for enhancement in tensile properties, high solubility of lithium salt in plastic crystal increase in free charge carrier concentration resulted in high ionic conductivity reaching the level of 10^{-4} S cm^{-1}. Those advantages in addition to the non-flammability, non-volatility, plasticity and high electrochemical and thermal stability, suggest that the wide use of TCSE concept in a range of indoor and outdoor electrochemical devices could soon be a reality.

Unquestionable advantage of TCSE concept is the fact that all formulation steps can be performed under ambient atmosphere. Studies performed by Das *et al.* [175] have shown that exposure of SCN, $LiClO_4$ and their mixture to a relative humidity of 50 – 60 % results in neither physical nor electrical changes when compared to samples prepared under inert atmosphere. Similarly, most of the commercial thermosetting resins are designed to be used under moderate humidity, which does not influence their properties.

Proposed experimental design methodology appeared to offer a sufficiently accurate mathematical modeling with a complete coverage of experimental trials while the total number of designed experiments has been significantly reduced. The identification of the critical composition factors via screening experiment was essential for the TCSE optimization.

6.5. Supporting information

This section provides supplementary information about real design matrix, significance analysis and ATR FT-IR frequencies assignment.

6.5.1. Real design matrix and measured values of responses

A real design matrix calculated for each set according to the analytical balance readings and measured values of selected parameters are presented in Table 6.2 and Table 6.3, respectively.

Table 6.2. Real factors for each experimental run calculated according to the analytical balance readings

Run	Factors (real values)						
	Mixture			Continuous			
	w_{CM}	w_{RPP}	w_{TiO2}	x_a	x_b	x_c	x_d
1	0.100	0.850	0.050	9.011	3.931	0.054	0.106
2	0.250	0.750	0	9.894	4.019	0.098	0.109
3	0.162	0.838	0	7.347	2.065	0.088	0.057
4	0.244	0.756	0	9.007	1.951	0.123	0
4[a]	0.246	0.754	0	8.856	1.976	0.137	0
5	0.198	0.752	0.050	5.997	3.973	0.050	0
5[a]	0.197	0.757	0.046	6.190	4.007	0.068	0
6	0.199	0.751	0.050	5.755	1.960	0.109	0
6[a]	0.200	0.749	0.051	5.812	2.688	0.103	0
7	0.102	0.886	0.012	5.620	2.014	0.101	0
8	0.101	0.899	0	9.893	2.086	0.053	0
9	0.249	0.751	0	5.137	4.025	0.110	0
10	0.101	0.847	0.052	5.572	2.005	0.052	0.098
10[a]	0.104	0.890	0.005	5.181	2.117	0.049	0.103
11	0.201	0.748	0.051	7.162	2.977	0.078	0.101
12	0.246	0.754	0	5.047	4.233	0.057	0.104
13	0.212	0.788	0	7.021	1.963	0.064	0
13[a]	0.209	0.791	0	5.108	1.986	0.072	0
14	0.197	0.753	0.050	8.982	2.021	0.085	0
15	0.173	0.827	0	5.237	3.031	0.098	0.104
16	0.101	0.899	0	5.358	4.043	0.052	0
17	0.100	0.882	0.018	6.986	2.998	0.052	0.105
18	0.100	0.900	0	9.225	3.978	0.101	0
19	0.232	0.768	0	9.007	2.122	0.047	0.096
20	0.199	0.751	0.050	9.021	4.116	0.104	0
21	0.100	0.900	0	5.021	2.057	0.077	0.117
22	0.165	0.812	0.023	9.543	2.066	0.075	0.055
23	0.249	0.751	0	5.334	3.508	0.055	0.052
24	0.101	0.848	0.051	5.316	4.010	0.102	0.102
25	0.250	0.750	0	9.889	4.021	0.084	0
26	0.100	0.849	0.051	7.887	3.023	0.073	0
27	0.100	0.850	0.051	9.395	2.101	0.102	0.106
28	0.235	0.751	0.014	5.184	2.007	0.102	0.109

[a] repeated experimental runs due to the low accuracy of weighting

Table 6.3. Measured values of selected responses corresponding to each experimental run

Run	Responses						
	$\log\sigma_{-10}$	$\log\sigma_0$	$\log\sigma_{RT}$	$\log\sigma_{40}$	$E_a^{\text{Zone A}}$	$E_a^{\text{Zona B}}$	E
					[eV]	[eV]	[MPa]
1	-8.17	-7.53	-6.41	-5.64	0.216[c]	0.403	1.170
2	-5.09[c]	-4.74[c]	-4.04	-3.54[c]	0.122	0.247	0.144
3	-6.88	-6.49	-5.44	-4.86	0.160	0.354	0.821
4	-5.65	-5.18	-4.33	-3.88	0.109	0.293	0.623
4[a]	-5.48	-5.02	-4.02[c]	-3.68	0.104[b]	0.325	0.255
5	-6.11	-5.57	-4.70	-4.20	0.135	0.312	0.212
5[a]	-6.10	-5.58	-4.63	-4.17	0.122	0.325	0.338
6	-6.13	-5.60	-4.72	-4.09	0.142	0.312	0.419
6[a]	-6.46	-5.91	-4.89	-4.44	0.128	0.348	0.638
7	-8.58	-7.89	-6.63	-5.98	0.206	0.433	1.051
8	-8.31	-7.52	-6.27	-5.56	0.210	0.449[c]	0.959
9	-5.71	-5.30	-4.50	-4.15	0.114	0.272	0.648
10	-8.56	-7.79	-6.59	-5.80	0.212	0.434	1.205
10[a]	-8.74[b]	-7.97	-6.75	-5.95	0.208	0.441	1.023
11	-6.16	-5.63	-4.85	-4.30	0.133	0.289	0.518
12	-5.41	-5.03	-4.34	-3.87	0.114	0.246	0.091[b]
13	-5.82	-5.42	-4.64	-4.09	0.146	0.279	0.234
13[a]	-5.97	-5.61	-4.81	-4.28	0.129	0.287	0.275
14	-5.98	-5.64	-4.93	-4.41	0.140	0.263	0.785
15	-6.60	-6.27	-5.45	-4.88	0.148	0.290	0.791
16	-8.03	-7.61	-6.51	-5.77	0.195	0.386	0.839
17	-8.68	-7.89	-6.86	-6.06	0.196	0.400	0.920
18	-8.61	-7.84	-6.70	-5.86	0.211	0.421	1.022
19	-5.70	-5.34	-4.66	-4.15	0.139	0.243	0.686
20	-5.87	-5.53	-4.80	-4.25	0.133	0.259	0.443
21	-8.57	-8.09[b]	-6.92	-6.08	0.214	0.413	1.406
22	-6.30	-5.98	-5.09	-4.44	0.159	0.312	0.287
23	-5.35	-5.17	-4.60	-4.14	0.125	0.200[b]	0.596
24	-8.38	-8.06	-6.94[b]	-6.12[b]	0.203	0.392	1.162
25	-5.14	-4.98	-4.37	-3.90	0.146	0.213	0.432
26	-8.30	-7.62	-6.52	-5.75	0.193	0.393	1.161
27	-8.41	-7.68	-6.51	-5.71	0.204	0.419	1.445[c]
28	-5.72	-5.28	-4.59	-4.10	0.134	0.250	0.355

[a] repeated experimental runs due to the low accuracy of weighting,
[b] minimum response obtained $Y_k^{\min}$,
[c] maximum response obtained $Y_k^{\max}$

6.5.2. Significance analysis

The significance analysis has been performed using Student's *t*-test statistics. Qualitatively and quantitatively estimated linear and quadratic effects of all factors and their interactions are shown in Table 6.4. Elements marked by (+) indicate these coefficients that were determined to be significant

and thus, which factor (or factor interactions) had a major effect on a particular response value quantifying their importance (by [number]).

Table 6.4. Factorial analysis of results obtained *via* Student's *t*-test statistics

Effect	Response model						
	$\log\sigma_{-10}$	$\log\sigma_{0}$	$\log\sigma_{RT}$	$\log\sigma_{40}$	$E_a^{\text{Zone A}}$	$E_a^{\text{Zona B}}$	E
w_{CM}	+ (2)	+ (2)	+ (2)	+ (2)	+ (2)	+ (2)	+ (2)
w_{RPP}	+ (1)	+ (1)	+ (1)	+ (1)	+ (1)	+ (1)	+ (1)
w_{TiO2}	-	+ (3)	+ (4)	-	+ (9)	-	+ (3)
$w_{CM}\cdot w_{RPP}$	-	+ (4)	+ (3)	+ (3)	+ (6)	-	+ (6)
$w_{CM}\cdot w_{TiO2}$	-	-	-	-	-	-	+ (4)
$w_{CM}\cdot x_a$	-	-	-	-	+ (7)	-	-
$w_{CM}\cdot x_b$	-	-	-	-	+ (5)	-	-
$w_{CM}\cdot x_c$	-	-	-	-	-	-	-
$w_{CM}\cdot x_d$	-	-	-	-	-	-	-
$w_{RPP}\cdot w_{TiO2}$	-	-	-	-	-	-	+ (5)
$w_{RPP}\cdot x_a$	-	-	-	-	-	-	-
$w_{RPP}\cdot x_b$	-	-	-	-	-	+ (4)	-
$w_{RPP}\cdot x_c$	-	-	-	-	-	-	-
$w_{RPP}\cdot x_d$	-	-	-	-	-	-	-
$w_{TiO2}\cdot x_a$	-	-	-	-	-	+ (3)	-
$w_{TiO2}\cdot x_b$	-	-	-	-	+ (8)	-	-
$w_{TiO2}\cdot x_c$	-	-	-	-	-	-	-
$w_{TiO2}\cdot x_d$	-	-	-	-	-	-	-
$x_a\cdot x_b$	-	-	-	-	+ (3)	-	-
$x_a\cdot x_c$	-	-	-	-	+ (4)	-	-
$x_a\cdot x_d$	-	-	-	-	-	-	-
$x_b\cdot x_c$	-	-	-	-	-	-	-
$x_b\cdot x_d$	-	-	-	-	-	-	-
$x_c\cdot x_d$	-	-	-	-	-	-	-
$x_a\cdot x_a$	-	-	-	-	-	-	-
$x_b\cdot x_b$	-	-	-	-	-	-	-
$x_c\cdot x_c$	-	-	-	-	-	-	-
$x_d\cdot x_d$	-	-	-	-	-	-	-

(-) not significant; (+) significant; (number) importance according to *t*-ratio value (1 corresponds to the most significant factor)

As the emphasis of DOE was screening the [number] indicate the most significant effects (starting from value [1]) sorted by the absolute value of the *t*-ratio which lists the test statistics for the hypothesis that each parameter is zero. Each *t*-ratio value expresses the ratio of particular parameter estimate to its standard error, and has a Student's *t*-distribution if the hypothesis is true. The model predicts in general that TCSE performance depends mainly on w_{CM} and w_{RPP}, while w_{TiO2} and x_a play minor role. Other concentrations, namely x_b, x_c and x_d were found to be on the verge of significance, showing only slight relevance when $E_a^{\text{Zone A}}$ and $E_a^{\text{Zone B}}$ responses are considered.

6.5.3. ATR FT-IR frequencies assignment

The characteristic fundamental vibrational modes and corresponding wave number collected from ATR FT-IR experimental spectra are listed in Table 6.5 and Table 6.6.

Table 6.5. ATR FT-IR vibrational frequencies assignment in the range of 3700 – 1250 cm^{-1}

Observed band [cm^{-1}]	Mixture component(s)	Band assignment	Reference
3548	$LiClO_4$ / H_2O	ν(O–H)	[173]
3080	Styrene	ν(C–H_2) asym.	[178]
3058	Styrene	ν(C–H) ring	[178]
3026	Styrene	ν(C–H) ring	[178]
3006	Styrene	ν(C–H_2) sym.	[178]
2988	SCN	ν(C–H) trans and gauche	[174]
2952	Styrene	ν(C–H) asym.	[179]
2950	SCN	ν(C–H) trans and gauche	[174]
2276	SCN / $LiClO_4$	Li^+–CN^- interaction	[175]
2254	SCN	ν(C≡N) trans and gauche	[174]
1726	UPR	ν(C=O) carbonyl ester	[179–181]
1645	UPR	ν(C=C)	[181]
1635	$LiClO_4$ / H_2O	ClO_4^-, δ(O–H)	[173, 176]
1629	Styrene	ν(C=C)	[178]
1600	Styrene	ν(C–C) ring	[178]
1578	Styrene	ν(C–C) ring	[178]
1494	Styrene	δ(C–H)	[178, 180]
1448	Styrene	δ_S(C=H_2); δ(C–H) ring	[178]
1425	SCN	δ(CH_2) trans and gauche	[174]
1411	Styrene	δ_S(C=H_2)	[178]
1375	UPR	δ(C–H)	[179]
1336	SCN	ω(C=H_2) gauche	[174]
1335	Styrene	δ(C–H) ring	[178]
1288	Styrene	ρ(C–H); ν(C–C)	[178]
1287	UPR	ν(C–O–C) aromatic ester, asym.	[179]
1271	SCN	ω(C=H_2) trans	[174]

ν - stretching; δ - bending; ω - wagging; τ - twist; ρ - rocking; δ_S - scissoring

Table 6.6. ATR FT-IR vibrational frequencies assignment in the range of 1250 – 600 cm^{-1}

Observed band [cm^{-1}]	Mixture component(s)	Band assignment	Reference
1231	SCN	$\tau(C{=}H_2)$ gauche	[174]
1197	Styrene	$\nu(C{-}C)$	[178]
1198	SCN	$\tau(C{=}H_2)$ trans and gauche	[174]
1180	Styrene	$\delta(C{-}H)$ ring	[178]
1160	UPR	$\nu(C{-}O{-}C)$ aliphatic ester, asym.	[179]
1134	UPR	$\nu(C{-}O{-}C)$ aromatic ester, asym.	[179]
1099	SCN	$C{=}H_2$ gauche	[160]
1093	$LiClO_4$	Formation of Li^+ ClO_4^-	[184]
1072	UPR	$\nu(C{-}O{-}C)$ aliphatic ester, asym.	[179]
1020	Styrene	$\rho(C{=}H_2)$; $\nu(C{-}C)$ ring	[178]
1001	SCN	$\rho(C{=}H_2)$ gauche	[174]
992	Styrene	τ (C=C); $\omega(C{-}H)$	[178, 181, 185]
982	UPR	$\nu(C{=}C)$	[181]
964	$LiClO_4$	ClO_4^-	[186]
963	SCN	$\nu(C{-}CN)$ gauche	[174]
917	SCN	$\nu(C{-}CN)$ trans	[174]
912	Styrene	$\delta(CH_2{-}CH)$	[185]
818	SCN	$\nu(C{-}CN)$ gauche; $\delta(CH_2)$ gauche	[156, 160, 174]
779	Styrene	C=C	[187]
761	SCN	$\rho(C{=}H_2)$ trans	[174]
747	UPR	Phenyl ring	[181]
705	UPR	$\omega(C{-}H)$ aromatic ring	[179]
701	Styrene	-	[180, 181]
636	$LiClO_4$	$Li^+{-}ClO_4^-$; free and bonded ClO_4^-	[161, 188]
624	$LiClO_4$	free ClO_4^-	[161, 175]
620	$LiClO_4$	$\delta(ClO_4^-)$; free ClO_4^-	[177, 188]
603	SCN	$\delta(C{-}C{-}C)$ gauche	[174]

ν - stretching; δ - bending; ω - wagging; τ - twist; ρ - rocking; δ_S - scissoring

Chapter 7

General discussion and conclusions

This chapter presents prototypes demonstrated in:

Wojcik, P.J., Pereira, L., Martins, R., Fortunato, E.: Statistical mixture design and multivariate analysis of inkjet printed *a*-$WO_3/TiO_2/WO_X$ electrochromic films. ACS Comb. Sci. 16 (1) 5-16 (2014

Wojcik, P.J., Cruz, A.S., Santos, L., Pereira, L., Martins, R., Fortunato, E.: Microstructure control of dual-phase inkjet-printed *a*-$WO_3/TiO_2/WO_X$ films for high-performance electrochromic applications. Journal of Materials Chemistry. 22, 13268 (2012).

Wojcik, P.J., Pereira, L., Martins, R., Fortunato, E.: Metal Oxide Nanoparticle Engineering for Printed Electrochemical Applications. In: Nano-Electrochemistry: Electrochemical Synthesis Methods, Properties and Characterization Techniques. Handbook of Springer **– in press**.

Wojcik, P.J., Santos, L., Pereira, L., Martins, R., Fortunato, E.: Tungsten Oxide Nanoparticle Engineering for Inkjet Printed Electrochromic Devices **– under submission.**

Wojcik, P.J., Santos, L., Pereira, L., Martins, R., Fortunato, E.: Formation mechanism and electrochromic response of WO_X nanoparticles synthesized *via* hydrothermal process **– under preparation.**

Wojcik, P.J., Cruz, A.S., Pereira, L., Martins, R., Fortunato, E.: Resin-based Thermosetting Composite Solid Electrolyte for Electrochromic Applications **– under submission.**

Wojcik, P.J., Santos, L., Pereira, L., Martins, R., Fortunato, E.: Resin-based Thermosetting Composite Solid Electrolyte: New Perspective on Printed Electrochemical Devices **– under preparation.**

Wojcik, P.J., Cruz, A.S., Butti, P., Pereira, L., Martins, R., Fortunato, E.: Effect of annealing on the electrochromic performance of inkjet printed WO_3 films **– under preparation.**

Chapter 7. General discussion and conclusions

Chapter 7. General discussion and conclusions

Summary

This chapter constitutes a comprehensive summary of the publications appended in this thesis. In the first part, a brief history of prototype development is presented in order to visualize a long stretch of technical research that was performed within this work. Although new results on device performance are not presented in this part, a synthesis of new conclusions by combining results from appended articles is provided in second part of the chapter. The main findings with regard to the research objectives are summarized. The general conclusions together with strengths and limitations of studies performed within presented thesis are also described.

7.1. Prototypes of printed EC devices

In this section some examples of EC devices developed within this PhD work are presented. There are three important stages in prototype development history presented in this thesis. Firstly, the development of inkjet printed EC films based on inorganic material (*i.e.* WO_3). Secondly, the development of all-solid-state rigid and flexible EC devices with use of printing methods for selected films. Finally, prototypes of fully printed EC devices on flexible substrates (*i.e.* PET and paper) developed in a R2R compatible processes, at low temperature.

All prototypes presented in this section incorporate inkjet or screen printed *a*-WO_3 or *a*-WO_3/TiO_2/WO_X film as an optically active material. A first demonstration whose purpose was to verify that the concept of printed inorganic EC films have the potential for real-world applications was performed at the end of 2008. One of the first prototypes comprising of two flexible substrates, an inkjet printed *a*-WO_3 and liquid electrolyte is presented in Figure 7.1. At this stage of studies, EC film was typically printed on top of commercial ITO PET foil or IZO coated (*via* in-house PVD system) paper substrate. The second electrode was provided by ITO PET or ITO glass substrate. Both electrodes were sandwiched with drop-casted liquid electrolyte.

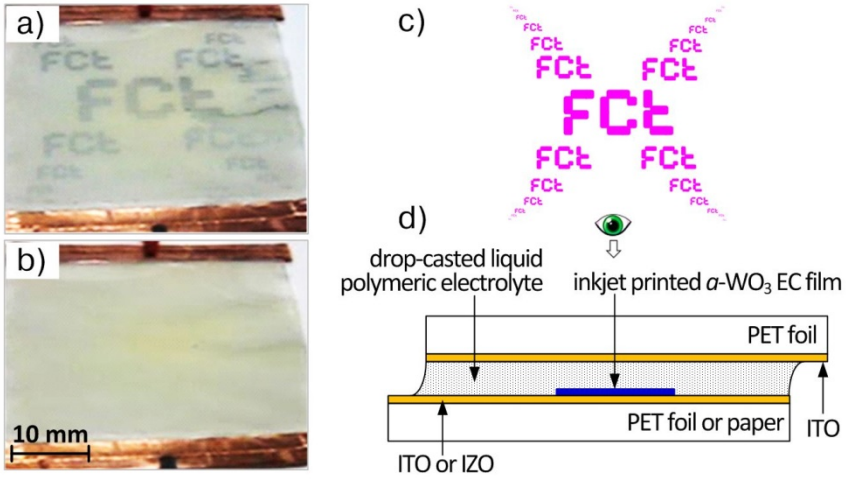

Figure 7.1 An example of EC display prototype in which inkjet printed *a*-WO_3 was applied as an optically active film in a) colored and b) bleached state with corresponding c) printing pattern and d) device structure scheme

Such device structure was sufficient to demonstrate optical change induced electrochemically in EC film, but inadequate for optical or electrochemical characterization. Those devices were not mechanically stable, and could work only for several hours due to the issues related to lack of encapsulation and liquid nature of electrolyte.

An *in-situ* optical and electrochemical evaluation of EC printed films was possible thanks to the development of lab-testing structure shown in Figure 7.2, used for a first time in early 2010.

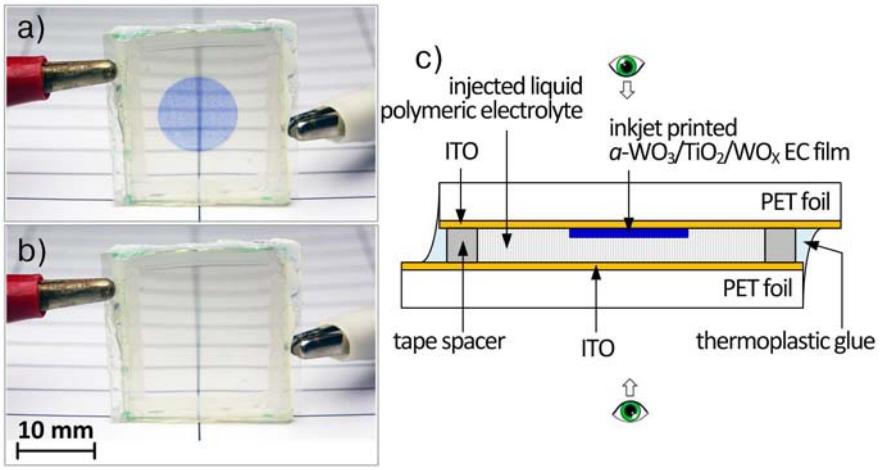

Figure 7.2 Lab-testing EC device in a) colored and b) bleached state with c) corresponding structure scheme

In this structure, an electrolyte is injected into the chamber constituted by both substrates and double side tape spacer with thickness of 1 mm. Sealing with thermoplastic glue, ensures mechanical integrity of the device and allows carrying out the necessary measurements in order to evaluate performance of printed EC film. Results obtained through experiments performed on these devices were analyzed and described in Chapters 2 and 3. However, this lab-testing EC device was still

containing liquid electrolyte based on volatile organic solvents which significantly reduces its life time (typically up to several days). In order to overcome these limitations, an all-solid-state structure was proposed as an alternative to previous devices, offering the advantage of high overall stability.

Starting from 2011, in parallel to work on TCSE described in Chapter 6, prototypes of all-solid-state EC displays were demonstrated. These devices were fabricated in order to evaluate whether optimized TCSE based on various thermosetting resins satisfy requirements concerning stability with changes in temperature and hydration, as well as electrochemical and chemical stability (effect of pH). An 8 x 8 EC passive matrix consisting of two 100 mm by 90 mm glass substrates (Xin Yan Technology, 1200 Å of ITO, 10 Ω/sq, T > 85 % at 550 nm) with 64 pixels, 1 cm^2 each, is shown in Figure 7.3.

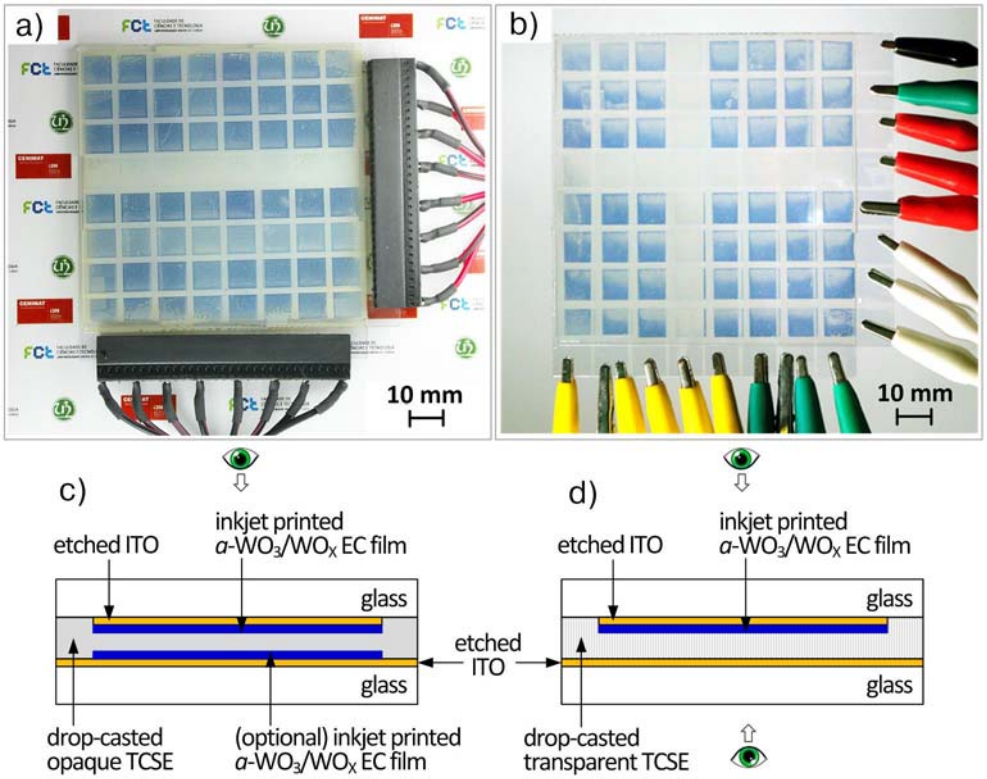

Figure 7.3 Prototypes of inkjet printed all-solid-state EC 8 x 8 passive matrixes (100 x 100 mm) on ITO glass substrates in a) opaque and b) transparent variant; corresponding schematic cross-sections of an individual pixel are presented in diagram c) and d), respectively

Two variants of this display were developed depending of the opacity of TCSE used (*i.e.* transparent and opaque). Prototypes of those passive displays were fabricated by selective ITO etching (through masking provided by 10 mm wide adhesive tape) in acidic solution (0.1M HCl at 60 °C), inkjet printing of optically active film (a-WO_3/WO_X) and drop-casting of the TiO_2 loaded pre-TCSE mixture. The pre-TCSE liquid was then uniformly distributed by squeezing with upper glass substrate and curing *in-situ* at ambient conditions. No additional encapsulation is required, as the cured TCSE

provides perfect sealing of the structure itself. The thickness of an electrolyte film in those devices lay in range between 50 and 100 μm and is provided by double side scotch tape used as spacer.

Each pixel of the developed EC matrix can be operated separately by applying a voltage between selected pair of electrodes. Rigid structure provided by glass substrates together with a strong adhesion of the TCSE assures excellent mechanical strength. Although, the long-time stability investigation of prototype have not been carried out according to standard methodology, the matrix was operated every ones in the while within 25 months till present, functioning with no apparent performance deterioration. No leakage of plastic crystal fraction was observed. The electrolyte adhesion to electrodes is still sufficiently high providing good electrical contact and preventing device delamination. These observations prove that this configuration of materials and processes results in excellent durability. The overall EC performance of these displays was additionally enhanced through application of WO_X NPs incorporated into the EC film, which synthesis and properties were described in Chapters 4 and 5.

Development of TCSE opened new possibilities for flexible EC devices. A prototype of bendable 1 cm^2 single EC pixel consisting of two ITO PET flexible substrates with dimensions of 25 x 25 mm is shown in Figure 7.4. Similarly to the rigid all-solid-state displays structure, the pre-TCSE mixture was drop-casted on top of the bottom substrate and distributed by squeezing with upper substrate followed by *in-situ* curing at ambient conditions. No additional encapsulation is required, as the cured TCSE exhibits good adhesion to PET and seals the structure by itself.

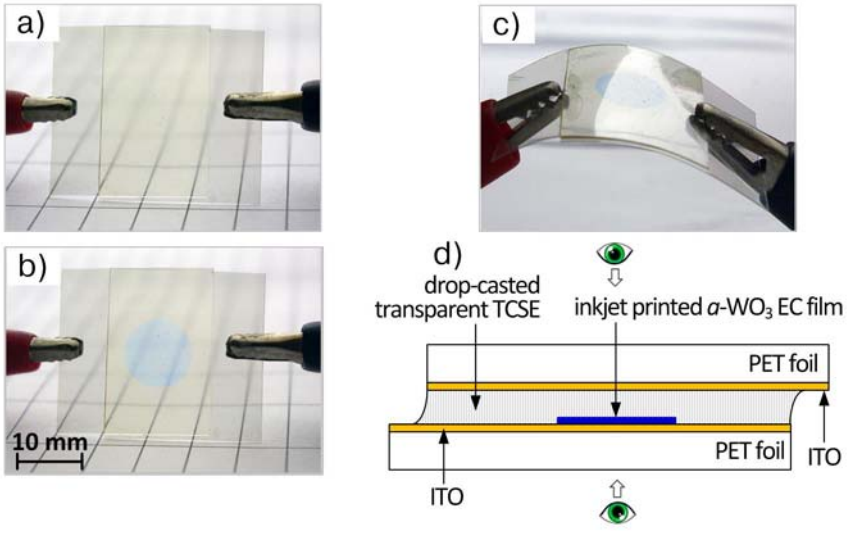

Figure 7.4. Prototype of a bendable single pixel constituted of two ITO PET foils (25 x 25 mm) in a) bleached and b) colored state c) subjected to bending during operation, with its d) schematic structure

In 2013, bendable all-solid-state device was also developed in a large area structure with intended application in EC windows. A prototype consists of two ITO PET flexible substrates with dimensions

of 100 x 100 mm. Inkjet printing of *a*-$WO_3/TiO_2/WO_X$ EC film was followed by doctor-blading of pre-TCSE mixture with thickness of ~100 μm defined by scotch tape (the tape is serving later as a spacer). The structure was sandwiched with the upper substrate and pre-TCSE mixture was UV-cured *in-situ* at ambient conditions. Such device can be affixed on existing window, and extend its functionality to smart-window.

Figure 7.5 shows that installed prototype of EC window foil was successfully operated between bleach and colored state by applying voltage between electrodes (*i.e.* ±3 V). However, it is evident at a glance that the device blurs the view through the window. It is expected, that an improvement can be achieved through application of pre-TCSE mixture based on UPR instead of acrylic resin used in this case. This concept is still under development, which means that processes and materials have not been optimized yet.

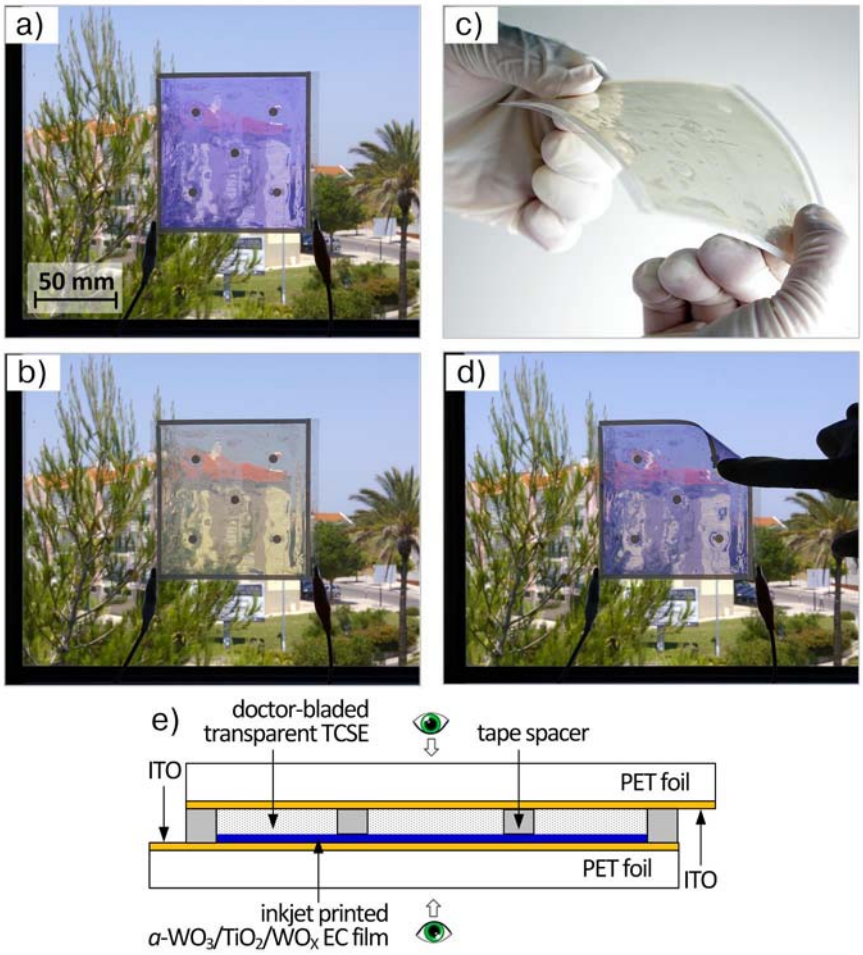

Figure 7.5 Prototype of large area bendable EC window foil installed in classical windows at a) colored and b) bleached state, with its c) schematic structure; photographs showing prototype subjected to bending d) before installation and e) during the operation of smart-window

In case of all previously presented prototypes the electrolyte was deposited either by drop-casting, injection or doctor-blading. These non-specific methods are very handy at lab-scale but bring many

issues when scaling-up to mass production. The last two prototypes described in this section were developed based solely on printing techniques.

The work on paper EC display has been performed since the beginning of presented PhD studies. However, only recently (2013) a fully printed paper display shown in Figure 7.6 was demonstrated. A prototype consists of paper substrate with silver and carbon conductive films deposited *via* flexographic printing (bottom electrode), and ITO PET foil with screen-printed $WO_3/TiO_2/WO_X$ EC film (top electrode). The pre-TCSE mixture based on acrylic resin was screen-printed on top electrode and subjected to UV-curing, resulting in a solid-state film with tacky surface. Both electrodes were then sandwiched together by applying low mechanical pressure. Additional reinforcement of the structure was provided by double side scotch tape with thickness of ~ 100 μm, approximately equal to the thickness of TCSE film.

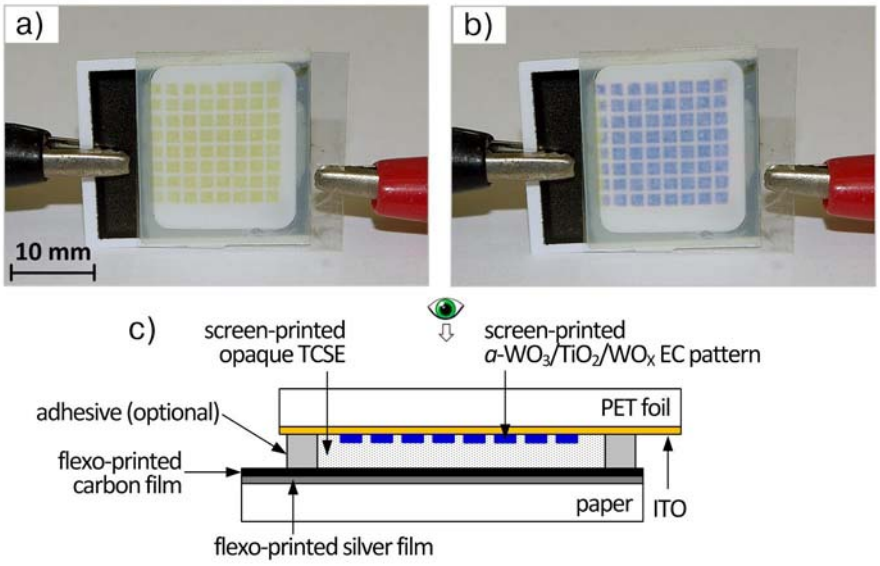

Figure 7.6 Fully printed paper EC display in a) bleached and b) colored state with its c) schematic structure

While the above mentioned sandwich structure is used in the great majority of the state-of-the-art prototypes of EC devices, it does not represent the only possibility. A prototype of fully printed EC display with a thin-film structure shown in Figure 7.7 has been developed within presented PhD research in 2013. Flexible EC thin-film passive display was built up on a single ITO PET foil substrate according to the stack structure shown in Figure 7.7c. Active display area was defined as 15.5 mm by 15.5 mm. The transparent conductive tracks of ITO were chemically etched using screen-printed polymer mask pattern, defining 64 pixels with dimensions of 1.65 mm by 1.65 mm each. In the consecutive printing steps following materials optimized for screen-printing processing were deposited:

- TiO_2 loaded UV-curable acrylic resin as optical passivation;

- WO_X NPs loaded PTA paste to form *a*-WO_3/WO_X EC film,
- TiO_2 loaded UV-curable pre-TCSE mixture,
- carbon counter electrode, and
- silver electrode;

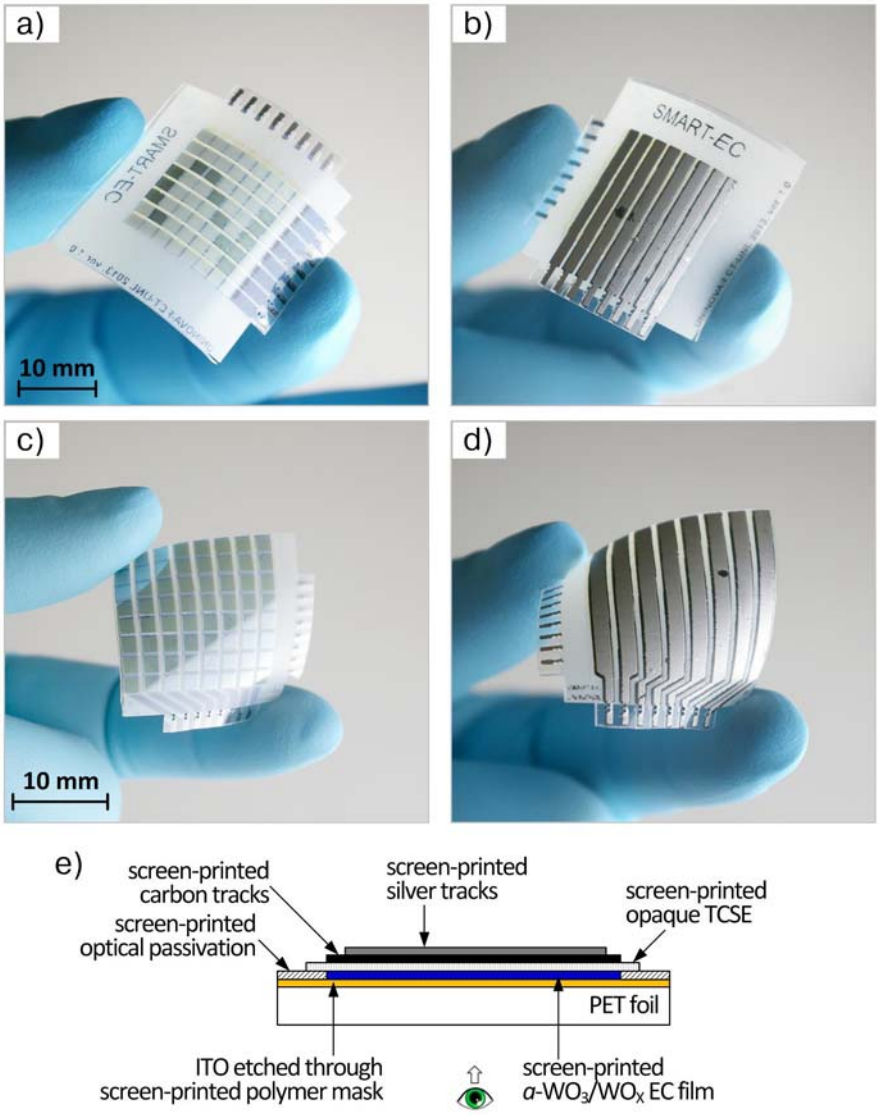

Figure 7.7 Prototypes of a fully screen-printed 64 pixel passive EC matrix based on *a*-WO_3/WO_X film developed on a single ITO PET foil substrate: photographs showing a) device with 1.65 x 1.65 mm pixel size displaying the pattern due to the memory effect, b) back side of the device with 1.65 x 1.65 mm pixel size, c) fully colored device with 2.4 x 2.4 mm pixel size and d) back side of the device with 2.4 x 2.4 mm pixel size; diagram presents b) schematic cross-section of an individual pixel.

Although, the performance measurements of the thin-film EC display was not carried out according to classical electrochemical methodology, it is evident that the matrix exhibits high optical contrast, while the switching time is comparable with the fastest lab-testing EC devices developed using liquid electrolyte (< 3 s for coloring and < 2.5 s for bleaching).

There are two key reasons why this type of approach is thought to be the most suitable for end user devices. First, the consumer demands are oriented toward reliable operation assured by all-solid-state structure of the EC device. Second, development of the EC devices using solely printing techniques facilitates scale-up process from a pilot plant operation to the production at commercial levels, using R2R facilities.

In order to demonstrate operation of prototypes presented in this section, a square wave potential with period of 60 s is typically used. The negative and positive voltage levels for device testing depend of the device configuration, conductivity of electrodes, type of electrolyte and electrochromic material. Some typical values determined at lab-conditions were summarized in Table 7.1.

Table 7.1. Electrical specification of EC devices operating at lab-conditions

	Nominal value		
Parameter	**minimum**	**typical**	**maximum**
Power specification			
Input voltage [V]	±1	±2	±4
Input current [$\mu A/cm^2$] for coloring			30[a]
Input current [$\mu A/cm^2$] for bleaching			100[a]
Peak power consumption for coloring [$\mu W/cm^2$]			10[a], 120[c]
Peak power consumption for bleaching [$\mu W/cm^2$]			400[c]
Working conditions			
Thermal cycling [°C]			115[b]
Thermal storage [°C]			115[b]
Direct water contact	should be avoided		
Performance			
Switching time [s]	2	~2.5	3
Optical modulation (ΔOD)			0.82
color	transparent/blue		

[a] for inkjet printed films; note that these films are not continuous and the area is calculated based on digital design of printed pattern

[b] for all-solid-state devices

[c] for screen-printed continuous film

7.2. Conclusions

Presented dissertation highlights the long stretch of technical research that was performed to realize printed EC devices for various applications. The research results obtained from focusing on the tasks concerning the development of materials and processes were presented within the constituent chapters.

The main empirical findings of this PhD research are chapter-specific and were summarized within the respective chapters. This paragraph synthesizes the obtained results to address objectives and research hypotheses, stated at the beginning of this thesis in Section 1.3. Presented results briefly concern three main concepts: (i) dual-phase inorganic EC material processed at low temperature,

(ii) MO_X NPs for enhancement of EC performance, and (iii) highly conductive and mechanically stable solid-state electrolyte compatible with printing techniques.

Prior to this study, there were no reports on printed inorganic EC materials. Moreover, all existing commercial solutions of EC devices were based on EC organic materials (conductive polymers). It can be inferred, that inorganic EC films were not considered for industrialization due to their processability *via* non-specific deposition techniques (*i.e.* spin-coating, dip-coating or electrodeposition) and high temperature post-processing. Printable EC MO_X precursor was therefore the missing link between research on films derived from inorganic sol-gel precursors and their commercialization. Proposed concept of printed dual-phase inorganic EC films processed at low temperature was implemented using statistical methods. Thanks to application of DOE, the behavior of resulted films was explored through reduced number of experimental trials (from 162 in alternative classical methodology down to 30 runs in this study). Proposed method was validated by means of statistical indicators, proving its abilities to model and optimize film composition. Devices developed using this approach showed superior EC performance when comparing with the state-of-the-art counterparts. This method, obtained results and their interpretation have been reported in Chapters 2 and 3 as well as in appended papers.

An in-depth analysis of printed EC films has revealed a room for further improvement through application of NPs with various morphologies and structures. Despite the great interest in nanosciences and nanotechnology reflected in large number of publications dealing with nanostructured MO_X materials, no significant support for this research have been found. To the author knowledge, there were no studies that combine electrochemistry of MO_X NPs with their processability trough printing techniques. This fact, together with personal ambitions has led to the undertaking of this topic for theoretical considerations presented in Chapter 5. The results of performed simulations, followed by critical interpretation have constituted a consistent theory that may impinge on existing knowledge and understanding on electrochemistry of printed films loaded with MO_X NPs. The proposed general concept of design rule outline for application of NPs in printed electrochemical devices has been furthermore specified to provide an integrated guide for inkjet printed EC devices described in Chapter 6. The proposed approach to incorporate previously synthesized WO_X NPs into EC film has been develop, tested and validated. Resulted films exhibited 2.5 times higher optical modulation, and 2 times faster coloration time, when comparing with pure amorphous film.

The final element of this *technological puzzle* was a solid-state electrolyte. Also in this case, a literature survey has failed in providing a solution that could satisfy both, low material price and compatibility with printing processing. Unsuitable or inconvenient nature of existing material systems has decided on taking the challenge to develop an alternative concept. The goal was reached by formulation of TCSE, which displays high ionic conductivity (up to 10^{-4} S cm^{-1}), high mechanical

resistance (Young's Modulus in the range of 0.1 - 1.4 MPa), wide range of optical properties (from transparent to opaque) and good thermal stability (operational temperature up to 115 °C).

Both concepts of materials systems *i.e.* dual-phase EC film and TCSE were developed based on cheap and widely accessible chemical compounds, followed by implementation in working devices *via* standard printing techniques. The presented approach offers a viable way for moving from lab-scale prototyping to mass production at industrial level.

This section would not be complete without a dose of self-criticism. The first point on such list concerns counter electrode material. This very important element of an electrochemical device has been consistently ignored when developing new prototypes. The role of counter electrode has been usually accounted to ITO electrode, which exhibits charge capacity high enough to balance the electrochemical reaction. However, this may lead to significant deterioration in long-term stability due to ITO degradation, which is also an EC material. In case of fully printed EC displays, the counter electrode is constituted by commercially available porous carbon conductive film which exhibits low charge transfer resistance and moderate series resistance. Elsewhere, some of developed opaque EC displays use the same WO_3 based EC film for both, working and counter electrode. Although the issue related with counter electrode is covered in all prototypes, a specific material system (*e.g.* printable NiO) has not been developed within presented research work.

Second missing element is related to characterization of EC devices. Long-term stability measurements, which could provide information on uniformity of optical modulation over time and/or number of cycles, were not performed. Although, some attempts have been made to stress EC displays with a high number of cycles, the experiments have not been carried out according to standard methodology. It is just worth mentioning, that some of all-solid-state prototypes were still operating after stressing with 10^3 cycles (square wave potential of ±2 V/cm^2, 30 s per pulse). However, quantitative information on properties deterioration has not been recorded.

Another remark concerns optical measurements performed on EC films, and specifically, the value of wavelength at which the optical contrast (*i.e.* ΔOD) was determined. The ΔOD was calculated at λ = 900 nm in Chapters 2 and 3, while λ = 800 nm in Chapter 5. Such choice was dictated by the highest optical modulation value, which was determined at this irradiation wavelength. However, some readers may point out that it would be probably more appropriate to determine ΔOD in a visible range (*i.e.* between 390 and 700 nm), as long as EC displays are concerned. Indeed, many authors use λ in range between 380 - 495 nm as it corresponds to violet and blue color. However, in the opinion of the author, selection of the specific wavelength in a visible range, to record transmittance at certain color may not be the best option. It should be noted, that the color of Li_yWO_3 depends of the fractional number of sites filled in the WO_3 lattice, and thus of the operational voltage level. Such doubt has led to the choice of λ from NIR region.

The last major point on the self-criticism list is related to the determination of the main EC performance indicator, which is the CE. In Chapter 3, a need for a new definition of CE was postulated, as the classical one does not reflect properties of non-continuous films, due to the issue with estimation of the active area value. However, no alternative definition was proposed.

All elements described in this thesis contribute to the fulfillment of the working plan. The results correspond well to the focus of the scope according to Section 1.3 of this thesis, as well as to the action plan determined within Smart-EC and A3Ple projects. The added-value of the presented results has been verified in terms of acceptance of papers to peer-reviewed journals and the feedback gained in scientific conferences in which the above research work was awarded.

In term of external validity of performed work, the research has been widely discussed with (among others): the representatives of printing electronics industry: ACREO Swedish ITC (Sweden), Leeuw Industrie & Diensten BV, LabelTech (The Nederlands); research institutions: VTT Research Center of Finland, Fraunhofer EMFT (Germany), Centre Technique du Papier - CTP (France), Commissariat à l'Energie Atomique – CEA (France); material manufacturer: Rockwood Pigments NA Inc. (United States); automotive industry: Centro Ricerche Fiat (Italy). No objections have been raised concerning developed materials, processes and applied methodology.

7.3. Future work

In line with the aims and delimitations set for this research studies, further work is required. The main future goal is to exploit material concepts and technology demonstrated in above dissertation to develop economically viable, energy efficient solutions for printed electronics. Transferring a laboratory results to industry, and scaling it to full production scale large area are the objectives of currently running FP7 projects Smart-EC and A3Ple. However, a substantial step in that direction has been already taken with the research presented in this thesis.

Before effective scaling-up, a technological optimization of fully printed EC devices is still required. The main issue related to this topic was a relatively low throughput yield. The number of fully operating EC display units coming out of a printing process was significantly lower than the number of units going into that process. The main source of device malfunction was identified as short-circuit between conductive electrodes in a stack structure. It was a consequence of the following factors: (i) limited control over the process parameters in a manual screen-printing stage such as squeegee pressure, angle of attack and print speed; (ii) limited positioning capability, precision and ease of adjustment between substrate and the screen; (iii) too small pattern overlaps between consecutive layers assumed in screen design. In order to eliminate these issues following actions have been planned for future work: (i) improvement of the alignment protocol; (ii) application of different laser cut alignment marks, (iii) improved pattern design with higher value of pattern overlaps.

Another point scheduled for future work concerns reproducibility of printed devices in terms of electrochromic performance. By comparing the printed EC film's properties with layers made *via* PVD techniques, fluctuation in performance in case of presented wet chemical techniques is noticed. Therefore, the future work will also focus on unifying stability and electrochromic performance of developed printed devices, or at least minimizing deterioration effects.

Finally, long-term stability measurements of printed displays are scheduled in order to provide information on uniformity of optical response over time and/or number of cycles.

References

1. Lee, D.-H., Choi, J.S., Chae, H., Chung, C.-H., Cho, S.M.: Screen-printed white OLED based on polystyrene as a host polymer. Current Applied Physics. 9, 161–164 (2009).

2. Shaheen, S.E., Radspinner, R., Peyghambarian, N., Jabbour, G.E.: Fabrication of bulk heterojunction plastic solar cells by screen printing. Applied Physics Letters. 79, 2996 (2001).

3. Krebs, F.C.: Polymer solar cell modules prepared using roll-to-roll methods: Knife-over-edge coating, slot-die coating and screen printing. Solar Energy Materials and Solar Cells. 93, 465–475 (2009).

4. Krebs, F.C., Jørgensen, M., Norrman, K., Hagemann, O., Alstrup, J., Nielsen, T.D., Fyenbo, J., Larsen, K., Kristensen, J.: A complete process for production of flexible large area polymer solar cells entirely using screen printing—First public demonstration. Solar Energy Materials and Solar Cells. 93, 422–441 (2009).

5. Mersal, G.A.M., Khodari, M., Bilitewski, U.: Optimisation of the composition of a screen-printed acrylate polymer enzyme layer with respect to an improved selectivity and stability of enzyme electrodes. Biosensors & bioelectronics. 20, 305–14 (2004).

6. Sung, J.H., Lee, J.Y., Kim, S., Suh, J., Kim, J., Ahn, K.H., Lee, S.J.: Effect of particle size in Ni screen printing paste of incompatible polymer binders. Journal of Materials Science. 45, 2466–2473 (2010).

7. Nelo, M., Sowpati, A.K., Palukuru, V.K., Juuti, J., Jantunen, H.: Utilization of screen printed low curing temperature cobalt nanoparticle ink for miniaturization of patch antennas. Progress in Electromagnetics Research. 127, 427–444 (2012).

8. Liu, J., Coleman, J.: Nanostructured metal oxides for printed electrochromic displays. Materials Science and Engineering A. 286, 144–148 (2000).

9. Möller, M., Leyland, N., Copeland, G., Cassidy, M.: Self-powered electrochromic display as an example for integrated modules in printed electronics applications. The European Physical Journal Applied Physics. 51, 33205 (2010).

10. Andersson, P., Forchheimer, R., Tehrani, P., Berggren, M.: Printable All-Organic Electrochromic Active-Matrix Displays. Advanced Functional Materials. 17, 3074–3082 (2007).

11. Mannerbro, R., Ranlöf, M., Robinson, N., Forchheimer, R.: Inkjet printed electrochemical organic electronics. Synthetic Metals. 158, 556–560 (2008).

12. Xia, Y., Zhang, W., Ha, M., Cho, J.H., Renn, M.J., Kim, C.H., Frisbie, C.D.: Printed Sub-2 V Gel-Electrolyte-Gated Polymer Transistors and Circuits. Advanced Functional Materials. 20, 587–594 (2010).

13. McGarry, S.P., Tarr, N.G.: Fabrication and modelling of screen-printed active electrolytic polymer devices. Semiconductor Science and Technology. 23, 055009 (2008).

14. Corr, D.: Coloured electrochromic “paper-quality” displays based on modified mesoporous electrodes. Solid State Ionics. 165, 315–321 (2003).

15. Said, E., Andersson, P., Engquist, I., Crispin, X., Berggren, M.: Electrochromic display cells driven by an electrolyte-gated organic field-effect transistor. Organic Electronics. 10, 1195–1199 (2009).

16. Andersson, P., Nilsson, D., Svensson, P., Chen, M., Malmström, A., Remonen, T.: Active Matrix Displays Based on All-Organic Electrochemical Smart Pixels Printed on Paper. Advanced Materials. 14, 1460–1464 (2002).

17. Kawahara, J., Ersman, P.A., Nilsson, D., Katoh, K., Berggren, M., Nakata, Y., Sandberg, M., Nilsson, M.: Flexible Active Matrix Addressed Displays Manufactured by Printing and Coating Techniques. Journal of Polymer Science, Part B: Polymer Physics. 51, 265–271 (2013).

18. Vincent, J.B., Babinec, S.J., Dermody, D.L., Chen, Y.: Electrochromic display device and compositions useful in making such devices. US Patent 6,879,424 B2. (2005).

19. Verrengia, J.: Smart Windows: Energy Efficiency with a View. NREL Newsroom Retrived from http://www.nrel.gov/news/features/feature_detail.cfm/feature_id=1555. (2010).

20. Wang, U.: A Startup Shows Off "Smart Windows" In San Francisco Hotel. Forbes Green Tech Retrived from http://www.forbes.com/sites/uciliawang/2012/11/12/a-startup-shows-off-smart-windows-in-san-francisco-hotel. (2012).

21. Shaffer, D.: A "smart glass" bet. StarTribune Business Retrived from http://www.startribune.com/business/110882379.html. (2010).

22. Prudenziati, M., J. Hormadaly eds: Printed Films: Materials Science and Applications in Sensors, Electronics and Photonics. Woodhead Pub Ltd (2012).

23. Cantatore, E. ed: Applications of Organic and Printed Electronics: A Technology-Enabled Revolution (Integrated Circuits and Systems). Springer (2013).

24. Pettersson, H., Gruszecki, T., Johansson, L.-H., Edwards, M.O.M., Hagfeldt, A., Matuszczyk, T.: Direct-driven electrochromic displays based on nanocrystalline electrodes. Displays. 25, 223–230 (2004).

25. Coleman, J.P., Lynch, A.T., Madhukar, P., Wagenknecht, J.H.: Printed, flexible electrochromic displays using interdigitated electrodes. Solar Energy Materials and Solar Cells. 56, 395–418 (1999).

26. Löffelmann, U., Wang, N., Mager, D., Smith, P.J., Korvink, J.G.: Solvent-free inkjet printing process for the fabrication of conductive, transparent, and flexible ionic liquid-polymer gel structures. Journal of Polymer Science Part B: Polymer Physics. 50, 38–46 (2012).

27. Dasgupta, S., Gottschalk, S., Kruk, R., Hahn, H.: A nanoparticulate indium tin oxide field-effect transistor with solid electrolyte gating. Nanotechnology. 19, 435203 (2008).

28. Dasgupta, S., Kruk, R., Mechau, N., Hahn, H.: Inkjet printed, high mobility inorganic-oxide field effect transistors processed at room temperature. ACS nano. 5, 9628–38 (2011).

29. Rose, A.: Considerations in formulation and manufacturing of thick film inks. Electrocomponent Science and Technology. 9, 43–49 (1981).

30. Glasnov, T.N., Tye, H., Kappe, C.O.: Integration of high speed microwave chemistry and a statistical “design of experiment” approach for the synthesis of the mitotic kinesin Eg5 inhibitor monastrol. Tetrahedron. 64, 2035–2041 (2008).

31. Altekar, M., Homon, C., Kashem, M., Mason, S., Nelson, R., Patnaude, L., Yingling, J., Taylor, P.: Assay Optimization: A Statistical Design of Experiments Approach. Journal of the Association for Laboratory Automation. 11, 33–41 (2006).

32. Lu, W.-B., Kao, W.-C., Shi, J.-J., Chang, J.-S.: Exploring multi-metal biosorption by indigenous metal-hyperresistant Enterobacter sp. J1 using experimental design methodologies. Journal of Hazardous Materials. 153, 372–81 (2008).

33. Vanatta, L., Coleman, D., Woodruff, a: Determination of chloride and sulfate in semiconductor-grade etchants comprised of acetic acid, nitric acid and phosphoric acid. Journal of Chromatography A. 997, 269–278 (2003).

34. Tye, H.: Application of statistical “design of experiments” methods in drug discovery. Drug Discovery Today. 9, 485–91 (2004).

35. Qazi, S., Samuel, N.K.P., Venkatachalam, T.K., Uckun, F.M.: Evaluating dissolution profiles of an anti-HIV agent using ANOVA and non-linear regression models in JMP software. International Journal of Pharmaceutics. 252, 27–39 (2003).

36. Rosario, A. V, Pereira, E.C.: Optimisation of the electrochromic properties of Nb2O5 thin films produced by sol – gel route using factorial design. Solar Energy Materials & Solar Cells. 71, 41–50 (2002).

37. Cornell, J.: Experiments with Mixtures: Design, Models, and the Analysis of Mixture Data. John Wiley & Sons, Inc., New York (2002).

38. McLeane, R.A., Anderson, V.L.: Extreme Vertices Design of Mixture Experiments. Technometrics. 8, 447–454 (1966).

39. Bacon, D.W., Lott, R.: Robustness of D-optimal Experimental Designs for Mixture Studies. Quality improvement through statistical methods. p. 237. Springer (1998).

40. SAS Institute Inc. 2009.: JMP 8 Design of Experiments Guide, Second Edition. Cary, NC: SAS Institute Inc.

41. Eriksson, L.: Design of Experiments: Principles and Applications. Umetrics Academy (2008).

42. Smith, W.F.: Experimental Design for Formulation. Society for Industrial and Applied Mathematics (2005).

43. Yamanaka, K., Oakamoto, H., Kidou, H., Kudo, T.: Peroxotungstic Acid Coated Films for Electrochromic Display Devices. Japanese Journal of Applied Physics. 25, 1420–1426 (1986).

44. Okamoto, H., Ishikawa, A., Kudo, T.: Amorphous and Crystalline Peroxopolytungstic Acid Formed from Tungsten and Hydrogen Peroxide. Bulletin of the Chemical Society of Japan. 62, 2723–2724 (1989).

45. Pecquenard, B., Castro-Garcia, S., Livage, J., Zavalij, P.Y., Whittingham, M.S., Thouvenot, R.: Structure of Hydrated Tungsten Peroxides [WO2(O2)H2O]·nH2O. Chemistry of Materials. 10, 1882–1888 (1998).

46. Kim, C.-Y., Lee, M., Huh, S.-H., Kim, E.-K.: WO3 thin film coating from H2O-controlled peroxotungstic acid and its electrochromic properties. Journal of Sol-Gel Science and Technology. 53, 176–183 (2009).

47. Barbosa, P.C., Rodrigues, L.C., Silva, M.M., Smith, M.J., Valente, P.B., Gonçalves, A., Fortunato, E.: Characterization of polyether-poly(methyl methacrylate)-lithium perchlorate blend electrolytes. Polymers for Advanced Technologies. 22, 1753–1759 (2011).

48. Sall, J.: Leverage Plots for General Linear Hypotheses. The American Statistician. 44, 308–315 (1990).

49. Derringer, G., Suich, R.: Simultaneous Optimization of Several Response Variables. Journal of Quality Technology. 12, 214–219 (1980).

50. Taylor, D.J., Cronin, J.P., Allard, L.F., Birniem, D.P.: Tungsten Oxide Films. Chemistry of Materials. 8, 1396–1401 (1996).

51. Deepa, M., Saxena, T., Singh, D., Sood, K., Agnihotry, S.: Spin coated versus dip coated electrochromic tungsten oxide films: Structure, morphology, optical and electrochemical properties. Electrochimica Acta. 51, 1974–1989 (2006).

52. Işık, D., Ak, M., Durucan, C.: Structural, electrochemical and optical comparisons of tungsten oxide coatings derived from tungsten powder-based sols. Thin Solid Films. 518, 104–111 (2009).

53. Deepa, M., Srivastava, A., Saxena, T., Agnihotry, S.: Annealing induced microstructural evolution of electrodeposited electrochromic tungsten oxide films. Applied Surface Science. 252, 1568–1580 (2005).

54. Deepa, M., Kar, M., Agnihotry, S.A.: Electrodeposited tungsten oxide films: annealing effects on structure and electrochromic performance. Thin Solid Films. 468, 32–42 (2004).

55. Choy, J.-H., Kim, Y.-I., Yoon, J.-B., Choy, S.-H.: Temperature-dependent structural evolution and electrochromic properties of peroxopolytungstic acid. Journal of Materials Chemistry. 11, 1506–1513 (2001).

56. Wu, W.-T., Liao, W.-P., Chen, J.-S., Wu, J.-J.: An efficient route to nanostructured tungsten oxide films with improved electrochromic properties. Chemphyschem. 11, 3306–12 (2010).

57. SAS Institute Inc. 2009.: JMP 8 Introductory guide, Second Edition. Cary, NC: SAS Institute Inc.

58. Karuppasamy, K., Subrahmanyam, A.: Studies on the correlation between electrochromic colouration and the relative density of tungsten trioxide (WO 3− x) thin films prepared by electron beam evaporation. Journal of Physics D: Applied Physics. 42, 1–6 (2009).

59. Sato, R., Kawamura, N., Tokumaru, H.: The coloration of tungsten-oxide film by oxygen deficiency and its mechanism. Applied Surface Science. 254, 7676–7678 (2008).

60. Costa, C., Pinheiro, C., Henriques, I., Laia, C.A.T.: Inkjet printing of sol-gel synthesized hydrated tungsten oxide nanoparticles for flexible electrochromic devices. Applied Materials & Interfaces. 4, 1330–40 (2012).

61. Granqvist, C.G.: Electrochromic tungsten oxide films: Review of progress 1993–1998. Solar Energy Materials and Solar Cells. 60, 201–262 (2000).

62. Krasnov, Y.: Electrochromism and reversible changes in the position of fundamental absorption edge in cathodically deposited amorphous WO3. Electrochimica Acta. 49, 2425–2433 (2004).

63. Faughnan, B.W., Crandall, R.S., Lampert, M.A.: Model for the bleaching of WO3 electrochromic films by an electric field. Applied Physics Letters. 27, 275–277 (1975).

64. Zheng, H., Ou, J.Z., Strano, M.S., Kaner, R.B., Mitchell, A., Kalantar-zadeh, K.: Nanostructured Tungsten Oxide - Properties, Synthesis, and Applications. Advanced Functional Materials. 1–22 (2011).

65. Naseri, N., Azimirad, R., Akhavan, O., Moshfegh, A.Z.: Improved electrochromical properties of sol–gel WO3 thin films by doping gold nanocrystals. Thin Solid Films. 518, 2250–2257 (2010).

66. Patil, P.S., Mujawar, S.H., Inamdar, A.I., Sadale, S.B.: Electrochromic properties of spray deposited TiO2 -doped WO3 thin films. Applied Surface Science. 250, 117–123 (2005).

67. Denesuk, M., Uhlmann, D.R.: Site-saturation model for the optical efficiency of tungsten oxide-based devices. Journal of the Electrochemical Society. 143, L186–L188 (1996).

68. Rauh, R.: Electrochromic windows: an overview. Electrochimica Acta. 44, 3165–3176 (1999).

69. Stein, A., Fendorf, M., Jarvie, T.P., Mueller, K.T., Benesi, A.J., Mallouk, T.E.: Salt-Gel Synthesis of Porous Transition-Metal Oxides. Chemistry of Materials. 7, 304–313 (1995).

70. Bernacka-Wojcik, I., Senadeera, R., Wojcik, P.J., Silva, L.B., Doria, G., Baptista, P., Aguas, H., Fortunato, E., Martins, R.: Inkjet printed and “doctor blade” TiO2 photodetectors for DNA biosensors. Biosensors & bioelectronics. 25, 1229–34 (2010).

71. Deepa, M., Srivastava, A.K., Sharma, S.N., Shivaprasad, S.M.: Microstructural and electrochromic properties of tungsten oxide thin films produced by surfactant mediated electrodeposition. Applied Surface Science. 254, 2342–2352 (2008).

72. Wang, W., Pang, Y., Hodgson, S.N.B.: XRD studies of thermally stable mesoporous tungsten oxide synthesised by a templated sol–gel process from tungstic acid precursor. Microporous and Mesoporous Materials. 121, 121–128 (2009).

73. Wang, W., Pang, Y., Hodgson, S.N.B.: On key factors for the fabrication of mesoporous tungsten oxide films from tungstic acid. Journal of Sol-Gel Science and Technology. 58, 135–141 (2010).

74. Lawrence Berkeley National Laboratory: PIER Final Project Report: A Design Guide for Early-Market Electrochromic Windows. , California Energy Commission, Berkley (2006).

75. Jiao, Z., Sun, X.W., Wang, J., Ke, L., Demir, H.V.: Hydrothermally grown nanostructured WO3 films and their electrochromic characteristics. Journal of Physics D: Applied Physics. 43, 285501 (2010).

76. Wang, J., Khoo, E., Lee, P.S., Ma, J.: Controlled Synthesis of WO3 Nanorods and Their Electrochromic Properties in H2SO4 Electrolyte. Journal of Physical Chemistry C. 113, 9655–9658 (2009).

77. Songara, S., Gupta, V., Kumar Patra, M., Singh, J., Saini, L., Siddaramana Gowd, G., Raj Vadera, S., Kumar, N.: Tuning of crystal phase structure in hydrated WO3 nanoparticles under wet chemical conditions and studies on their photochromic properties. Journal of Physics and Chemistry of Solids. 73, 851–857 (2012).

78. Law, M., Greene, L.E., Johnson, J.C., Saykally, R., Yang, P.: Nanowire dye-sensitized solar cells. Nature materials. 4, 455–9 (2005).

79. Li, J., Xu, D.: Tetragonal faceted-nanorods of anatase TiO2 single crystals with a large percentage of active {100} facets. Chemical communications (Cambridge, England). 46, 2301–3 (2010).

80. Hong, S.J., Jun, H., Borse, P.H., Lee, J.S.: Size effects of WO3 nanocrystals for photooxidation of water in particulate suspension and photoelectrochemical film systems. International Journal of Hydrogen Energy. 34, 3234–3242 (2009).

81. Wang, H., Lindgren, T., He, J., Hagfeldt, A., Lindquist, S.: Photolelectrochemistry of Nanostructured WO3 Thin Film Electrodes for Water Oxidation: Mechanism of Electron Transport. The Journal of Physical Chemistry B. 104, 5686–5696 (2000).

82. Sartoretti, J.C., Alexander, B.D., Solarska, R., Rutkowska, I., Augustynski, J., Cerny, R.: Photoelectrochemical oxidation of water at transparent ferric oxide film electrodes. The Journal of Physical Chemistry. B. 109, 13685–92 (2005).

83. Sun, C.H., Yang, X.H., Chen, J.S., Li, Z., Lou, X.W., Li, C., Smith, S.C., Lu, G.Q.M., Yang, H.G.: Higher charge/discharge rates of lithium-ions across engineered TiO2 surfaces leads to enhanced battery performance. Chemical Communications (Cambridge, England). 46, 6129–31 (2010).

84. Huang, K., Pan, Q., Yang, F., Ni, S., Wei, X., He, D.: Controllable synthesis of hexagonal WO3 nanostructures and their application in lithium batteries. Journal of Physics D: Applied Physics. 41, 155417 (2008).

85. Lang, X., Hirata, A., Fujita, T., Chen, M.: Nanoporous metal/oxide hybrid electrodes for electrochemical supercapacitors. Nature Nanotechnology. 6, 232–6 (2011).

86. Deng, W., Ji, X., Chen, Q., Banks, C.E.: Electrochemical capacitors utilising transition metal oxides: an update of recent developments. RSC Advances. 1, 1171 (2011).

87. Bruce, P.G., Scrosati, B., Tarascon, J.-M.: Nanomaterials for rechargeable lithium batteries. Angewandte Chemie (International ed. in English). 47, 2930–46 (2008).

88. Zhang, H., Liu, T., Huang, L., Guo, W., Liu, D., Zeng, W.: Hydrothermal synthesis of assembled sphere-like WO3 architectures and their gas-sensing properties. Physica E: Low-dimensional Systems and Nanostructures. (2012).

89. Liu, S., Zhang, F., Li, H., Chen, T., Wang, Y.: Acetone detection properties of single crystalline tungsten oxide plates synthesized by hydrothermal method using cetyltrimethyl ammonium bromide supermolecular template. Sensors and Actuators B: Chemical. 162, 259–268 (2012).

90. Yan, A., Xie, C., Zeng, D., Cai, S., Li, H.: Synthesis, formation mechanism and illuminated sensing properties of 3D WO3 nanowall. Journal of Alloys and Compounds. 495, 88–92 (2010).

91. Wang, K., Xu, J.-J., Chen, H.-Y.: Biocomposite of cobalt phthalocyanine and lactate oxidase for lactate biosensing with MnO2 nanoparticles as an eliminator of ascorbic acid interference. Sensors and Actuators B: Chemical. 114, 1052–1058 (2006).

92. Ansari, A., Alhoshan, M., Alsalhi, M., Aldwayyan, A.: Nanostructured metal oxides based enzymatic electrochemical biosensors. In: Serra, P.A. (ed.) Biosensors. pp. 23–46. INTECH, Croatia (2010).

93. Goesmann, H., Feldmann, C.: Nanoparticulate functional materials. Angewandte Chemie (International ed. in English). 49, 1362–95 (2010).

94. Bisquert, J.: Photovoltaic, Photoelectronic, and Electrochemical Devices Based on Metal-Oxide Nanopaerticles and Nanostructures. In: Rodríguez, J.A. and Fernández-García, M. (eds.) Synthesis, Properties, and Applications of Oxide Nanomaterials. pp. 451–490. John Wiley & Sons, Inc., Hoboken, NJ, USA (2007).

95. Zhou, L., Zou, J., Yu, M., Lu, P., Wei, J., Qian, Y., Wang, Y., Yu, C.: Green Synthesis of Hexagonal-Shaped WO3.0.33H2O Nanodiscs Composed of Nanosheets. Crystal Growth & Design. 8, 3993–3998 (2008).

96. Khoo, E., Lee, P.S., Ma, J.: Electrophoretic deposition (EPD) of WO3 nanorods for electrochromic application. Journal of the European Ceramic Society. 30, 1139–1144 (2010).

97. Takahashi, K., Wang, Y., Cao, G.: Growth and electrochromic properties of single-crystal V2O5 nanorod arrays. Applied Physics Letters. 86, 053102 (2005).

98. Wang, J., Lee, P.S., Ma, J.: One-Pot Synthesis of Hierarchically Assembled Tungsten Oxide (Hydrates) Nano/Microstructures by a Crystal-Seed-Assisted Hydrothermal Process. Crystal Growth & Design. 9, 2293–2299 (2009).

99. Jiang, J., Li, Y., Liu, J., Huang, X., Yuan, C., Lou, X.W.D.: Recent advances in metal oxide-based electrode architecture design for electrochemical energy storage. Advanced Materials. 24, 5166–80 (2012).

100. Woodward, P.M., Sleight, A.W., Vogt, T.: Ferroelectric Tungsten Trioxide. Journal of Solid State Chemistry. 131, 9–17 (1997).

101. Frenzer, G., Maier, W.F.: Amorphous Porous Mixed Oxides: Sol-Gel Ways to a Highly Versatile Class of Materials and Catalysts. Annual Review of Materials Research. 36, 281–331 (2006).

102. Kim, Y.-H., Heo, J.-S., Kim, T.-H., Park, S., Yoon, M.-H., Kim, J., Oh, M.S., Yi, G.-R., Noh, Y.-Y., Park, S.K.: Flexible metal-oxide devices made by room-temperature photochemical activation of sol-gel films. Nature. 489, 128–32 (2012).

103. Sandu, I., Brousse, T., Santos-Pena, J.: Comparison of the electrochemical behaviour of SnO2 and PbO2 negative electrodes for lithium ion batteries. Ionics. 8, 27–35 (2002).

104. Granqvist, C.G.: Electrochromic materials: Microstructure, electronic bands, and optical properties. Applied Physics A Solids and Surfaces. 25, 269–12 (1993).

105. Poizot, P., Laruelle, S., Grugeon, S., Dupont, L., Tarascon, J.M.: Nano-sized transition-metal oxides as negative-electrode materials for lithium-ion batteries. Nature. 407, 496–9 (2000).

106. Yebka, B., Pecquenard, B., Julien, C., Livage, J.: Electrochemical Li+ insertion in WO3 – xTiO2 mixed oxides. Solid State Ionics. 104, 169–175 (1997).

107. Pyun, S.-I., Bae, J.-S.: Lithium ion transport in r.f.-magnetron sputtered WO3 film as a function of lithium content. Journal of Alloys and Compounds. 245, L1–L4 (1996).

108. Mohammad, A. Al: Synthesis, Separation and Electrical Properties of WO3−x Nanopowders via Partial Pressure High Energy Ball-Milling. Acta Physica Polonica A. 116, 240–244 (2009).

109. Karunakaran, C., Dhanalakshmi, R., Manikandan, G., Gomathisankar, P.: Photodegradation of carboxylic acids on Al2O3 and SiO2 nanoparticles. Indian Journal of Chemistry. 50A, 163–170 (2011).

110. Nunes, P., Fortunato, E., Tonello, P., Fernandes, F.B., Vilarinho, P.: Effect of different dopant elements on the properties of ZnO thin films. Vacuum. 64, 281–285 (2002).

111. Nunes, P., Costa, D., Fortunato, E., Martins, R.: Performances presented by zinc oxide thin films deposited by r.f. magnetron sputtering. Vacuum. 64, 293–297 (2002).

112. Nunes, P.U., Fortunato, E., Martins, R.: Influence of the post-treatment on the properties of ZnO thin films. Thin Solid Films. 383, 277–280 (2001).

113. Assuncao, V., Ferreira, I., Martins, R., Fortunato, E., Marques, A., Aguas, H.: Influence of the deposition pressure on the properties of transparent and conductive ZnO Ga thin-film produced by r.f. sputtering at room temperature. Thin Solid Films. 427, 401–405 (2003).

114. Fortunato, E., Pimentel, a., Gonçalves, a., Marques, a., Martins, R.: High mobility amorphous/nanocrystalline indium zinc oxide deposited at room temperature. Thin Solid Films. 502, 104–107 (2006).

115. Zhang, Q., Chou, T.P., Russo, B., Jenekhe, S. a, Cao, G.: Aggregation of ZnO nanocrystallites for high conversion efficiency in dye-sensitized solar cells. Angewandte Chemie (International ed. in English). 47, 2402–6 (2008).

116. Zhang, Q., Dandeneau, C.S., Zhou, X., Cao, G.: ZnO Nanostructures for Dye-Sensitized Solar Cells. Advanced Materials. 21, 4087–4108 (2009).

117. Jolivet, J.-P., Cassaignon, S., Chanéac, C., Chiche, D., Durupthy, O., Portehault, D.: Design of metal oxide nanoparticles: Control of size, shape, crystalline structure and functionalization by aqueous chemistry. Comptes Rendus Chimie. 13, 40–51 (2010).

118. Navrotsky, A.: Energetics of nanoparticle oxides: interplay between surface energy and polymorphism. Geochemical Transactions. 4, 34 (2003).

119. Klabunde, K., Richards, R.M.: Nanoscale Materials in Chemistry. John Wiley & Sons, Inc., New York, USA (2001).

120. Murphy, C.J., Jana, N.R.: Controlling the Aspect Ratio of Inorganic Nanorods and Nanowires. Advanced Materials. 14, 80–82 (2002).

121. Jayalakshmi, M., Rao, M.M., Kim, K.: Effect of Particle Size on the Electrochemical Capacitance of α-Ni(OH)2 in Alkali Solutions. International Journal of Electrochemcal Science. 1, 324–333 (2006).

122. Klabunde, K.J., Stark, J., Koper, O., Mohs, C., Park, D.G., Decker, S., Jiang, Y., Lagadic, I., Zhang, D.: Nanocrystals as Stoichiometric Reagents with Unique Surface Chemistry. Journal of Physical Chemistry. 100, 12142–12153 (1996).

123. Kadam, P.M., Tarwal, N.L., Shinde, P.S., Patil, R.S., Bhosale, A.K., Deshmukh, H.P., Patil, P.S.: Enhanced optical modulation due to SPR in gold nanoparticles embedded WO3 thin films. Journal of Alloys and Compounds. 3–7 (2010).

124. Vidotti, M., Torresi, S.I.C. De: Nanochromics: old materials, new structures and architectures for high performance devices. Journal of the Brazilian Chemical Society. 19, 1248–1257 (2008).

125. Baraton, M.-I., Merhari, L.: Influenece of the Particle Size on the Surface Reactivity and Gas Sensing Properties of SnO2 Nanopowders. Materials Transactions. 42, 1616–1622 (2001).

126. Franke, M.E., Koplin, T.J., Simon, U.: Metal and metal oxide nanoparticles in chemiresistors: does the nanoscale matter? Small. 2, 36–50 (2006).

127. Liu, J., Guo, Z., Zhu, K., Wang, W., Zhang, C., Chen, X.: Highly porous metal oxide polycrystalline nanowire films with superior performance in gas sensors. Journal of Materials Chemistry. 21, 11412 (2011).

128. Hagfeldt, A., Boschloo, G., Sun, L., Kloo, L., Pettersson, H.: Dye-sensitized solar cells. Chemical Reviews. 110, 6595–663 (2010).

129. Lee, J.-H.: Gas sensors using hierarchical and hollow oxide nanostructures: Overview. Sensors and Actuators B: Chemical. 140, 319–336 (2009).

130. Gu, Z., Zhai, T., Gao, B., Sheng, X., Wang, Y., Fu, H.: Controllable Assembly of WO3 Nanorods / Nanowires into Hierarchical Nanostructures. Journal of Physical Chemistry B. 110, 23829–23836 (2006).

131. Mueller, S., Llewellin, E.W., Mader, H.M.: The rheology of suspensions of solid particles. Proc. R. Soc. A. 466, 1201–1228 (2009).

132. Duan, F., Kwek, D., Crivoi, A.: Viscosity affected by nanoparticle aggregation in Al2O3-water nanofluids. Nanoscale Research Letters. 6, 248 (2011).

133. Pastoriza-Gallego, M.J., Casanova, C., Páramo, R., Barbés, B., Legido, J.L., Piñeiro, M.M.: A study on stability and thermophysical properties (density and viscosity) of Al2O3 in water nanofluid. Journal of Applied Physics. 106, 064301 (2009).

134. Cooper-White, J.J., Fagan, J.E., Tirtaatmadja, V., Lester, D.R., Boger, D.V.: Drop formation dynamics of constant low-viscosity, elastic fluids. Journal of Non-Newtonian Fluid Mechanics. 106, 29–59 (2002).

135. Furbank, R.J., Morris, J.F.: An experimental study of particle effects on drop formation. Physics of Fluids. 16, 1777 (2004).

136. Tuladhar, T.R., Mackley, M.R.: Filament stretching rheometry and break-up behaviour of low viscosity polymer solutions and inkjet fluids. Journal of Non-Newtonian Fluid Mechanics. 148, 97–108 (2008).

137. Khoo, H.S., Lin, C., Huang, S.-H., Tseng, F.-G.: Self-Assembly in Micro- and Nanofluidic Devices: A Review of Recent Efforts. Micromachines. 2, 17–48 (2011).

138. Huang, Y., Duan, X., Wei, Q., Lieber, C.M.: Directed assembly of one-dimensional nanostructures into functional networks. Science (New York, N.Y.). 291, 630–3 (2001).

139. Ham, D.J., Phuruangrat, A., Thongtem, S., Lee, J.S.: Hydrothermal synthesis of monoclinic WO3 nanoplates and nanorods used as an electrocatalyst for hydrogen evolution reactions from water. Chemical Engineering Journal. 165, 365–369 (2010).

140. Huang, R., Shen, Y., Zhao, L., Yan, M.: Effect of hydrothermal temperature on structure and photochromic properties of WO3 powder. Advanced Powder Technology. 23, 211–214 (2012).

141. Phuruangrat, A., Ham, D.J., Hong, S.J., Thongtem, S., Lee, J.S.: Synthesis of hexagonal WO3 nanowires by microwave-assisted hydrothermal method and their electrocatalytic activities for hydrogen evolution reaction. Journal of Materials Chemistry. 20, 1683–1690 (2009).

142. Huirache-Acuña, R., Paraguay-Delgado, F., Albiter, M. a., Lara-Romero, J., Martínez-Sánchez, R.: Synthesis and characterization of WO3 nanostructures prepared by an aged-hydrothermal method. Materials Characterization. 60, 932–937 (2009).

143. Balaji, S., Djaoued, Y., Albert, A.-S., Ferguson, R.Z., Brüning, R.: Hexagonal Tungsten Oxide Based Electrochromic Devices: Spectroscopic Evidence for the Li Ion Occupancy of Four-Coordinated Square Windows. Chemistry of Materials. 21, 1381–1389 (2009).

144. Jiayin, L., Jianfeng, H., Jianpeng, W., Liyun, C., Yanagisawa, K.: Morphology-controlled synthesis of tungsten oxide hydrates crystallites via a facile, additive-free hydrothermal process. Ceramics International. 38, 4495–4500 (2012).

145. Wang, J., Lee, P., Ma, J.: Synthesis, growth mechanism and room-temperature blue luminescence emission of uniform WO3 nanosheets with W as starting material. Journal of Crystal Growth. 311, 316–319 (2009).

146. Yayapao, O., Thongtem, T., Phuruangrat, A., Thongtem, S.: CTAB-assisted hydrothermal synthesis of tungsten oxide microflowers. Journal of Alloys and Compounds. 509, 2294–2299 (2011).

147. Sungpanich, J., Thongtem, T., Thongtem, S.: Large-scale synthesis of WO3 nanoplates by a microwave-hydrothermal method. Ceramics International. 38, 1051–1055 (2012).

148. Ruppi, S.: Deposition, microstructure and properties of texture-controlled CVD α-Al2O3 coatings. International Journal of Refractory Metals and Hard Materials. 23, 306–316 (2005).

149. Castro-García, S., Pecquenard, B., Bender, A., Livage, J., Julien, C.: Electrochromic properties of tungsten oxides synthesized from aqueous solutions. Ionics. 3, 104–109 (1997).

150. Deery, M.J., Howarth, O.W., Jennings, K.R.: Application of electrospray ionisation mass spectrometry to the study of dilute aqueous oligomeric anions and their reactions. Journal of the Chemical Society, Dalton Transactions. 4783–4788 (1997).

151. Oskam, G.: Metal oxide nanoparticles: synthesis, characterization and application. Journal of Sol-Gel Science and Technology. 37, 161–164 (2006).

152. Pfeifer, J., Guifang, C., Tekula-Buxbaum, P., Kiss, B.A., Frakas-Jahnke, M., Vadasdi, K.: A Reinvestigation of the Preparation of Tungsten Oxide Hydrate WO3, 1/3H20. Journal of Solid State Chemistry. 119, 90–97 (1995).

153. Wang, J., Khoo, E., Lee, P.S., Ma, J.: Synthesis, Assembly, and Electrochromic Properties of Uniform Crystalline WO3 Nanorods. Journal of Physical Chemistry C. 112, 14306–14312 (2008).

154. Pradhan, D.K., Samantaray, B.K., Karan, N.K., Katiyar, R.S.: Effect of Plasticizer on Structural and Electrical Properties of Polymer Nanocompsoite Electrolytes. International Journal of Electrochemical Science. 2, 861 – 871 (2007).

155. Pringle, J.M., Howlett, P.C., MacFarlane, D.R., Forsyth, M.: Organic ionic plastic crystals: recent advances. Journal of Materials Chemistry. 20, 2056 (2010).

156. Das, S., Prathapa, S.J., Menezes, P. V, Row, T.N.G., Bhattacharyya, A.J.: Study of ion transport in lithium perchlorate-succinonitrile plastic crystalline electrolyte via ionic conductivity and in situ cryo-crystallography. The Journal of Physical Chemistry B. 113, 5025–31 (2009).

157. Long, S.: Ionic conduction in doped succinonitrile. Solid State Ionics. 175, 733–738 (2004).

158. Long, S.: Fast ion conduction in molecular plastic crystals. Solid State Ionics. 161, 105–112 (2003).

159. Zhou, Z.-B., Matsumoto, H.: Lithium-doped, organic ionic plastic crystal electrolytes exhibiting high ambient-temperature conductivities. Electrochemistry Communications. 9, 1017–1022 (2007).

160. Patel, M., Chandrappa, K., Bhattacharyya, A.: Increasing ionic conductivity and mechanical strength of a plastic electrolyte by inclusion of a polymer. Electrochimica Acta. 54, 209–215 (2008).

161. Fan, L.-Z., Wang, X.-L., Long, F.: All-solid-state polymer electrolyte with plastic crystal materials for rechargeable lithium-ion battery. Journal of Power Sources. 189, 775–778 (2009).

162. Fan, L.-Z., Hu, Y.-S., Bhattacharyya, a. J., Maier, J.: Succinonitrile as a Versatile Additive for Polymer Electrolytes. Advanced Functional Materials. 17, 2800–2807 (2007).

163. Fan, L.-Z., Maier, J.: Composite effects in poly(ethylene oxide)–succinonitrile based all-solid electrolytes. Electrochemistry Communications. 8, 1753–1756 (2006).

164. Ha, H.-J., Kwon, Y.H., Kim, J.Y., Lee, S.-Y.: A self-standing, UV-cured polymer networks-reinforced plastic crystal composite electrolyte for a lithium-ion battery. Electrochimica Acta. (2011).

165. Ha, H.-J., Kil, E.-H., Kwon, Y.H., Kim, J.Y., Lee, C.K., Lee, S.-Y.: UV-curable semi-interpenetrating polymer network-integrated, highly bendable plastic crystal composite electrolytes for shape-conformable all-solid-state lithium ion batteries. Energy & Environmental Science. 5, 6491 (2012).

166. Ryou, M.-H., Lee, D.J., Lee, J.-N., Lee, H.K., Seo, M., Lee, H., Shin, W.H., Lee, Y.M., Choi, J.W., Park, J.-K.: Cross-linkable Polymer Matrix for Enhanced Thermal Stability of Succinonitrile-based Polymer Electrolyte in Lithium Recharge- able Batteries. Journal of Electrochemical Science and Technology. 2, 198–203 (2011).

167. Pringle, J.M., Shekibi, Y., MacFarlane, D.R., Forsyth, M.: The influence of different nanoparticles on a range of organic ionic plastic crystals. Electrochimica Acta. 55, 8847–8854 (2010).

168. Shekibi, Y., Pringle, J.M., Sun, J., Pas, S.J., Rocher, N.M., Clare, B.R., Hill, A.J., MacFarlane, D.R., Forsyth, M.: Lithium-functionalised silica nanoparticles for enhanced ionic conductivity in an organic ionic plastic crystal. Journal of Materials Chemistry. 20, 338 (2010).

169. Kuo, T.-H., Hsu, C.-Y., Lee, K.-M., Ho, K.-C.: All-solid-state electrochromic device based on poly(butyl viologen), Prussian blue, and succinonitrile. Solar Energy Materials and Solar Cells. 93, 1755–1760 (2009).

170. Hu, C.-W., Lee, K.-M., Chen, K.-C., Chang, L.-C., Shen, K.-Y., Lai, S.-C., Kuo, T.-H., Hsu, C.-Y., Huang, L.-M., Vittal, R., Ho, K.-C.: High contrast all-solid-state electrochromic device with 2,2,6,6-tetramethyl-1-piperidinyloxy (TEMPO), heptyl viologen, and succinonitrile. Solar Energy Materials and Solar Cells. 1–6 (2011).

171. Wu, C.-H., Hsu, C.-Y., Huang, K.-C., Nien, P.-C., Lin, J.-T., Ho, K.-C.: A photoelectrochromic device based on gel electrolyte with a fast switching rate. Solar Energy Materials and Solar Cells. 99, 148–153 (2012).

172. Abouimrane, A., Whitfield, P.S., Niketic, S., Davidson, I.J.: Investigation of Li salt doped succinonitrile as potential solid electrolytes for lithium batteries. Journal of Power Sources. 174, 883–888 (2007).

173. Chen, Y., Zhang, Y., Zhao, L.: ATR-FTIR spectroscopic studies on aqueous LiClO4 , NaClO4 , and Mg(ClO4)2 solutions. Phys. Chem. Chem. Phys. 6, 537–542 (2004).

174. Fengler, O.I., Ruoff, A.: O.I. Fengler *, A. Ruoff. Spectrochimica Acta. Part A. 57, 105–117 (2001).

175. Das, S., Bhattacharyya, A.J.: Influence of water and thermal history on ion transport in lithium salt-succinonitrile plastic crystalline electrolytes. Solid State Ionics. 181, 1732–1739 (2010).

176. Sim, L.H., Gan, S.N., Chan, C.H., Yahya, R.: ATR-FTIR studies on ion interaction of lithium perchlorate in polyacrylate/poly(ethylene oxide) blends. Spectrochimica Acta. Part A. 76, 287–92 (2010).

177. Wilmshurst, J.K.: Vibrational Spectra of Inorganic Molecules. IV. Infrared Reflection Spectra of Liquid Lithium, Sodium, Potassium and Silver Chlorates, and Liquid Lithium Perchlorate. The Journal of Chemical Physics. 36, 2415 (1962).

178. Choi, C.H., Kertesz, M.: Conformational Information from Vibrational Spectra of Styrene , trans-Stilbene , and cis-Stilbene. J. Phys. Chem. A. 101, 3823–3831 (1997).

179. Jia, Z., Li, X., Zhao, Q.: Effect of artificial weathering on surface properties of unsaturated polyester (UP) resin. Materials Chemistry and Physics. 121, 193–197 (2010).

180. Pucic, I.: Phase separation during radiation crosslinking of unsaturated polyester resin. Radiation Physics and Chemistry. 67, 415–419 (2003).

181. Jurkin, T., Pucić, I.: Post-irradiation crosslinking of partially cured unsaturated polyester resin. Radiation Physics and Chemistry. 75, 1060–1068 (2006).

182. Patel, M., Menezes, P. V, Bhattacharyya, A.J.: Ion transport in a polymer-plastic solid soft matter electrolyte in the light of solvent dynamics and ion association. The Journal of Physical Chemistry B. 114, 5233–40 (2010).

183. Hore, S., Dinnebier, R., Wen, W., Hanson, J., Maier, J.: Structure of Plastic Crystalline Succinonitrile: High-Resolution in situ Powder Diffraction. Zeitschrift für anorganische und allgemeine Chemie. 635, 88–93 (2009).

184. Licoccia, S., Trombetta, M., Capitani, D., Proietti, N., Romagnoli, P., Di Vona, M.L.: ATR–FTIR and NMR spectroscopic studies on the structure of polymeric gel electrolytes for biomedical applications. Polymer. 46, 4670–4675 (2005).

185. Cao, X.: Control of volume shrinkage and residual styrene of unsaturated polyester resins cured at low temperatures. II. Effect of comonomer. Polymer. 44, 1507–1516 (2003).

186. Grondin, J., Talaga, D., Lasse, J., Henderson, W.A.: Raman study of crystalline solvates between glymes CH3(OCH2CH2)nOCH3 (n=1, 2 and 3) and LiClO4. Phys. Chem. Chem. Phys. 6, 938–944 (2004).

187. Marais, S., Metayer, M., Nguyen, T.Q., Labbe, M., Saiter, J.M.: Diffusion and permeation of water through unsaturated polyester resins -influence of resin curing. European Polymer Journal. 36, 453–462 (2000).

188. Rocco, A.M., Fonseca, C.P., Pereira, R.P.: A polymeric solid electrolyte based on a binary blend of poly(ethylene oxide), poly(methyl vinyl ether-maleic acid) and LiClO4. Polymer. 43, 3601–3609 (2002).

List of publications

Included in this thesis:

1. Wojcik, P.J., Cruz, A.S., Santos, L., Pereira, L., Martins, R., Fortunato, E.: Microstructure control of dual-phase inkjet-printed *a*-$WO_3/TiO_2/WO_X$ films for high-performance electrochromic applications. Journal of Materials Chemistry. 22, 13268 (2012).
2. Wojcik, P.J., Pereira, L., Martins, R., Fortunato, E.: Statistical mixture design and multivariate analysis of inkjet printed *a*-$WO_3/TiO_2/WO_X$ electrochromic films. ACS Comb. Sci. 16 (1) 5-16 (2014).
3. Wojcik, P.J., Pereira, L., Martins, R., Fortunato, E.: Metal Oxide Nanoparticle Engineering for Printed Electrochemical Applications. In: Nano-Electrochemistry: Electrochemical Synthesis Methods, Properties and Characterization Techniques. Handbook of Springer – in press.
4. Wojcik, P.J., Santos, L., Pereira, L., Martins, R., Fortunato, E.: Tungsten Oxide Nanoparticle Engineering for Inkjet Printed Electrochromic Devices – under submission.
5. Wojcik, P.J., Santos, L., Pereira, L., Martins, R., Fortunato, E.: Formation mechanism and electrochromic response of WO_X nanoparticles synthesized via hydrothermal process – under preparation.
6. Wojcik, P.J., Cruz, A.S., Pereira, L., Martins, R., Fortunato, E.: Resin-based Thermosetting Composite Solid Electrolyte for Electrochromic Applications – under submission.
7. Wojcik, P.J., Santos, L., Pereira, L., Martins, R., Fortunato, E.: Resin-based Thermosetting Composite Solid Electrolyte: New Perspective on Printed Electrochemical Devices – under preparation.
8. Wojcik, P.J., Cruz, A.S., Butti, P., Pereira, L., Martins, R., Fortunato, E.: Effect of annealing on the electrochromic performance of inkjet printed WO_3 films – under preparation.

Not included in this thesis:

9. Bernacka-Wojcik, I., Senadeera, R., Wojcik, P.J., Silva, L.B., Doria, G., Baptista, P., Aguas, H., Fortunato, E., Martins, R.: Inkjet printed and "doctor blade" TiO_2 photodetectors for DNA biosensors. Biosensors & bioelectronics. 25, 1229–34 (2010).
10. Bernacka-Wojcik, I., Lopes, P., Catarina Vaz, A., Veigas, B., Jerzy Wojcik, P., Simões, P., Barata, D., Fortunato, E., Viana Baptista, P., Aguas, H., Martins, R.: Bio-microfluidic platform for gold nanoprobe based DNA detection-application to Mycobacterium tuberculosis. Biosensors & bioelectronics. 48, 87–93 (2013).
11. Veigas, B., Branquinho, R., Pinto, J. V., Wojcik, P.J., Martins, R., Fortunato, E., Baptista, P. V.: Ion sensing (EIS) real-time quantitative monitorization of isothermal DNA amplification. Biosensors and Bioelectronics. 52, 50–55 (2013).

12. Contreras, J., Martins, R., Wojcik, P., Filonovich, S., Aguas, H., Gomes, L., Fortunato., E., Ferreira, I.: Color sensing ability of an amorphous silicon position sensitive detector array system. Sensors & Actuators A: Physical, 205, 26-37, (2014)

List of presentations

Oral presentations:

1. Wojcik, P.J., Cruz, A.S., Santos, L., Ramos, A.M., Pereira, L., Martins, R., Fortunato, E.: Inkjet Printed Inorganic Electrochromic Devices, The International Chemical Congress of Pacific Basin Societies – Pacyfichem 2010, 15-20 December, 2010, Honolulu, Hawaii, USA.
2. Wojcik, P.J., Bernacka-Wojcik, I., Fortunato, E., Martins, R.: Inkjet printed dye sensitized solar cells, The International Chemical Congress of Pacific Basin Societies – PacifiChem 2010, 15-20 December, 2010, Honolulu, Hawaii, USA.
3. Wojcik, P.J., Martins, R., Fortunato, E., Inkjet printing of inorganic materials for electrochromic window and dye-sensitized solar cell applications, Printed Electronic and Foil Assembly, Fraunhofer Workshop & Summerschool, 7-10 June, 2011, Munich, Germany.
4. Wojcik, P.J., Cruz, A.S., Ramos, A.M., Pereira, L., Martins, R., Fortunato, E.: Plastic crystal/polymer/metal oxide composites as ion-conductive membranes for high performance flexible electrochromic devices, European Materials Research Society (E-MRS) 2011 Fall Meeting, 19 - 23 September, 2011, Warsaw, Poland.
5. Wojcik, P.J., Cruz, A.S., Santos, L., Pereira, L., Martins, R., Fortunato, E.: Dual-phase inkjet printed a-WO_3/TiO_2/WO_X electrochromic films, European Materials Research Society (E-MRS) 2011 Fall Meeting, 19 - 23 September, 2011, Warsaw, Poland.
6. Wojcik, P.J., Pereira, L., Martins, R., Fortunato, E.: High performance all-solid-state electrochromic devices based on inorganic inkjet printed films and plastic crystal/polymer/metal oxide electrolyte, European Materials Research Society (E-MRS) 2012 Spring Meeting, 14-18 May, 2012, Strasbourg, France – **Young Scientist Award.**
7. Wojcik, P.J., Pereira, L., Martins, R., Fortunato, E.: All-solid-state Printed Electrochromic Devices Based on WO_3 Films and Thermosetting Composite Solid Electrolyte, Fraunhofer Autumn Workshop & Summer School, 19-20 November, 2012, Munich, Germany.
8. Wojcik, P.J., Santos, L., Pereira, L., Martins, R., Fortunato, E.: Metal Oxide Nanoparticle Engineering for Inkjet Printing Technology, Fraunhofer Autumn Workshop & Summer School, 19-20 November, 2012, Munich, Germany.
9. Wojcik, P.J., Pereira, L., Martins, R., Fortunato, E.: High Performance All-solid-state Electrochromic Devices Based on Printed Inorganic Films and Thermosetting Solid State Electrolyte, 2012 Materials Research Society (MRS) Fall Meeting & Exhibit, 25-30 November, 2012, Boston, USA – **Best Presentation Award.**

10. Wojcik, P.J., Santos, L., Pereira, L., Martins, R., Fortunato, E.: All-solid-state printed devices based on inorganic electrochromic films and thermosetting solid state electrolyte, 3as Jornadas do CENIMAT, 28 June, 2013, Monte da Caparica, Portugal.
11. Wojcik, P.J., Pereira, L., Martins, R., Fortunato, E.: Fully Printed, Flexible Electrochromic Display Based on Tungsten Oxide and Thermosetting Solid State Electrolyte, 6th International Symposium on Flexible organic Electronics – ISFOE13, 8-11 July, 2013, Thessaloniki, Greece.
12. Wojcik, P.J., Santos, L., Pereira, L., Martins, R., Fortunato, E.: Metal Oxide Nanoparticle Engineering for Printed Electrochemical Applications, 10th Interntional Conference on Nanosciences & Nanotechnologies – NN13, 9-12 July, 2013, Thessaloniki, Greece.
13. Wojcik, P.J., Delattre, A., Pereira, L., Martins, R., Fortunato, E.: Fully Printed Electrochromic Display on Paper, European Materials Research Society (E-MRS) 2013 Fall Meeting, 16-20 September, 2013, Warsaw, Poland.

Contribution in oral presentations:

14. Bernacka-Wojcik, I., Senadeera, R., Wojcik, P.J., Silva, L.B., Doria, G., Baptista, P., Aguas, H., Fortunato, E., Martins, R.: From gold nanoparticles to "toothpaste" for DNA detection, Workshop Nano09-Shaping the Future, International Iberian Nanotechnology Institute – INL, 10-11 December 2009, Braga, Portugal.
15. Bernacka-Wojcik, I., Senadeera, R., Wojcik, P.J., Silva, L.B., Doria, G, Baptista, P., Aguas, H., Fortunato, E., Martins, R.: Colorimetric DNA biosensor based on gold nanoparticles and inkjet printed TiO_2 photodetector, Jornadas Tecnologicas da FCT 2010 – JORTEC, 3 May, 2010, Caparica, Portugal.
16. Ram, S.K., Bernacka-Wojcik, I., Vicente, A., Barata, D., Wojcik, P.J., Busani, T., Diaconu, B., Aguas, H., Fortunato, E., Martins, R.: Single step preparation technique of multidimensional microfluidic system, European Materials Research Society (E-MRS) 2011 Fall Meeting, 19 - 23 September, 2011, Warsaw, Poland.
17. Ram, S.K., Bernacka-Wojcik, I., Vicente, A., Wojcik, P.J., Busani, T., Barata, D., Diaconu, B., Aguas, H., Fortunato, E., Martins, R.: Non-lithographic approach to create periodic nanowrinkled microchannels for ultrasensitive sensors detection, European Materials Research Society (E-MRS) 2011 Fall Meeting, 19 - 23 September, 2011, Warsaw, Poland.
18. Santos, L., Wojcik, P.J., Pereira, L., Martins, R., Fortunato, E.: Hydrothermal synthesis of tungsten oxide nanocrystals for electrochromic inkjet printed thin films, European Materials Research Society (E-MRS) 2011 Fall Meeting, 19 - 23 September, 2011, Warsaw, Poland.
19. Bodoardo, S., Garino, N., Fortunato, E., Martins, R., Nair, J.R., Penazzi, N., Pereira, L., Vankova, S., Wojcik, P.J., Zanarini, S.: Application of gel polymer electrolytes in fast switching and flexible

WO_3 based electrochromic devices, European Materials Research Society (E-MRS) 2011 Fall Meeting, 19 - 23 September, 2011, Warsaw, Poland.

20. Martins, R., Pinto, J.V., Bernacka-Wojcik, I., Wojcik, P.J., Branquinho, R., Viegas, B. Silva, L.B., Baptista, P., Fortunato, F.: Nanobiodetection based on optical nano sensors and gold nanoparticles probe systems, Plastic Electronics 2011, Conference & Exhibition, 11-13 October, 2011, Messe Dresden, Germany.
21. Santos, L., Wojcik, P.J., Pereira, L., Martins, R., Fortunato, E.: Hydrothermal synthesis of nanostructured WO_3 and its application in electrochromic inkjet printed thin films, European Materials Research Society (E-MRS) 2012 Spring Meeting, 14-18 May, 2012, Strasbourg, France.
22. Santos, L., Wojcik, P.J., Pereira, L., Martins, R., Fortunato, E.: Synthesis and characterization of various metal oxides nanoparticles, Fraunhofer Autumn Workshop & Summer School, 19-20 November, 2012, Munich, Germany
23. Santos, L., Wojcik, P.J., Pereira, L., Martins, R., Fortunato, E.: Hydrothermal synthesis of nanostructured WO_3 and its application in EC inkjet printed thin films, 3rd Forum on Electrochemistry and Innovation, 16-17 September, 2013, Vila Real, Portugal.

Posters:

1. Wojcik, P.J., Bernacka-Wojcik, I., Senadeera, R., Baptista, P., Fortunato, E., Martins, R.: Inkjet printed titanium dioxide for dye sensitized photodetectors, Plastic Electronics Europe 2009, 27-29 October, 2009, Dresden, Germany.

2. Wojcik, P.J., Cruz, A.S., Santos, L., Ramos, A.M., Pereira, L., Martins, R., Fortunato, E.: Inkjet printed nanostructured materials – application of titanium dioxide and tungsten trioxide nanocrystals for photovoltaic and electrochromic window applications, 3rd Inrenational Conference on Advanced Nano Materials – ANM 2010, September 12-15, 2010, Agadir, Morocco.

3. Wojcik, P.J., Cruz, A.S., Santos, L., Ramos, A.M., Pereira, L., Martins, R., Fortunato, E.: Inkjet Printed Tungsten Trioxide for Electrochromic Applications, 3rd International Symposium on Transparent Conductive Materials (former TCO) – TCM 2010, 17-21 October, 2010, Analipsi/Hersonissos, Crete, Greece – **Young Scientist Best Poster Award.**

4. Wojcik, P.J., Ramos, A.M., Costa, R., Cruz, A.S., Santos, L., Pereira, L., Martins, R., Fortunato, E.: Solid state electrolytes based on plastic crystals dispersed in a polymer matrix for paper electronics, I3N – III Annual Meeting 2011, 11-12 February, 2011, Fatima, Portugal

5. Wojcik, P.J., Cruz, A.S., Santos, L., Ramos, A.M., Pereira, L., Martins, R., Fortunato, E.: Inkjet printed tungsten trioxide for electrochromic applications, I3N – III Annual Meeting 2011, 11-12 February, 2011, Fatima, Portugal.

6. Wojcik, P.J., Bernacka-Wojcik, J., Fortunato, E., Martins, R: Inkjet printed Dye-sensitized solar cells, I3N – III Annual Meeting 2011, 11-12 February, 2011, Fatima, Portugal.
7. Wojcik, P.J., Cruz, A.S., Santos, L., Pereira, L., Martins, R., Fortunato, E.: High performance all-solid-state electrochromic devices based on inorganic inkjet printed films and plastic crystal/polymer/metal oxide electrolyte, I3N – IV Annual Meeting 2012, 09-10 March, 2012, Figueira da Foz, Portugal.
8. Wojcik, P.J., Santos, L., Pereira, L., Martins, R., Fortunato, E.: Metal Oxide Nanoparticle Engineering for Inkjet Printing Technology: Nanostructured WO_x Synthesis for Electrochromic Application, 2012 Materials Research Society (MRS) Fall Meeting & Exhibit, 25-30 November, 2012, Boston, USA.

Contribution in posters:

9. Costa, C., Gonçalves, A., Wojcik, P.J., Martins, R., Henriques, I., Fortunato, E.: Inkjet printing technique to build several printed electronic devices, Primeiro Encontro - I3N, 3-4 October, 2008, Fátima, Portugal.
10. Bernacka-Wojcik, I., Senadeera, R., Wojcik, P.J., Silva, L.B., Doria, G., Baptista, P., Aguas, H., Fortunato, E., Martins, R.: Inkjet printed and "doctor blade" TiO_2 photodetectors for DNA biosensors, NanoBioTech 2009 Conference, 16 - 18 November, 2009, Montreux, Switzerland.
11. Bernacka-Wojcik, I., Senadeera, R., Wojcik, P.J., Silva, L.B., Doria, G., Baptista, P., Aguas, H., Fortunato, E., Martins, R.: Inkjet printed and "doctor blade" TiO_2 photodetectors for DNA biosensors, Biosensors 2010 Congress, 26-28 May, 2010, Glasgow, United Kingdom.
12. Bernacka-Wojcik, I., Senadeera, R., Wojcik, P.J., Silva, L.B., Doria, G., Baptista, P., Aguas, H., Fortunato, E., Martins, R.: Colorimetric DNA biosensor based on gold nanoparticles and inkjet printed nanocrystalline TiO_2 photodetector, 3rd Inrenational Conference on Advanced Nano Materials – ANM 2010, 12-15 September, 2010, Agadir, Morocco.
13. Bernacka-Wojcik, I., Barata, D., Busani, T., Wojcik, P.J., Fortunato, E., Martins, R., Aguas, H.: Microfabrication of high aspect ratio features in SU-8 layer for biosensing applications, I3N – III Annual Meeting 2011, 11-12 February, 2011, Fatima, Portugal.
14. Santos, L., Wojcik, P.J., Pereira, L., Martins, R., Fortunato, E.: Hydrothermal synthesis of nanostructured tungsten oxide for electrochromic inkjet printed thin films, IV International Meeting of I3N, 9-10 March, 2012, Quiaios, Portugal.
15. Santos, L., Wojcik, P.J., Pereira, L., Martins, R., Fortunato, E.: Solid-state Electrolyte-gated TFT's, 3as Jornadas of CENIMAT, 28 June, 2013, Monte da Caparica, Portugal.

16. Santos, L., Wojcik, P.J., Pereira, L., Martins, R., Fortunato, E.: Synthesis and characterization of various metal oxide nanoparticles, International Conference on Nanoscience and Nanotechnology – NanoPT, 13-15 February, 2013, Porto, Portugal.

Appendix 1

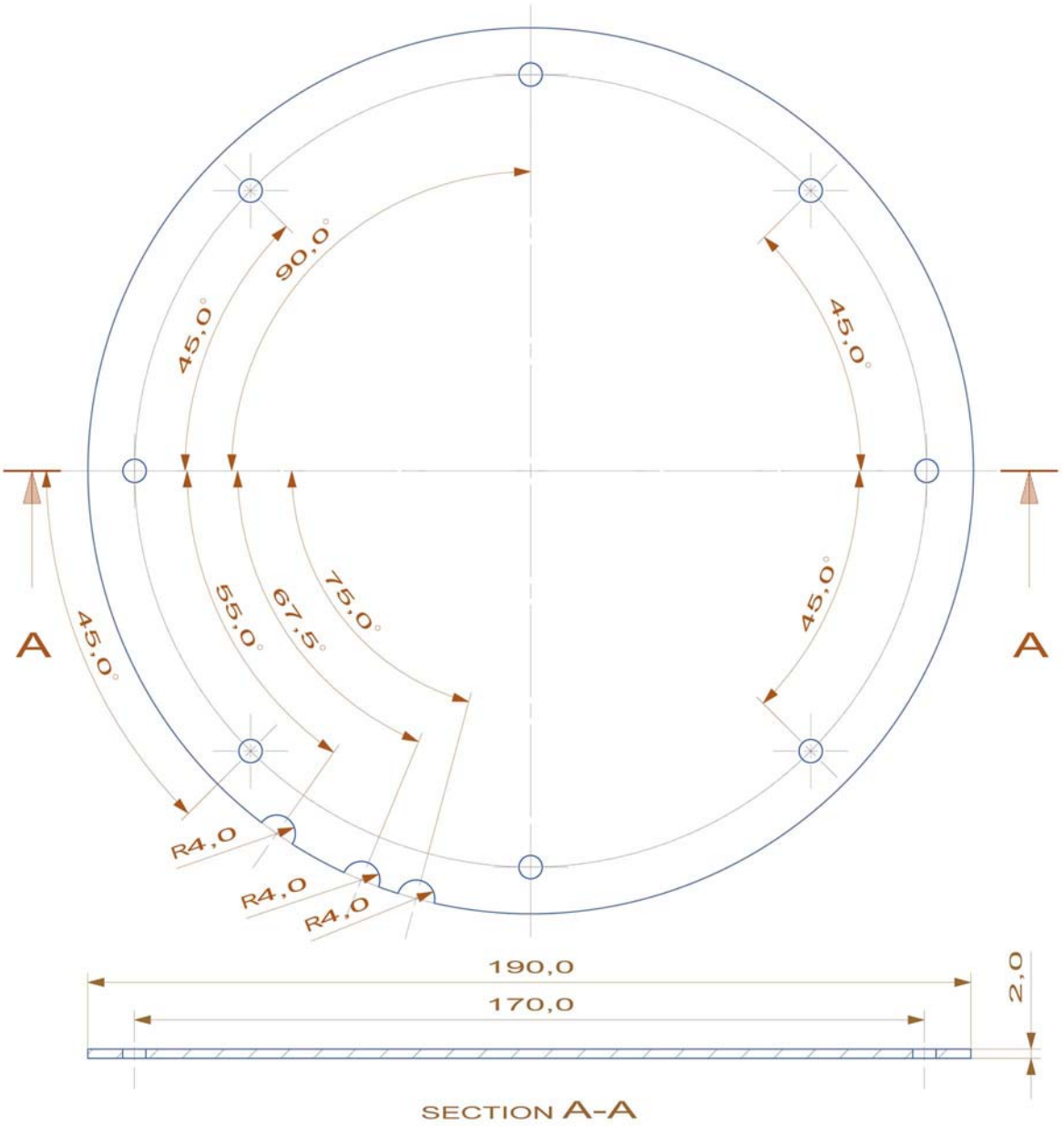

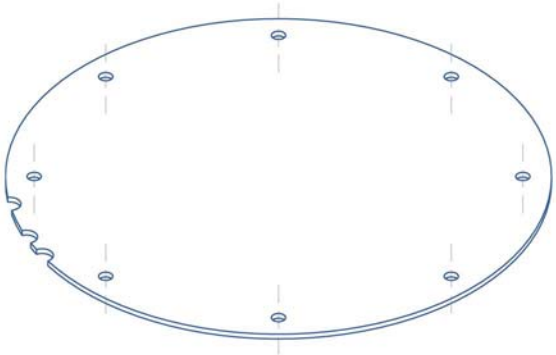

Part name:	mold for TCSE casting – bottom plate
Material:	Stainless steel
QTY:	1
Designer:	P.J. Wojcik, p.wojcik@campus.fct.unl.pt

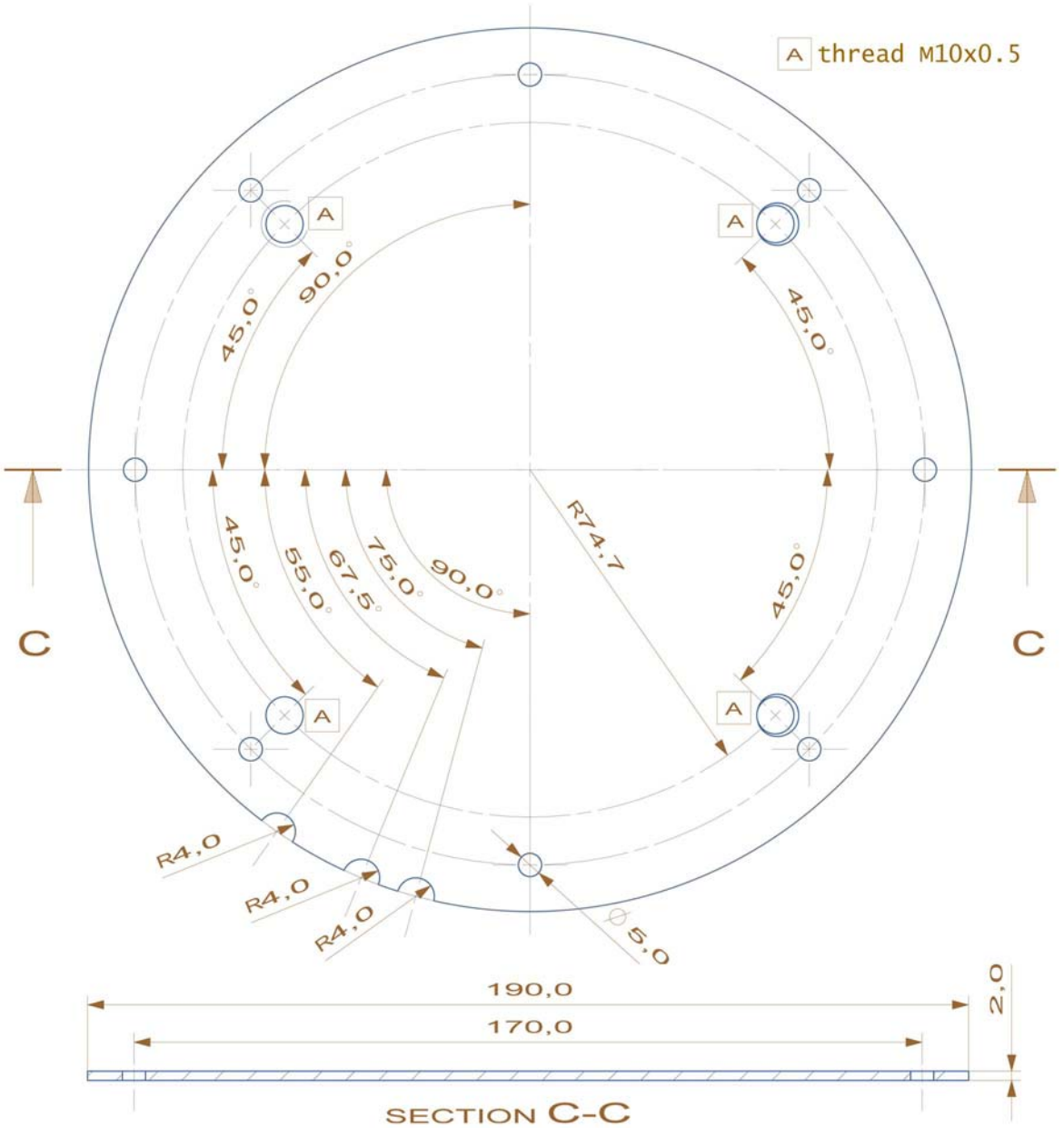

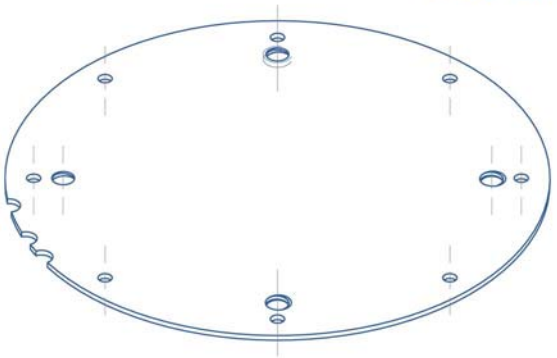

Part name:	mold for TCSE casting – top plate
Material:	Stainless steel
QTY:	1
Designer:	P.J. Wojcik, p.wojcik@campus.fct.unl.pt

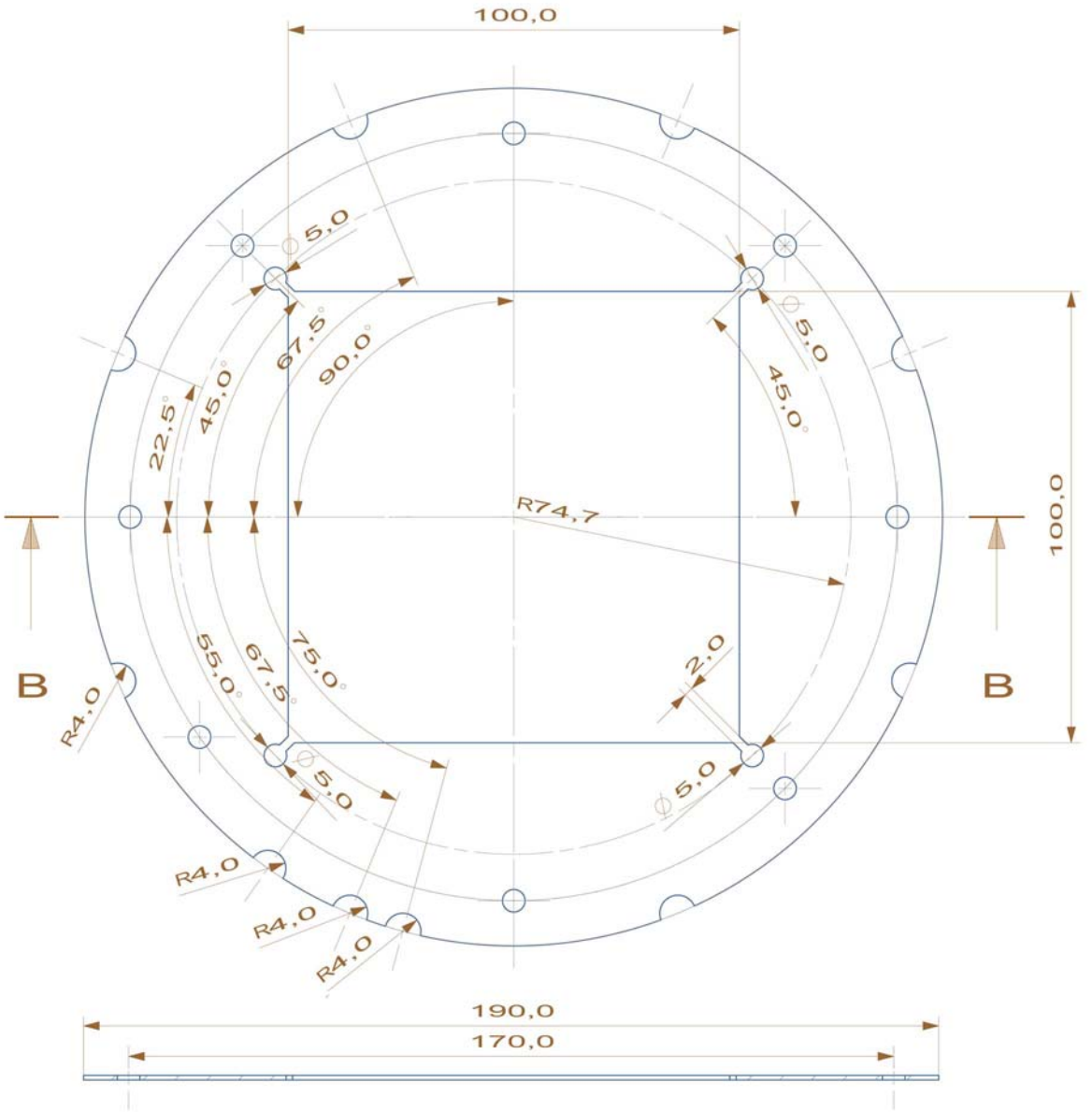

SECTION B-B

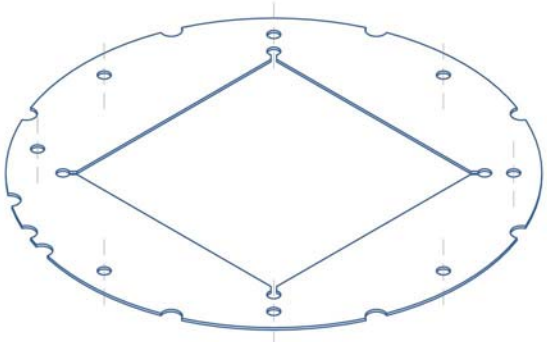

Part name:	mold for TCSE casting – gasket
Material:	Stainless steel
Thickness:	0.5; 1; 1.5 mm
Designer:	P.J. Wojcik, p.wojcik@campus.fct.unl.pt

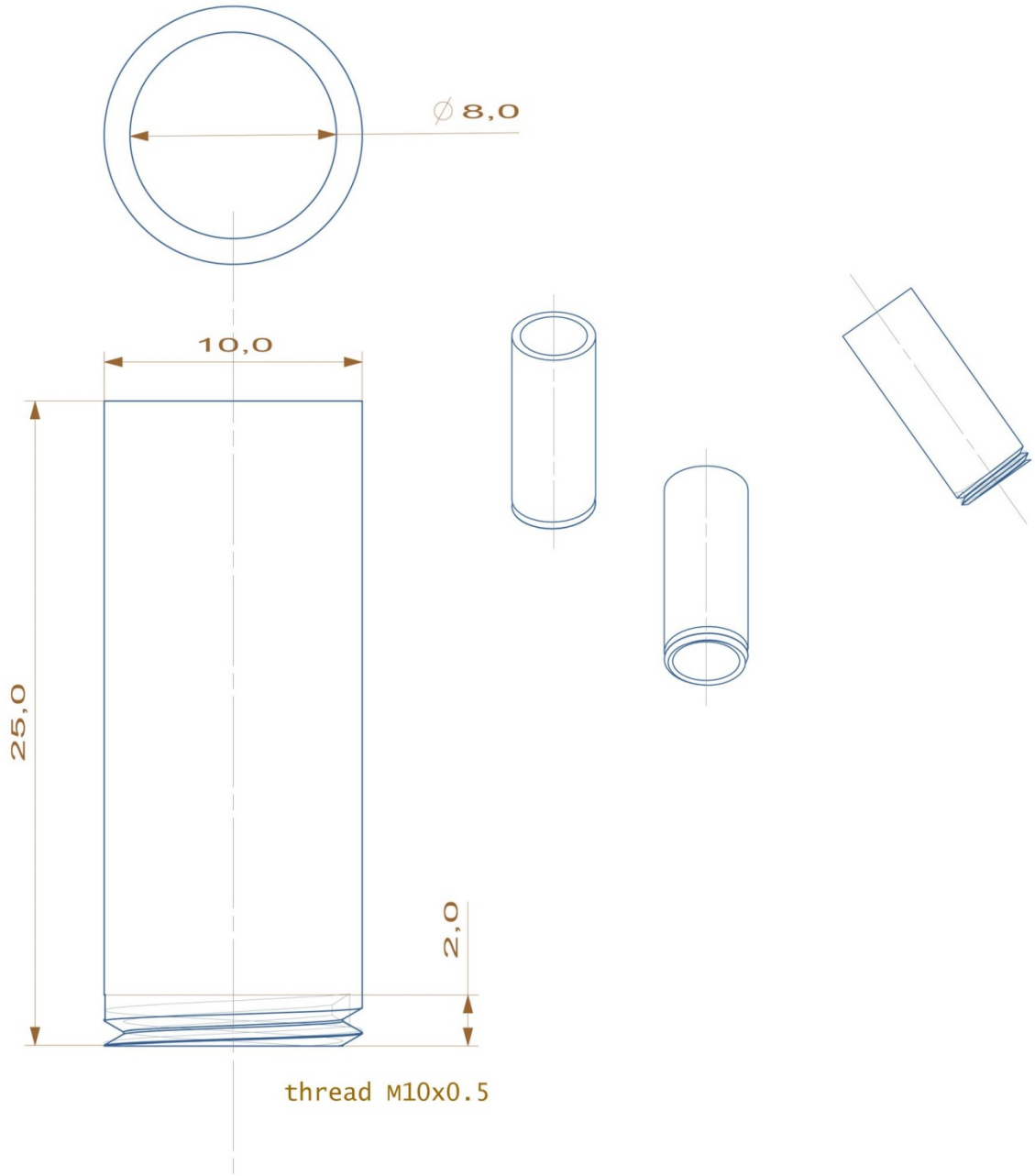

Part name:	mold for TCSE casting – inlet
Material:	Stainless steel
QTY:	4
Designer:	P.J. Wojcik, p.wojcik@campus.fct.unl.pt

Appendix 2

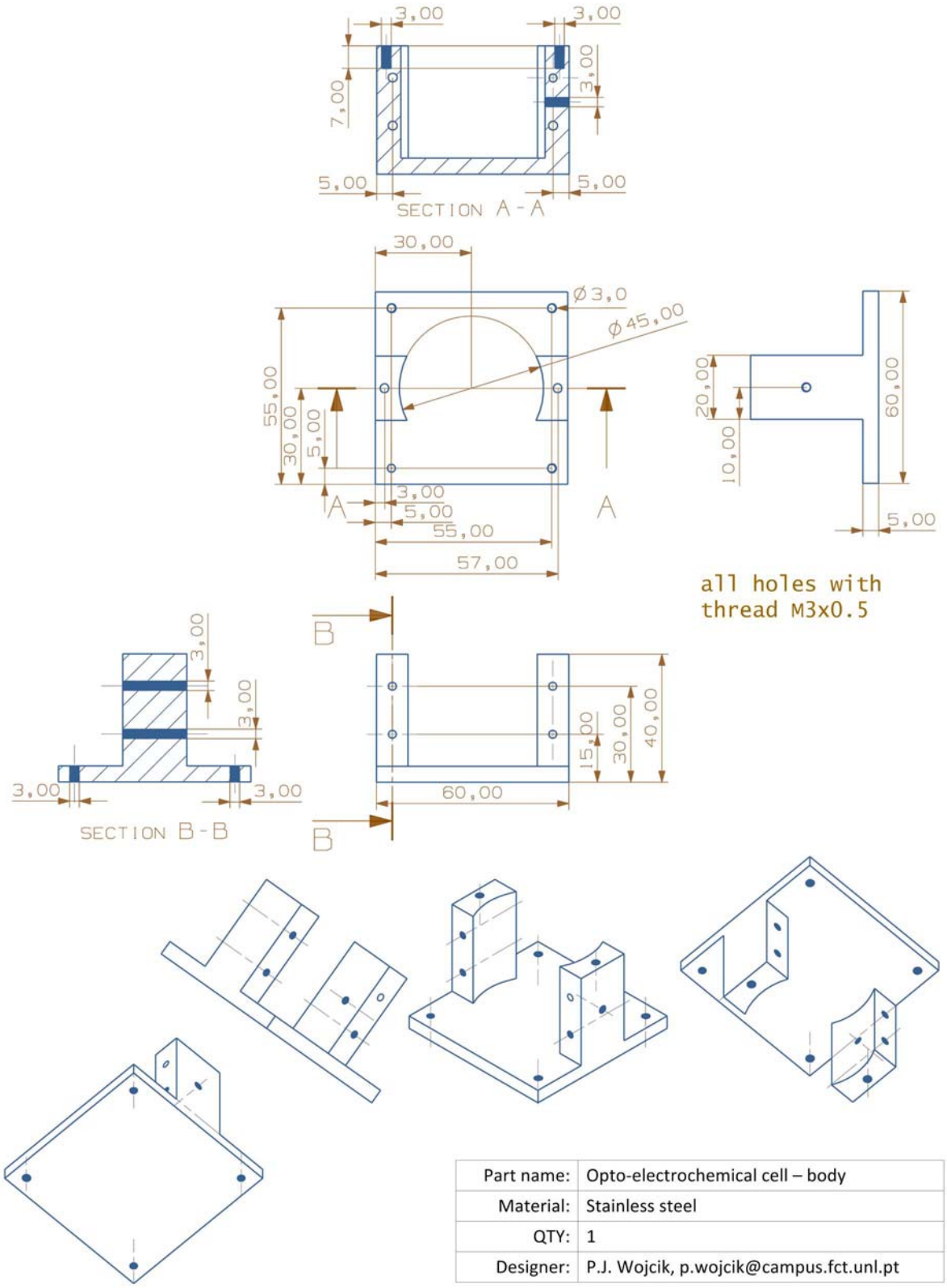

Part name:	Opto-electrochemical cell – body
Material:	Stainless steel
QTY:	1
Designer:	P.J. Wojcik, p.wojcik@campus.fct.unl.pt

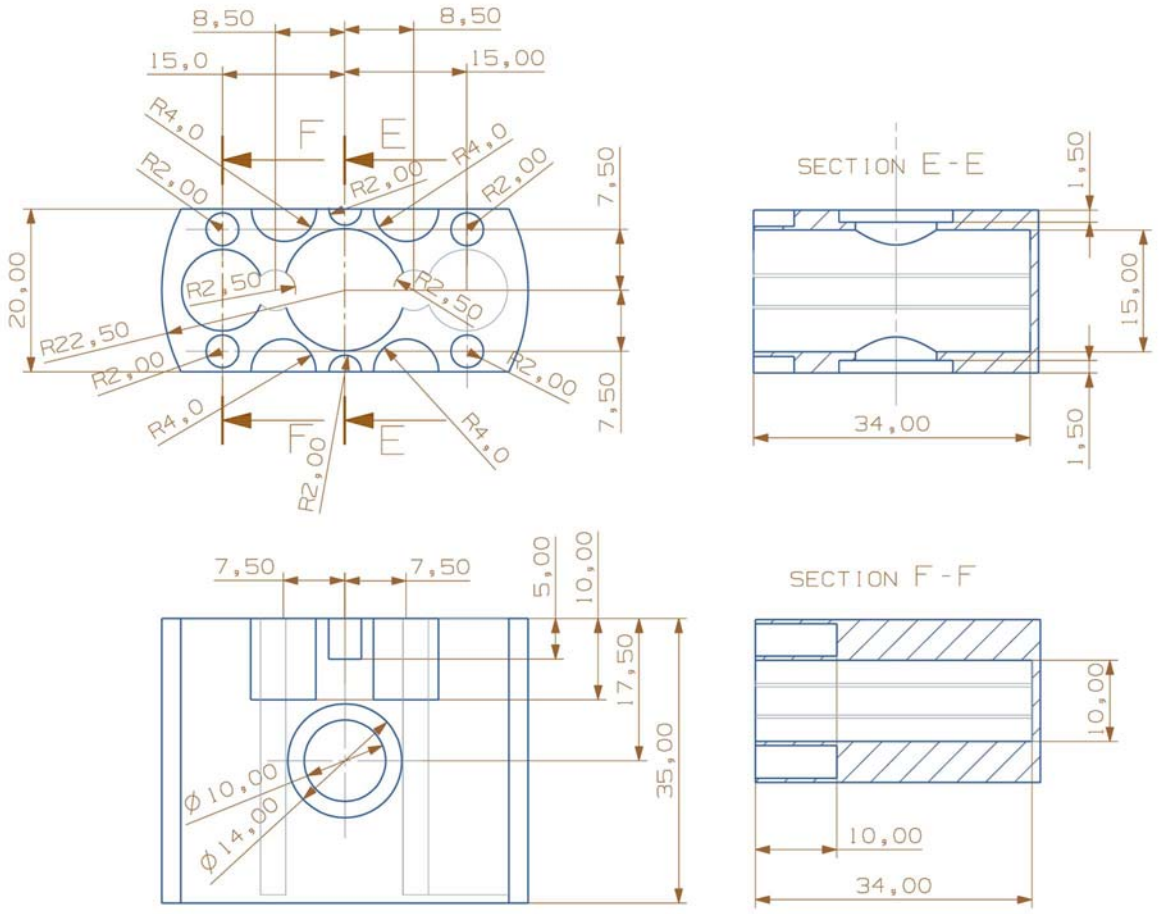

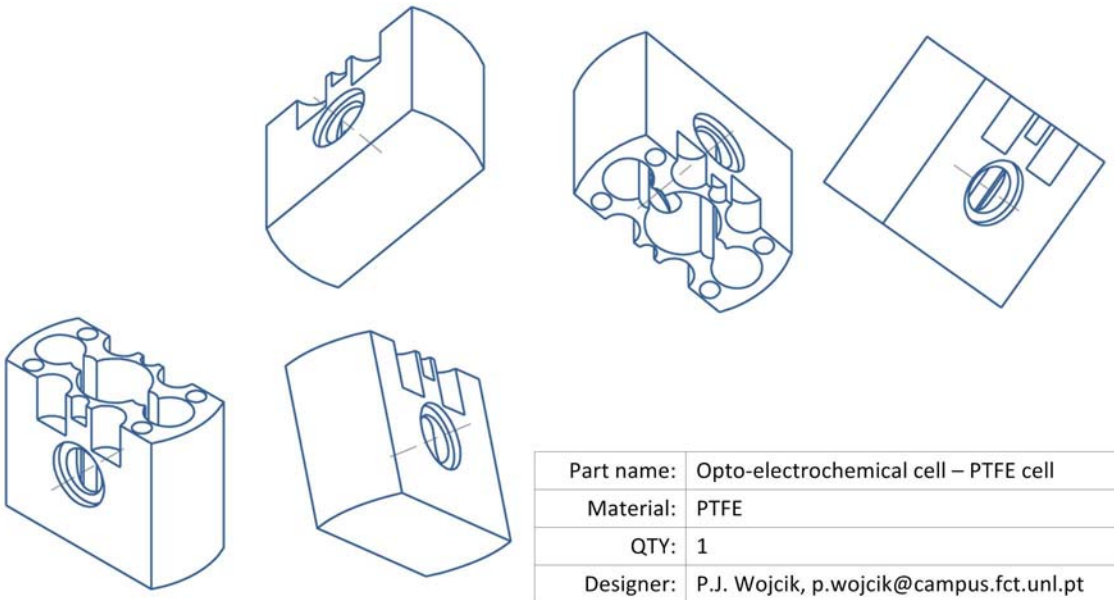

Part name:	Opto-electrochemical cell – PTFE cell
Material:	PTFE
QTY:	1
Designer:	P.J. Wojcik, p.wojcik@campus.fct.unl.pt

Appendix 3

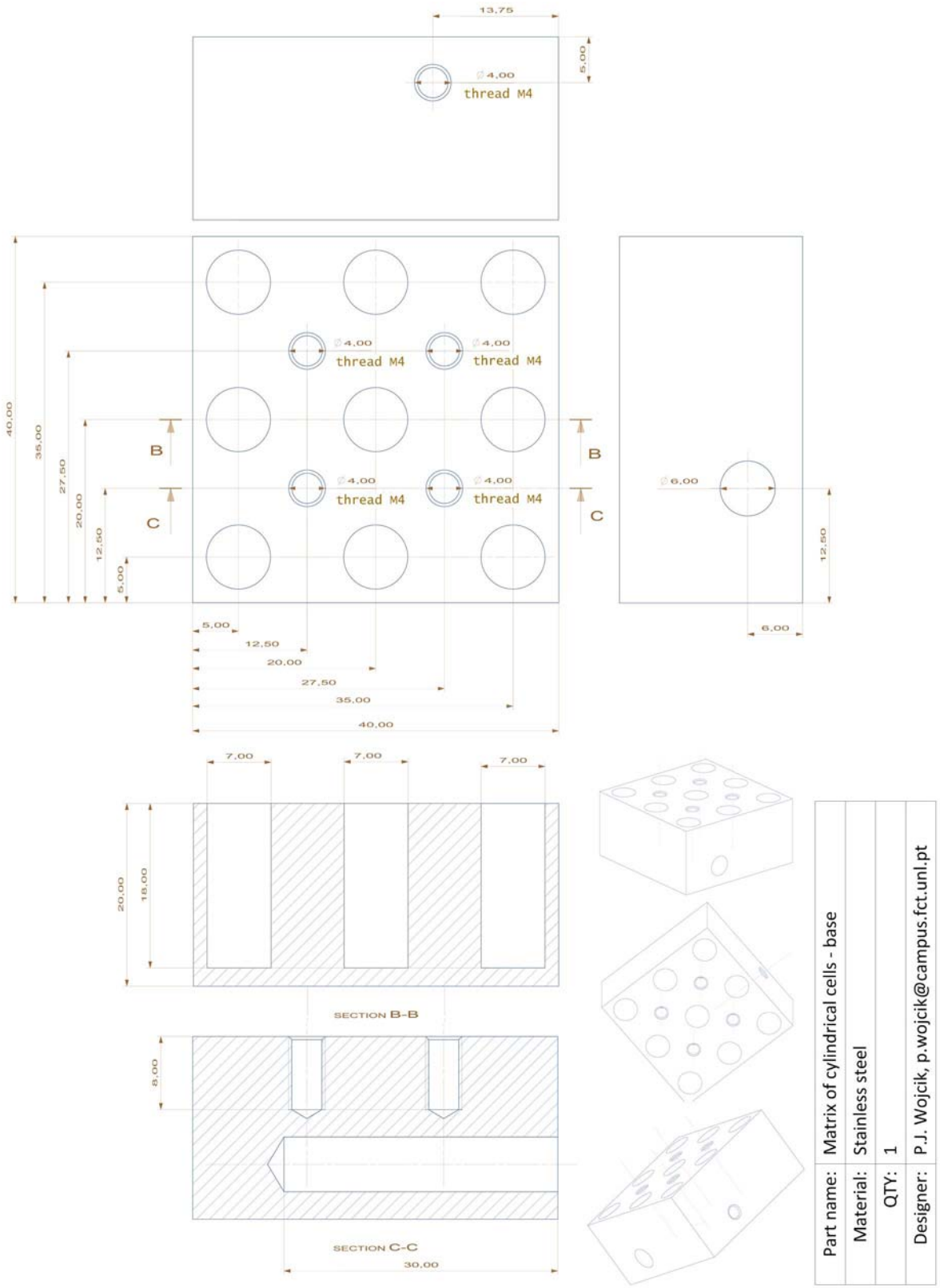
13,75
5,00
Ø4,00
thread M4
Ø4,00
thread M4
Ø4,00
thread M4
Ø4,00
thread M4
Ø4,00
thread M4
B
B
C
C
40,00
35,00
27,50
20,00
12,50
5,00
Ø6,00
12,50
6,00
5,00
12,50
20,00
27,50
35,00
40,00
7,00
7,00
7,00
20,00
18,00
SECTION B-B
8,00
SECTION C-C
30,00
Part name: Matrix of cylindrical cells - base
Material: Stainless steel
QTY: 1
Designer: P.J. Wojcik, p.wojcik@campus.fct.unl.pt

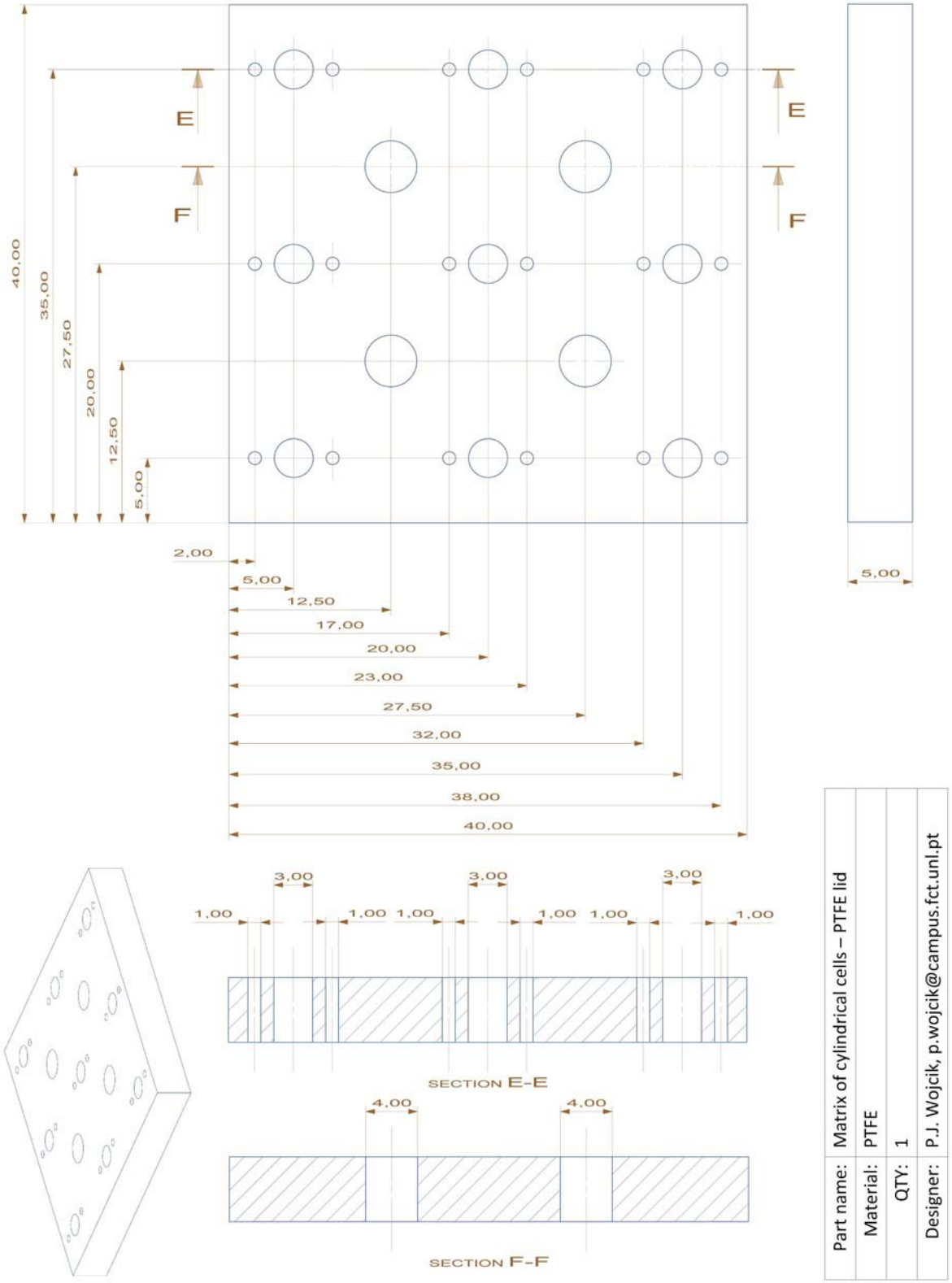
E
F
E
F
40,00
35,00
27,50
20,00
12,50
5,00
2,00
5,00
12,50
17,00
20,00
23,00
27,50
32,00
35,00
38,00
40,00
5,00
3,00
3,00
3,00
1,00
1,00
1,00
1,00
1,00
1,00
1,00
SECTION E-E
4,00
4,00
SECTION F-F
Part name: Matrix of cylindrical cells – PTFE lid
Material: PTFE
QTY: 1
Designer: P.J. Wojcik, p.wojcik@campus.fct.unl.pt

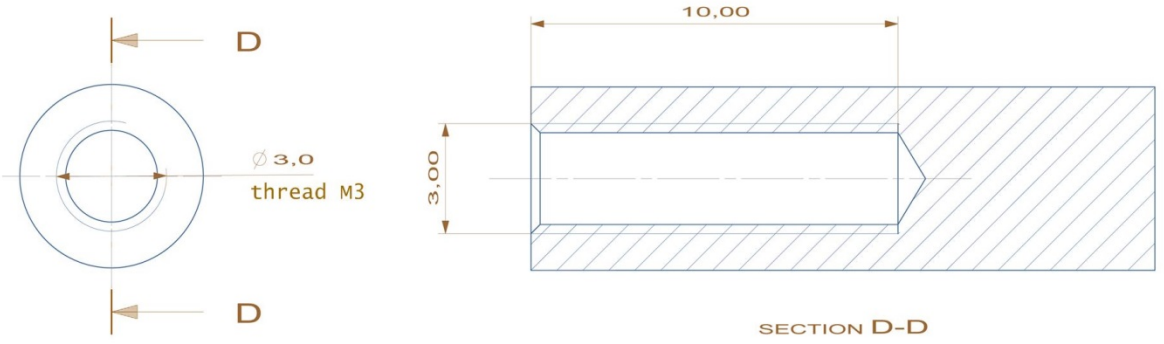

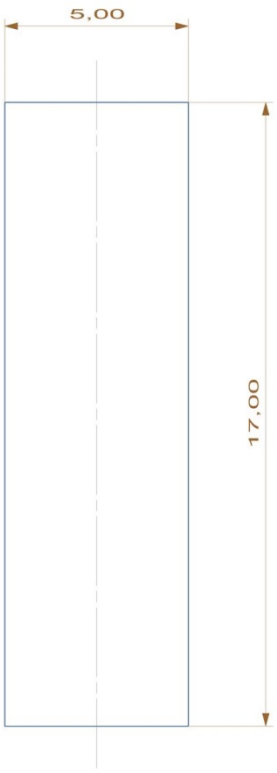

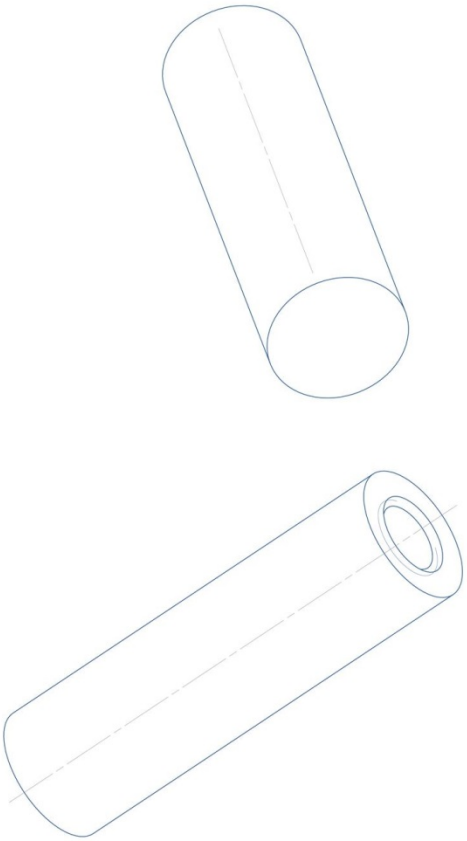

Part name:	Matrix of cylindrical cells – top elecrode
Material:	Stainless steel
QTY:	9
Designer:	P.J. Wojcik, p.wojcik@campus.fct.unl.pt

Appendix 4

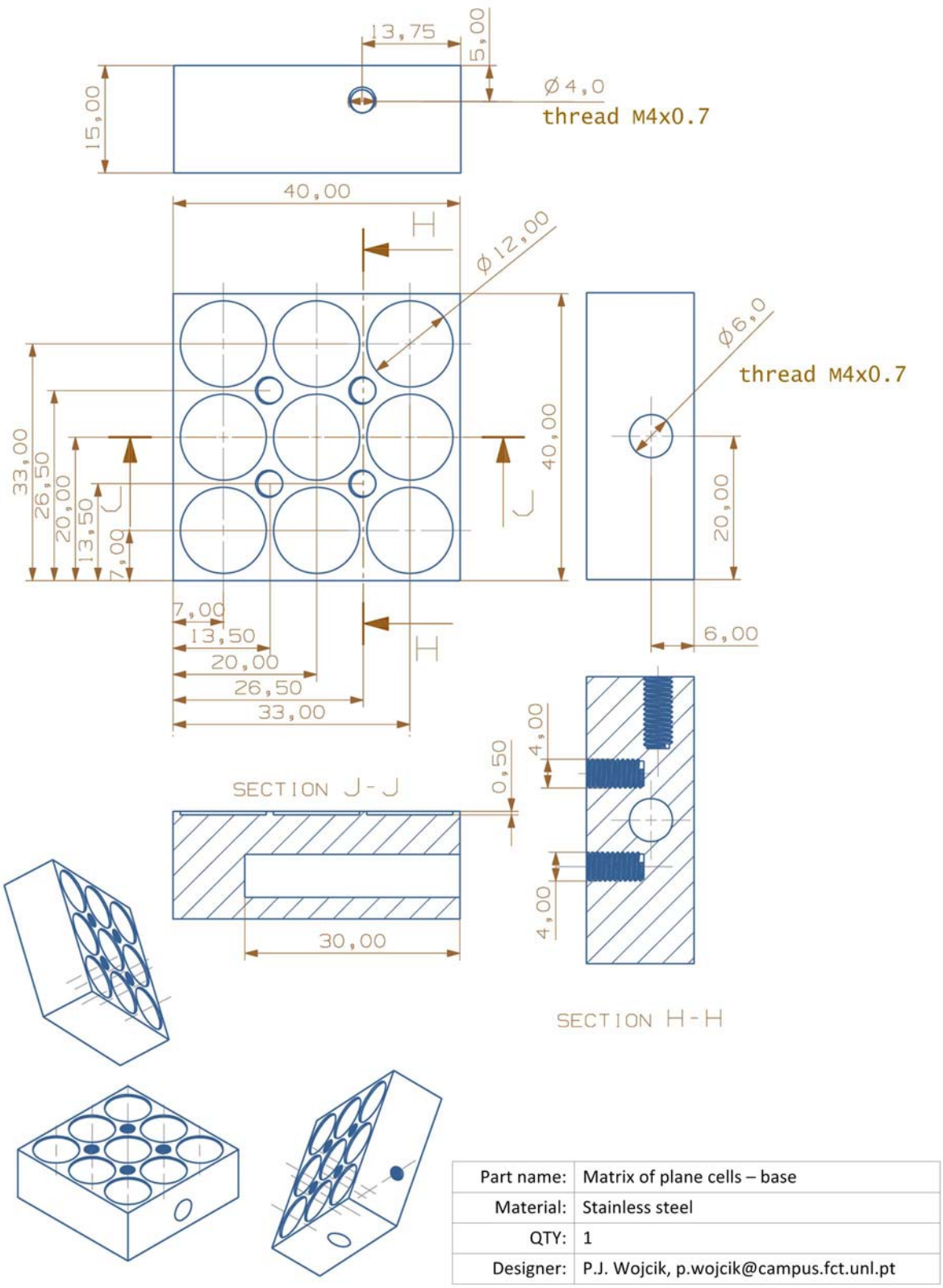

Part name:	Matrix of plane cells – base
Material:	Stainless steel
QTY:	1
Designer:	P.J. Wojcik, p.wojcik@campus.fct.unl.pt

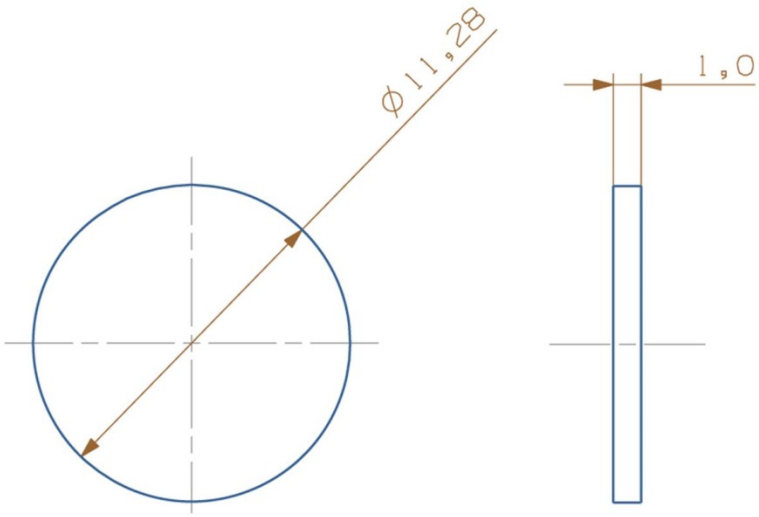

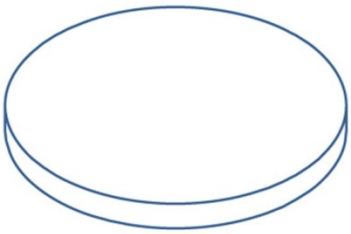

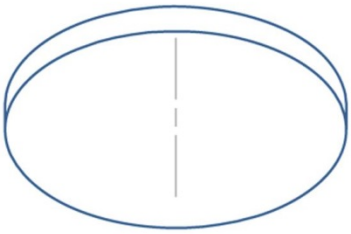

Part name:	matrix of plane cells – top electrode
Material:	Stainless steel
QTY:	18
Designer:	P.J. Wojcik, p.wojcik@campus.fct.unl.pt

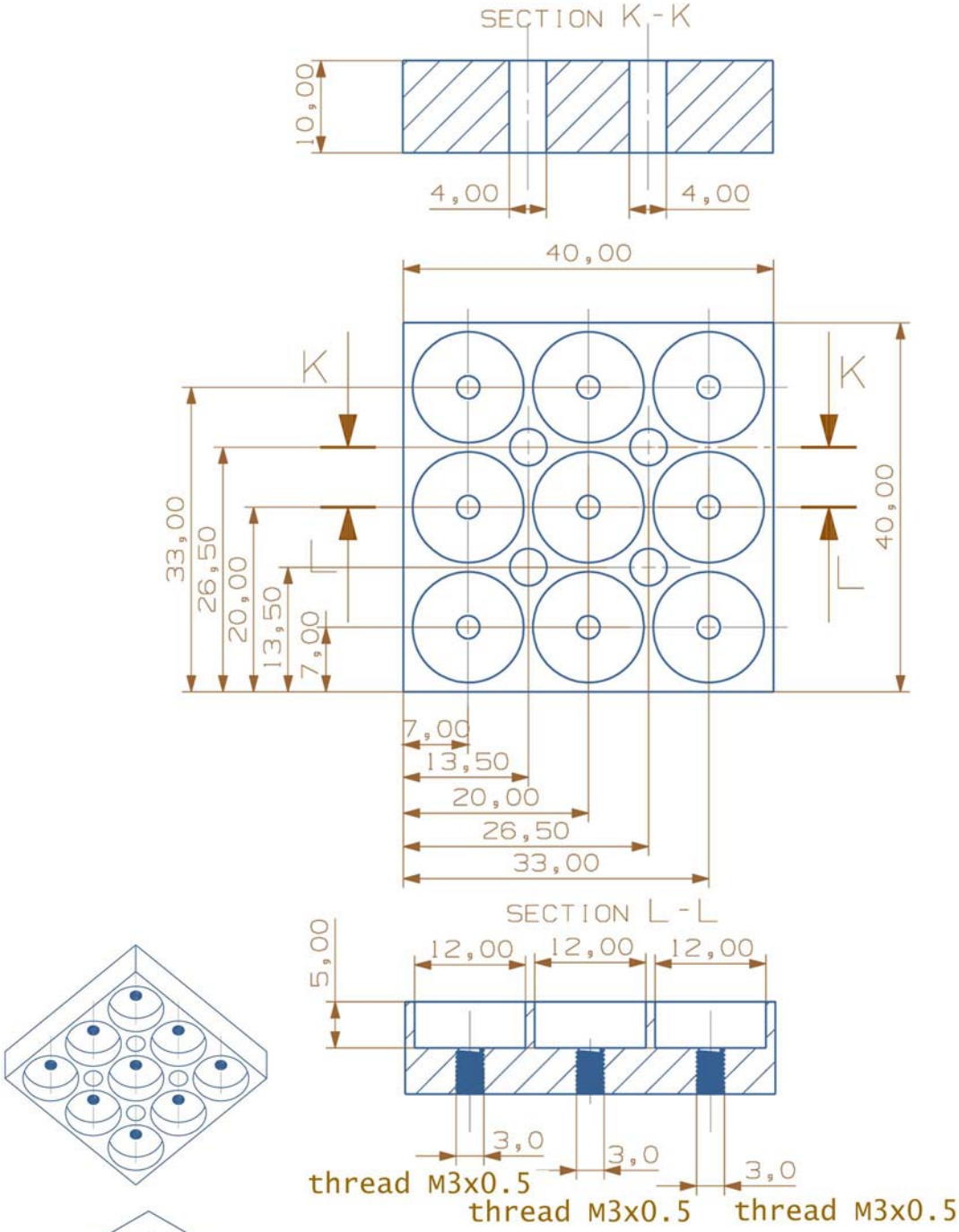

Part name:	Matrix of plane cells – PTFE lid
Material:	PTFE
QTY:	1
Designer:	P.J. Wojcik, p.wojcik@campus.fct.unl.pt